# DAMAGE INITIATION IN UNIDIRECTIONAL POLYMERIC COMPOSITES WITH MANUFACTURING INDUCED IRREGULARITIES

A Dissertation

by

SARAH AHMED EASSA ELNEKHAILY

Submitted to the Office of Graduate and Professional Studies of
Texas A&M University
in partial fulfillment of the requirements for the degree of

DOCTOR OF PHILOSOPHY

| | |
|---|---|
| Chair of Committee, | Ramesh Talreja |
| Committee Members, | Tahir Cagin |
| | Terry Creasy |
| | Anastasia Muliana |
| | Ankit Srivastava |
| Head of Department, | Ibrahim Karaman |

May 2018

Major Subject: Materials Science and Engineering

# ABSTRACT

In this work, the initiation of the first failure event in unidirectional polymer composites subjected to different loading conditions is studied. Two energy based point failure criteria – critical dilatational and critical distortional energy densities – are considered. Local stress fields are calculated by finite element models using micromechanical simulations to evaluate damage initiation in the matrix by a brittle failure mechanism (cavitation) and by an inelastic (yielding) process.

The disorder in the fiber distribution induced by manufacturing is quantified by defining the degree of nonuniformity (NU) of fiber distribution in the composite cross section. An algorithm to create simulations of the nonuniform distribution of fibers at different overall fiber volume fractions (FVFs) and different degrees of nonuniformity is developed. Representative volume elements (RVEs), with their minimum size determined on the basis of statistical analysis of interfiber distances are established for different fiber volume fractions.

Under tension applied normal to the fibers, brittle cavitation is found to occur before yielding in the matrix. This first failure event is assumed to induce local debonding of the fiber/matrix interface. Effects of variables such as the degree of nonuniformity and the fiber volume fraction, as well as the ratio of matrix to fiber stiffness modulus, on the initiation of brittle cavitation are studied.

Combined loading consisting of transverse tension and axial shear applied to unidirectional composites is studied next. It is found that under certain axial shear/transverse

tensile stress ratios brittle cavitation requirements are fulfilled. When only axial shear is imposed, cavitation requirements are not satisfied. Instead, matrix yielding is found to occur.

A parametric study of the matrix/fiber stiffness ratio shows that the mechanical strain to onset of cavitation under transverse tension increases as this ratio increases and approaches a constant value at high ratios under given fiber volume fractions and degree of nonuniformity. Also, under these conditions and under axial shear, the mechanical strain at which yielding initiates is found to increase with increasing the matrix/fiber stiffness ratio.

A limited study of the effects of matrix voids was also conducted and the preliminary results showed that the presence of voids affects the initiation of brittle cavitation by altering the local stress fields near the fiber/matrix interfaces.

# DEDICATION

TO MY FATHER,

TO MY MOTHER,

TO MY HUSBAND AND KIDS

(SAAD, AHMED, AND MAHMOUD)

# ACKNOWLEDGEMENTS

I would like to thank my committee chair, Dr. Ramesh Talreja for his continuous encouragement, guidance and support throughout my time at Texas A&M University. I would like to extend my appreciation to Dr. Tahir Cagin, Dr. Terry Creasy, Dr. Anastasia Muliana and Dr. Ankit Srivastava for serving as committee members.

Thanks also go to my friends and colleagues and the department faculty and staff for making my time at Texas A&M University a great experience.

I also want to extend my gratitude to our colleagues from IMDEA-materials, Madrid, Spain for their contributions through discussions providing insight and expertise that assisted this work.

Finally, I wish to express my love and gratitude to my beloved family; my parents (my beloved father and beloved mother), my husband and my kids for their encouragement, patience, understanding, and endless love.

# CONTRIBUTORS AND FUNDING SOURCES

## Contributors

This work was supervised by a dissertation committee consisting of Professor Ramesh Talreja, Professor Tahir Cagin, Associate Professor Terry Creasy, and Assistant Professor Ankit Srivastava of the Department of Materials Science and Engineering and Professor Anastasia Muliana of the Department of Mechanical Engineering.

All of the work conducted for the dissertation was completed by the student, under the advisement of Professor Ramesh Talreja of the Department of Materials Science and Engineering.

The periodic boundary condition given in Chapter 6 was provided by Mr. Herraez IMDEA-materials, Madrid, Spain.

## Funding Sources

Graduate study was supported by a scholarship from the Cultural Affairs and Missions Sector, The ministry of Higher Education, Arab Republic of Egypt.

# NOMENCLATURE

| | |
|---|---|
| FRP | Fiber reinforced polymer |
| UD | Unidirectional |
| FE | Finite element |
| GFRP | Glass fiber reinforced polymer |
| LM | Liquid molding |
| RTM | Resin transfer molding |
| VARI | Vacuum-assisted resin infusion |
| NU | Nonuniformity |
| FVF | Fiber volume fraction |
| VF | Volume fraction |
| Xt | Longitudinal tensile strength |
| Yt | Transverse tensile strength |
| $X_c$ | Longitudinal compressive strength |
| $Y_c$ | Transverse compressive strength |
| $\tau_{12(ult)}$ | Ultimate shear strength |
| $\varepsilon_{11\,(ult)}$ | Ultimate longitudinal strain |
| $\varepsilon_{22\,(ult)}$ | Ultimate transverse strain |
| $\gamma_{12(ult)}$ | Ultimate shear strain |
| T' | Transverse shear strength |
| T | Axial shear strength |
| FEA | Finite element analysis |

| | |
|---|---|
| RVE | Representative volume element |
| K(r) | Ripley's K function |
| A | Observable area |
| r | Radial distance from a selected fiber center |
| $I_k(r)$ | Number of fiber centers within the circle of radius r |
| $w_k$ | Correction factor |
| g(r) | Pair distribution function |
| x | The normal distance between the fiber surfaces |
| D | Fiber diameter |
| L | RVE side length |
| $U_v$ | Dilatational strain energy density |
| $U_d$ | Distortional strain energy density |
| $\Delta T$ | Thermal cooldown |
| $E_m$ | Elastic modulus for matrix |
| $E_f$ | Elastic modulus for fibers |
| $\nu_m$ | Poisson's ratio for matrix |
| $\nu_f$ | Poisson's ratio for fibers |
| $\alpha_m$ | Thermal expansion coefficient for matrix |
| $\alpha_f$ | Thermal expansion coefficient for fibers |
| u | Applied displacement |
| $\tau_y^{oct}$ | Octahedral shear stress at yielding |
| $\tau_{yo}^{oct}$ | Octahedral shear stress at yielding in pure shear |
| $\mu$ | Coefficient of internal friction |

| | |
|---|---|
| $p$ | Hydrostatic tensile stress |
| PBCs | Periodic boundary conditions |
| $\delta_x$ | Displacement applied in x direction |
| $\delta_z$ | Displacement applied in z direction |
| $\delta_y$ | Displacement applied in y direction |
| $U_x$ | Tensile displacement |
| $U_{xz}$ | Shear displacement |

TABLE OF CONTENTS

Page

ABSTRACT ..... ii

DEDICATION ..... iv

ACKNOWLEDGEMENTS ..... v

CONTRIBUTORS AND FUNDING SOURCES ..... vi

NOMENCLATURE ..... vii

TABLE OF CONTENTS ..... x

LIST OF FIGURES ..... xiii

LIST OF TABLES ..... xxv

1. INTRODUCTION ..... 1

2. DAMAGE IN UNIDIRECTIONAL FRP COMPOSITES ..... 8

2.1. Damage in unidirectional FRP composites ..... 8
2.1.1. Fiber dominated damage mechanisms ..... 9
2.1.2. Non- Fiber dominated damage mechanisms ..... 13
2.2. Manufacturing induced defects ..... 19
2.3. The interaction between manufacturing defects and damage ..... 21
2.4. Thermal residual stresses ..... 25

3. FAILURE THEORIES AT DIFFERENT SCALES ..... 28

3.1. Failure theories for unidirectional FRP composites ..... 28
3.1.1. Macro-scale ..... 29
3.1.2. Micro-scale ..... 35
3.2. Periodic versus random distribution ..... 36
3.3. Representative volume element (RVE) ..... 37
3.3.1. RVE minimum size ..... 39
3.3.2. RVE construction methodology ..... 41
3.4. Statistical description ..... 43
3.4.1. Ripley's K function ..... 44
3.4.2. Pair distribution function ..... 45
3.4.3. Nearest neighbor orientation ..... 46
3.4.4. Nearest neighbor distances ..... 47

3.4.5. Voronoi tessellation ..... 47
3.5. The aim of this work ..... 47

4. RVE CONSTRUCTION ..... 49

4.1. Algorithm for RVE generation ..... 49
4.2. Statistical characterization ..... 57
4.2.1. Second order intensity function ..... 57
4.2.2. Pair distribution function (g-function) ..... 59
4.2.3. Nearest neighbor orientation function ..... 61
4.2.4. Nearest neighbor distance function ..... 62
4.3. Determination of the RVE size ..... 62
4.3.1. Interfiber distances analysis ..... 63
4.3.2. von Mises and mean stress analysis ..... 71
4.4. Summary and conclusion ..... 74

5. DAMAGE INITIATION UNDER TRANSVERSE TENSILE LOADING ..... 76

5.1. Finite element analysis ..... 77
5.1.1. Overall/global mesh convergence ..... 78
5.1.2. Local mesh convergence ..... 79
5.1.3. Displacement versus traction boundary conditions ..... 84
5.2. Failure analysis ..... 87
5.3. Results and discussion ..... 91
5.3.1. Effect of fiber volume fraction ..... 99
5.3.2. Effect of degree of nonuniformity ..... 99
5.3.3. Effect of matrix/fiber stiffness ratio ..... 102
5.4. The effect of the presence of voids ..... 103
5.5. Summary and conclusion ..... 109

6. DAMAGE INITIATION UNDER AXIAL SHEAR LOADING ..... 110

6.1. Periodic boundary conditions ..... 110
6.2. Failure analysis ..... 117
6.3. Results and discussion ..... 120
6.3.1. Effect of degree of nonuniformity ..... 120
6.3.2. Effect of fiber volume fraction ..... 122
6.3.3. Effect of matrix stiffness ..... 124
6.4. Summary and conclusion ..... 126

7. DAMAGE INITIATION UNDER BIAXIAL LOADING ..... 127

7.1. Equi-biaxial tensile load ..... 128
7.1.1. Applied boundary condition ..... 128
7.1.2. Failure analysis ..... 129
7.2. Axial shear and transverse tensile load ..... 130
7.2.1. Boundary condition ..... 132
7.2.2. Failure analysis ..... 133

7.2.3. Summary and conclusion ..... 153

8. CONCLUSION ..... 155

8.1. Conclusion ..... 156
8.2. Recommended future work ..... 158

REFERENCES ..... 160

APPENDIX A NEAREST NEIGHBOR FUNCTIONS FOR DIFFERENT RVE REALIZATIONS ..... 188

APPENDIX B DAMAGE INITIATION SITES ..... 195

LIST OF FIGURES

Page

Figure 1. X-ray radiograph sequence of damage evolution by fibers breakage under increasing load. Reprinted from [21]. ..... 10

Figure 2. Damage of glass fiber composite by fiber splitting. Reprinted from [37]. ..... 12

Figure 3. Damage of carbon fiber composite by the formation of kink band. Reprinted from [37]. ..... 12

Figure 4. Initiation of damage in HTA/RTM6 [$90_2/0_7/90_2$]. Reprinted from [70]. ..... 14

Figure 5. a) Fiber-matrix debonds and b) debonds coalescence forming transverse cracks in glass fibers and vinyl-ester. Reprinted from [64]. ..... 15

Figure 6. Inclined matrix cracking under axial shear loading. Reprinted from [72]..... 16

Figure 7. The poker-chip test set-up. Reprinted from [75] ..... 18

Figure 8. Damage initiation by cavity formation from a poker chip test. Reprinted from [76]..... 18

Figure 9. Secondary cracks and fiber bridging due to the presence of voids. Reprinted from [92]. ..... 22

Figure 10. Nonuniform distribution of glass fibers in epoxy matrix. Reprinted from [90]. . 23

Figure 11. Nonuniform distribution of carbon fibers in epoxy matrix composites. Reprinted from [93]. ..... 23

Figure 12. The back and front of a nearly uniform glass fiber distribution in epoxy matrix with a transverse crack after a transverse tensile quasi-static test. Reprinted from [94]..... 24

Figure 13. Damage initiation at a resin-rich area. Reprinted from [14]. ..... 25

Figure 14. Fracture plane of a unidirectional lamina. The resolved normal stress $\sigma_n$ and shear stresses $\tau_{nl}$ and $\tau_{nt}$ acting on the plane. Reprinted from [137]. ..... 34

Figure 15. Estimation of Ripley's K function (K(r)) with edge effects in an observable area A. Reprinted from [66]..... 45

Figure 16. Different point patterns and the corresponding Ripley's K function (K(r)). Reprinted from [169]. ..... 45

Figure 17. The pair distribution function for different points pattern. Reprinted from [169]..... 46

Figure 18. Illustration of the maximum deviation from the initial fiber center position in a uniform square pattern for 50% fiber volume fraction. ..... 51

Figure 19. Illustration of the subcircle with 100% NU for 50% fiber volume fraction ..... 52

Figure 20. Examples of two possible new positions of fiber M for 100% NU for 50% fiber volume fraction ..... 53

Figure 21. Illustration of the maximum deviation from the initial fiber center position in a uniform square pattern for 40% fiber volume fraction. ..... 54

Figure 22. (a) The RVEs of the 40% fiber volume fraction, (b) The RVEs of the 30% fiber volume fraction with 100%, 60% and 30% of NU. ..... 55

Figure 23. Flowchart of the algorithm for constructing an RVE realization. ..... 56

Figure 24. Ripley's K function for three different fiber volume fractions (40%, 50%, 54% and 60%) for 100 % of NU. ..... 58

Figure 25. Ripley's K function for the generated fiber distributions with 100%, 60%, and 30% of NU as well as a square uniform distribution for 40% fiber volume fraction. ..... 58

Figure 26. The pair distribution function (g) for the generated distributions with 100%, 60%, and 30% of NU as well as a square uniform distribution for 40% fiber volume fraction. ..... 59

Figure 27. The pair distribution function (g) for the generated distributions with 100%, 60%, and 30% of NU as well as a square uniform distribution for 50% fiber volume fraction. ..... 60

Figure 28. The pair distribution function (g) for the generated distributions with 100%, 60%, and 30% of NU as well as a square uniform distribution for 50% fiber volume fraction. ..... 60

Figure 29. Nearest neighbor orientation function for a 30% fiber volume fraction and different degrees of NU. ..... 61

Figure 30. Nearest neighbor orientation function for a 50% fiber volume fraction and 100 % NU and uniform pattern. ..... 62

Figure 31. Frequency of occurrence of the first nearest neighbor distance (from center to center) in μm within the RVE realizations for 50% fiber volume fraction and degrees of NU of (a)100%, (b) 60% and (c) 30% for 484, 400, 100 and 16 fibers in an RVE. ..... 65

Figure 32. Frequency of occurrence of the second nearest neighbor distance (from center to center) in μm within the RVE realizations for 50% fiber volume fraction and degrees of NU of (a)100%, (b) 60% and (c) 30% for 484, 400, 100 and 16 fibers in an RVE. ..... 66

Figure 33. Frequency of occurrence of the third nearest neighbor distance (from center to center) in μm within the RVE realizations for 50% fiber volume fraction and degrees of NU of (a)100%, (b) 60% and (c) 30% for 484, 400, 100 and 16 fibers in an RVE. ..... 67

Figure 34. The maximum, mean and minimum frequencies of occurrence of the first nearest neighbor distances averaged over all distances plotted for 50% fiber volume fraction and degrees of NU of (a)100%, (b) 60% and (c) 30% NU for different RVE sizes. ..... 68

Figure 35. The maximum, mean and minimum frequencies of occurrence of the second nearest neighbor distances averaged over all distances plotted for 50% fiber volume fraction and degrees of NU of (a)100%, (b) 60% and (c) 30% NU for different RVE sizes. ..... 69

Figure 36. The maximum, mean and minimum frequencies of occurrence of the third nearest neighbor distances averaged over all distances plotted for 50% fiber volume fraction and degrees of NU of (a)100%, (b) 60% and (c) 30% NU for different RVE sizes. ..... 70

Figure 37. (a) The average von Mises stress and (b) the average mean stress for 40% fiber volume fraction and 100% NU for different RVE sizes at 0.4% transverse tensile strain. ..... 72

Figure 38. (a) The average von Mises stress and (b) the average mean stress for 50% fiber volume fraction and 100% NU for different RVE sizes at 0.3% transverse tensile strain. ..... 72

Figure 39. The dilatational strain energy density in MPa for different RVE sizes (a) 5x5 inner window, (b) 10x10 inner window and (c) 20x20 inner window for 40% fiber volume fraction and 100% NU at 0.4% mechanical strain ..... 73

Figure 40. (a) The average von Mises stress and (b) the average shear stress S13 for 40% fiber volume fraction and 100% NU for different RVE sizes at axial shear stress of 0.285 MPa. ..... 74

Figure 41. RVE construction with total 24x24 fibers and an inner window of 20x20 fibers. ..... 77

Figure 42. RVE-averaged von Mises stress against the number of elements for 50% fiber volume fraction and 100% NU. ..... 78

Figure 43. Different mesh sizes for local mesh convergence analysis. ..... 80

Figure 44. (a) The maximum von Mises stress (MPa) and (b) the maximum dilatational energy density (MPa) for 40% fiber volume fraction and 100% NU for different RVE sizes at 0.3% transverse tensile strain. ..... 81

Figure 45. Mises stress distribution in MPa (a) with linear elements, (b) with quadratic elements for the sub model shown in Figure 43 at 0.3% transverse tensile strain 82

Figure 46. Mises stress distribution in MPa (a) with linear elements, (b) with quadratic elements for the sub model shown in Figure 43 at 0.5% transverse tensile strain. ..... 82

Figure 47. Uniaxial transverse displacement boundary condition on a RVE realization. .... 83

Figure 48. The maximum values of dilatational energy density $U_v$ and distortional energy density $U_d$ as well as the principal stress ratios attained within RVEs versus applied transverse tensile strain with (a) Displacement boundary conditions and (b) Traction boundary conditions, for 40% fiber volume fraction and 100% degree of nonuniformity. ..... 85

Figure 49. The maximum values of dilatational energy density $U_v$ and distortional energy density $U_d$ as well as the principal stress ratios attained within RVEs versus applied transverse tensile strain with (a) Displacement boundary conditions and (b) Traction boundary conditions, for 50% fiber volume fraction and 100% degree of nonuniformity. ..... 86

Figure 50. The maximum values of dilatational energy density $U_v$ and distortional energy density $U_d$ as well as the principal stress ratios attained within RVEs versus applied transverse tensile strain with (a) Displacement boundary conditions and (b) Traction boundary conditions, for 60% fiber volume fraction and 100% degree of nonuniformity. ..... 87

Figure 51. Local positions where both dilatational and distortional energy densities may reach their threshold values. Reprinted from [76]. ..... 88

Figure 52. The maximum values of distortional energy density $U_d$ attained within RVEs versus applied axial shear strain for 54% fiber volume fraction and 100% degree of nonuniformity. ..... 90

Figure 53. An RVE with 50% fiber volume fraction and 100 % nonuniformity, showing the position of maximum dilatational and distortional energy densities under transverse tensile loading. ..... 93

Figure 54. The principal stress ratios and the ratio of maximum/mean principal stress versus applied strain for RVE shown in Figure 53. ..... 94

Figure 55. The maximum values of dilatational energy density $U_v$ and distortional energy density $U_d$ attained within RVEs versus applied strain for RVE shown in Figure 53. ..... 94

Figure 56. The maximum values of dilatational $U_v$ and distortional $U_d$ energy densities attained within different RVEs versus applied strain for 40% fiber volume fraction and (a) 100%, (b) 60% and (c) 30% NU. Solid lines represent distortional energy density and dotted lines represent dilatational energy density. ..... 96

Figure 57. The maximum values of dilatational $U_v$ and distortional $U_d$ energy densities attained within different RVEs versus applied strain for 50% fiber volume fraction and (a) 100%, (b) 60% and (c) 30% NU. Solid lines represent distortional energy density and dotted lines represent dilatational energy density. ..... 97

Figure 58. The maximum values of dilatational $U_v$ and distortional $U_d$ energy densities attained within different RVEs versus applied strain for 60% fiber volume fraction and (a) 100%, (b) 60% and (c) 30% NU. Solid lines represent distortional energy density and dotted lines represent dilatational energy density. ..... 98

Figure 59. Effect of FVF on the cavitation strain for (a) 40% FVF and (b) 60% FVF with uniform fiber distribution. ..... 100

Figure 60. Effect of FVF on the cavitation strain for (a) 40% FVF and (b) 50% FVF with 100% nonuniformity. ..... 101

Figure 61. The average mechanical strain at onset of cavitation versus the percent degree of nonuniformity for 40%, 50%, and 60 % fiber volume fraction in addition to maximum and minimum values. ..... 102

Figure 62.The effect of matrix/fiber stiffness ratio on the average mechanical strain at cavitation for 50% fiber volume fraction and 100% nonuniformity. ..... 103

Figure 63. The effect of the presence of circular void on cavitation near the initial cavity site, (a) part of the original RVE showing the void and the position of cavitation without voids, (b) The principal stress ratios and the ratio of maximum/mean principal stress versus applied strain and (c) The maximum values of dilatational energy density $U_v$ and distortional energy density $U_d$ attained within RVEs versus applied strain. ..... 104

Figure 64. The effect of the presence of circular void on cavitation away from the initial cavity site, (a) part of the original RVE showing the void and the position of cavitation without voids, (b) The principal stress ratios and the ratio of maximum/mean principal stress versus applied strain and (c) The maximum values of dilatational energy density $U_v$ and distortional energy density $U_d$ attained within RVEs versus applied strain. ..... 105

Figure 65. The effect of the presence of elliptical void on cavitation placed horizontally with loading direction, (a) part of the original RVE showing the void and the position of cavitation without voids, (b) The principal stress ratios and the ratio of maximum/mean principal stress versus applied strain and (c) The maximum values of dilatational energy density $U_v$ and distortional energy density $U_d$ attained within RVEs versus applied strain. ..... 106

Figure 66. The effect of the presence of elliptical void on cavitation placed vertically with loading direction, (a) part of the original RVE showing the void and the position of cavitation with and without void, (b) The principal stress ratios and the ratio of maximum/mean principal stress versus applied strain and (c) The maximum values of dilatational energy density $U_v$ and distortional energy density $U_d$ attained within RVEs versus applied strain. ..... 107

Figure 67. The effect of the presence of elliptical void with high aspect ratio on cavitation placed vertically with loading direction, (a) part of the original RVE showing the void and the position of cavitation with and without void, (b) The principal stress ratios and the ratio of maximum/mean principal stress versus applied strain and (c) The maximum values of dilatational energy density $U_v$ and distortional energy density $U_d$ attained within RVEs versus applied strain. 108

Figure 68. Nodes numbering of RVE for application of PBCs. ..... 112

Figure 69. 3D RVE construction with total 14x14 fibers. ..... 115

Figure 70. The maximum values of dilatational energy density $U_v$ and distortional energy density $U_d$ attained within RVEs versus applied transverse tensile strain with (a) Ordinary boundary conditions and (b) Periodic boundary conditions (PBCs) for 40% fiber volume fraction and 100% degree of nonuniformity. ..... 116

Figure 71. The principal stress ratios and the ratio of maximum/mean principal stress versus applied transverse tensile strain with (a) Ordinary boundary conditions and (b) Periodic boundary conditions (PBCs) for 40% fiber volume fraction and 100% degree of nonuniformity. ..... 117

Figure 72. The maximum values of dilatational energy density $U_v$ and distortional energy density $U_d$ attained within RVEs versus applied axial shear strain for 54% fiber volume fraction and 100% degree of nonuniformity. A nearly constant value of Uv =0.043 MPa is maintained at all applied shear strain values. ..... 118

Figure 73. The principal stress ratios and the ratio of maximum/mean principal stress versus applied axial shear strain for 54% fiber volume fraction and 100% degree of nonuniformity. ..... 119

Figure 74. The maximum values of dilatational energy density $U_v$ and distortional energy density $U_d$ attained within RVEs versus applied axial shear strain for 54% fiber volume fraction and 60% degree of nonuniformity. A nearly constant value of Uv =0.066 MPa is maintained at all applied shear strain values. ..... 119

Figure 75. The maximum values of dilatational energy density $U_v$ and distortional energy density $U_d$ attained within RVEs versus applied axial shear strain for 60% fiber volume fraction and 100% degree of nonuniformity. A nearly constant value of Uv =0.056 MPa is maintained at all applied shear strain values. ..... 120

Figure 76. The mean of the maximum values of distortional energy density $U_d$ attained within RVEs versus applied axial shear strain for 40% fiber volume fraction and different degree of nonuniformity. The values plotted are averages of multiple RVE realizations. ..... 121

Figure 77. The mean of the maximum values of distortional energy density $U_d$ attained within RVEs versus applied axial shear strain for 54% fiber volume fraction and different degree of nonuniformity. The values plotted are averages of multiple RVE realizations with maximum and minimum values. ..... 121

Figure 78. The mean of the maximum values of distortional energy density $U_d$ attained within RVEs versus applied axial shear strain for 60% fiber volume fraction and different degree of nonuniformity. The values plotted are averages of multiple RVE realizations with maximum and minimum values. ..... 122

Figure 79. The maximum values of distortional energy density $U_d$ attained within RVEs versus applied axial shear strain for 40%, 54% and 60% fiber volume fraction and 100 % of nonuniformity. ..... 123

Figure 80. The maximum values of distortional energy density $U_d$ attained within RVEs versus applied axial shear strain for 40%, 54% and 60% fiber volume fraction and 0% of NU (uniform distribution). ..... 123

Figure 81. The maximum values of distortional energy density $U_d$ attained within RVEs versus applied axial shear strain for 54% fiber volume fraction and 60% nonuniformity for two matrix stiffness values; 2.07 and 3.35 GPa. ..... 125

Figure 82. The maximum values of distortional energy density $U_d$ attained within RVEs versus applied axial shear strain for 40% fiber volume fraction and 0% nonuniformity for two matrix stiffness values; 2.07 and 3.35 GPa. ..... 125

Figure 83. A schematic illustration of commonly used biaxial fatigue specimens: a) Tubular, b) Cruciform and c) Off-axis flat. Reprinted from [212] ..... 127

Figure 84. Boundary conditions for an equi-biaxial displacement load. ..... 129

Figure 85. (a)The maximum values of dilatational energy density Uv and distortional energy density Ud and (b) Principal stress ratios and the ratio of maximum/mean principal stress, attained within RVEs versus applied strain under equi-biaxial tensile loads. ..... 130

Figure 86. A realization of 54% fiber volume fraction and 100 % nonuniformity. ..... 134

Figure 87. The principal stress ratios and the ratio of maximum/mean principal stress versus applied transverse tensile stress for the realization shown in figure 86. ..135

Figure 88. The maximum values of dilatational energy density $U_v$ and distortional energy density $U_d$ attained within RVEs versus applied transverse stress for the realization shown in figure 86. .....135

Figure 89. The principal stress ratios and the ratio of maximum/mean principal stress versus applied transverse stress attained within RVEs at axial shear stress/ transverse tensile stress ratio of 1/1 for the realization shown in figure 86. .....137

Figure 90. The maximum values of dilatational energy density $U_v$ and distortional energy density $U_d$ attained within RVEs at axial shear stress/ transverse tensile stress ratio of 1/1 for the realization shown in figure 86. .....137

Figure 91. The principal stress ratios and the ratio of maximum/mean principal stress versus applied transverse stress attained within RVEs at axial shear stress/ transverse tensile stress ratio of 1/8 for the realization shown in figure 86. .....139

Figure 92. The maximum values of dilatational energy density $U_v$ and distortional energy density $U_d$ attained within RVEs at axial shear stress/ transverse tensile stress ratio of 1/8 for the realization shown in figure 86. .....139

Figure 93. The principal stress ratios and the ratio of maximum/mean principal stress versus applied transverse stress attained within RVEs at axial shear stress/ transverse tensile stress ratio of 1/12 for the realization shown in figure 86. .....140

Figure 94. The maximum values of dilatational energy density $U_v$ and distortional energy density $U_d$ attained within RVEs at axial shear stress/ transverse tensile stress ratio of 1/12 for the realization shown in figure 86. .....140

Figure 95. The principal stress ratios and the ratio of maximum/mean principal stress versus applied transverse stress attained within RVEs at axial shear stress/ transverse tensile stress ratio of 1/20 for the realization shown in figure 86. .....141

Figure 96. The maximum values of dilatational energy density $U_v$ and distortional energy density $U_d$ attained within RVEs at axial shear stress/ transverse tensile stress ratio of 1/20 for the realization shown in figure 86. .....141

Figure 97. The principal stress ratios and the ratio of maximum/mean principal stress versus applied transverse stress attained within RVEs at axial shear stress/ transverse tensile stress ratio of 1/100 for the realization shown in figure 86. ...142

Figure 98. The maximum values of dilatational energy density $U_v$ and distortional energy density $U_d$ attained within RVEs at axial shear stress/ transverse tensile stress ratio of 1/100 for the realization shown in figure 86. .....142

Figure 99. Axial shear stress versus transverse tensile stress in MPa, for the realization shown in figure 86. Solid line represents the axial shear stress/ transverse tensile stress ratios with minimum principal stresses difference where cavitation requirements are fulfilled. The short-dashed lines describe the range in which the cavitation mechanism can occur because of the tolerance of 20% given to the attainment of hydrostatic tension. ..... 143

Figure 100. Axial shear stress versus transverse tensile stress in MPa for 40% fiber volume fraction and 0% nonuniformity. Solid line represents the axial shear stress/ transverse tensile stress ratios with minimum principal stresses difference where cavitation requirements are fulfilled. The short-dashed lines describe the range in which the cavitation mechanism can occur because of the tolerance of 20% given to the attainment of hydrostatic tension..... 144

Figure 101. Axial shear stress versus transverse tensile stress in MPa for 40% fiber volume fraction and 60% nonuniformity for three different realizations, a) realization 1, b) realization 2 and c) realization 3. Solid line represents the axial shear stress/ transverse tensile stress ratios with minimum principal stresses difference where cavitation requirements are fulfilled. The short-dashed lines describe the range in which the cavitation mechanism can occur because of the tolerance of 20% given to the attainment of hydrostatic tension..... 145

Figure 102. Axial shear stress versus transverse tensile stress in MPa for 40% fiber volume fraction and 100% nonuniformity for three different realizations, a) realization 1, b) realization 2 and c) realization 3. Solid line represents the axial shear stress/ transverse tensile stress ratios with minimum principal stresses difference where cavitation requirements are fulfilled. The short-dashed lines describe the range in which the cavitation mechanism can occur because of the tolerance of 20% given to the attainment of hydrostatic tension..... 146

Figure 103. Axial shear stress versus transverse tensile stress in MPa for 54% fiber volume fraction and 0% nonuniformity. Solid line represents the axial shear stress/ transverse tensile stress ratios with minimum principal stresses difference where cavitation requirements are fulfilled. The short-dashed lines describe the range in which the cavitation mechanism can occur because of the tolerance of 20% given to the attainment of hydrostatic tension..... 147

Figure 104. Axial shear stress versus transverse tensile stress in MPa for 54% fiber volume fraction and 60% nonuniformity for three different realizations, a) realization 1, b) realization 2 and c) realization 3. Solid line represents the axial shear stress/ transverse tensile stress ratios with minimum principal stresses difference where cavitation requirements are fulfilled. The short-dashed lines describe the range in which the cavitation mechanism can occur because of the tolerance of 20% given to the attainment of hydrostatic tension..... 148

Figure 105. Axial shear stress versus transverse tensile stress in MPa for 54% fiber volume fraction and 100% nonuniformity for three different realizations, a) realization 1, b) realization 2 and c) realization 3. Solid line represents the axial shear stress/ transverse tensile stress ratios with minimum principal stresses difference where cavitation requirements are fulfilled. The short-dashed lines describe the range in which the cavitation mechanism can occur because of the tolerance of 20% given to the attainment of hydrostatic tension.....149

Figure 106. Axial shear stress versus transverse tensile stress in MPa for 60% fiber volume fraction and 0% nonuniformity. Solid line represents the axial shear stress/ transverse tensile stress ratios with minimum principal stresses difference where cavitation requirements are fulfilled. The short-dashed lines describe the range in which the cavitation mechanism can occur because of the tolerance of 20% given to the attainment of hydrostatic tension.....150

Figure 107. Axial shear stress versus transverse tensile stress in MPa for 60% fiber volume fraction and 60% nonuniformity for three different realizations, a) realization 1, b) realization 2 and c) realization 3. Solid line represents the axial shear stress/ transverse tensile stress ratios with minimum principal stresses difference where cavitation requirements are fulfilled. The short-dashed lines describe the range in which the cavitation mechanism can occur because of the tolerance of 20% given to the attainment of hydrostatic tension.....151

Figure 108. Axial shear stress versus transverse tensile stress in MPa for 60% fiber volume fraction and 100% nonuniformity for three different realizations, a) realization 1, b) realization 2 and c) realization 3. Solid line represents the axial shear stress/ transverse tensile stress ratios with minimum principal stresses difference where cavitation requirements are fulfilled. The short-dashed lines describe the range in which the cavitation mechanism can occur because of the tolerance of 20% given to the attainment of hydrostatic tension.....152

Figure 109. Frequency of occurrence of the first nearest neighbor distance (from center to center) in μm within the RVE realizations for 40% fiber volume fraction and degrees of NU of (a)100%, (b) 60% and (c) 30% for 484, 400, 100 and 16 fibers in an RVE. .....189

Figure 110. Frequency of occurrence of the second nearest neighbor distance (from center to center) in μm within the RVE realizations for 40% fiber volume fraction and degrees of NU of (a)100%, (b) 60% and (c) 30% for 484, 400, 100 and 16 fibers in an RVE.....190

Figure 111. Frequency of occurrence of the third nearest neighbor distance (from center to center) in μm within the RVE realizations for 40% fiber volume fraction and degrees of NU of (a)100%, (b) 60% and (c) 30% for 484, 400, 100 and 16 fibers in an RVE. .....191

Figure 112. Frequency of occurrence of the first nearest neighbor distance (from center to center) in μm within the RVE realizations for 60% fiber volume fraction and degrees of NU of (a)100%, (b) 60% and (c) 30% for 484, 400, 100 and 16 fibers in an RVE. ..... 192

Figure 113. Frequency of occurrence of the second nearest neighbor distance (from center to center) in μm within the RVE realizations for 60% fiber volume fraction and degrees of NU of (a)100%, (b) 60% and (c) 30% for 484, 400, 100 and 16 fibers in an RVE..... 193

Figure 114. Frequency of occurrence of the third nearest neighbor distance (from center to center) in μm within the RVE realizations for 60% fiber volume fraction and degrees of NU of (a)100%, (b) 60% and (c) 30% for 484, 400, 100 and 16 fibers in an RVE. ..... 194

Figure 115. Different RVEs (a-e) with 40% fiber volume fraction and 100% nonuniformity, showing the position of maximum dilatational $U_v$ and maximum distortional $U_d$ energy densities under transverse loading. ..... 196

Figure 116. Different RVEs (a-e) with 40% fiber volume fraction and 60% nonuniformity, showing the position of maximum dilatational Uv and maximum distortional Ud energy densities under transverse loading. ..... 197

Figure 117. Different RVEs (a-e) with 40% fiber volume fraction and 30% nonuniformity, showing the position of maximum dilatational Uv and maximum distortional Ud energy densities under transverse loading. ..... 198

Figure 118. Different RVEs (a-e) with 50% fiber volume fraction and 100% nonuniformity, showing the position of maximum dilatational Uv and maximum distortional Ud energy densities under transverse loading. ..... 199

Figure 119. Different RVEs (a-e) with 50% fiber volume fraction and 60% nonuniformity, showing the position of maximum dilatational Uv and maximum distortional Ud energy densities under transverse loading. ..... 200

Figure 120. Different RVEs (a-e) with 50% fiber volume fraction and 30% nonuniformity, showing the position of maximum dilatational Uv and maximum distortional Ud energy densities under transverse loading. ..... 201

Figure 121. Different RVEs (a-e) with 60% fiber volume fraction and 100% nonuniformity, showing the position of maximum dilatational Uv and maximum distortional Ud energy densities under transverse loading. ..... 202

Figure 122. Different RVEs (a-e) with 60% fiber volume fraction and 60% nonuniformity, showing the position of maximum dilatational Uv and maximum distortional Ud energy densities under transverse loading. ..... 203

Figure 123. Different RVEs (a-e) with 60% fiber volume fraction and 30% nonuniformity, showing the position of maximum dilatational Uv and maximum distortional Ud energy densities under transverse loading. ..... 204

LIST OF TABLES

Page

Table 1. Materials properties for transverse tensile loading ..... 83

Table 2. Nodes with maximum dilatational and distortional energy densities for the RVE shown in Figure 53 ..... 95

Table 3. Applications of different load types using PBCs ..... 114

Table 4. Materials properties for combined axial shear and transverse tension..... 132

# 1. INTRODUCTION

The end of the first few decades of the 20$^{th}$ century experienced very wide and mature steps in the development of composites industry. Composites are categorized as new materials and materials of the future, although they were introduced in the early man's civilization stages. In fact, they have been present since the beginning of time. The general definition of composite material is that it is a material that is composed of at least one discontinuous phase (reinforcement) in a continuous one (the binder or matrix). This definition is observed in many objects surrounding us, e.g., wood, plants, birds and animals and even human beings.

Maybe man recognized these properties in composite materials surrounding him and with his needy potentials, managed to produce his manmade composite structures. Back at 6000 B.C. ancient Egyptians were the first to create composite structures based on the main reinforcement-binder concept by mixing different components together. They were the first to produce mud bricks composites in which straws were embedded -as a fibrous reinforcing material - in mud to increase its strength [1]. These bricks are still in use in Egypt's countryside.

Ancient Egyptians are also the first to be known in the production of papyrus writing papers. In their production, layers of papyrus plant are placed on top of each other where one layer is at a right angle to the other, which is known nowadays as a cross ply laminate. Papyrus papers were an advance in such civilization by which information managed to be inherited to subsequent generations [1].

Another form of a composite material showed incredible significance in the field of construction is concrete [2]. Concrete is known to be the main structural material in the Roman Empire. Concrete alone -as a mixture of cement, aggregates (gravel, crushed stones) and sand- can withstand compressive loading only. To increase its resistance against tension, it is reinforced by embedding steel rods. At first it was suggested that steel rods are added to increase the cohesion of concrete not to increase its tensile strength [3]. Today, concrete is considered an economic and pioneering architectural building material.

Despite the continues improvement over the centuries, the past fifty years has experienced a tremendous increase in the development of composite materials. Developments took place either in the type of reinforcement and/or matrix materials or in their manufacturing techniques.

Composites, in general, can be classified based on the type of matrix to: polymer matrix, metallic matrix and ceramic matrix composites or based on the geometry of the reinforcing component to fiber, particulate and whisker/flakes reinforced composites.

Glass fibers are the most common of all reinforcing fibers for their relatively low cost and high strength. They are produced as continuous/long fibers or discontinuous/short fibers. Continuous glass fibers are very popular. The first known attempt to produce glass fibers was by the ancient Egyptians, although they were coarse in diameter. Centuries and generations went by till the year 1939, when the first mass production of glass fibers took place by “Owens-Corning Fiberglass Corporation” [4]. Soon after, fiber glass gained an extensive experience in different fields especially the aerospace industry for both civilian and military products particularly in polymeric matrix composites. For example, E-Glass laminates has been used in aerospace industry for many years starting with the Boeing 707

in the 1950s. Now fiber glass becomes a superior in other non-aerospace applications, for example; automotive, bridges and wind energy because of their tensile strength, temperature resistance and dimensional stability.

Fiber reinforced polymeric (FRP) matrix composites are being used in different fields, among them are aerospace, automotive and wind energy applications. They are exceedingly replacing traditional structural components. The composite materials are selected to fulfil the application requirements which is usually a high strength to weight ratio. Polymer matrices act as binders to the fibers and transfer the loads to them.

The polymer material is selected providing that it fulfils required physical and mechanical properties. They can be classified into thermoplastics and thermosettings, based on their structure. Thermoplastics consist of linear or branched hydrocarbon chains that can be melted when heated and thus can be reformed. Examples include polyethylene, nylons and polyether imide. Thermosetting polymers have cross-linked or network structures with an irreversible bonding when formed. Once solidified they cannot melt when heated, instead they will decompose. Common examples of thermosets are epoxy and polyester that are extensively used in different engineering applications with high performance reinforcing fibers such as glass fibers [5]. In the meanwhile, there is a tendency to use thermoplastic polymers because of their ability for recycling [6,7].

Despite that the aerospace industry was the first to benefit from glass FRP matrix composites, wind turbine structural components are fastest growing application. There is a universal interest nowadays to alternate from a fossil fuel to a renewable energy source. Wind energy is one of the most important renewable energy resources. By the year 2022, the Egyptian government is determined to produce 20% of the generated electricity from

renewable energy. This includes a 12% contribution from wind energy, translating about 7200 MW grid-connected wind farms [8]. In 2016, wind turbines in the United States were the source of nearly 6% of total electricity generated. The US government aims to increase the wind power supplies to be 10% of the nation's electrical demand in 2020, 20% in 2030, and 35% in 2050 [9].

Composite components are usually affected by a complex multi-axial loading, both mechanically and thermally. Ensuring high reliability becomes an essential issue especially when it comes to large sizes composites such as wind turbine blades that work against high wind and gravitational loads for 20-25 years. Thus, failure studies of such materials are essential to ensure its long service life.

The composite microstructure is a primary parameter in the field of damage and failure.

Enhancing the properties will be achieved by controlling the microstructure and the properties in the micro and nano scales [10,11]. The microstructure includes details concerning the composite structure as well as all existing defects. The choice of a manufacturing process for a polymeric matrix composite strongly influences its microstructure. There are different types of manufacturing processes in the field of unidirectional polymeric composites. Depending on the application, the nature of matrix material, and the shape and form of the reinforcement added, the manufacturing process is selected.

For thermosetting polymer matrix composites, fabrication processes can be broadly classified into wet -forming processes and processes using prepregs. Wet-forming processes include hand lay-up, resin transfer molding, filament winding and pultrusion [12]. Prepregs

are usually partially cured sheets of fibers or woven. Processes use prepregs include bulk molding compounds and sheet molding compounds. Fibers distribution are more uniform in processes using prepregs compared to wet-forming processes. They also allow maintaining high fiber volume fractions for high quality composite structures which are high in cost, typical for aerospace industry.

Composite applications, particularly in non-aerospace fields, can be further increased, if the performance requirements can be met at reduced cost. Reducing cost leads to less-controlled manufacturing and thus, different defects such as voids, resin rich areas, fiber nonuniform distribution, and fiber misalignments are created.

To what extent would these defects affect the composite performance? It is known that defects can be considered the main source of damage initiation. For example, in metallic materials the presence of microcracks, inclusions or even sharp-edged phases will act as stress raisers. These stress concentration sites might lead to the initiation and propagation of cracks that cause final failure.

A reliable and consistent performance assessment strategy must therefore account for such defects and their consequences on failure. Currently, the industry does not have adequate tools to evaluate the effects of these defects on composite performance. The common approach is to conduct tests, and based on these they design with factors of safety. This approach adds cost and does not allow using the data if the manufacturing process changes. Besides, it is just a difficult task to experimentally study local stress and local strain distributions at the scale of a conventional specimen size [13].

Not only does the microstructural details affect the damage and failure of composites, but also the type of loading imposed at such anisotropic materials affects the type of damage

mechanism that could be encountered. Because of the anisotropic nature of unidirectional/continuous fiber composites, more than one damage mechanism could be observed. The type as well as the direction of loading will determine the damage mechanism. In general, damage mechanisms could be classified to fiber dominated and matrix dominated. However, matrix dominated damage mechanisms are observed to be the first to take place.

Prediction of the damage and failure mechanisms in composite structures and the use of developed numerical and/or analytical technologies are worldwide interests. Those researches manage to lower the dependency on experimental work.

The evolution in the micromechanical analysis manages to consider the effect of the constituents of the composite on the contrary to the macro or homogenized techniques. Properties such as thermal expansion coefficient can be accounted for each component. Thus, in the micromechanical analysis, thermal residual stresses can be implemented which proved to be important when damage or failure are studied.

The question now is that: Shall we deal with the whole structure of a real component under investigation in the micro-scale? The answer is NO. It will take a lot of effort and time to study damage of the whole structure in the micro-scale. Instead, a representative volume element of the whole structure is adopted.

The work presented here is aimed at studying damage initiation by conducting a systematic study of the effect of nonuniform fiber distribution, as a manufacturing defect, on damage initiation under different loading conditions in unidirectional composites. The focus here is to find the lowest applied loading condition that initiates damage. In many applications, this can provide a good basis for design, particularly when no damage is allowed. If causes of damage initiation are addressed properly, then higher service life of components could be achieved.

# 2. DAMAGE IN UNIDIRECTIONAL FRP COMPOSITES

A great effort is being made to establish a complete understanding of the damage and failure mechanisms encountered in FRP composites. The complex nature of such materials increases the difficulty in this subject. A reliable way to do so is to study their damage and failure mechanisms under different length scales. Experimentally, this is not an easy subject especially when dealing with small length scales such as micro or nano scales. Micro-mechanical analysis is taking very wide steps in the field. But before giving details of such analysis, an overview of the possible damage mechanisms encountered in FRP composites should be presented. In this chapter, different damage mechanisms of unidirectional FRP composites are given. From this, one can find out how damage mechanisms of such materials depend on the type of loading and on the loading direction with respect to the fiber axis. In addition to that, the manufacturing induced defects such as voids and the nonuniform distribution of fibers will be surveyed along with their contribution to damage.

## 2.1. Damage in unidirectional FRP composites

Damage is defined as an irreversible reaction that results in properties degradation. Because of the complex structure of the unidirectional/continuous (UD) fiber composites, damage initiation mechanism depends on several factors. In fibrous composites, fibers are aligned in certain direction. The type as well as the direction of loading will determine the damage mechanism. In general, damage could be fibers dominated or non-fibers dominated (either in the matrix or in the fiber-matrix interface) [14]. A transverse loading is referred to the loading taken place at a normal direction to fibers' axis. On the other hand, an on-axis loading refers to that loading that is within the same direction as the fibers' axis. The first

form of damage that is observed, however, is the initiation of microcracks in the matrix [15]. These microcracks, usually named transverse micro cracks, are transverse to the loading direction. When they form they lead to degradation in both strength and stiffness which reduces the efficiency of the composite component. Below is a brief illustration of different failure mechanisms observed in a unidirectional composite.

### 2.1.1. Fiber dominated damage mechanisms

#### 2.1.1.1. On-axis tensile loading

It is observed that when either quasi static or tension-tension fatigue loading are applied to fiber composite along fiber axis, fiber breakage is taken place when the tensile load is sufficiently high. Stochastic fiber failure follows the Weibull distribution when a monotonic loading of a UD fiber composites is applied [16]. When under on-axis tensile loading, failure is developed by two features: (1) the Weibull distribution of fiber strength and (2) the stress redistribution around a broken fiber [17].

It is believed that when a fiber breaks, it will lose its ability to transfer load which will be concentrated to adjacent fibers [18,19]. The probability of failure of the adjacent fibers increases and at certain applied load, fiber clusters will fail [20]. The clusters grow in size with increasing strain. Final failure of the composite occurs when one of the developed clusters reaches a critical size.

Fibers fracture within certain steps before the catastrophic failure of the whole composite [21]. This was in-situ observed in [21] using a composite with DGEBA epoxy as a matrix and quartz fibers as the reinforcement. Few fibers where initially broken and because of their low number, it was called singlets fracture followed by doublets, triplets,

etc., till N number of fibers are failed, just before the complete failure of the composite, Figure 1.

The stress redistributions around single fiber breaks have been investigated extensively either theoretically e.g., by shear-lag analysis [22,23,24] or numerically using the finite element (FE) method [25-31].

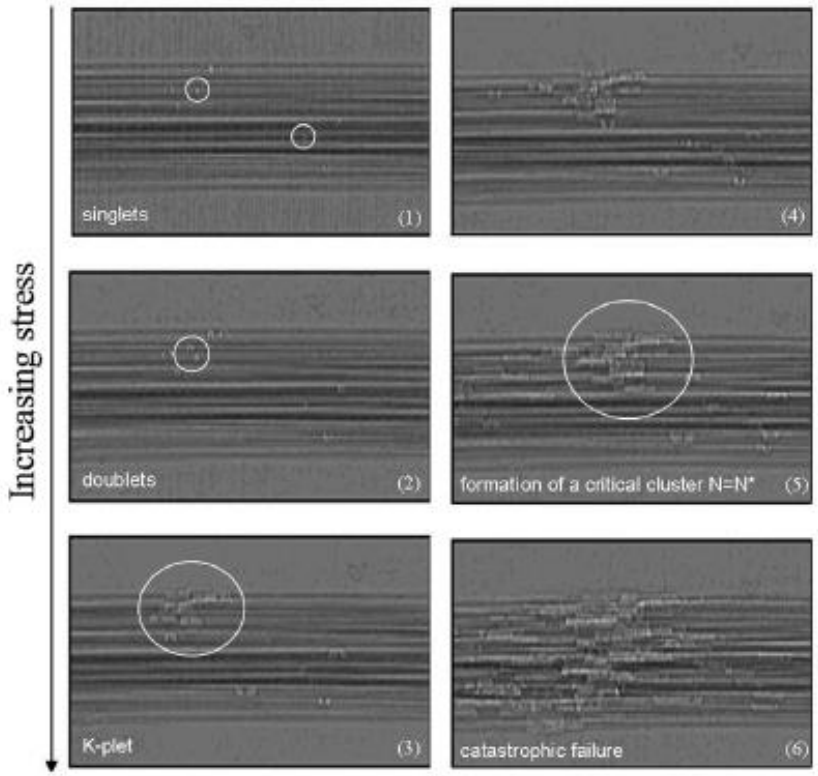


**Figure 1. X-ray radiograph sequence of damage evolution by fibers breakage under increasing load. Reprinted from [21].**

#### 2.1.1.2. On-axis compressive loading

It is unusual to observe a pure compressive loading applied to composite structures along the fibers axis. However, compressive stresses could be established from multiaxial

loading, bending and impact loadings. In general, when applying compressive load components, having high length/cross sectional area aspect ratios, buckling occurs. This concept is the basis of models and analysis concerning UD fiber composites. Previous intensive studies of compressive failure have been carried out [32-45].

Compressive failure has been studied using different theoretical and numerical models. The first models used elasticity theories in analysis e.g.; Rosen [32, 46] and Schuerch [47]. They were then followed by models taking into consideration the inelastic behavior of matrix materials e.g.; Argon [35] and Budiansky [48] including initial fiber misalignments as an initial defect. Other defects were studied such as fibers waviness [49].

It was pointed out in [50] that in case of fibers aligned in the direction of loading, four mechanisms of failure have been identified, elastic micro buckling, matrix failure, plastic micro buckling and fiber crushing or splitting, Figure 2.

Models carried out by Kyriakides et al [51] followed by those of Hsu et al [52], confirmed that composite kink bands are formed after microbuckling, Figure 3.

It is proved that the presence of fibers imperfections such as misalignments, affects the compressive strength of a composite [43], as well as facilitate the kink band formation. Although some numerical models [41, 53] have shown that kink bands are to be formed even if we are dealing with perfect aligned fibers or straight fibers.

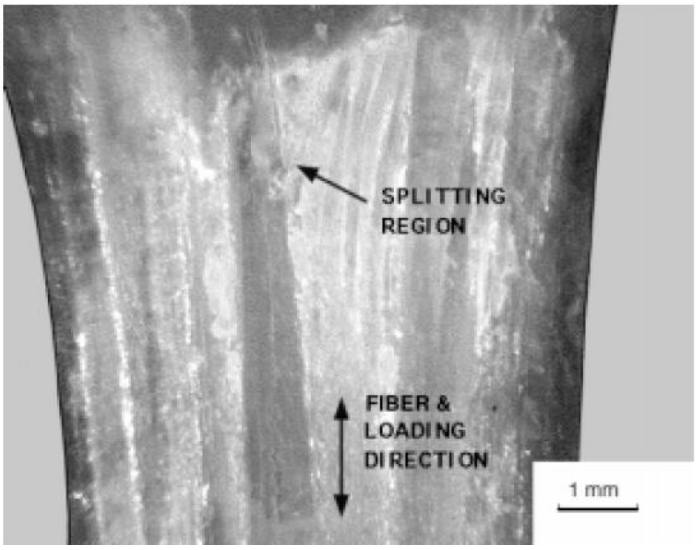


**Figure 2. Damage of glass fiber composite by fiber splitting. Reprinted from [**37].

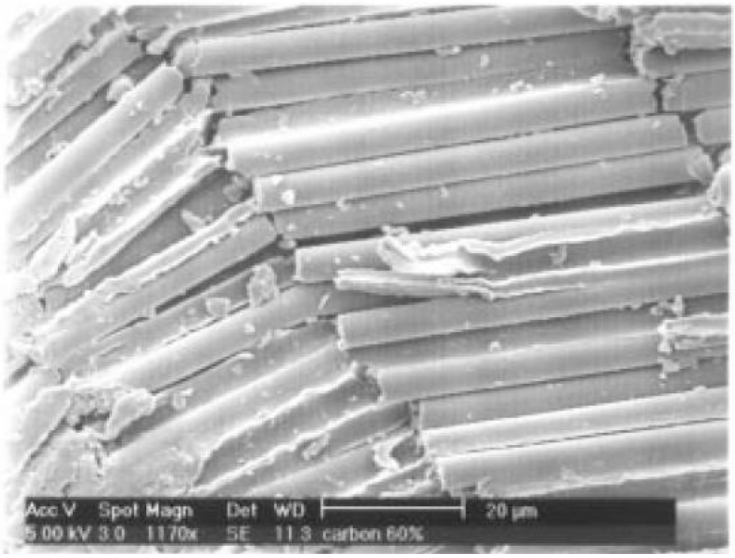


**Figure 3. Damage of carbon fiber composite by the formation of kink band. Reprinted from [37**].

### 2.1.2. Non- Fiber dominated damage mechanisms

#### 2.1.2.1. Transverse/off axis compressive loading

The initiation of compressive damage usually occurs through the formation of transverse cracks [54]. There have been many extensive studies to determine the crack angle under uniaxial compressive loading. This angle was found to be in the range 50-60$^{o}$ for UD composites [44,55-58] although this angle in neat epoxies shows several degrees lower than that when epoxies are being the matrices [59-61].

Zhou et al [62] conducted both experimental and computational microscale studies in unidirectional glass fiber reinforced polymer composites (GFRP) under axial and off-axis compressive loading. Mechanisms of damage initiation and propagation were studied under scanning electron microscope at various off axis angles including 90$^{o}$ (transverse loading). It was concluded that shear cracking is the main failure mechanism when the angle between fibers axis and the loading axis is relatively high.

#### 2.1.2.2. Transverse tensile loading

Numerous observations, e.g. [63-68], have shown that fiber-matrix debonding is the most likely first mechanism of failure under transverse tensile loading with a subsequent transverse ply cracking, while matrix yielding leading to shear band and subsequent crack formation are also possible mechanisms.

Jun Koyanagi et al [69] studied the damage mechanism of carbon/epoxy composite under transverse loading with different strain rates and different temperatures. Based on their observations, it was concluded that the damage mechanism under transverse tension can take place either within the matrix or at the fiber/matrix interface depending on the strain rate. It

was found that at high strain rates damage is dominant at the fiber/matrix interface, while matrix damage is observed when lower strain rates are applied.

In [70] two composites with two types of carbon fibers with different composite layups were investigated under three-point bending tests. Scanning electron microscope was used for the in-situ observation of the onset of microscopic composite failure. It was found that the tensile stress acting on the $90^o$ ply resulted in transverse ply cracking which was initiated by fiber/matrix debonding, Figure 4.

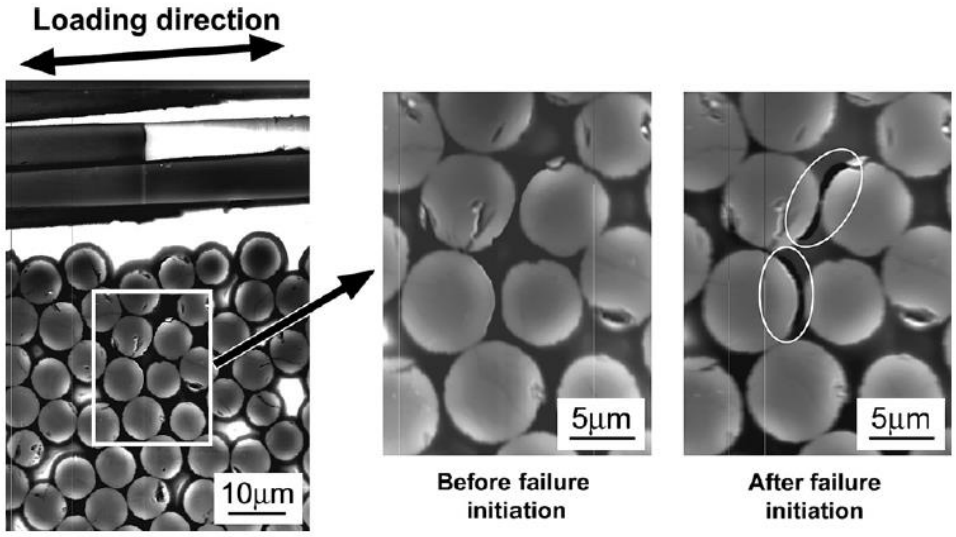


**Figure 4. Initiation of damage in HTA/RTM6 [$90_2/0_7/90_2$]. Reprinted from [70**].

In [64] a cross-ply laminate with a $[0, 90]_s$ layup composed of glass fibers and vinyl-ester resin were tested under fatigue loading. To observe the mechanism behind the formation of transverse cracks, static tensile test was performed. An in-situ observation for the onset of damage was taken place in transverse plies. It was suggested that debonds

occurred first, then by increasing the load, these debonds coalesced forming a macroscopic transverse crack, Figure 5.

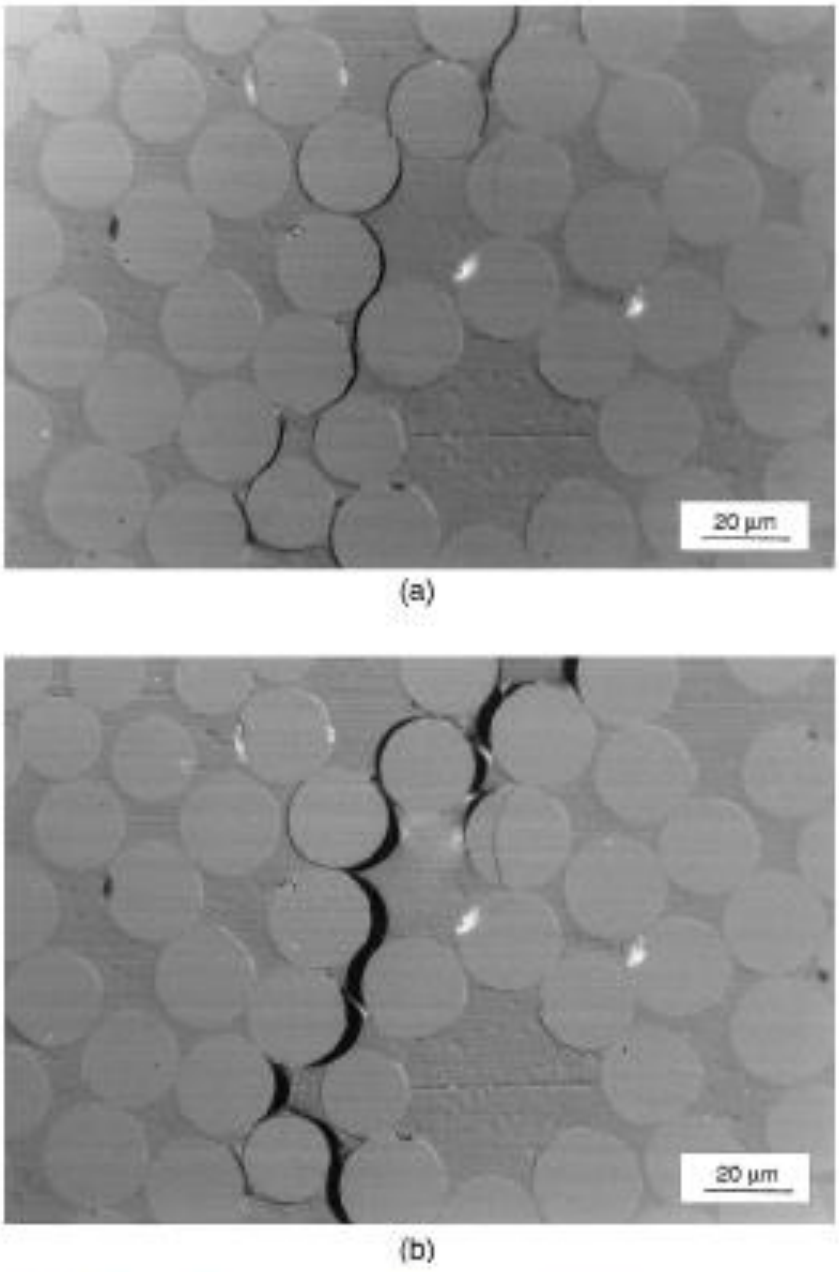


**Figure 5. a) Fiber-matrix debonds and b) debonds coalescence forming transverse cracks in glass fibers and vinyl-ester. Reprinted from** [**64**].

### 2.1.2.3. Inclined loading

Plumtree et al [71] studied the damage mechanisms in a unidirectional carbon fiber reinforced epoxy matrix composite under off-axis cyclic loading. From microstructure examination, they found matrix shear fracture in the form of inclined matrix cracks between the fibers. These cracks were observed in the resin rich areas. Gamstedt et al [72] also observed inclined matrix cracks under an applied axial shear stress, Figure 6. It is suggested in [73] that the inclined cracks are the result of the tensile component of the local stress in the matrix.

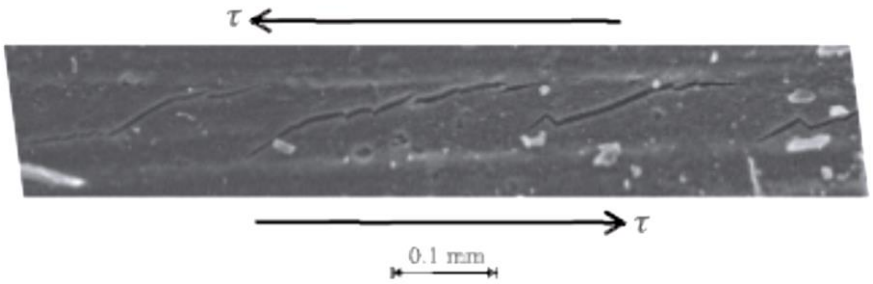


**Figure 6. Inclined matrix cracking under axial shear loading. Reprinted from [72].**

The strain to failure in polymer matrix composites under transverse tension is lower than the strain to failure of pure polymers. A triaxial stress state is highly suggested to be established in the matrix in the vicinity of fibers/matrix interface. This triaxial stress state is due to the fiber-fiber interaction and thus it depends on the inter-fiber distances.

Asp et al. [74,75,76] analyzed damage initiation either by cavitation or by yielding in glassy polymers reinforced by stiff fibers. In those studies, experiments were established under different stress states, e.g., uniaxial tension, uniaxial compression, biaxial tension, biaxial compression and triaxial tension. They accounted for the fact that the local stress

state in the matrix between fibers is triaxial even when a uniaxial transverse tension is applied to the composite. They then studied the failure modes in glassy polymers under triaxial stress states and identified cavitation in the polymer matrix as a brittle failure mechanism when the stress state is hydrostatic tension, i.e. with equal tensile principal stresses. The energy required to form cavitation was determined by an independent test, known as the poker-chip test [75] on four different epoxy materials.

The specimen in the poker-chip test is in the form of a poker-chip and it is placed under an equiaxial stress state, Figure 7. The specimen is held between two rigid bodies and a triaxial tensile stress state is maintained to account for that established in the composite when under tensile loading. It was observed that failure occurred in these materials by the formation of a cavity, Figure 8. Thus, it was suggested that within the composite, the matrix between the fibers will be under a triaxial stress state that will lead to the formation of a cavity within the matrix near the fiber/matrix interface.

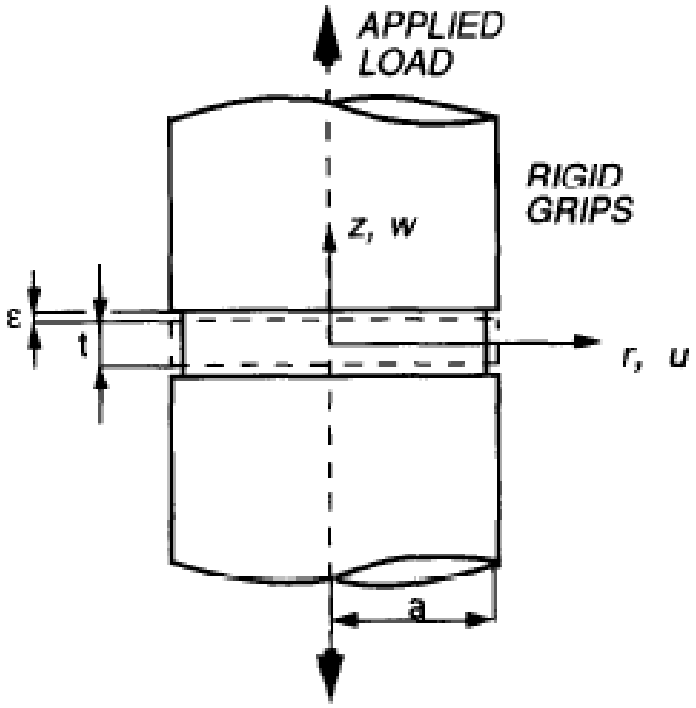


**Figure 7. The poker-chip test set-up. Reprinted from [75]**

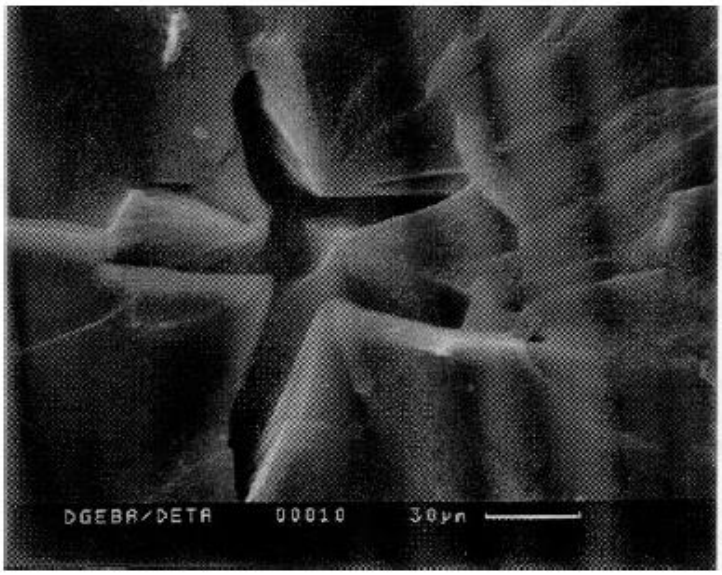


**Figure 8. Damage initiation by cavity formation from a poker chip test. Reprinted from [76].**

## 2.2. Manufacturing induced defects

It is seldom or nearly impossible to produce a material that is free of defects. Defects are introduced either because of the lack of the structural design or because of uncontrollable manufacturing tools. There are different manufacturing tools used in the production of unidirectional FRP composites. Manufacturing tools such as pressure, curing temperature, viscosity, permeability, fiber volume fraction (FVF), and resin filling time, all will affect the final composite microstructure and the type and amount of existing material defects [77]. There are different manufacturing processes that are used in the production of unidirectional FRP composites. Each can create manufacturing induced defects in the fibers, matrix and the fiber/matrix interface. For more information about manufacturing processes, one can refer to [78].

Autoclaving process is a common manufacturing technique for thermosetting polymeric composites especially for aerospace applications. Autoclave process either using prepregs or wet lay-ups gives a very high composite quality and are known to be high in cost. Unfortunately, one cannot use it when it comes to the production of very large structures. e.g. wind turbine blades that can reach lengths to up to 134 meters. In addition, because of its high accuracy, there will be a tradeoff between quality and cost. It is found also that any insufficient pressure or vacuum might lead to the creation of defects, such as voids, fiber misalignment and resin rich areas. Thermoset prepregs were developed to obtain composite parts with high fiber volume fractions (~65%) with less than 2% of voids content [79].

Liquid molding (LM) processes, on the other hand, is considered one of the widely used techniques in the production of such composites. The resin is forced to infuse into a dry

preform in which the resin is cured. The driving force to infuse the resin comes from the pressure gradient established between both the inlet and the outlet of the mold [80,81]. LM processes can be classified to closed molding techniques, such as resin transfer molding (RTM), and open molding ones, such as vacuum-assisted resin infusion (VARI). Both, are adopted in many other non-aerospace applications. Examples of those applications are automotive and wind energy in which higher production rates with an adequate part quality at low cost are now all manufacturers interests. However, the low-cost liquid molding, using open mold techniques, are usually adopted for large composite structures. Unfortunately, lowering the cost of manufacturing often leads to less control of the manufacturing process, which in turn induces material defects. Different defects are observed that are introduced within the infusion step. The most encountered defects are dry zones, voids, fibers' misalignment and fibers' nonuniform distribution.

It is a worldwide challenge to produce polymeric composites free of defects or at least to reduce those uncontrollable defects. It is worth mentioning that today different techniques are used which are based on automation, although they are still limited to certain manufacturing processes such as Filament winding (FW), Automated tape layup (ATL) and Automated fiber placement (AFP). A lot of research is conducted to expand composites manufacturing automation. The main aim is to increase the speed of production and at the same time, increase manufacturing accuracy. This procedure is in higher priority for aerospace applications [82,83,84]. Automation will also decrease the cost of production and lead to limiting manual layups dependence [82]. It is recommended to review such novel manufacturing techniques in reference [79].

Defects within a single ply could be in the matrix (e.g; voids, porosity, resin-rich areas, inclusions (e.g. dust)), in the fiber (e.g; fiber breakage, waviness, fibers cluster and fibers' nonuniform distribution) or at the fiber matrix interface (e.g; unbonded fiber/matrix interface) [14, 66,67,85-90]. These defects can affect the mechanism of damage initiation and subsequent damage propagation.

### 2.3. The interaction between manufacturing defects and damage

Voids are one of the most common defects in nearly all manufacturing techniques. The presence of voids and air entrapped are known to reduce the materials' mechanical properties. These defects are established from two main origins 1) the gas entrapped during lay-ups or during resin infusion and 2) the volatiles and moisture forming during curing step. Other sources such as incomplete filling due to processing disturbances, differences in the fiber volume fraction or due to changes in the textile architecture are also possible.

Because of the applied pressure in the autoclave molding process, the formation of volatiles and gas bubbles from the moisture are suppressed to a large extent. For LCM processes and because there is no such application of high pressure, more gas and volatiles are created that act as origins of voids. That is why such processes usually yield much higher void content than the autoclave molding. Experimental results have shown that void formation depends on the ratio between viscous and capillary forces [91].

The presence of voids might lead to the formation of cracks that contribute to the damage and final failure of the composite. In [92], experimental tests were carried out to study the influence of voids on damage initiation. It was found that voids affected the damage initiation and the formation of edge cracks through influencing the strain for crack to be initiated, Figure 9.

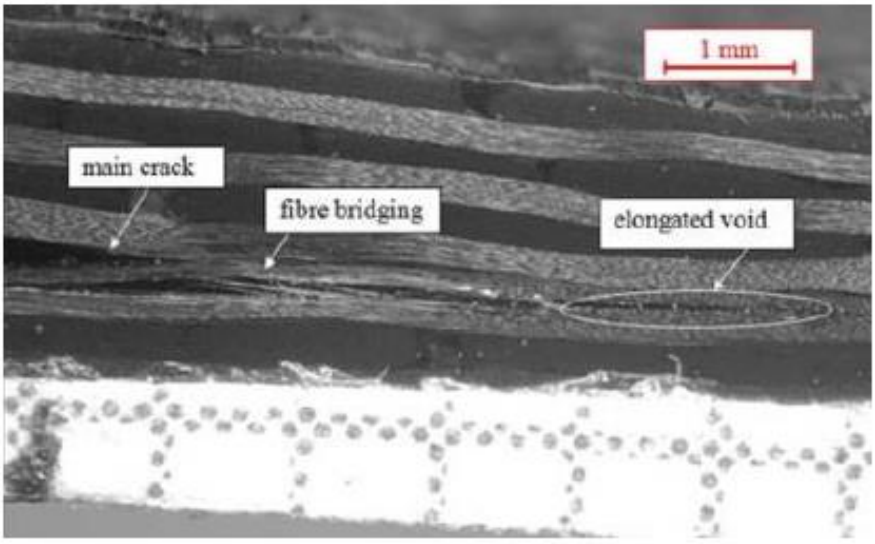


**Figure 9. Secondary cracks and fiber bridging due to the presence of voids. Reprinted from [92].**

The nonuniform distribution of fibers is considered another common defect in all processes, especially using liquid resin infusion, Figures 10 and 11. The nonuniformity (NU) comes from the influence of resin flow that manages to alter the willing uniform fibers positions. This nonuniformity will create regions having high fiber volume fractions and resin rich areas. Real composites always have such defect, although the degree of nonuniform fiber distribution might alter form a process type to the other.

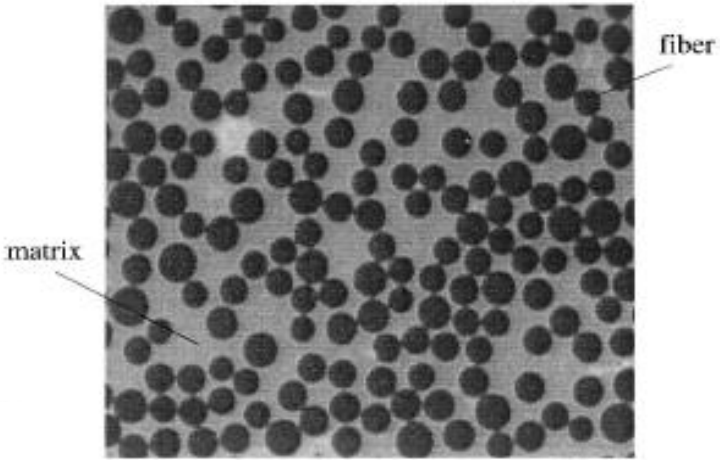


**Figure 10. Nonuniform distribution of glass fibers in epoxy matrix. Reprinted from [90].**

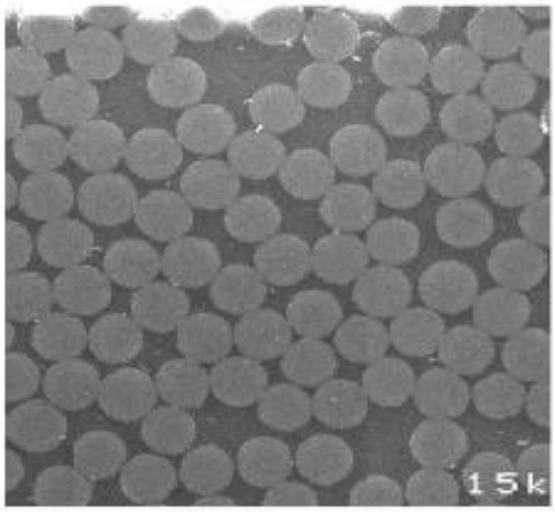


**Figure 11. Nonuniform distribution of carbon fibers in epoxy matrix composites. Reprinted from [93].**

On the level of lab work, only few studies were reported to create a uniform or, better to say, a well-controlled fiber distribution within the composite. For example, Vejen, N. and Pyrz Ryszard [94] managed to create a fiber glass epoxy composite with a uniform distribution of fibers. The fibers with a diameter of 50 μm were aligned in a way that preserved a nearly uniform distribution. The fiber alignments were carried out using a device

that was established for the purpose. Quasi-static transverse tensile tests were carried out till fracture and the crack path was studied, as shown in Figure 12.

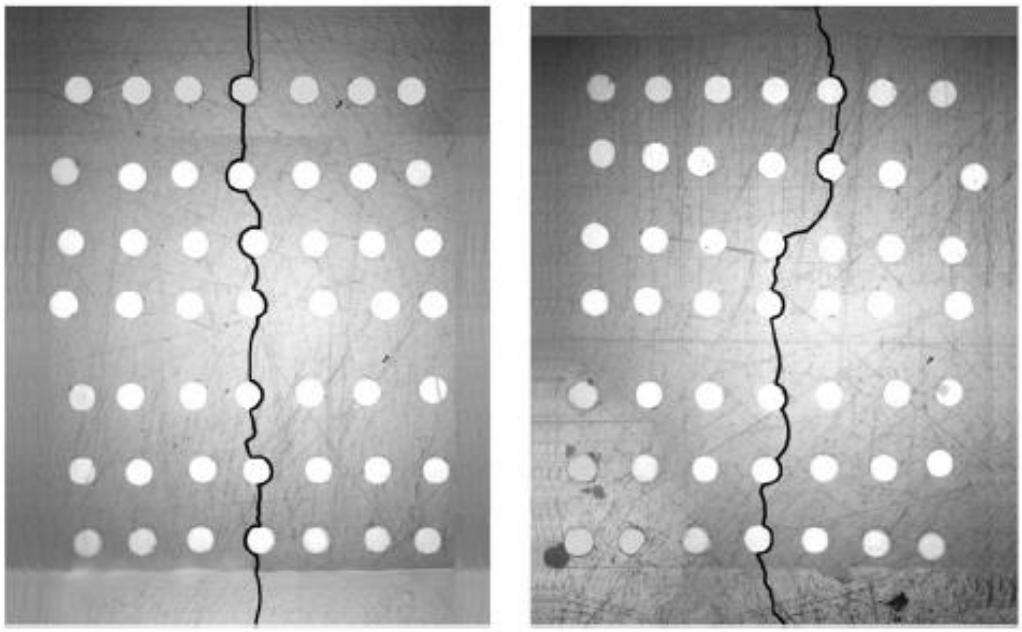

**Figure 12**. **The back and front of a nearly uniform glass fiber distribution in epoxy matrix with a transverse crack after a transverse tensile quasi-static test. Reprinted from [94]**

The presence of nonuniform distribution of fibers and resin rich areas might enhance the formation of matrix cracks in the resin rich areas [14] as shown in the figure 13.

The fibers' nonuniform distribution has a great influence on the damage initiation in composite materials. Even only after curing stage and the formation of thermal residual stresses, variation in interfiber distances affects the magnitude as well as the type of stresses between the fibers. Sørensen and Talreja [95] extensively studied the effects of nonuniformity of fiber distribution on thermally induced residual stresses in ceramic matrix composites. They found that compressive stress sites are established between the closest

fibers at the point of contact. Stress distribution and maximum stresses were found to be dependent on the fibers configuration including fiber clustering and resin rich areas.

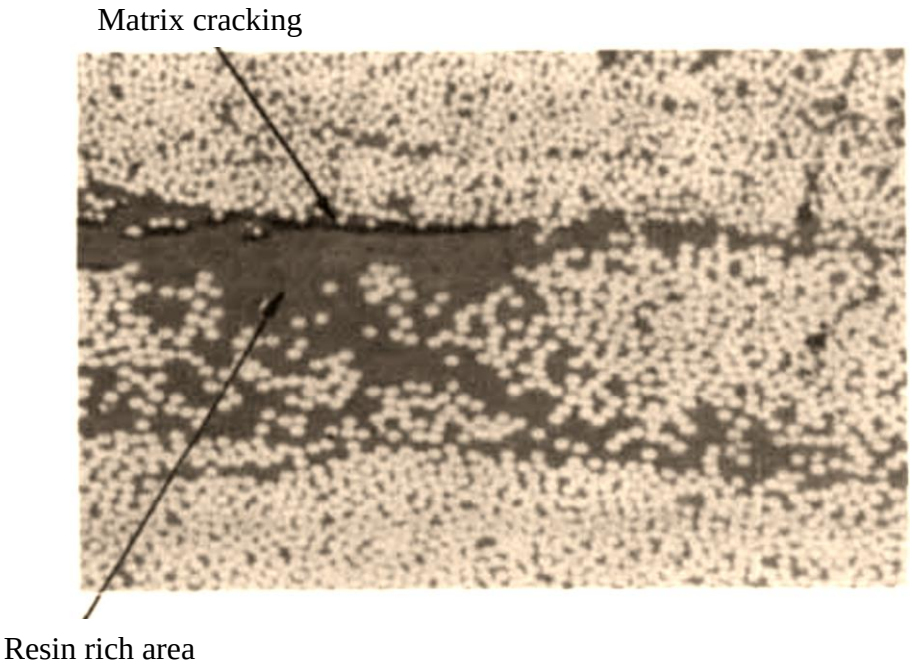


**Figure 13. Damage initiation at a resin-rich area. Reprinted from [14].**

## 2.4. Thermal residual stresses

In the manufacturing of FRP composites, a high temperature curing procedure is carried out. The curing process is mainly for the polymer matrix. It consists of two main steps, 1-Polymerization, in which the polymer is cured and subsequently shrinks due to the polymerization chemical reaction at a relatively high temperature with no changes in the fibers but with polymer density increase. 2- Cooling procedure; in this step and due to the different thermal expansion coefficients of both the fiber and matrix materials, both materials shrink in different amount. This results in the creation of thermal residual stresses at the

fiber-matrix interface, in the matrix and inside the fibers. Thermal residual stresses in cured polymeric composites are mostly unavoidable because of different properties between matrix and reinforcements. The major residual stresses are because of the fiber/matrix properties mismatch [96,97,98]. In general, the thermal expansion coefficient of the epoxy matrix is much higher than that of the glass fibers. Thus, tensile stress appears in the matrix and compressive in the fibers [97,99].

Thermal stresses have a significant effect on the mechanical behaviors of composites [100], and on the interfacial properties between the matrix and the fiber [101,102]. It has been a researchers' concern to evaluate the thermal stresses either experimentally or theoretically. A good review about thermal residual stresses is given by Favre [97]. The review covers thermal residual stresses, their origin, influences and their predicted values.

There are different experimental techniques that have been, or are used, to evaluate thermal residual stresses. Residual stresses can be determined with one of the following experimental methods 1- destructive, 2 non-destructive methods. Destructive methods, such as Sectioning/cutting [103], hole drilling [104,105,106], and first ply failure [107]. In these methods, the material fails and cannot be used in further in-situ investigations. Non-destructive tests, such as the measurement of warpage and established curvature [108], using sensors, such as strain gauges and fiber optics, using x-rays or neutron diffraction analysis [109,110,111], and using Raman spectroscopy [112,113,114].

Measuring the chemical shrinkage in polymers is a difficult task. The prediction of chemical shrinkage due to curing in polymeric materials can be carried out with the aid of molecular dynamics [115,116]. In [115] the molecular dynamics is done in several steps: 1) Pre-crosslinking, 2) Crosslinking: in which the system is cured through necessary chemical

reactions, and 3) Annealing: in which the system is cooled to the room temperature. Various degrees of curing were established from which different properties were predicted.

Different parameters affect the thermal residual stresses in both their sign and their magnitude. These parameters include; local fiber volume fraction or fiber distribution [93,98,99,117-122] curing temperature [123], cooling rate [124,125].

The work by Asp et al [74], showed that thermal residual stresses depend on the fiber volume fraction including the position and fiber distribution. It was shown that these residual stresses will affect the transverse strength of the composite.

In the work by Bulsara et al [120], they are highly suggesting that the fibers spatial distribution cannot be neglected when thermal induced failure is considered.

Yang et al [99] studied the effect of fibers distribution as well as interfiber distances on the created thermal residual stresses using cohesive zone model. It was concluded that interfiber distances and thermal residual stress affect the transverse failure behavior of composites.

In [118], Fletcher and Oakeshott studied the influence of fiber distribution on the thermal residual stresses in a unidirectional carbon fiber epoxy composite. They found that the maximum stress is affected by the interfiber distances. In addition, the stress field created is critical when dealing with an irregular fiber array.

In [121] it was concluded that thermal residual stresses are dependent on the fibers distribution within the composite especially under higher fiber volume fraction. The composite was subjected to a cooling process (-100$^{o}$C). Volume fractions from 10% to 60% were examined. Normal, shear and tangential stresses were monitored in polar coordinates.

# 3. FAILURE THEORIES AT DIFFERENT SCALES

Because of the complex nature of composite materials, different damage mechanisms are observed. In service, structural composite materials suffer from complex mechanical and thermal loadings, static and dynamic.

Damage and failure of composites have attracted numerous researchers over the last decades. There are many failure theories that were constructed for failure and damage of composites at different scales [73,126,127,128], all will give complementary knowledge about different damage mechanisms that could take place.

A brief survey is given in this chapter about the most encountered failure theories used in industry and in related researches.

Because microscale analysis is our main concern, the methodology in using this scale in the field of damage of composite, especially with finite element analysis FEA, will be pointed out. The methodology usually includes the construction of a representative volume element (RVE) of fibers embedded in the matrix, the RVE minimum/optimum size and its statistical description that gives insight on the way the fibers are distributed.

## 3.1. Failure theories for unidirectional FRP composites

Damage initiation usually occurs in a lamina that, when propagated, might led to a catastrophic failure. It is our concern to know more about damage initiation. Suppressing the sources where damage starts might help in avoiding catastrophic failures.

For heterogeneous materials, failure theories can be either at the macro or micro scale. An intermediate scale is usually added which is called a mesoscale to represent the

analysis of a single ply or lamina. In this scale, the ply is considered as a homogeneous structure. Sometimes ply analysis is considered as macro-scale analysis.

The macro scale represents the whole composite laminates as a homogeneous continuum structure. Thus, theories based on macro scale analysis assume a homogeneous material out of an anisotropic and heterogeneous one. In microscale models, on the contrary, details about the fibers and matrix are given, also the presence of defects could be considered.

### 3.1.1. Macro-scale

The whole structure with all its details, is considered a homogeneous one. Theories based on a macro-scale analysis look at the damage or failure as to be in its last steps. Macro-scaled theories will not capture the damage initiation mechanisms within the fiber and matrix level. Besides, factors that could affect the damage evolution are difficult to be considered. In addition, individual properties for composite constituents, such as the thermal expansion coefficients, cannot be applied and hence their effects, including thermal residual stresses, will not be considered.

Attempts were made to construct a failure theory for a single lamina/ply in the macro-scale, and most of them are strength based. Failure theories proposed could be divided into two main groups: a) Failure criteria not associated with physical failure mechanisms e.g., Tsai-Hill, Azzi & Tsai, Tsai & Wu, and b) Failure criteria associated with physical failure mechanisms, e.g., Hashin and Puck. Those criteria are widely used despite their shortcomings mainly because their simplicity and their easiness to be implemented in analysis [128,129,130]. A brief discussion about those failure theories is given below.

#### 3.1.1.1. Failure criteria not associated with physical failure mechanisms

**Maximum stress theory**

Failure is predicted in a lamina if any of the stress components in the local axes of a lamina is equal to or exceeds the corresponding threshold value. It is similar to theories applied to isotropic materials. It is a non-interactive theory. This means that it assumes that any failure mechanism is independent of any other failure mode taking place simultaneously under the same or under different loading directions [131].

| | | |
|---|---|---|
| Tensile stress | $\sigma_{11} < X_t$ | |
| | $\sigma_{22} < Y_t$ | |
| Compressive stress | $\lvert\sigma_{11}\rvert < \lvert X_c\rvert$ | (1) |
| | $\lvert\sigma_{22}\rvert < \lvert Y_c\rvert$ | |
| Shear stress | $\lvert\tau_{12}\rvert < \tau_{12(ult)}$ | |

**Maximum strain theory**

Similar to the maximum stress theory, the maximum strain theory is a non-interacting theory, but it is about strains not stresses. Thus, the material fails if one of the strain components reaches its threshold value.

| | | |
|---|---|---|
| Tensile strain | $\varepsilon_{11} < \varepsilon_{11(ult)}$ | |
| | $\varepsilon_{22} < \varepsilon_{22(ult)}$ | |
| Compressive strain | $\lvert\varepsilon_{11}\rvert < \lvert\varepsilon_{11(ult)}\rvert$ | (2) |
| | $\lvert\varepsilon_{22}\rvert < \lvert\varepsilon_{22(ult)}\rvert$ | |
| Shear strain | $\lvert\gamma_{12}\rvert < \gamma_{12(ult)}$ | |

Polynomial strength criteria (e.g. Norris criterion) were first applied to anisotropic materials, such as wood and fibrous composites. They require a lot of tests using uniaxial and biaxial loading conditions. Parameters of the polynomial equation are determined according to the test results.

The quadratic forms of the tensorial equation are widely used. Among them are what have been known as Tsai-Hill [132], and Tsai-Wu [133]. In the following section, the mostly known criteria will be briefly pointed out.

**Tsai-Hill**

Tsai- Hill failure criterion is a quadratic interactive theory that considers the multi-axial stress state [132].

The quadratic equation (3) is mainly based on Hill's anisotropic plasticity theory that is based on the von Mises' distortional energy yield criterion to anisotropic materials.

$$\left(\frac{\sigma_L}{X}\right)^2 + \left(\frac{\sigma_T}{Y}\right)^2 - \frac{\sigma_L \sigma_T}{X^2} + \left(\frac{\tau_{LT}}{T}\right)^2 = 1 \qquad (3)$$

where, $\sigma_L = \sigma_{11}$ and $\sigma_T = \sigma_{22}$.

The Tsai- Hill theory does not give the mode of failure like the maximum stress and maximum strain failure theories. It does not distinguish between the compressive and tensile strengths. Thus, X and Y can either be in tension or compression. But it takes into account the interaction between different stress components necessary for failure to initiate.

**Tsai-Wu**

Tsai-Wu theory assumes interactive modes of failure which is proposed in a polynomial equation through the interaction between different components of the stress tensor [131,133].

The general formula is given by:

$$F_{ij}\,\sigma_i\,\sigma_j + F_i\,\sigma_i = 1 \qquad (4)$$

where, $F_i$ and $F_{ij}$ are strength coefficients. One drawback of this theory is that the interaction terms $F_{ij}$ for $i \neq j$ requires difficult biaxial loading tests to determine their values. Despite the simplicity of the polynomial equation, recognizing different damage mechanisms is not yet possible.

Those criteria were then followed by others that considered damage mechanisms. Argon [35], for example, considered the kink band formation as a mode of failure under compressive loading in the fibers' direction [73].

**Hoffman**

Hoffman's failure criterion is non-interactive. Although it does not consider the different modes of failure in the composite, it accounts the different tensile and compressive strengths unlike Tsai-Wu criterion [134].

**3.1.1.2. Failure criteria associated with physical failure mechanisms**

**Hashin**

Hashin critically analyzed quadratic formulations and stated that they are mathematically based and they only rely on curve fitting consideration without any physical reflection [135]. For his criterion, he suggested different modes of failure under tension and compression in fibers axis and normal to it. Four distinct failure modes are considered separately. His criterion is deemed as piecewise smooth. He proposed separate failure criteria for tensile fiber mode, compressive fiber mode, tensile matrix mode and compressive matrix mode.

Fiber modes

- *Tensile fiber mode;* $\sigma_{11} > 0$

$$\left(\frac{\sigma_{11}}{X_T}\right)^2 + \left(\frac{\sigma_{12}}{T}\right)^2 = 1 \quad (5)$$

- *Compressive fiber mode;* $\sigma_{11} < 0$.

$$\frac{\sigma_{11}}{X_c} = 1 \quad (6)$$

Matrix modes

The main idea is based on Columb- Mohr failure theory of soil.

- *Tensile matrix mode;* $\sigma_{22} > 0$

$$\left(\frac{\sigma_{22}}{Y}\right)^2 + \left(\frac{\sigma_{12}}{T}\right)^2 = 1 \quad (7)$$

- *Compressive matrix mode;* $\sigma_{22} < 0$

$$\left(\frac{\sigma_{22}}{2T'}\right)^2 + \left[\left(\frac{Y_c}{2T'}\right)^2 - 1\right]\frac{\sigma_{22}}{Y'} + \left(\frac{\sigma_{12}}{T}\right)^2 = 1 \quad (8)$$

$Y_c$ is the transverse compressive strength, $T'$ is the transverse shear strength and T is the axial shear strength. Till now, Hashin's criterion does not fit all experimental results especially when it comes to fiber and matrix failures under compressive stresses [136]. Limitation in Hashin's failure criterion comes when dealing with matrix failure as the plane of failure in the matrix is difficult to recognize.

**Puck**

Puck and Schürmann [137] modified Hashin's criterion and distinguished between the inter-fiber-failure (IFF) and fiber failure (FF). In the former, failure is suggested to occur by matrix cracking and fiber/matrix debonding. Puck also managed to modify the matrix failure criterion proposed by Hashin. The shear strength in the matrix under transverse

compression is enhanced by a component that is proportional to the normal stress acting on the matrix fracture plane, Figure 14. Puck pointed out that under in-plane shear, the matrix fracture plane is parallel to the fiber axis. But when under transverse compression the plane angle reaches $40^o$ and can reach approximately a value of $53^o$.

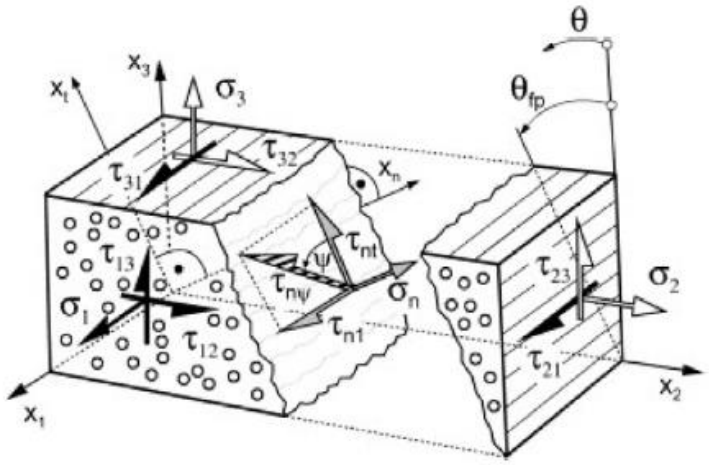


**Figure 14. Fracture plane of a unidirectional lamina. The resolved normal stress $\sigma_n$ and shear stresses $\tau_{nl}$ and $\tau_{nt}$ acting on the plane. Reprinted from [137].**

Most of the existing failure theories are formulated in stresses (or strains). This is best valid for metallic materials, and dislocation dynamics [73,138,139]. The main criticism is given in strength measurements. It is known that strength is the load carrying capacity. The stress strain curve for composite materials usually gives a nonlinear relation that is related to the damage progression from different damage modes. Talreja [73] points out that to give a better failure assessment for such materials, several approaches should be developed and be considered as remedies for the classical formulations of composite failure theories. These remedies are: 1) Multi-scale analysis of failure, 2) Analysis of constrained

failure, and 3) Analysis of manufacturing defects. First and third remedies could be seen as single ply remedies as they involve a micro-scale analysis. But the second remedy requires dealing with composite laminates where each ply has its own fiber directionality. In the first remedy, the multi-scale analysis of failure helps to capture failure initiation in the composite. A microscale analysis facilitates recognizing the initiation of damage in either the matrix, fibers and/or at the fiber/matrix interface.

Available failure theories proposed in the literature do not consider simultaneously all parameters that lead to failure or damage. Heterogeneity, anisotropy and type and direction of loading all will contribute to one or more of the failure modes that might be established.

### 3.1.2. Micro-scale

The micromechanical scale is that scale at which the composite components can be distinguished. When failure analysis is performed at the micro-scale level, damage initiation mechanisms can be predicted as well as their sites. Damage initiation sites, whether in the matrix, fibers and fiber/matrix interface, could be captured. In addition, irregularities, such as fibers' nonuniform distribution and various manufacturing defects, such as voids and fibers misalignments, could be considered.

Recently, it has been found that micromechanical analysis has made a remarkable contribution in the field of damage and failure of composite materials using finite element analysis (FEA). The micro scale level attracted researchers to deal with more relevant microstructural details. Fibers distribution is found to be one of the most important microstructural details that affects, to a large extent, damage initiation and propagation. Most encountered manufacturing defects will be addressed briefly in the next section.

It is still a challenge, however, to make a direct and clear observation of the mechanical behavior of polymers. In the meanwhile, various molecular theories have been established, for example; 1) Transition state theories (e.g., Eyring), 2) Free volume theories, 3) Conformational change theories, 4) Dislocation/disclination theories, 5) Segmental motion theories (e.g., Yannas) and 6) Continuum theories [140] that cover the field of mechanical behavior of polymers and their yielding phenomenon.

Molecular dynamics are now becoming a vital tool in studying polymers behavior at atomistic levels [141-151]. Recently, a study was conducted by Neogi et al. [152] that studies the damage behavior of epoxy resin (EPON-862+DETDA) taking into consideration cavitation as a plausible failure mechanism. The study was conducted by applying uniaxial, equi-biaxial and triaxial tension on a crosslinked simulation cell made of epoxy at different strain rates and at different temperatures. Results have shown that voids volume fraction depends on the stress state and that about 50% volume fraction of voids has been created under equi-triaxial tension. This finding supports what was suggested by Asp et al, in previous studies [74,75,76].

### 3.2. Periodic versus random distribution

Micromechanical models were first applied to periodic/uniform fiber distributions. This might be due to the sake of simplicity or because of the obscurity of the significance of fibers' nonuniformity on stress and failure analysis. The uniform distribution is mostly taken as a square or hexagonal array. Because of this assumption, a unit cell with a single fiber surrounded by the matrix material was usually adopted e.g. [153]. But it was shown later that the effect of fibers' nonuniform distribution cannot be ignored. Numerically, it was found that regular/uniform fiber arrangement could lead to inaccurate mechanical behavior

predictions and can give an underestimation of damage initiation and propagation [63,154,155]. For example, Beicha et al [156] compared effective transverse elastic properties between a hexagonal array and a random one for different fiber volume fractions. Stresses created in this study had higher values within a random distribution than in the periodic one of the same fiber volume fraction. Trias et al [155] compared stress and strain distributions between a periodic and a random fiber distribution in carbon fiber reinforced composites. They found that periodic models underestimated damage initiation and crack propagation. Their conclusion relied on the analysis of failure related variables, such as effective strain, von Mises stress and the dilatational energy density. They also concluded that periodic distribution can be used when effective properties needed to be evaluated, but for statistical failure analysis random distributions should be considered. Also in [157] results within an embedded hexagonal cell placed in the center of an RVE, surrounded by a detailed region of randomly distributed fibers, were compared to a complete random distribution. It was concluded that periodic models could predict the global effective elastic properties, but they could not predict accurately the local behavior and hence local damage and failure. This is due to the presence of higher local stresses caused by closer interfiber distances in randomly distributed fibers.

Fibers' nonuniformity is usually captured in a representative volume element (RVE). The RVE should contain the heterogeneities and irregularities that are assumed to be responsible for damage to be initiated.

### 3.3. Representative volume element (RVE)

Numerical investigations are taking very wide steps in the field of micromechanics of composites. Computer power and technology nowadays help researchers to use larger

RVEs with larger number of inclusions and irregularities than old times. Within the RVE, both matrix and reinforcements can be implemented individually. Usually, in the micro scale, each component is assumed as a homogeneous material. In addition, thermal history effects, such as thermal residual stresses, can be accounted for. Individual properties, such as thermal expansion coefficients, elastic moduli and Poison's ratio, for matrix and fibers, can be implemented independently. The micro-stress and strain distribution created from the interaction between the matrix and fibers under external loads can be monitored. Hence, damage initiation can be well analyzed and/or predicted locally at a scale of a size of a reinforcement.

Taking into consideration all microstructural details is a very difficult task. It is impractical to use a large RVE with a size equals to or nearly equals to the size of the whole structure and contains a very large number of heterogeneities (such as a very large number of fibers). On the other hand, a very small RVE might not be enough to include sufficient number of heterogeneities -microstructural details- that are responsible for damage to initiate, for example when an RVE includes only one fiber surrounded by a matrix. In this case, results will be strongly dependent on the fiber/matrix volume ratio, besides the influence of interfiber distances resulting from the nonuniform fiber distribution, will be ignored.

It is of interest to develop an RVE that is large enough to include sufficient number of microstructural heterogeneities.

### 3.3.1. RVE minimum size

When it comes to a heterogeneous material, microstructural irregular details should be accounted for even in the definition of an RVE. The problem of the minimum size of RVE was first treated by Hill [158] who was the first to define an RVE as:

"(a) structurally representative of the mixture of constituents on average, and (b) contain a sufficient number of inclusions for the apparent overall moduli to be effectively independent of the surface values of traction and displacement, as long as these are macroscopically uniform".

Drugan and Willis [159] defined the RVE to be:

"the smallest material volume element of the composite for which the usual spatially constant "overall modulus" macroscopic constitutive representation is a sufficiently accurate model to represent mean constitutive response".

These definitions work effectively if only the overall properties are of one's concern. But when it comes to study damage initiation with intensive analysis of micro-stress and micro-strain distributions, the concept of an RVE might be altered.

The composite microstructure is full of irregularities that comes from the fibers as well as the matrix and their manufacturing defects. Reinforcements, in general, could have several forms of irregularities, such as size distribution, fibers breakage, warpage, misalignments and fibers' nonuniform distribution.

The nonuniform distribution of fibers have been studied in several works. In these studies, the significance of fibers distribution within the composite in determining damage initiation sites was pointed out. Not only that, but also to predict the damage initiation mechanism that can be encountered under specific loading condition.

Nonuniformity comes from the uncontrolled tools that govern the production technique of the composite. As the distribution becomes more nonuniform, the RVE size should include an adequate representation of this nonuniformity. In another word; if for a well-controlled manufacturing procedure, a highly uniform microstructure will be created. Thus, a single fiber surrounded by matrix maintaining a certain volume fraction is enough to be presented in the RVE if low fibers volume fraction is considered. At higher fiber volume fractions, the interactions between the fibers are higher due to the small values of inter-fiber distances. On the other hand, if uniformity is highly uncontrollable then a sufficient number of nonuniform fibers should be included within the RVE.

The minimum RVE size has been addressed in several studies in the literature. For instance, 30 fibers were used in the cross section of a unidirectional composite to construct a two-dimensional RVE for failure analysis under transverse compression [44] and under transverse compression and out-of-plane shear [160]. In both cases, the authors found that their results did not change significantly when compared to RVEs with 70 fibers.

Bulsara et al [120] adopted the pair correlation function as a statistical descriptor of a real (observed) microstructure. In their work, several RVE sizes with different number of fibers were investigated for one fiber volume fraction. Under transverse loading condition, a square RVE of side length 142 μm with 27 fibers was found to have the least scatter in the damage statistics, which were based on the radial matrix cracking and interface debonding damage modes.

Trias et al. [161] conducted an extensive study of the minimum RVE based on different criteria ranging from the Hill condition [158] to statistical variation of the local stress and strain fields to the mutual fiber distances. In their analysis, different mechanical

and statistical variables were used to determine the minimum size possible to construct an RVE containing nonuniform carbon fibers in epoxy. For instance, Effective properties and distance distributions. They performed a finite element based analysis on RVEs generated with the fiber volume fraction of 0.5. Comparing the minimum RVE size with respect to different criteria, they concluded, for the composite they studied, that the RVE side length should be a minimum of 50 times the fiber radius. This size was adopted by other investigators, e.g. [162,163].

Romanov et al [63] suggested 40 to 50 fibers to be enough for establishing an RVE based on the number of realizations investigated. In their work, simulated microstructures were compared to the real ones. Comparison of fiber positions and the stress fields were conducted using statistical descriptors.

Depending on the fiber diameter, Riaño et al [164] created a random distribution of fibers in an RVE to simulate mechanical behavior of the glass/polymer composite under periodic and symmetrical boundary conditions. They suggested that the RVE size/fiber size ratio should be $\geq 8$.

In [165] several microstructure models were constructed from the composite material using a moving window technique. In that approach, it was found that the RVE size depends on the volume fraction of the inclusion as well as the constituents' stiffness ratio. Others used number of fibers as large as 484 [154].

### 3.3.2. RVE construction methodology

How fibers are distributed within an RVE is another essential consideration. Different techniques for distributing fibers have been proposed.

#### 3.3.2.1. Real image techniques

Approaches based on real images have been introduced in different studies, e.g. [63,93,162,165]. Other studies create simulated nonuniform distributions by algorithms using interfiber distances as the main parameter. For example, in [162] the actual experimental distribution of a high strength carbon fiber was analyzed by digital image processing and an equivalent random microstructure using the 1st and 2nd nearest neighbor distance functions was created. From image analysis, some researchers determined the fiber diameter distribution [90,166]. However, Gusev et al. [90] found that this variation does not have a significant effect for the RVE transverse elastic properties. The main drawback of image based approaches is that they require highly sophisticated software and are costly and time consuming. Moreover, they require available experimental data that deal only with certain fiber volume fraction and specific microstructure [63,154,167,168].

#### 3.3.2.2. Hardcore model

In the hardcore model for generating fiber distributions [66,169], one places fibers randomly within the RVE keeping a minimum distance between any two fibers. This procedure gives limitation in the fiber volume fraction that can be achieved. This limitation is called “the Jamming effect” [170]. Attempts to overcome this limitation have been addressed in several studies. Melro et al [163] built an algorithm where the original hardcore model is applied followed by stirring the fibers to create resin rich areas. This allowed more fibers to be added, increasing the final fiber volume fraction. Yang et al. [168] modified the hardcore model by adjusting the interfiber distances, creating different fiber volume fractions.

#### 3.3.2.3. Stirring/shaking technique

Another approach to generate nonuniform fiber distributions from an initially uniform one is based on a so-called “shaking process”, which displaces the initial positions of fiber by a prespecified method [154,166,167,171]. In [154] fibers are perturbed from their periodic positions to random ones by giving each fiber a unit velocity with a random direction. If two fibers overlap, then a collision algorithm is implemented to change the velocities. In [166,167] a collision algorithm was applied to generate random fiber distributions for fibers of a constant diameter [166] and of varying diameters [167]. Wongsto and Li [171] proposed a method that used an initial hexagonal fiber pattern to generate a random fiber distribution by a shaking process. Using a sub-domain of the total region placed sufficiently away from the boundaries, they constructed a random distribution of fibers with a two-step process for shift of each fiber (disc). First, a random angle between 0 and $360^{o}$ is selected and then a random shift in this direction is assigned to the fiber. Recently, Pathan et al. [172] developed an algorithm that used a constrained optimization formulation for a given fiber volume fraction, RVE size and fiber size distribution. Using the input variables, an initial guess for filling the RVE domain with fibers is generated. This configuration is iteratively improved under the constraints that the fibers do not overlap or intersect the RVE boundary.

### 3.4. Statistical description

To characterize the type of distribution of fibers, statistical descriptors, e.g. the second order intensity function and the pair distribution function, are utilized. Below is an illustration of different descriptors usually adopted to describe fibers distribution.

### 3.4.1. Ripley's K function

Known also as (Second Order Intensity Function). Pyrz [66] illustrated the use of the second order intensity function originally proposed by Ripley [173]. The function is given by

$$K(r) = \frac{A}{N^2} \sum_{k-1}^{N} w_k^{-1} I_k\ (r) \qquad (9)$$

Where N is the number of fibers in the observation area A, Figure 15. The variable r is the radial distance from a selected fiber center and $I_k(r)$ is the number of other fiber centers within the circle of radius r. The correction factor $w_k$ is introduced to account for the fibers that intersect the edges of the observation area. It is defined as the ratio of the circumference of the circle of radius r that is contained within the area A to the complete circumference. Thus, $w_k$ acts as a weight function that is equals to 1 if that circle of radius r is completely within the observation area A. The weight function $w_k$ diminishes as radius r increases. Pyrz suggested that this radius r should be within the range 0-0.3 with a square observation area A.

Ripley's K function manages to discriminate between different patterns given within an RVE. When drawn with the circle radius r, different curves shapes might result. If the fibers (or points) are in a uniform pattern, then Ripley's K functions shows a stair shaped curve. The curve gets smoother as the fibers distribution are deviated from uniformity. Figure 16 describes different K functions for different points pattern. As can be observed, a uniform distribution gives a saw shaped curve, while a Poisson's distribution gives a smooth Ripley's Function.

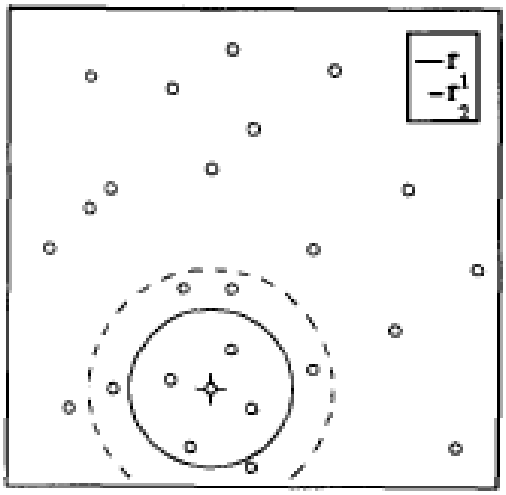

**Figure 15. Estimation of Ripley's K function (K(r)) with edge effects in an observable area A. Reprinted from [66].**

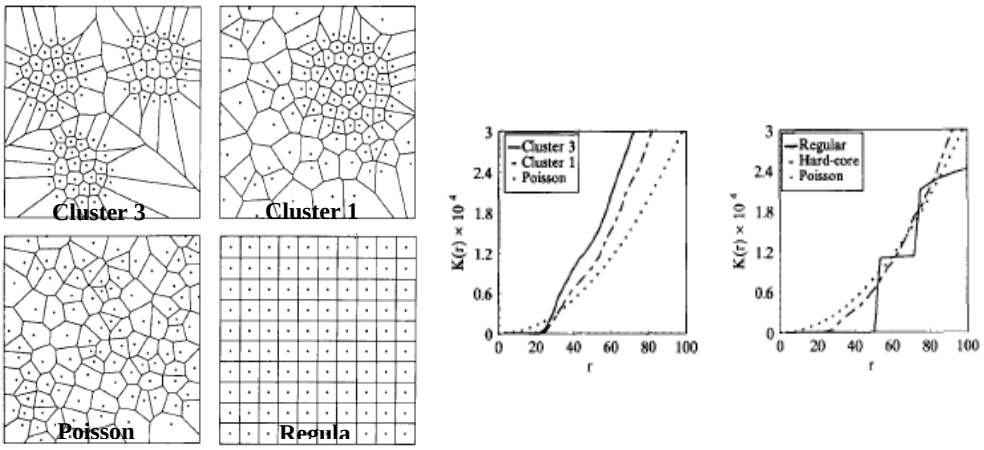


**Figure 16. Different point patterns and the corresponding Ripley's K function (K(r)). Reprinted from [169].**

### 3.4.2. Pair distribution function

Also known as (Radial Distribution Function). For describing local interaction between fibers, the pair distribution function, proposed by Pyrz [169], is useful. It is given by,

$$g(r) = \frac{A}{2\pi r N} \frac{dK(r)}{dr} \qquad (10)$$

Although, mathematically, it is related to the second order intensity function K(r), it gives a totally different information. This function provides information on the inter-fiber distances and their intensity, and is therefore relevant to the local stress field between fibers. Below is a plot of the g function for different points patterns, Figure 17. For a Poisson's distribution, as suggested to be a complete random distribution, the g function g(r) =1. As the distribution is shifted towards regularity, the g function shows sharp peaks, indicating the increased frequency of the interfiber distances maintained.

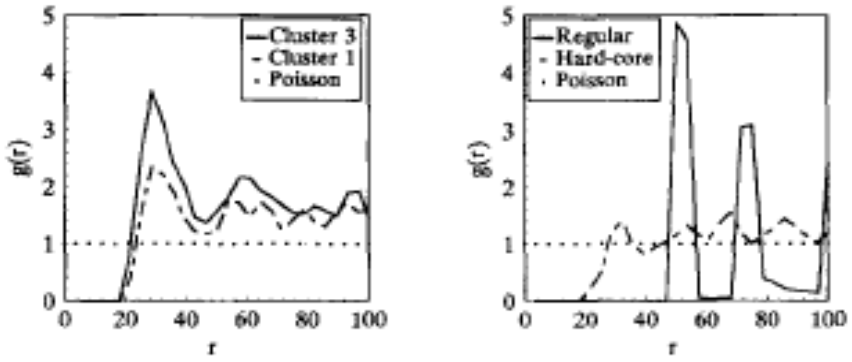


**Figure 17. The pair distribution function for different points pattern. Reprinted from [169].**

### 3.4.3. Nearest neighbor orientation

The distribution of the fibers orientation is usually given in a cumulative distribution function, as given in [163,168]. This function gives information about the number of nearest fibers that are oriented within the same direction. A perfect or complete randomness -as defined in the literature-in the RVE is established when the cumulative function is a straight line (as a diagonal of a square). If the fibers are in a regular distribution, then there will be a preferred orientation for the fibers and the cumulative function shows a stair type curve.

### 3.4.4. Nearest neighbor distances

The nearest neighbor function can be given as a probability density function. It provides information about the nearest distances between each fibers pair. If this distance is between a fiber and its first nearest neighbor, this is called the first nearest neighbor function. If the probability density is determined for the second nearest fibers, this is called the second nearest neighbor distance function and so on. Usually it is enough to determine the first three density functions to give a comprehensive description about the fibers distribution and the minimum distances established.

### 3.4.5. Voronoi tessellation

Voronoi tessellation gives information about the zone of influence of each fiber. A polygon around each fiber center is constructed by connecting the mid-perpendiculars to the segments joining the center of this fiber with its neighbors' centers. If there is a regular distribution, then the area or the Voronoi tessellation will be the same, and each fiber will provide the same influence. When dealing with a nonuniform distribution then each fiber will show different influence and subsequently different zone area [169]. From this tessellation, the standard deviation is determined, which indicates the deviation from the average polygon area [174,175].

## 3.5. The aim of this work

The aim of this work is to study the damage initiation in UD polymer composites subjected to different loading conditions, and to quantify the disorder in the fiber arrangement that results from a manufacturing process by what we define as the "degree of nonuniformity" (NU). For this purpose, we develop an algorithm to construct a representative volume element RVE and generate realizations for different degrees of

nonuniform fibers' distribution each for different fiber volume fractions (FVFs). For each case, a statistical analysis of the fiber distribution is conducted and represented by appropriate functions expressing the interfiber distance characteristics. Local stress fields are calculated by finite element models using a finite element simulation software (ABAQUS) to evaluate damage initiation under each loading condition by a brittle failure process (cavitation) and by an inelastic (yielding) process. This is performed using appropriate criteria in terms of dilatational and distortional components of the strain energy density. Parametric studies are also conducted to study the effects of matrix/fiber stiffness ratio.

# 4. RVE CONSTRUCTION [1]

Nearly all algorithms for constructing RVEs proposed in the literature are capable of creating nonuniform fiber distributions [120,154,161,163,166,167,171]. If the manufacturing process is a well-controlled one, then fibers should be distributed more likely in a uniform pattern. But because the uncontrolled parameters during manufacturing especially when it involves the infusion of polymers, then fibers will experience deviation from their expected uniform positions. The degree of this deviation depends on the degree of manufacturing accuracy. Thus, in this work we propose an algorithm that generates RVEs with a specified measure of the degree of nonuniformity.

## 4.1. Algorithm for RVE generation

The concept behind our proposed quantification of nonuniformity (NU) is a measure based on how much a fiber deviates from its expected position in a uniform pattern. To do this, we consider the distance available between surfaces of adjacent fibers in a uniform (square) pattern. This distance depends on the fiber diameter and the fiber volume fraction and sets the limit to the deviation of a fiber center from its uniform pattern position. We construct a linear measure, where zero degree of NU refers to the uniform array and a 100 degree of NU corresponds to the maximum possible deviation each fiber can move. The 100 % of NU ranges from the zero position (uniform position) to the possible maximum

[1] Reprinted with a permission from "Damage initiation in unidirectional fiber composites with different degrees of nonuniform fiber distribution", by Sarah A. Elnekhaily, Ramesh Talreja, (2018) Composites Science and Technology, 155, 22-32. https://doi.org/10.1016/j.compscitech.2017.11.017. Copyright 2018 by Elsevier.

deviation (the distance available between surfaces of adjacent fibers in the uniform (square) pattern).

To illustrate the construction of an RVE, consider nine neighboring fibers in a square array with 50% fiber volume fraction, as shown in Figure 18. The normal distance between the fiber surfaces is denoted by 'x'. From the center of a given fiber (top-right in Figure 18), we draw a circle of radius x. For the degree of NU of 100%, we assume that the fiber can move during manufacturing such that its center takes any position within this circle (The red circle for fiber A), Figure 19. We adopt a linear measure and assume that for any degree of NU less than 100%, the radius of the circle will be proportionately smaller. Obviously, for 0% of NU, the circle shrinks to the fiber center, giving no deviation from the uniform pattern.

We construct first a square RVE containing fibers of equal diameter arranged in a square pattern with a predefined fiber volume fraction (e.g. 40, 50, 54 and 60%). For the sake of illustrating the failure analysis here, we take three different degrees of NU (30, 60 or 100%). The algorithm to generate an RVE of a selected degree of NU is as follows. Each fiber center is given a random position within the circle of radius equals to the distance x (described above) times the degree of NU. This circle is divided into concentric subcircles with the radius ranging from zero to the maximum in increments of 0.1% of the largest circle. A circle is then randomly selected from these subcircles and the center of the displaced fiber is placed on this circle by a random selection of the angular position between zero and $2\pi$ measured from a reference axis. The algorithm then checks if there is any overlapping, i.e., if the distance between any two adjacent fiber centers is less than D, the fiber diameter, and if any fiber is totally or partially outside the RVE region. If so, then this fiber is given a new random position starting again from its initial uniform one. If not, then a new position is

given to the next fiber, as explained above, and so on. For better illustration, two possible new positions of fiber M are shown in Figure 20 for a 100% NU. This procedure does not change the fiber volume fraction from the initial one in the uniform distribution.

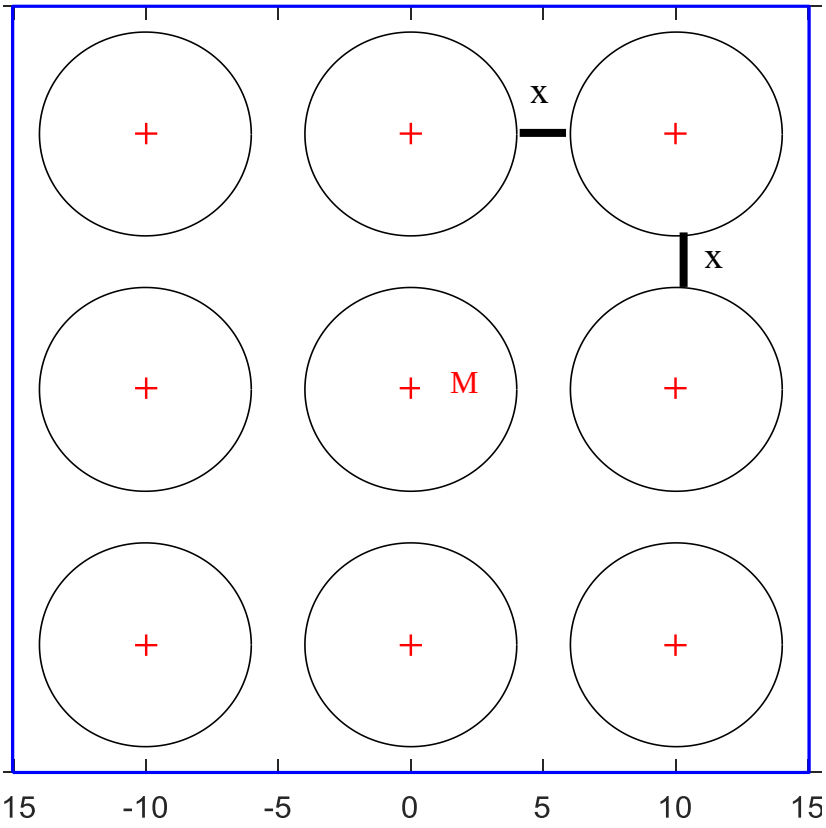


**Figure 18. Illustration of the maximum deviation from the initial fiber center position in a uniform square pattern for 50% fiber volume fraction.**

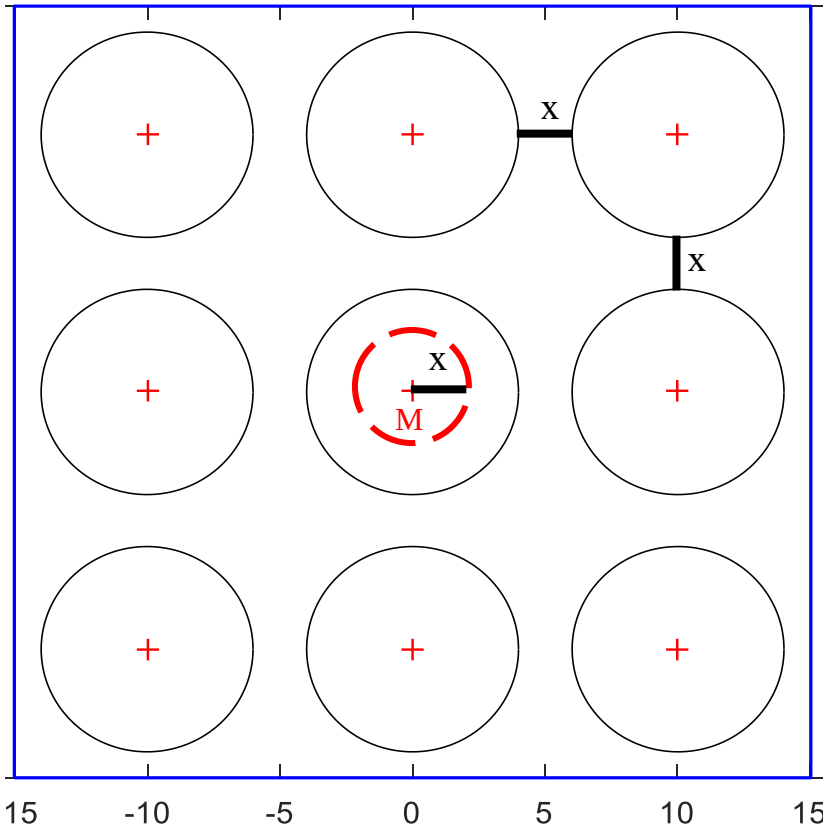


**Figure 19. Illustration of the subcircle with 100% NU for 50% fiber volume fraction**

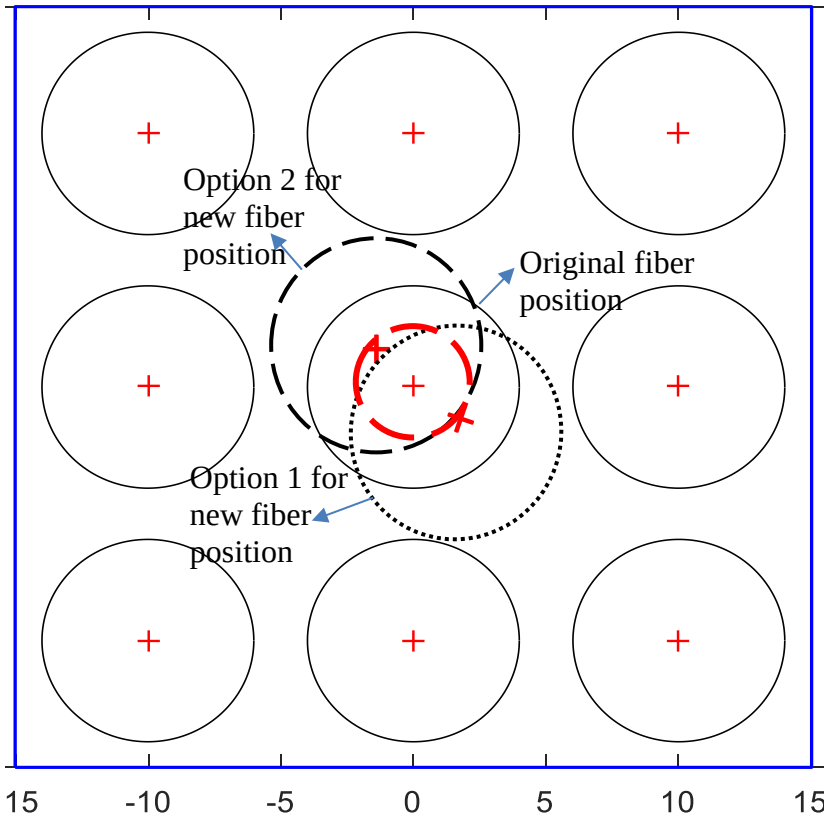


**Figure 20. Examples of two possible new positions of fiber M for 100% NU for 50% fiber volume fraction**

The maximum deviation a fiber can move from its original uniform position will depend on the fiber volume fraction attained. Consider for example a uniform array with 40% fiber volume fraction with the same fiber diameter 8 μm as shown in Figure 21. The maximum deviation for 100% NU is ~ 3.21 μm, instead of ~2 μm for 50% fiber volume fraction. That is why at low fiber volume fractions the impact of the NU is higher. Also, the degree of NU will affect the final distribution. In Figure 22 sub-regions of RVEs corresponding to three different degrees of NU for 40% and 30% fiber volume fractions are displayed. These visual images show that as expected, the fibers deviate increasingly from

their initial square distribution as the degree of NU increases. A flow chart to illustrate the procedure of RVE construction is given in Figure 23.

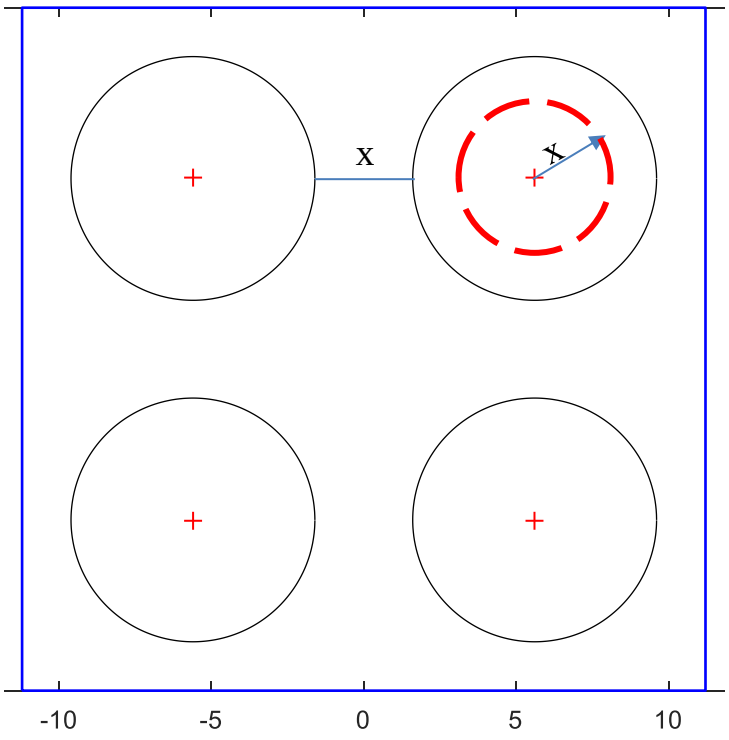


**Figure 21. Illustration of the maximum deviation from the initial fiber center position in a uniform square pattern for 40% fiber volume fraction.**

It is important to note that the nonuniformity of fiber distribution generated by the algorithm proposed here is subjected to constraints imposed by a fixed fiber volume fraction, a constant fiber diameter and a required minimum distance between two neighboring fibers to allow mesh discretization for stress analysis. The impact of having a constant fiber diameter is likely to be insignificant, as suggested by Gusev et al [90]. However, the maximum nonuniformity generated by the algorithm is strongly dependent on the fiber

volume fraction. Consider, for instance, that all fibers in the initial square pattern are in contact with neighbors. At this fiber volume fraction for the given fiber diameter, there is no fiber mobility and hence no nonuniformity. Thus, at high fiber volume fraction there will be less nonuniformity compared to the low fiber volume fraction for the same fiber diameter. More on this will be described below.

It is noted that in generating the RVE realizations, a minimum distance between fiber surfaces of 0.07 times the fiber radius has been kept having adequate discretization when finite element meshes are placed in the numerical analysis [63,176].

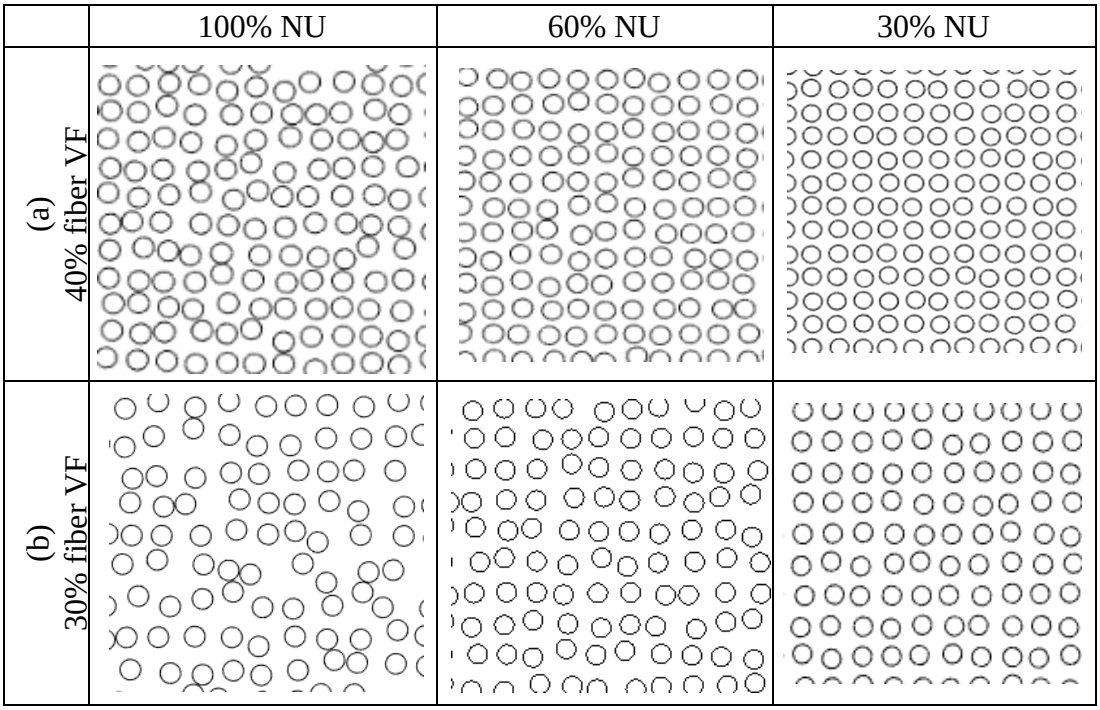


**Figure 22. (a) The RVEs of the 40% fiber volume fraction, (b) The RVEs of the 30% fiber volume fraction with 100%, 60% and 30% of NU.**

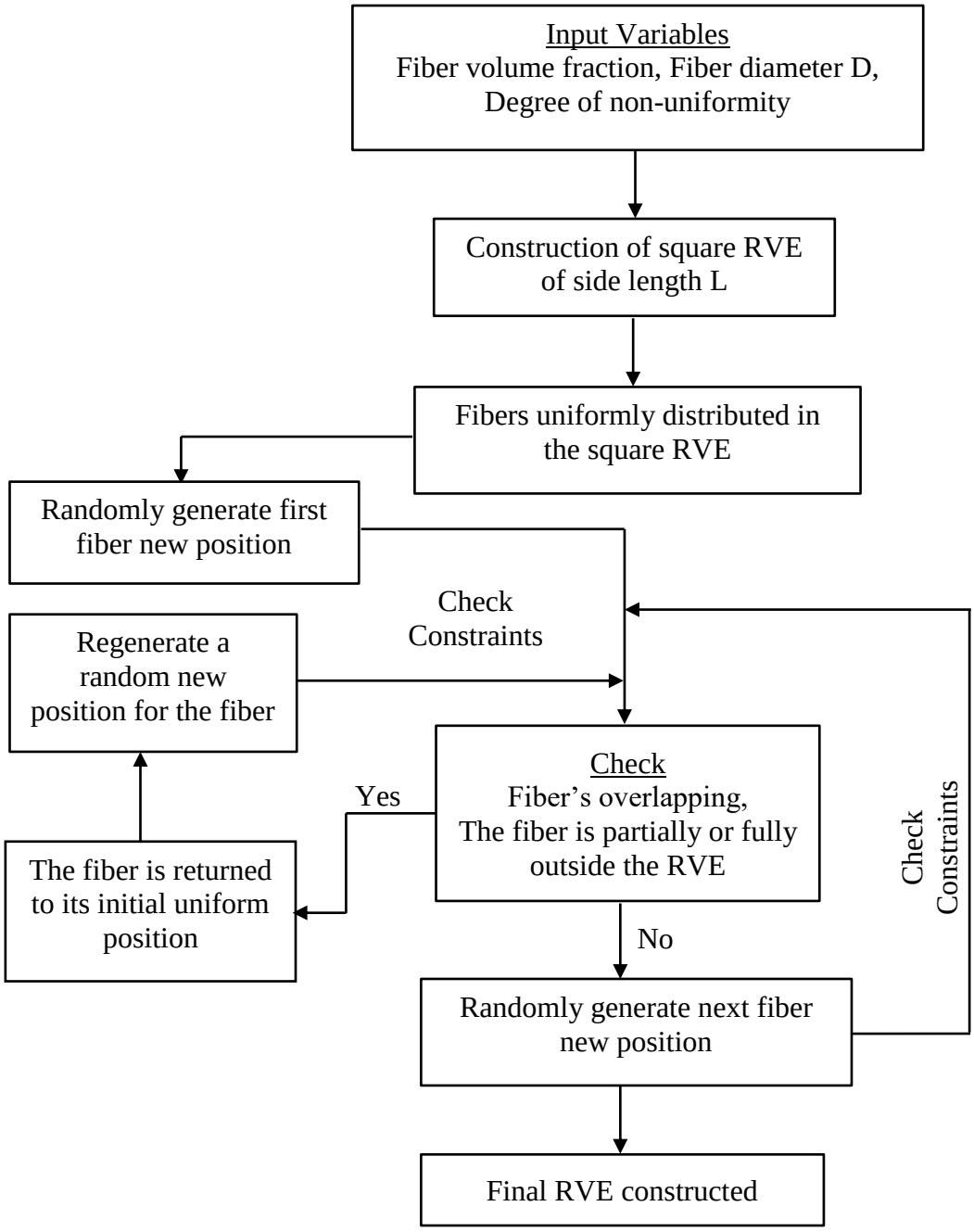


**Figure 23. Flowchart of the algorithm for constructing an RVE realization.**

## 4.2. Statistical characterization

A MATLAB code is constructed to calculate Ripley's K function and the pair distribution function for the constructed RVEs to statistically describe them. Also, the first, second and third nearest neighbor functions are analyzed as well as the cumulative orientation function for the RVEs of different FVFs and different degrees of NU.

### 4.2.1. Second order intensity function

Figure 24 shows Ripley's K function for the generated fiber distributions for four different fiber volume fractions at 100% NU. All four curves resemble the characteristic features shown by Pyrz [66] for the Poisson point process. This process corresponds to the random positions occupied by the fiber centers independently of each other. The curves in Figure 24 are not completely smooth because of the constraint imposed by the fiber diameter to the random positions of the fiber centers. Thus, there is some mutual dependence of the fiber positions on each other. While the K-curve for a Poisson pattern is a smooth, exponentially rising curve, it is a staircase-like curve for a uniform pattern [66]. In Figure 25, K-curves are plotted for three degrees of NU at 40% fiber volume fraction along with zero NU for the same volume fraction. In the expanded view of a part of the curve in the figure, it can be seen that the staircase shape of the curve becomes increasingly smooth as the degree of NU increases.

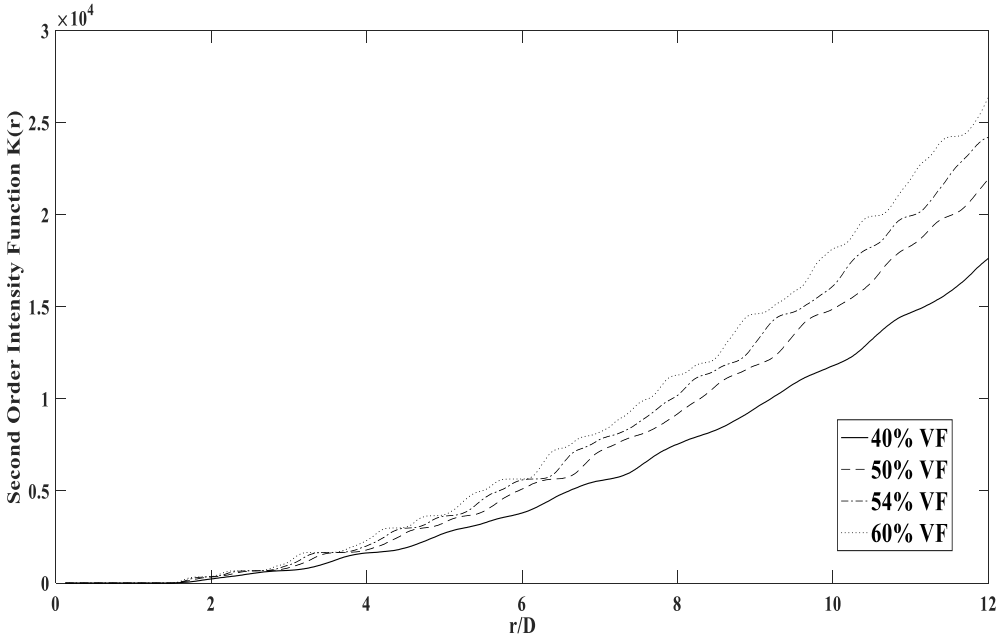


**Figure 24. Ripley's K function for three different fiber volume fractions (40%, 50%, 54% and 60%) for 100 % of NU.**

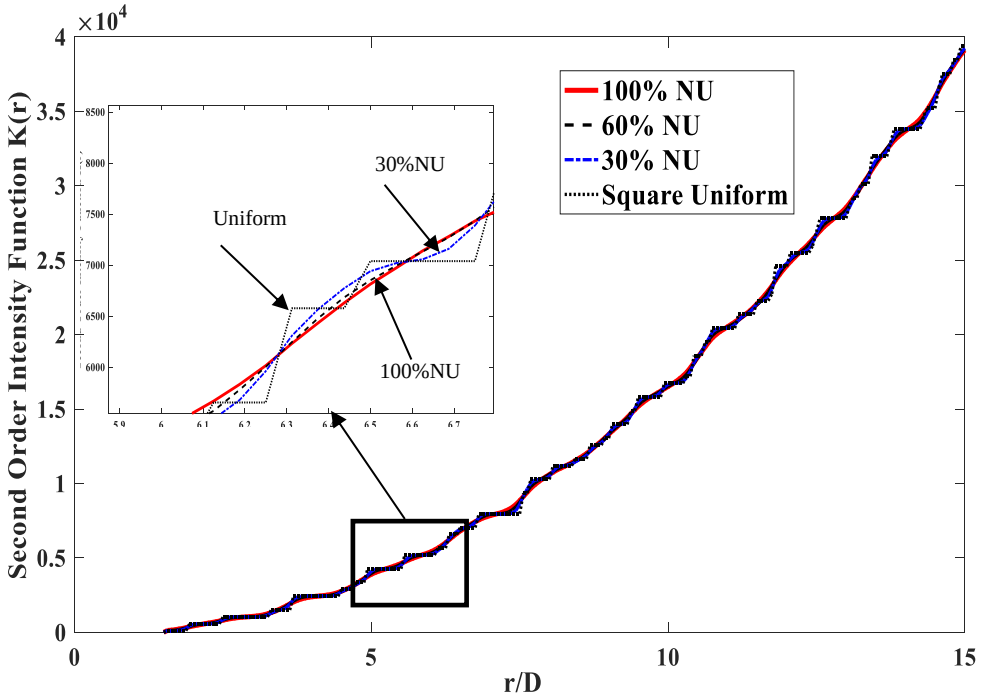


**Figure 25. Ripley's K function for the generated fiber distributions with 100%, 60%, and 30% of NU as well as a square uniform distribution for 40% fiber volume fraction.**

### 4.2.2. Pair distribution function (g-function)

The pair distribution functions g(r) of the generated RVEs for different degrees of nonuniformity and 40% fiber volume fraction are shown in Figure 26. A characteristic feature of the g-curves for nonuniform fiber distributions is an initial peak at a low r-value, followed by decreasing peaks as the r-value increases, until eventually reaching a fluctuation of the g-function about g = 1. For the 100% NU, these features are distinct, while as the degree of nonuniformity decreases, the g-curve approaches that for the uniform pattern, also shown in the figure. The g-curves calculated by 50 and 60% fiber volume fractions show similar trend Figures 27 and 28 respectively although the impact of nonuniformity becomes less for the 60% FVF.

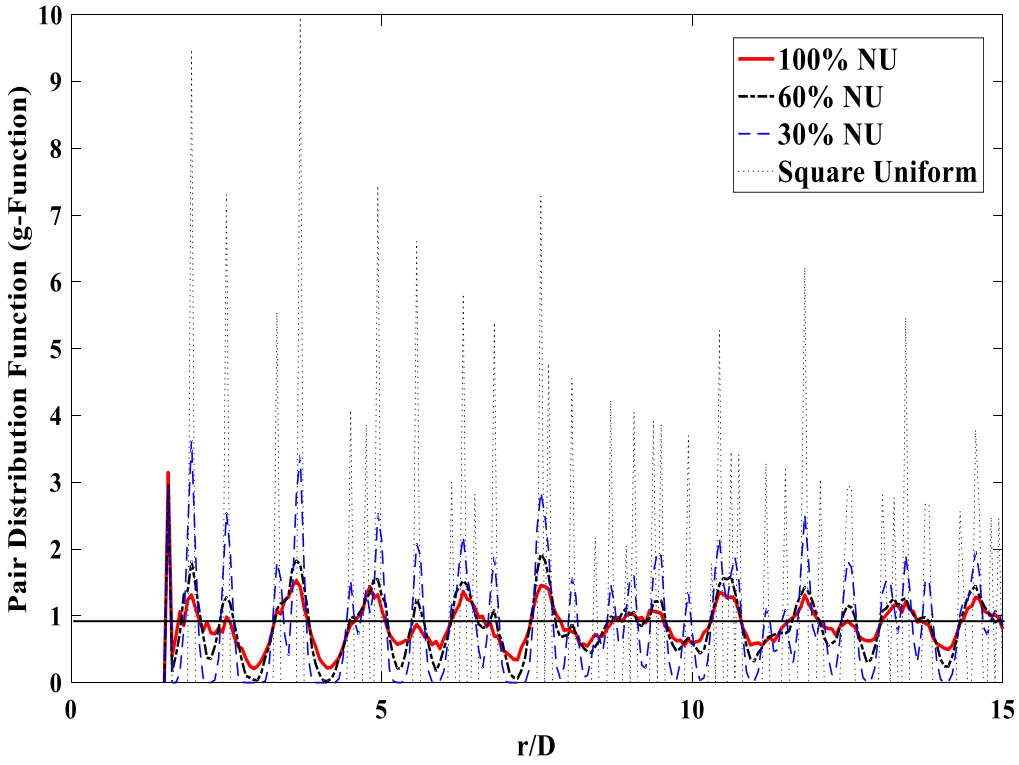


**Figure 26. The pair distribution function (g) for the generated distributions with 100%, 60%, and 30% of NU as well as a square uniform distribution for 40% fiber volume fraction.**

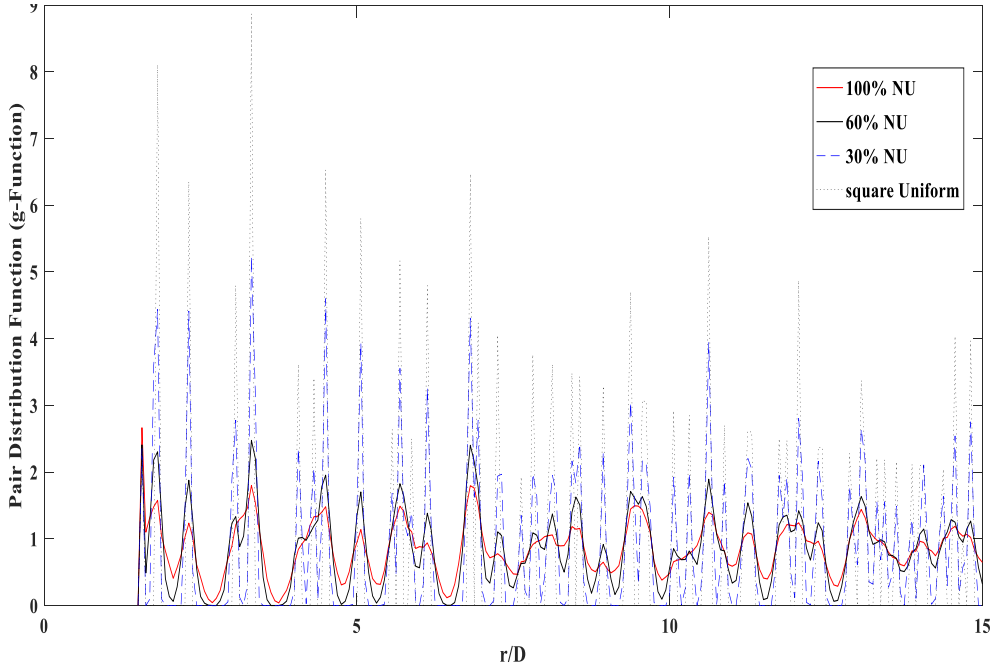


**Figure 27. The pair distribution function (g) for the generated distributions with 100%, 60%, and 30% of NU as well as a square uniform distribution for 50% fiber volume fraction.**

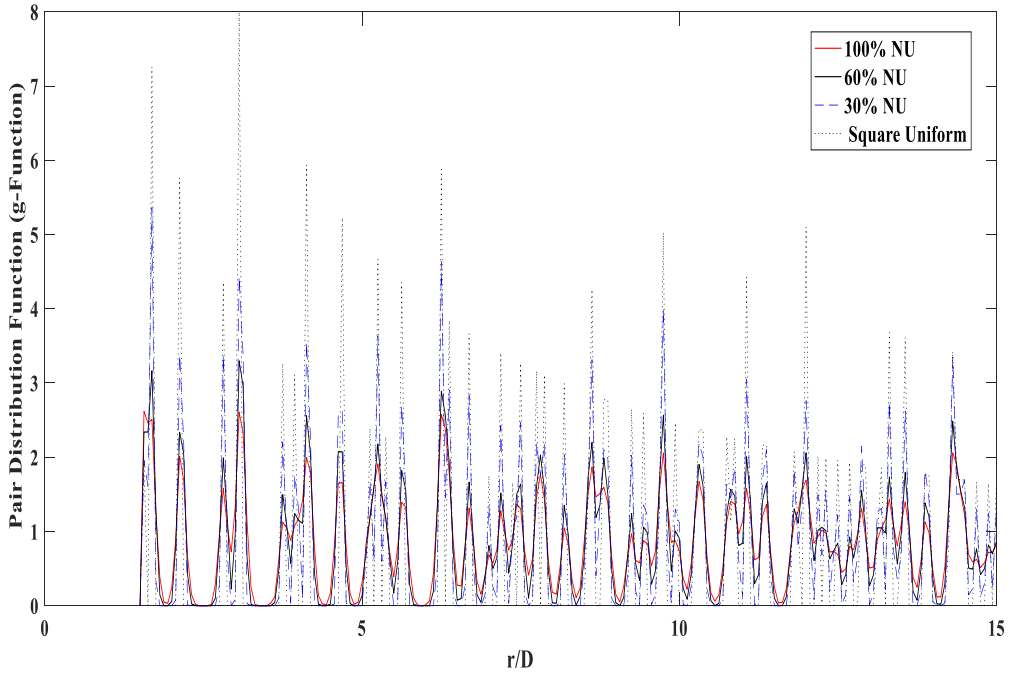


**Figure 28. The pair distribution function (g) for the generated distributions with 100%, 60%, and 30% of NU as well as a square uniform distribution for 50% fiber volume fraction.**

### 4.2.3. Nearest neighbor orientation function

Using our algorithm, the cumulative distribution function is given for a two different fiber volume fractions, 30 and 50%, Figures 29 and 30 respectively. In the first figure, the cumulative distribution function shows a stair shaped curve for the uniform pattern, and the curve is getting smoother and nearly looks like a straight line when the degree of nonuniformity is increased reaching 100%. For higher fiber volume fraction for example 50%, figure 30, a straight diagonal line is not established although it is smoother and completely different than that of the uniform distribution. As defined in the literature, when a square straight-line diagonal is established, the distribution is considered as completely random. In present algorithm, each fiber is given the possibility of not changing its uniform position. Each fiber can deviate with any distance from zero to the maximum possible deviation depending on the degree of nonuniformity given.

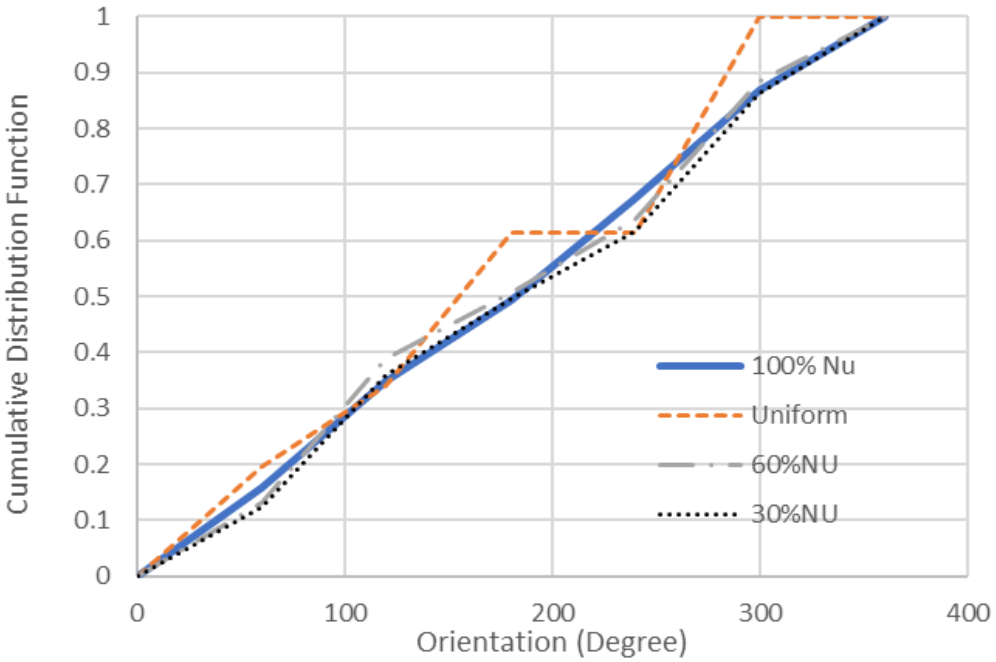


**Figure 29. Nearest neighbor orientation function for a 30% fiber volume fraction and different degrees of NU.**

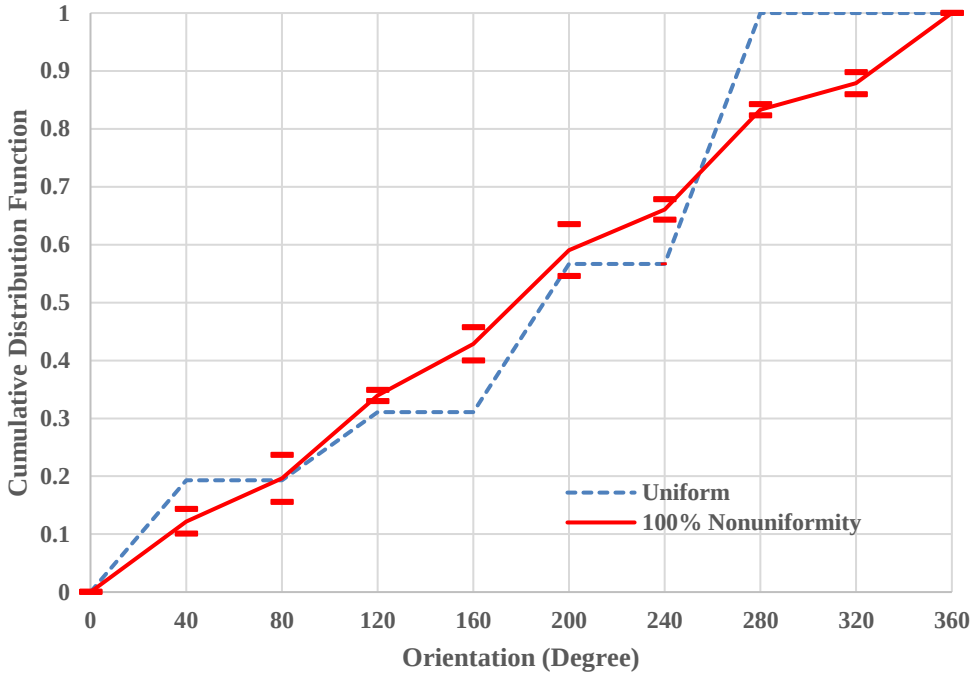


**Figure 30. Nearest neighbor orientation function for a 50% fiber volume fraction and 100 % NU and uniform pattern.**

#### 4.2.4. Nearest neighbor distance function

The first, second and third nearest neighbor distances are analyzed for the RVE constructed with 40, 50 and 60%fiber volume fractions and 30,60 and 100% NU as well as in the uniform distribution. The analysis is described in the following section, when determining the minimum RVE size.

### 4.3. Determination of the RVE size

An RVE should be large enough to contain representation of the fiber distribution irregularities that are expected to affect damage initiation. As fibers get closer together than their interfiber distance in the uniform distribution pattern, the mutual stress field perturbation increases. Therefore, we assume the interfiber distance to be an important parameter affecting damage initiation. Using the procedure proposed in [162] we identify

the first, second and third nearest neighbors in a RVE realization and calculate the frequency of their center-to-center distances. We performed these calculations for 16, 49, 100, 196, 256, 400 and 484 fibers giving different RVE sizes to determine the minimum RVE size needed for capturing the fiber interactions adequately. Results are shown for 16, 100, 400 and 484 fibers for better illustration.

### 4.3.1. Interfiber distances analysis

At least five realizations were generated for each RVE size corresponding to three different volume fractions (40, 50 and 60 %) and three degrees of NU (100, 60 and 30%) in addition to the 0 degree of NU (uniform distribution) with 8μm fiber diameter.

The frequencies of occurrence of the interfiber center-to-center distances between fibers (called the nearest neighbors) are plotted at 100, 60 and 30% NU for 40, 50 and 60% FVFs. Results for 50% fiber volume fraction are shown in this chapter. The nearest neighbor functions for the 40 and 60% fiber volume fractions are presented in APPENDIX A. As seen in Figure 31, the frequency peaks for the first nearest neighbor are fewer for the smallest RVE size (16 fibers), while these are more numerous and distributed more evenly over the interfiber distances as the number of fibers increases. In Figure 31(a), the interfiber distance for the uniform distribution (frequency of 1.0) is marked. The frequencies were also calculated for the second and third nearest neighbor cases (Figures 32 and 33) and the trends also here were found to be largely the same.

As noted above, at least five realizations were constructed for each RVE size. From the frequency peaks, such as those shown in Figures (31-33), the maximum, mean and minimum frequencies are averaged over all nearest neighbor distances (first, second and third) and these are plotted against the number of fibers in an RVE (RVE size) in Figures (34 -36) for 100%, 60% and 30% degrees of nonuniformity for illustration. The same trend in the variation of the frequencies as those seen in Figures (34-36) also holds for all other volume fractions and degrees of nonuniformity. The trend suggests that beyond a certain RVE size, the statistical content of the RVE does not change, at least as far as the interfiber distances are concerned. It would suffice then to use the first nearest neighbor case for consideration of the RVE size.

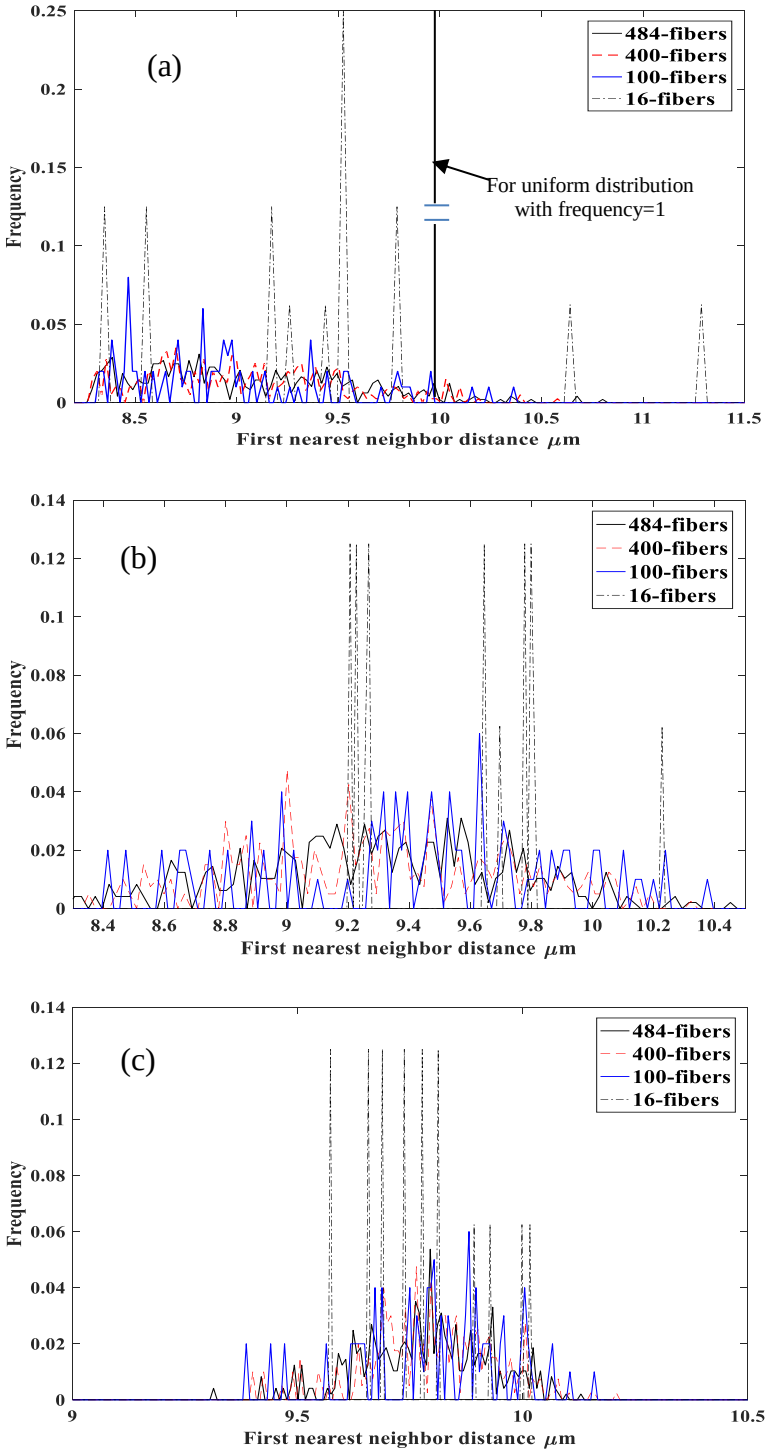


**Figure 31. Frequency of occurrence of the first nearest neighbor distance (from center to center) in μm within the RVE realizations for 50% fiber volume fraction and degrees of NU of (a)100%, (b) 60% and (c) 30% for 484, 400, 100 and 16 fibers in an RVE.**

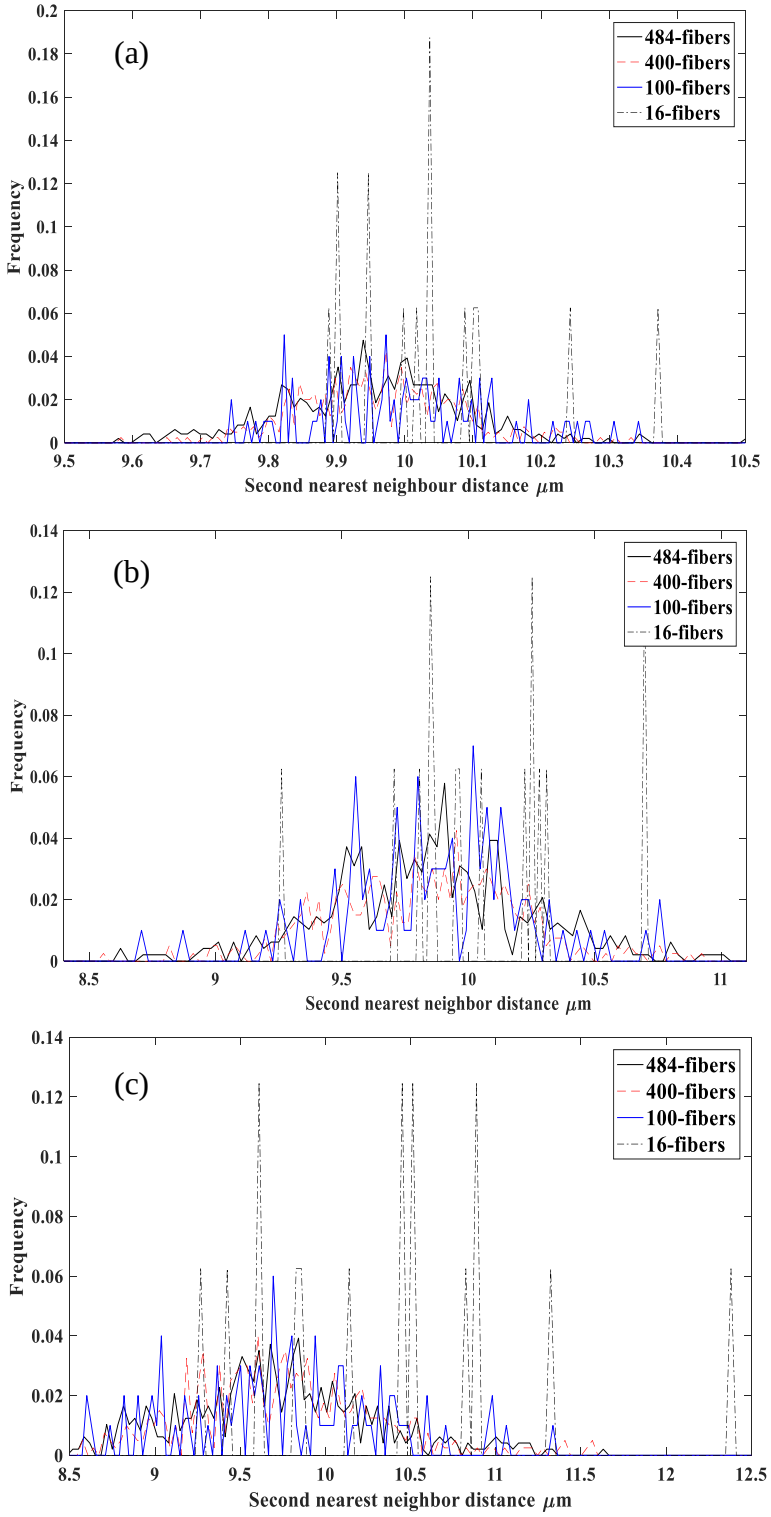


**Figure 32. Frequency of occurrence of the second nearest neighbor distance (from center to center) in µm within the RVE realizations for 50% fiber volume fraction and degrees of NU of (a)100%, (b) 60% and (c) 30% for 484, 400, 100 and 16 fibers in an RVE.**

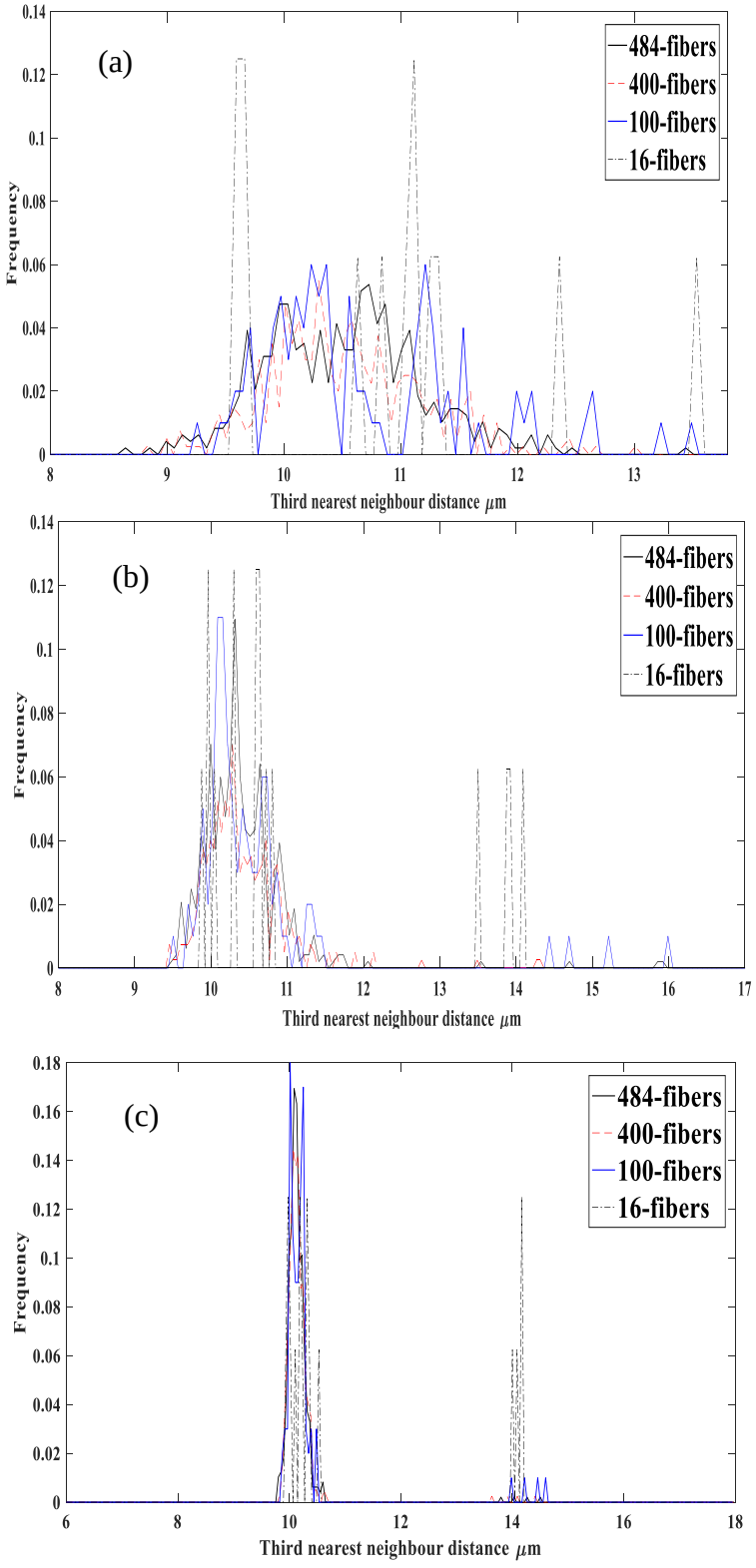


**Figure 33. Frequency of occurrence of the third nearest neighbor distance (from center to center) in µm within the RVE realizations for 50% fiber volume fraction and degrees of NU of (a)100%, (b) 60% and (c) 30% for 484, 400, 100 and 16 fibers in an RVE.**

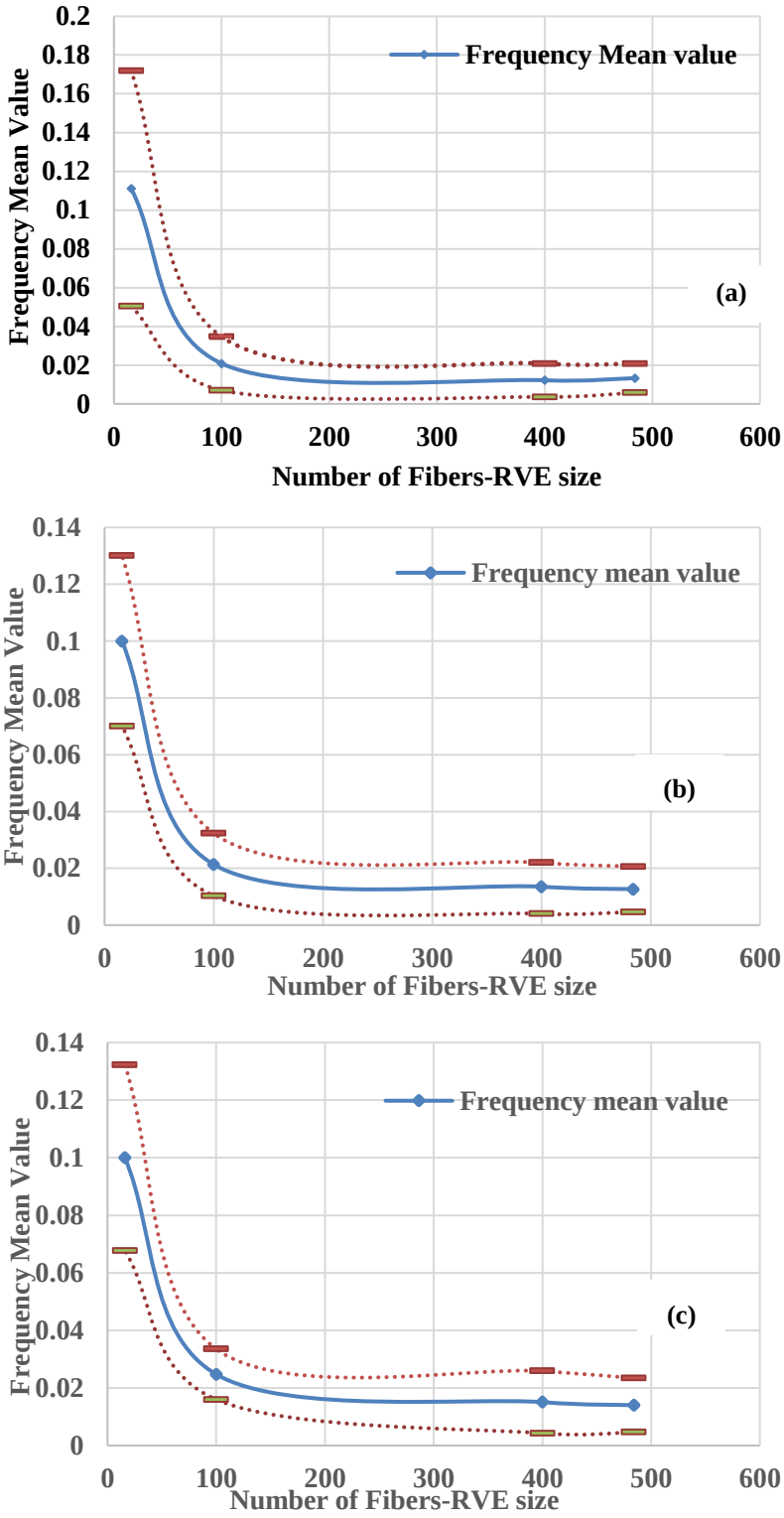


**Figure 34. The maximum, mean and minimum frequencies of occurrence of the first nearest neighbor distances averaged over all distances plotted for 50% fiber volume fraction and degrees of NU of (a)100%, (b) 60% and (c) 30% NU for different RVE sizes.**

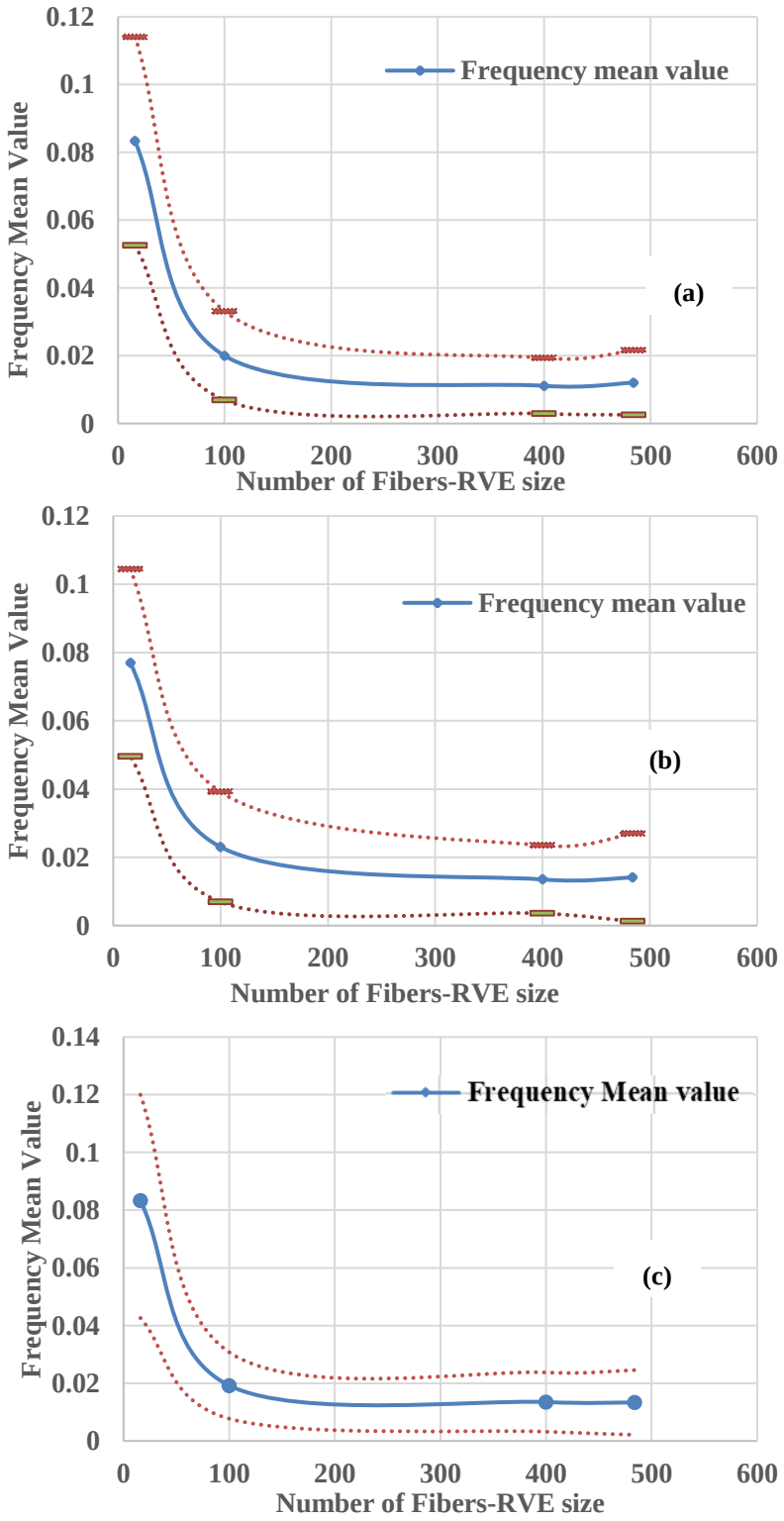


**Figure 35. The maximum, mean and minimum frequencies of occurrence of the second nearest neighbor distances averaged over all distances plotted for 50% fiber volume fraction and degrees of NU of (a)100%, (b) 60% and (c) 30% NU for different RVE sizes.**

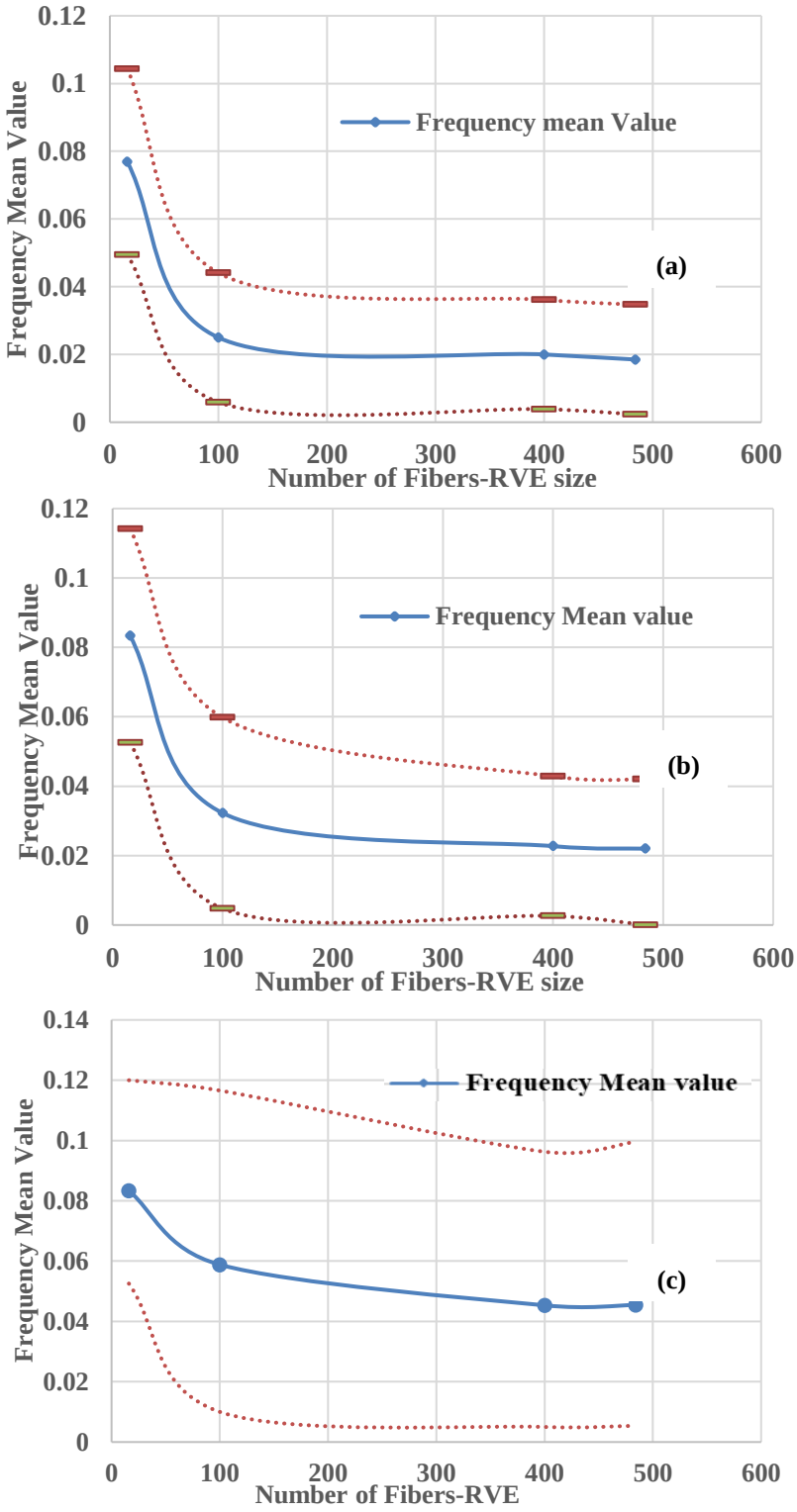


**Figure 36. The maximum, mean and minimum frequencies of occurrence of the third nearest neighbor distances averaged over all distances plotted for 50% fiber volume fraction and degrees of NU of (a)100%, (b) 60% and (c) 30% NU for different RVE sizes.**

### 4.3.2. von Mises and mean stress analysis

As described above, the minimum RVE size can be determined based on the interfiber distance statistics. Implicit in this procedure is the assumption that the local stress field in the matrix between the fibers depends on the interfiber distance. In fact, Pyrz [169] showed that the local stress field is correlated with the interfiber distance. To gain more confidence in this correlation, we examine the averages of two stress invariants: the von Mises equivalent stress and the mean stress. These two quantities are calculated for different RVE sizes (25, 81, 225 and 400 fibers), and their RVE-averaged values are plotted against the RVE size for two loading conditions, under transverse tension and under axial shear loadings.

#### 4.3.2.1. Under transverse tension

The von Mises equivalent stress and the mean stress are calculated for different RVE sizes (25, 81, 225 and 400 fibers) and their RVE-averaged values are plotted against the RVE size under transverse tension, as shown in Figure 37, for one case of 40% fiber volume fraction and 100% NU, as an example. As can be seen in the figure, these averages essentially do not change for RVE size > 200 fibers. Similar results are found for other fiber volume fractions (50% and 60%). Figure 38 shows the results for 50% fiber volume fraction.

For the failure analysis under transverse tension, the dilatational strain energy density ($U_v$) is the relevant local quantity. In Figure 39, the contours of this quantity are displayed for different RVE sizes (5x5, 10x10, and 20x20 fibers) for 40% fiber volume fraction and 100% NU. As can be seen in these images, higher values of the dilatational energy density occur for shorter interfiber distances. The probability of finding a location where the critical

value of the dilatational energy density occurs increases with the RVE size. The procedure for determining the critical conditions for failure will be described in more detail.

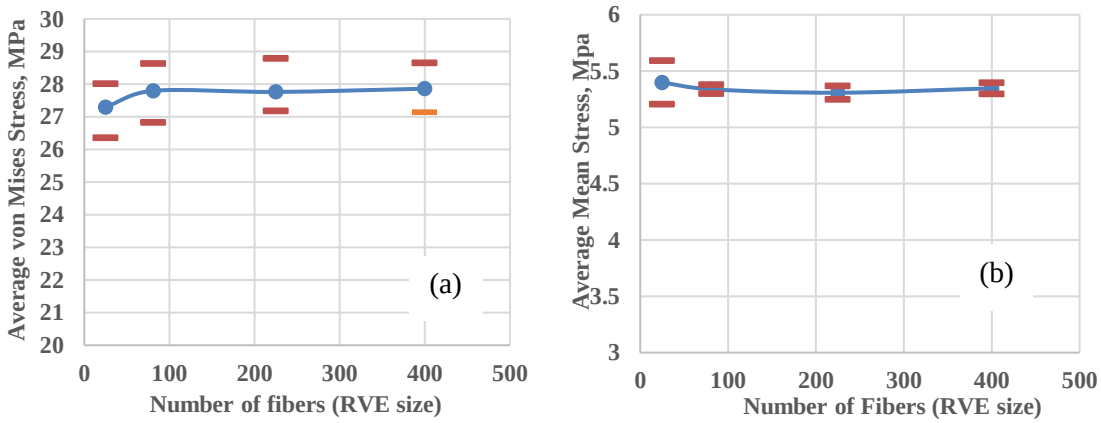


**Figure 37. (a) The average von Mises stress and (b) the average mean stress for 40% fiber volume fraction and 100% NU for different RVE sizes at 0.4% transverse tensile strain.**

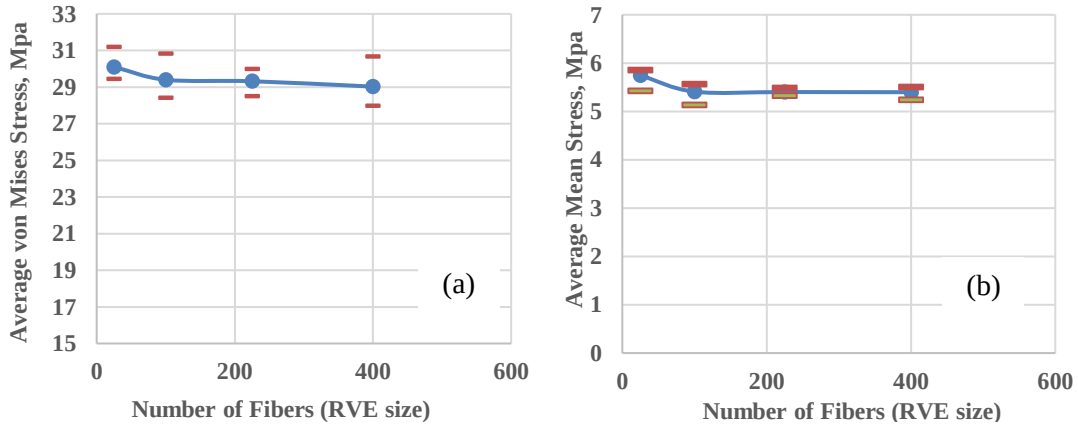


**Figure 38. (a) The average von Mises stress and (b) the average mean stress for 50% fiber volume fraction and 100% NU for different RVE sizes at 0.3% transverse tensile strain.**

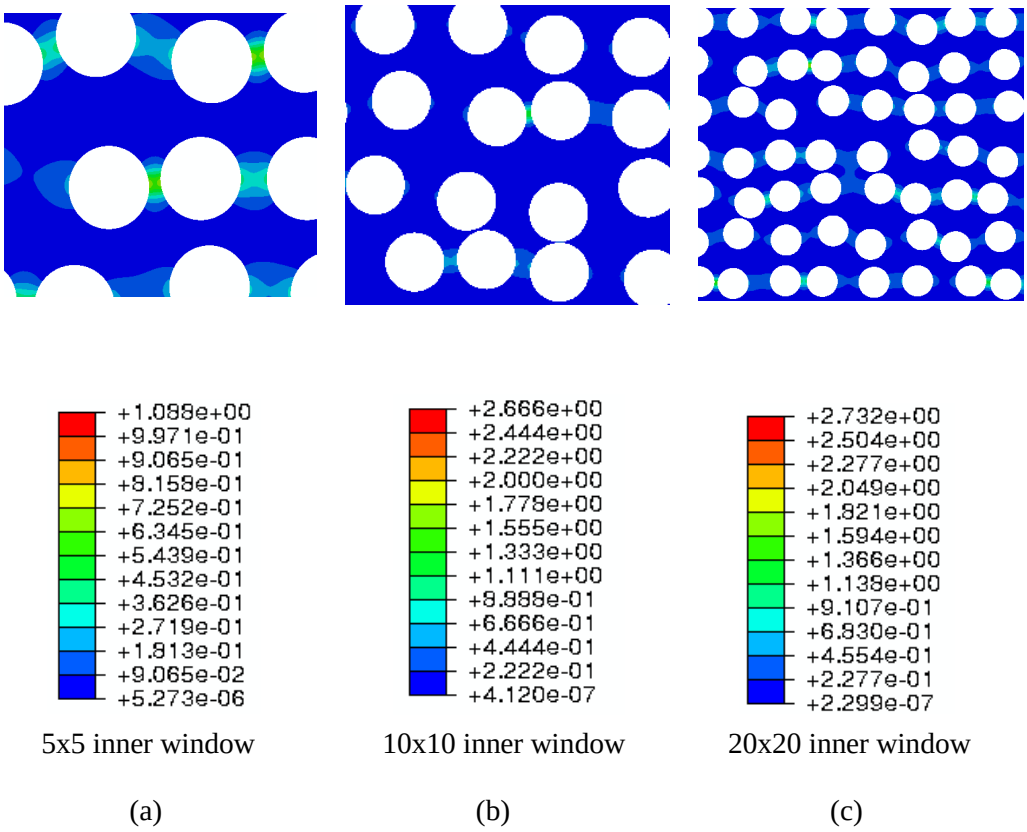


**Figure 39. The dilatational strain energy density in MPa for different RVE sizes (a) 5x5 inner window, (b) 10x10 inner window and (c) 20x20 inner window for 40% fiber volume fraction and 100% NU at 0.4% mechanical strain**

#### 4.3.2.2. Under axial shear

A minimum RVE size should be determined in the case of applying axial shear loading. Besides the first, second and third inter-fiber distances, we examined the averages of two stress invariants: the von Mises equivalent stress and the average shear stress S13. A three-dimensional RVE is used when an axial shear loading is imposed. The boundary condition as well as the 3D RVE used are discussed in detail in chapter 6. The von Mises equivalent stress and the average shear stress are plotted in figure 40. These two quantities are calculated for different RVE sizes (25, 100,196 and 225 fibers) for five different realizations. Figures 40 (a) and 40 (b) show these two quantities for 40% fiber volume

fraction and 100 % NU for the considered RVEs. From the figures- as well as the interfiber distances functions- it can be suggested that ~ 200 fibers are suffice for constructing an RVE under axial shear stress. Similar findings are found for the 50 and 60 fiber volume fractions.

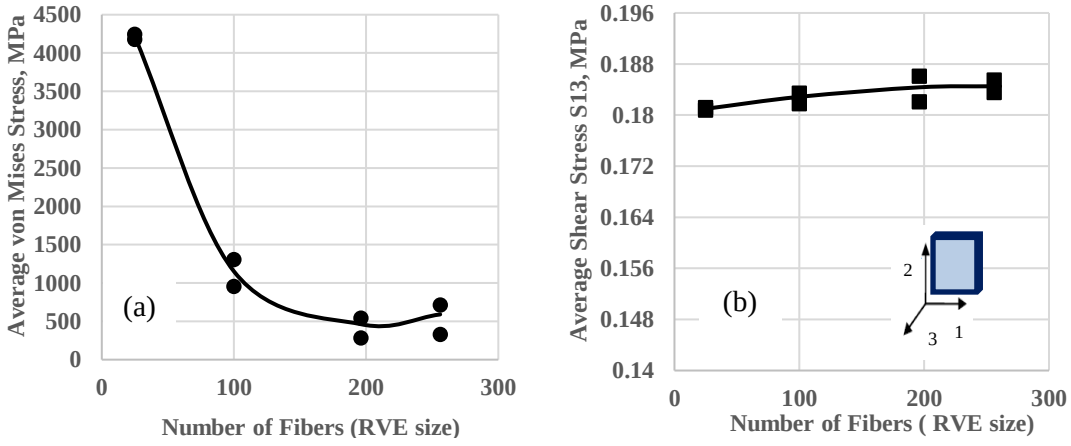


**Figure 40. (a) The average von Mises stress and (b) the average shear stress S13 for 40% fiber volume fraction and 100% NU for different RVE sizes at axial shear stress of 0.285 MPa.**

It is noted that in generating the RVE realizations, a minimum distance between fiber surfaces of 0.07 times the fiber radius has been kept for having adequate discretization when finite element meshes are placed in the numerical analysis [63,176].

### 4.4. Summary and conclusion

In this chapter, a new algorithm is developed to construct a representative volume element which is able to quantify the disorder in the fiber arrangement resulting from a manufacturing process by what we define as the “degree of nonuniformity”. For this purpose, we develop an algorithm to create realizations of the RVE and implement it for different degrees of nonuniformity each for different fiber volume fractions. The degree of nonuniformity has been quantified by a linear measure of the displacements of fibers from

their expected positions in a uniform square pattern. For each case, a statistical analysis of the fiber distribution is maintained provided by appropriate functions describing the interfiber distance characteristics and the nearest neighbor orientation function. The following conclusion can be drawn:

- Assuming that the interfiber distances govern the local stress fields and therefore the initiation of failure, the statistics of nearest fiber distances within an RVE provide a reliable way to determine the minimum RVE size needed for failure analysis. The first nearest neighbor distances have been found to suffice for this purpose, as no significant change in the minimum RVE size was found when the second and third nearest neighbor distances are considered.
- For all fiber volume fractions considered (40, 50 and 60%), the minimum RVE size for 100% degree of nonuniformity was found to be adequately given by 200 fibers under transverse tension and under axial shear loadings.
- The statistical analysis of the RVEs generated for different degrees of nonuniformity using the second order intensity function and the pair distribution function show clear tendency in the statistics going from the uniform distribution to Poisson's point process as the degree of nonuniformity increases.

# 5. DAMAGE INITIATION UNDER TRANSVERSE TENSILE LOADING [1,2]

On transverse loading, distortions at the RVE edges occur due to the presence of fibers near the edges. To eliminate this problem, several studies have applied periodic boundary conditions [44,154,160,162,177-181]. Other micromodels are based on the embedded cell approach [176,161] to minimize the effects of the finite boundaries. In these approaches, the volume element is embedded in a frame of a homogenized composites having the same average properties as the composite embedded in that homogeneous medium. Trias et al [161] used the homogenized frame size to be equal to twice the number of fibers in the domain multiplied by the fibers radius.

Wongsto and Li [171] performed an extensive numerical study of the effects of the boundary distortion on the stress fields within the RVE. Based on their results, they recommended to consider the stress fields in a sub-domain within the RVE away from the external boundaries by at least a couple of average inter-fiber distances.

In the present work, a MATLAB code is constructed to create the RVE to be used in the analysis. The code is established so that parameters, such as fiber volume fraction, degree of NU and the numbers of fibers, are to be implemented. 2D square RVEs with 24 x 24 fibers are constructed with different fiber volume fractions (40%, 50%, and 60 %) and with

---

[1] Reprinted with a permission from "Damage initiation in unidirectional fiber composites with different degrees of nonuniform fiber distribution", by Sarah A. Elnekhaily, Ramesh Talreja, (2018), Composites Science and Technology, 155, 22-32. https://doi.org/10.1016/j.compscitech.2017.11.017 Copyright 2018 by Elsevier.

[2] Reprinted with a permission from "Damage Initiation in Unidirectional Fiber Reinforced Polymeric Composites Under Transverse and Shear Loading", Sarah A. Elnekhaily, Ramesh Talreja. Proceedings of the American Society for Composites: Thirty-second Technical Conference, 2017. Lancaster, PA: DEStech Publications, Inc..

different degrees of NU (30%, 60%, and 100%). At least five different realizations are created for each condition. The RVEs are then implemented in the software ABAQUS for meshing and subsequent finite element stress analysis.

Following Wongsto and Li [171], the local stress fields are examined within the RVE in an inner window of 20 x 20 fibers, as indicated in Figure 41. The size of the inner window satisfied the minimum RVE according to the discussion above.

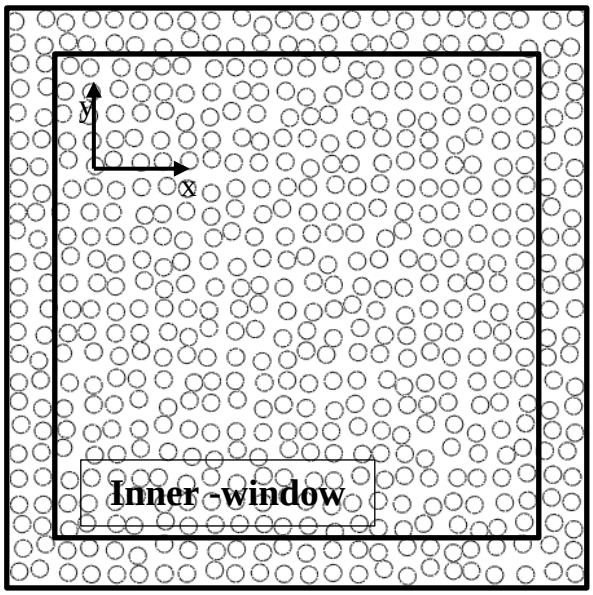


**Figure 41. RVE construction with total 24x24 fibers and an inner window of 20x20 fibers.**

### 5.1. Finite element analysis

In numerical studies, mesh convergence is a necessary step. Because of the relatively large RVE size and the nonuniform nature of the stress fields, a trade-off should be struck between the computation time and accuracy. Mesh convergence in this study is obtained

with the condition that a minimum of two elements between any neighboring pair of fiber surfaces is maintained.

Mesh convergence is analyzed using two techniques 1- overall mesh convergence, 2- Local mesh convergence.

### 5.1.1. Overall/global mesh convergence

Both maximum Mises stress and maximum dilatational energy density were determined within the RVE with different mesh sizes and hence different number of linear generalized plane-strain elements. Figure 42 shows the RVE-averaged von Mises stress against the number of linear elements for 50% fiber volume fraction and 100% NU under 0.3% transverse tensile strain.

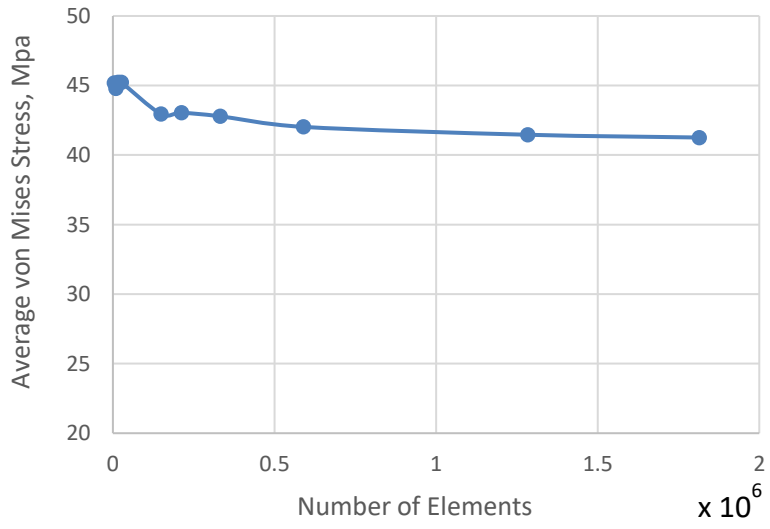


**Figure 42. RVE-averaged von Mises stress against the number of elements for 50% fiber volume fraction and 100% NU.**

### 5.1.2. Local mesh convergence

Because the matrix between the closest fibers are difficult to mesh, proper mesh should be constructed in these areas. To reassure that the mesh discretization is adequate at those areas, mesh convergence is analyzed within the matrix for both maximum Mises stress and maximum dilatational energy density through local convergence. Local mesh convergence is examined by constructing sub models, enclosing the area having the maximum Mises stress and maximum dilatational strain energy density values with mesh sizes smaller and larger than used previously in the overall mesh convergence, taken it as mesh index 4, as shown in Figure 43. Local maximum Mises stress and maximum dilatational strain energy density values are compared for different mesh sizes. For example, in Figure 44 results are shown when 0.3% transverse tensile strain is applied. As shown in the figure 44 (a), by increasing the mesh index (decreasing the local mesh size) the maximum Mises stress becomes nearly constant. Also, the dilatational strain energy density ($U_v$) for each local mesh size is plotted, Figure 44 (b). Nearly the same $U_v$ values are obtained for mesh indices 2,3,4 and 5. But for the coarse mesh size (index 1), $U_v$ shows lower values especially at high applied strains > 0.4%. From both figures 44 (a & b), it can be suggested that the mesh size of a mech index 4 is an adequate size for subsequent finite element analyses.

Linear elements are compared with quadratic elements at different applied strains and similar results are found. Figure 45 shows the Mises stress distribution for the sub models described above with linear and quadratic elements at 0.3% transverse strain, and Figure 46 shows the results at 0.5% transverse strain. Very similar results are found when using either linear or quadratic elements at both applied strains. In addition to this finding,

and for the sake of conserving the time of the analysis, the finite element analysis is conducted with approximately 1,300,000 linear quadrilateral generalized plane-strain elements of type CPEG4 and approximately 60000 linear triangular generalized plane-strain elements of type CPEG3.

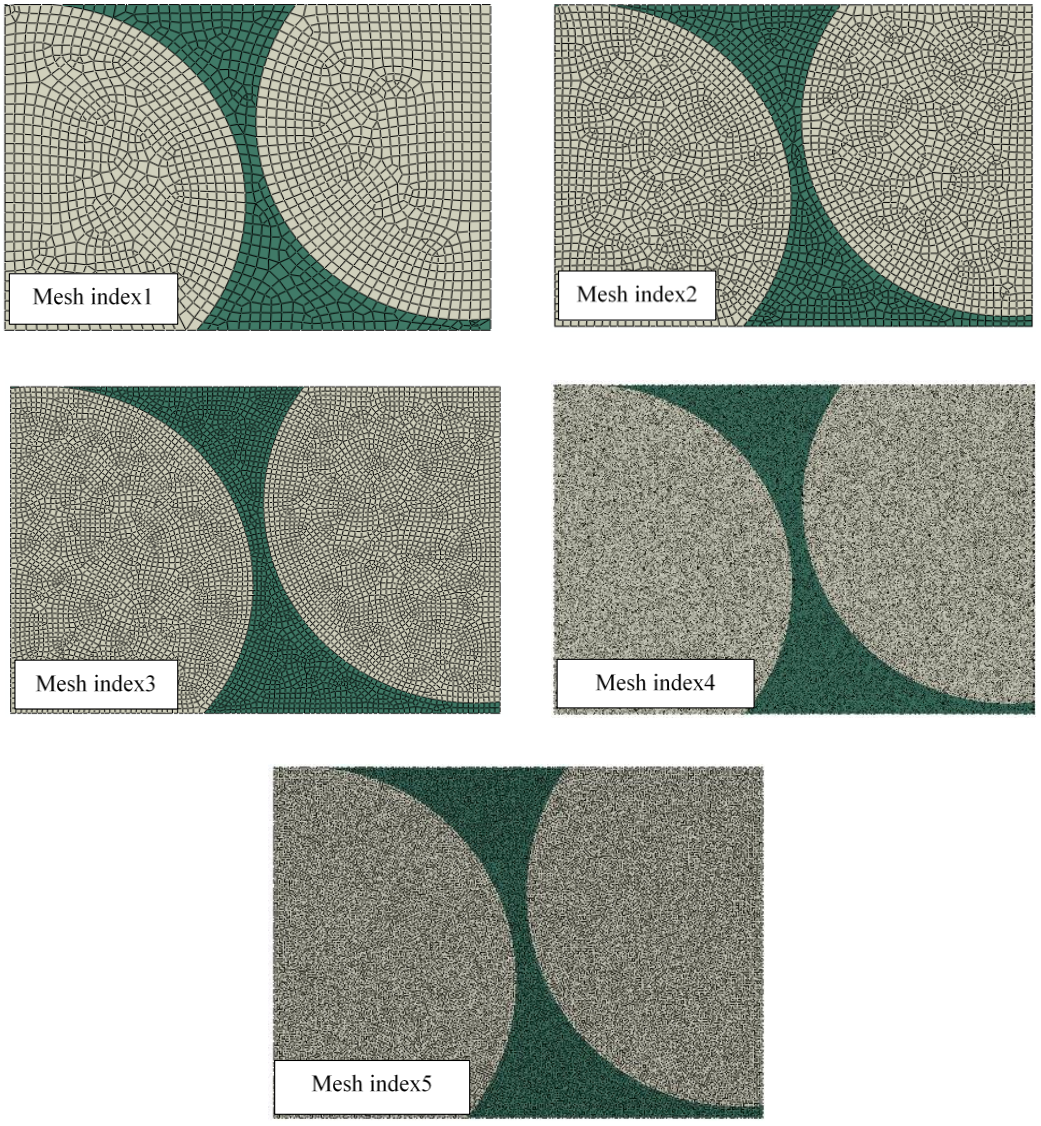


**Figure 43. Different mesh sizes for local mesh convergence analysis.**

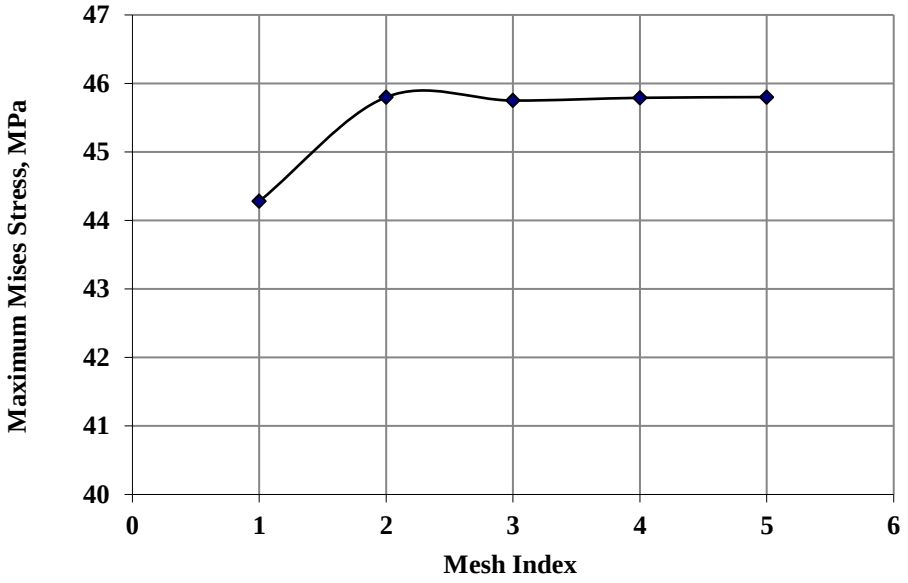


(a)

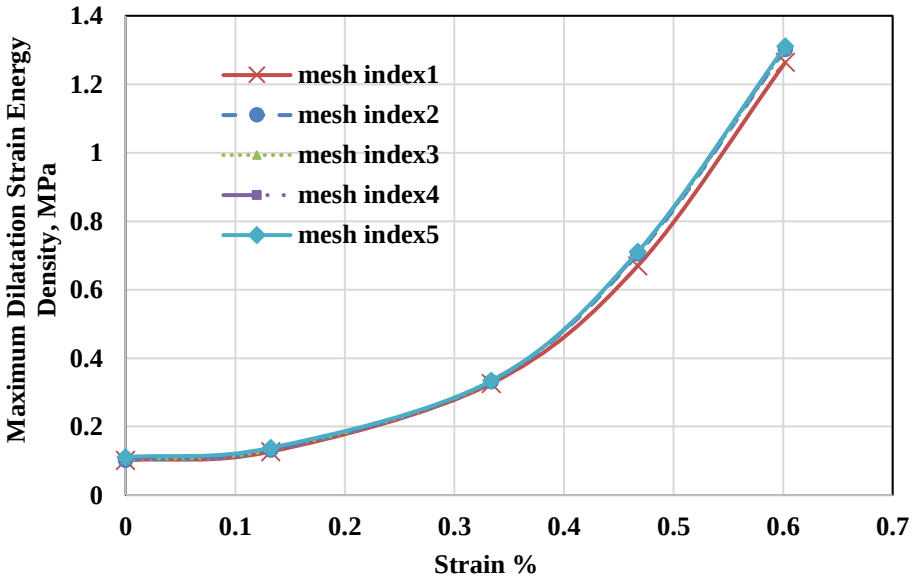


(b)

**Figure 44. (a) The maximum von Mises stress (MPa) and (b) the maximum dilatational energy density (MPa) for 40% fiber volume fraction and 100% NU for different RVE sizes at 0.3% transverse tensile strain.**

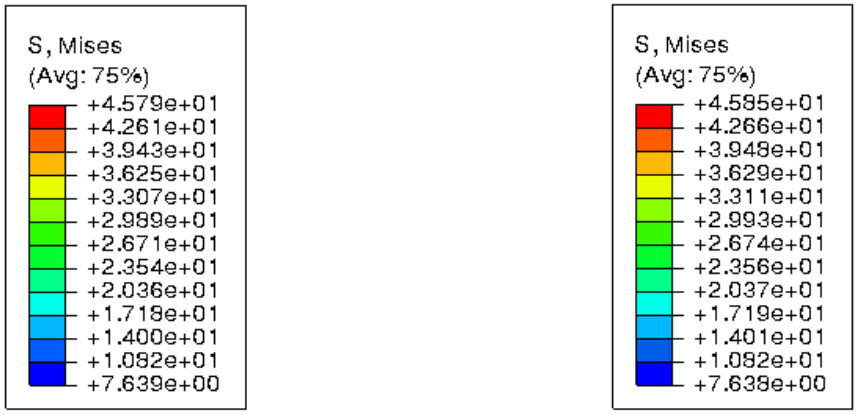


(a) (b)

**Figure 45. Mises stress distribution in MPa (a) with linear elements, (b) with quadratic elements for the sub model shown in Figure 43 at 0.3% transverse tensile strain**

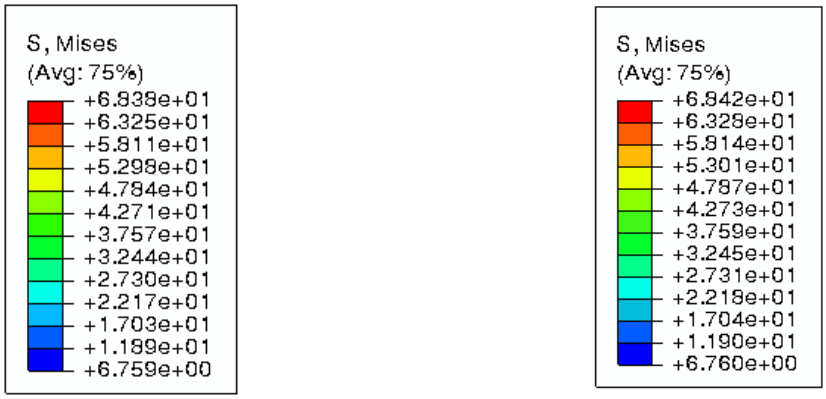


(a) (b)

**Figure 46. Mises stress distribution in MPa (a) with linear elements, (b) with quadratic elements for the sub model shown in Figure 43 at 0.5% transverse tensile strain.**

In micromechanical models, constituent material properties are utilized. Besides that, some researchers use the fiber/matrix interface characteristics [181], which are difficult to measure experimentally although many efforts are given to accurately measure them. Interfacial toughness, are mostly based on a single fiber tests, such as fiber pull out [182,183]. Other tests are conducted to determine the interfacial shear stress, such as fragmentation tests [184,185], micro-indentation tests [186] and microdroplet shear tests

[185]. Results of such tests show large discrepancy [187,188,189]. A good description about such tests is given in [190].

In the present work, matrix and fibers are assumed to be linear elastic and isotropic with a perfect bonding between them at the interface. The materials properties used in this analysis are presented in table 1. The epoxy system has a yield strength of 140 MPa which is typical for the case of MTM57 epoxy system [191].

**Table 1. Materials properties for transverse tensile loading**

| | **Young's modulus (E) GPa** | **Poisson's ratio (ν)** | **Thermal expansion coefficient (α)** |
|---|---|---|---|
| **Fiber glass** | 72 | 0.2 | $5x10^{-6}$ |
| **Epoxy matrix** | 3.35 | 0.35 | $66x10^{-6}$ |

The local stress fields are determined under thermal cooldown $\Delta T = -82^{o}C$, which is typical of glass-epoxy composites, followed by a transverse displacement (Figure 47) in which the RVE sides are free from constraints.

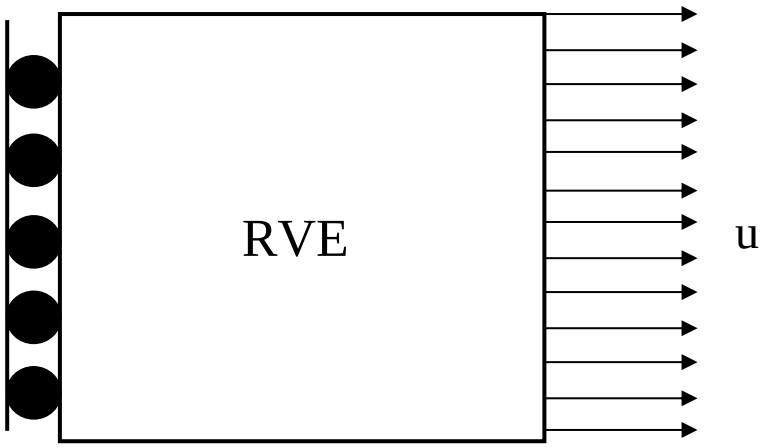


**Figure 47. Uniaxial transverse displacement boundary condition on a RVE realization.**

### 5.1.3. Displacement versus traction boundary conditions

According to Hill [158], the size of an RVE should be such that the overall properties are independent of the applied boundary conditions, whether traction or displacement. In present work, local stress and strain fields of the constructed RVEs are compared when under traction versus under displacement boundary conditions. For example, the same RVE for 40% fiber volume fraction and 100% NU, was under traction boundary condition in one analysis, and under displacement boundary condition in another analysis. Figure 48 shows the distortional and dilatational strain energy densities and the principal stress ratios curves for both cases (their significance in failure analysis will be discussed later). As can be observed, they both give similar results. Figures 49 and 50, show the comparison between the two boundary conditions for the 50% and the 60% fiber volume fraction and 100% NU, respectively. Results indicate that the size of the RVE is adequate as suggested by Hill [158]. Throughout this work, displacement boundary condition is applied.

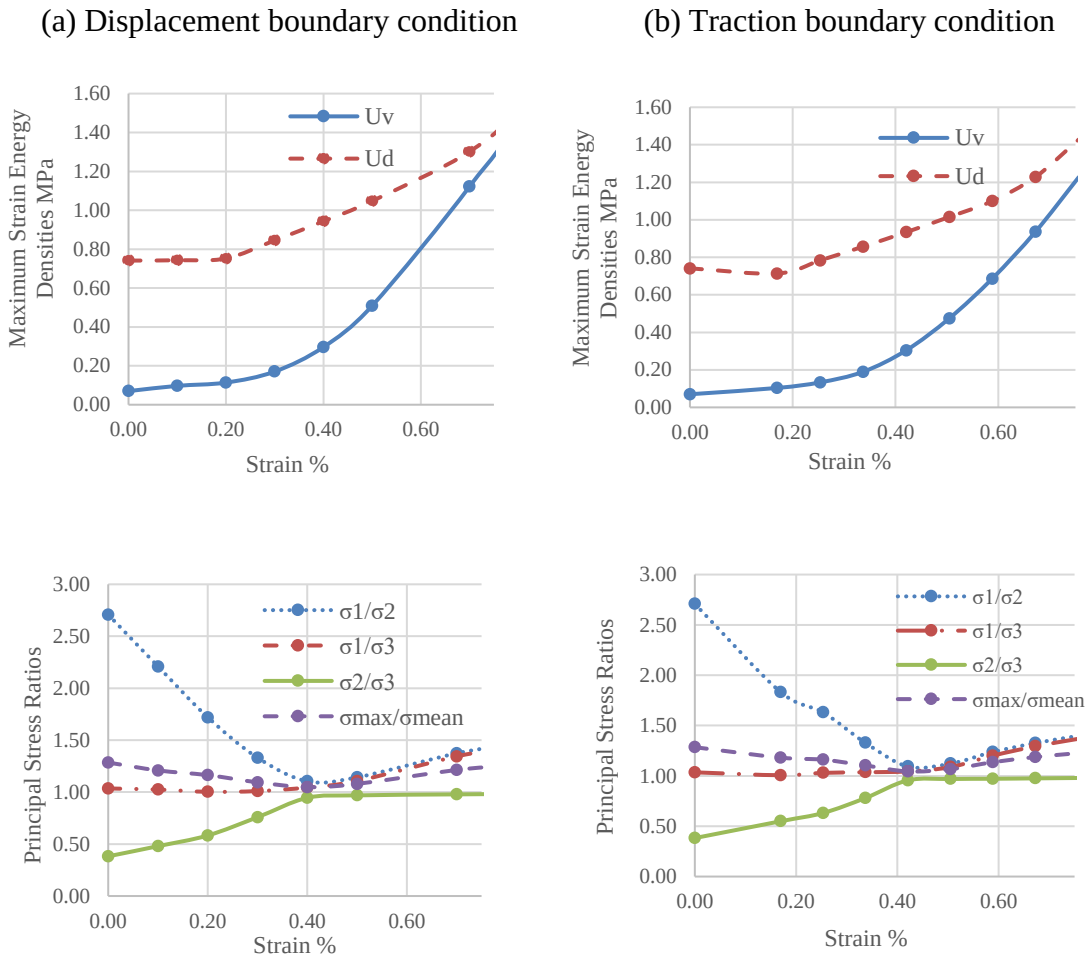


**Figure 48. The maximum values of dilatational energy density $U_v$ and distortional energy density $U_d$ as well as the principal stress ratios attained within RVEs versus applied transverse tensile strain with (a) Displacement boundary conditions and (b) Traction boundary conditions, for 40% fiber volume fraction and 100% degree of nonuniformity.**

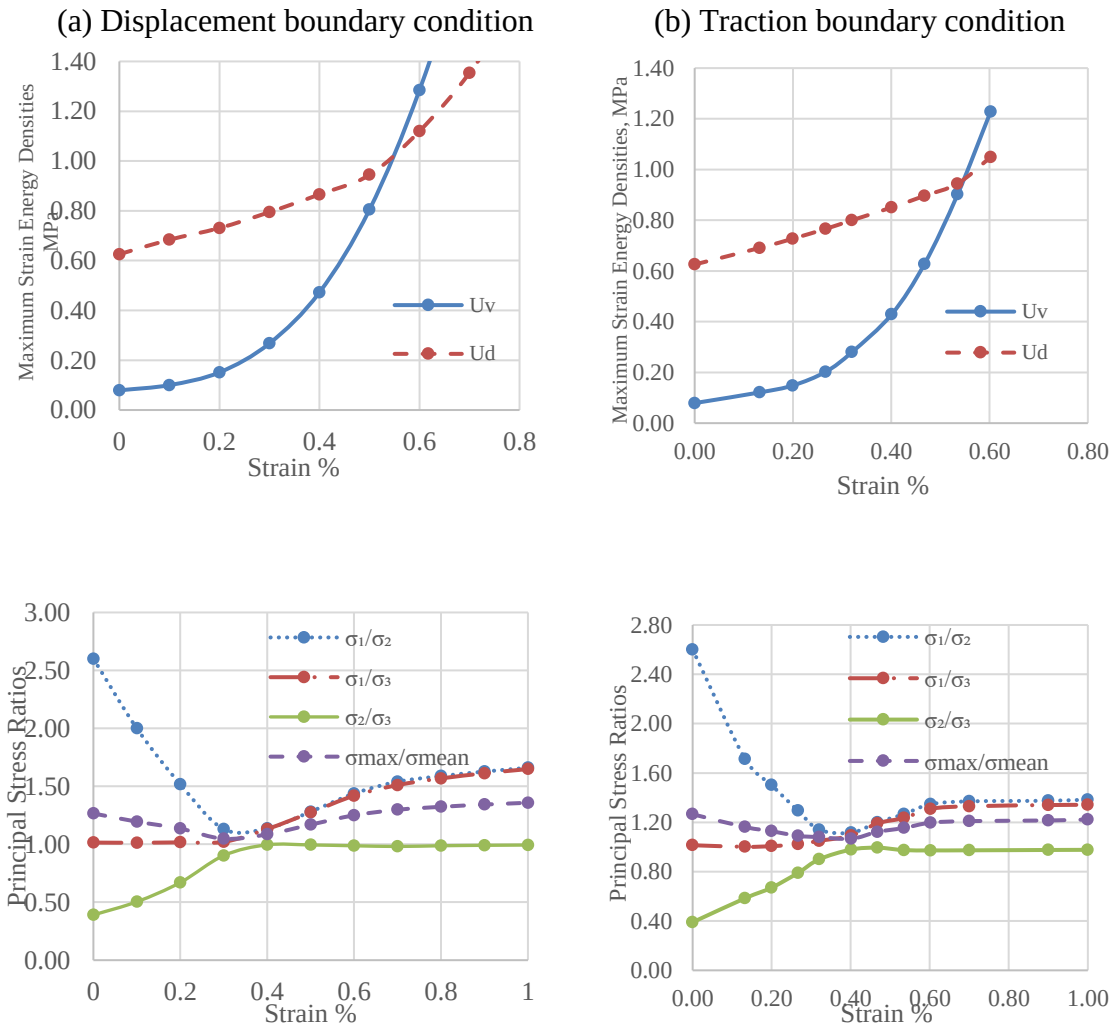


**Figure 49. The maximum values of dilatational energy density $U_v$ and distortional energy density $U_d$ as well as the principal stress ratios attained within RVEs versus applied transverse tensile strain with (a) Displacement boundary conditions and (b) Traction boundary conditions, for 50% fiber volume fraction and 100% degree of nonuniformity.**

(a) Displacement boundary condition (b) Traction boundary condition

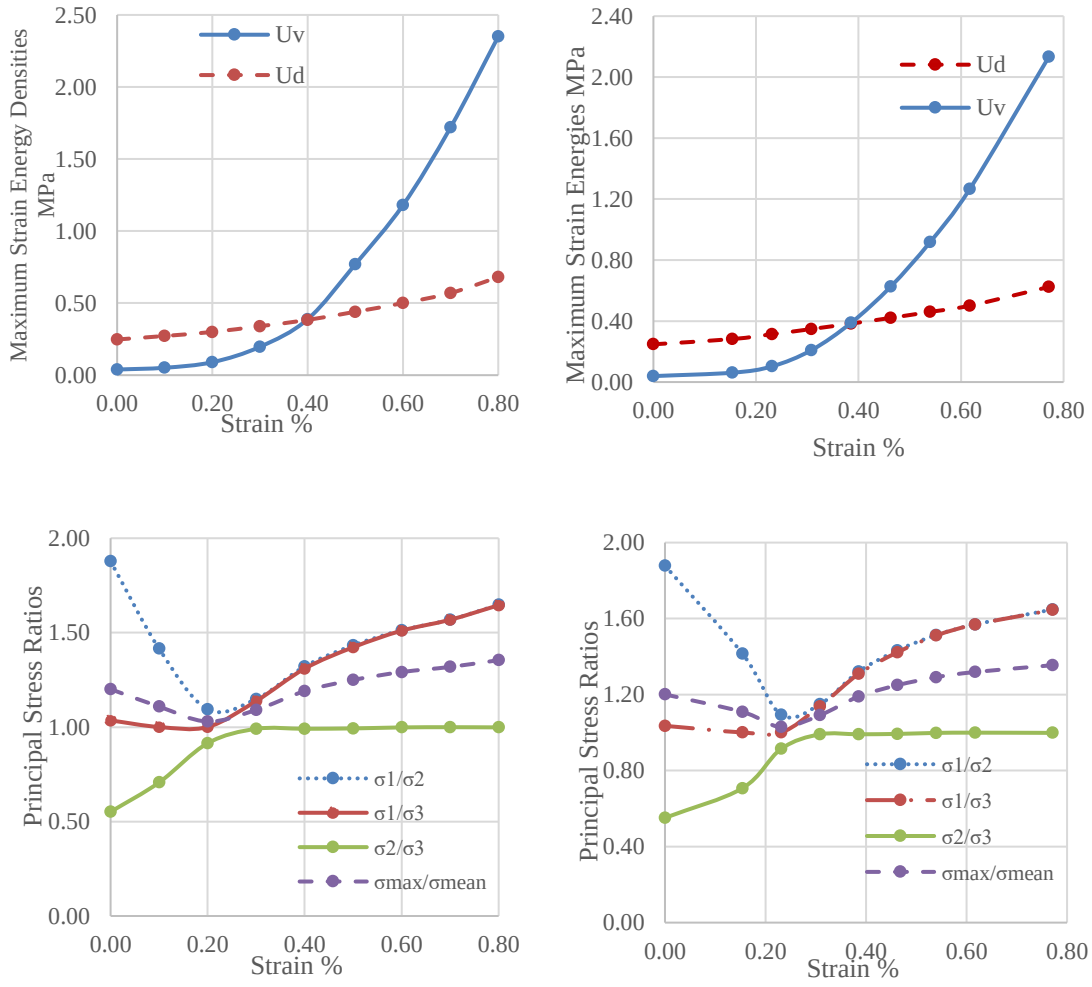


**Figure 50. The maximum values of dilatational energy density $U_v$ and distortional energy density $U_d$ as well as the principal stress ratios attained within RVEs versus applied transverse tensile strain with (a) Displacement boundary conditions and (b) Traction boundary conditions, for 60% fiber volume fraction and 100% degree of nonuniformity.**

## 5.2. Failure analysis

The first failure event that takes place within an RVE under transverse tension is studied. The criterion for failure initiation considered here is critical energy dissipation, either through debonding, depending on the value of dilatational energy density ($U_v$), or through matrix yielding, depending on distortional energy density ($U_d$). As mentioned

earlier, Asp et al [76] suggested a criterion for a failure mechanism prior to debonding which they named “Cavitation”. The threshold for such mechanism is given as a material property as dilatational energy density value. This value is in a range of 0.13-0.2 MPa, which was determined from the Poker-chip test conducted on three different polymers. Requirements for cavity formation besides reaching the threshold value is to have equal or nearly equal principal stresses. On the other hand, for yielding to occur in the matrix, the distortional energy density should reach the threshold value required for the matrix to yield. Cavitation is suggested in [76] to take place in the matrix close to the fiber/matrix interface, but yielding is to occur in the resin rich areas, Figure 51.

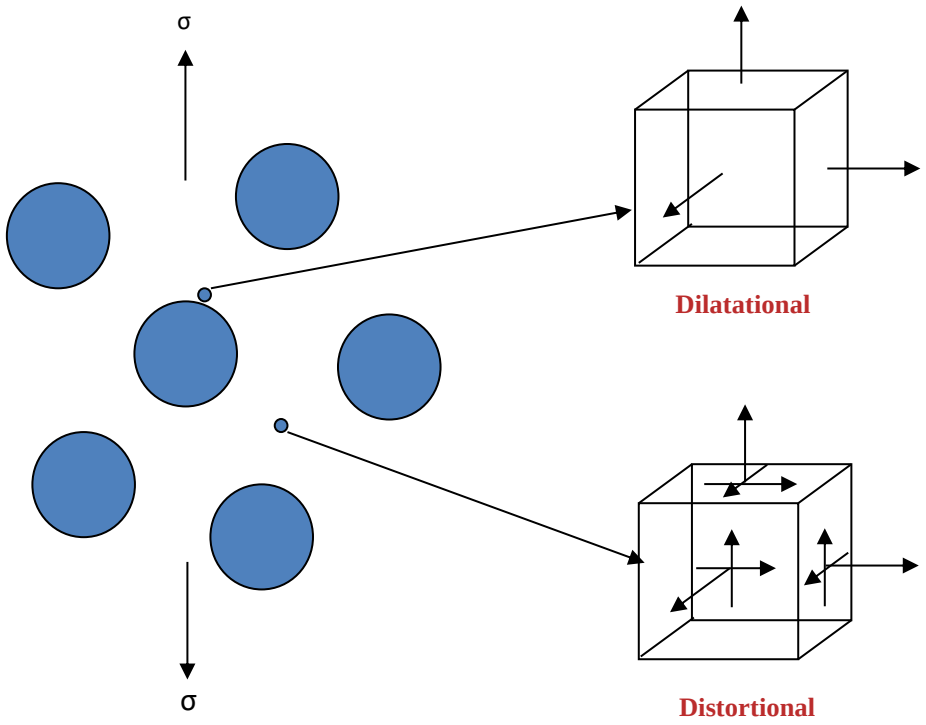


**Figure 51. Local positions where both dilatational and distortional energy densities may reach their threshold values. Reprinted from [76].**

The two thresholds are material properties given by critical values of dilatational energy density for cavitation and of distortional energy density for yielding. Both are point-failure criteria, and therefore the failure analysis requires determining at which points within the RVE the two criteria are met.

For initiation of yielding (inelastic deformation) in polymers, the von Mises distortional energy density for metals is modified to include the effect of hydrostatic stress in polymers as follows:

$$\boldsymbol{\tau_y^{oct}} = \tau_{\mathbf{yo}}^{\mathbf{oct}} - \mu p \qquad (11)$$

where $\boldsymbol{\tau_y^{oct}}$ is the octahedral shear stress at yielding, $\tau_{\mathbf{yo}}^{\mathbf{oct}}$ is the octahedral shear stress at yielding in pure shear, $\mu$ is the coefficient of internal friction, and p is the hydrostatic tensile stress, which is equal to $(\sigma_1 + \sigma_2 + \sigma_3)/3$. The coefficient of internal friction has values in the range 0.157-0.21 [192,193]. In present work, based on stress analysis, results are compared using $\mu$=0.157, 0.175 and 0.21 as well as with no modification, i.e., $\mu$=0. Figure 52 shows the maximum distortional energy density for a 54% fiber volume fraction and 100% nonuniformity for $\mu$= 0, 0.175 and 0.21. Since the differences in the results are small, the value of $\mu$ is taken as 0.175 throughout this work.

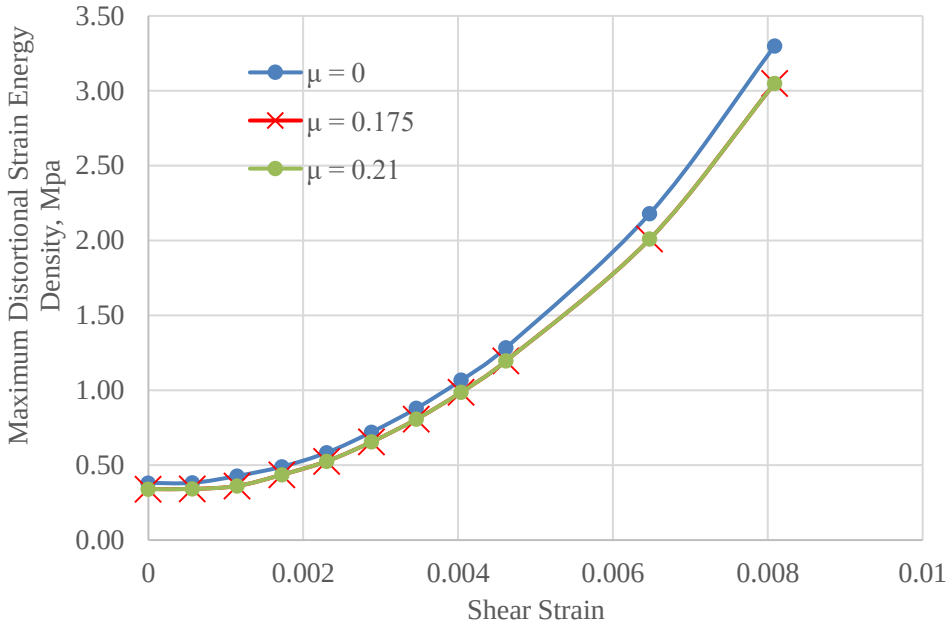


**Figure 52. The maximum values of distortional energy density $U_d$ attained within RVEs versus applied axial shear strain for 54% fiber volume fraction and 100% degree of nonuniformity.**

$U_v$ for a linear elastic solid is given by,

$$Uv = \frac{1-2\nu}{6E}(\sigma_1 + \sigma_2 + \sigma_3)^2 \qquad (12)$$

where $\sigma_1$, $\sigma_2$ and $\sigma_3$ are the principal stresses, E is the Young's modulus and $\nu$ is the Poisson's ratio. As was argued in [76], although the dilatational energy density criterion can be expressed in terms of the mean stress, it would generally imply that the critical mean stress is temperature dependent, which was shown not to be the case. In subsequent studies [74, 76] it was found that under a transversely applied tension on a unidirectional composite, the maximum dilatational energy density occurs close to the fiber-matrix interface and has lower values compared to the maximum distortional energy density, which tends to occur in resin rich areas. This result was also found in another study by Bulsara [194], reported in [73], where RVEs with nonuniform spatial distribution of fibers were considered. Thus, two

possible mechanisms can occur under transverse tension in unidirectional composites, and formation of a transverse crack would then depend on the fiber distribution and the critical values of the two energy densities for a given polymer.

Since the dilatational energy density criterion applies strictly when the three principal stresses are tensile and equal, we must find a point where this condition is met, and at the same time, the dilatational energy density at that point equals or exceeds the critical value for cavitation. Because of the randomness in the local stress field, it was found necessary to relax the stress equality condition to capture the points of cavitation of high probability of occurrence. Thus, we adopt an approximation allowing the three principal stresses to be within a narrow band of 20% deviation from equality, i.e., the ratios of the principal stresses to be

$$0.8 \leq \frac{\sigma_i}{\sigma_j} \leq 1.2 \qquad (13)$$

where *i* and *j* take values 1, 2 and 3. With this restriction, a realization of a given RVE is searched to find the required location of the point. This is done with each increment of 0.1% of the applied mechanical strain.

**5.3. Results and discussion**

The local stress states are analyzed for each constructed realization for 40%, 50% and 60% fiber volume fractions and 0%, 30%, 60% and 100% of nonuniformity. An ABAQUS subroutine is built to calculate the dilatational and distortional energy densities at every node within the RVE at each applied strain for all combinations of fiber volume fractions and the preselected degree of nonuniformity. The maximum dilatational energy density is determined as well as its node, providing that the three principal stresses are tensile. At this node, the principal stress ratios are determined along with the ratio between

the maximum to the mean principal stresses. The maximum dilatational energy density value will then represent a point in a corresponding curve of maximum dilatational energy density against applied strain. Also, at each node in the RVE, the distortional energy density is determined and the maximum value represents a point in the distortional energy density-strain curve without any restrictions. For example, in the RVE for 50% fiber volume fraction and 100% nonuniformity, shown in Figure 53, both the nodes at which maximum dilatational and maximum distortional energy densities are determined. The principal stress ratios along with the ratio between the maximum to the mean principal stresses are plotted for the nodes having the maximum $U_v$, Figure 54. From the figure, one can determine the transverse tensile strain at which the three principal stresses are equal or nearly equal with a tolerance of 20% difference as mentioned before for a cavity to form. For example, the principal stresses are within the 20% difference at ~ 0.3%. At this strain, we can see that the dilatational strain energy density exceeds the threshold value given in [76] giving a value of about 0.3 MPa as shown in Figure 55. At the same strain, the distortional energy is below its threshold for yielding for this epoxy which is ~ 2.62 MPa. For this epoxy, yielding will occur at a higher transverse strain value than that required for cavitation. Thus, it can be suggested that cavitation at this node is the first event of failure when comparing the two mechanisms.

The nodes of maximum dilatational and maximum distortional energy densities are changed/shifted from one node to another until reaching higher applied strain. In table 2, it can be observed that the nodes of maximum dilatation and distortion energy densities are changed till a strain of 0.5% for dilatational energy and 0.3% for distortional are reached. Also, when analyzing these nodes, it was found the following; 1- the node at which maximum distortion is maintained is within the matrix between the closest fibers pairs, 2-

the node at which maximum dilatational energy density is determined - providing that the requirements for cavitation as mentioned earlier are fulfilled- is observed to be near or at the fiber/matrix interface between two fibers lying parallel to the loading direction. This is also found in all RVEs of different fiber volume fractions and different degree of nonuniformity.

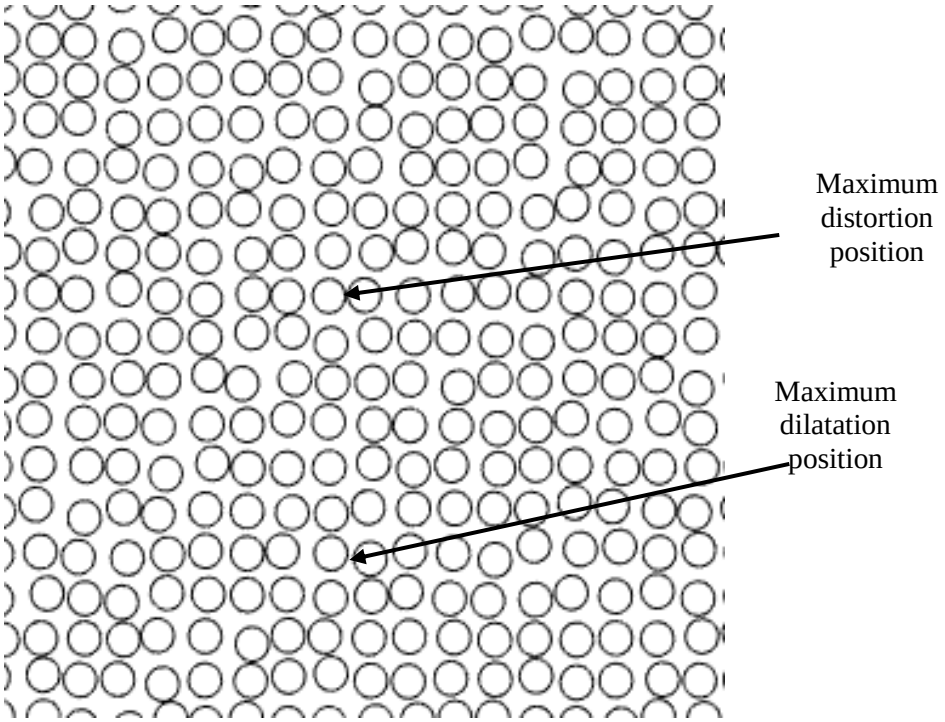


**Figure 53. An RVE with 50% fiber volume fraction and 100 % nonuniformity, showing the position of maximum dilatational and distortional energy densities under transverse tensile loading.**

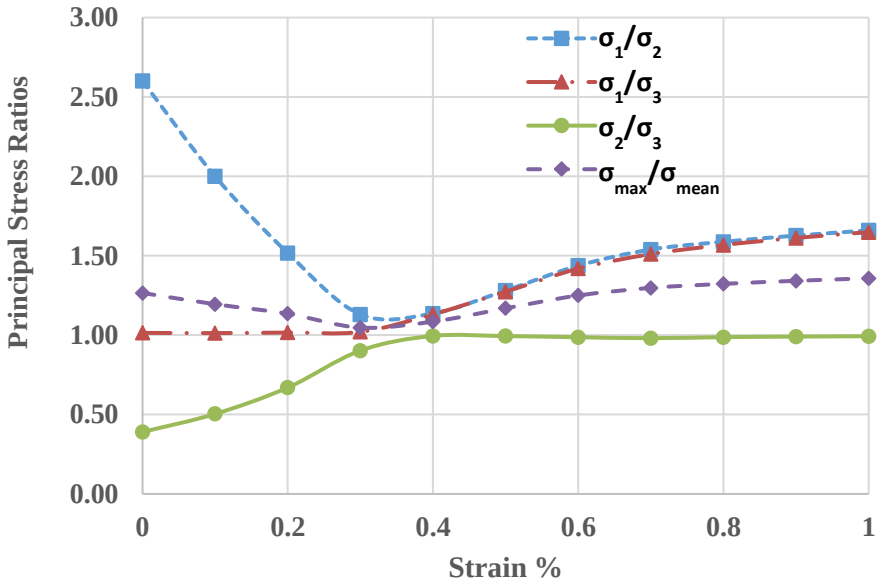


**Figure 54. The principal stress ratios and the ratio of maximum/mean principal stress versus applied strain for RVE shown in Figure 53.**

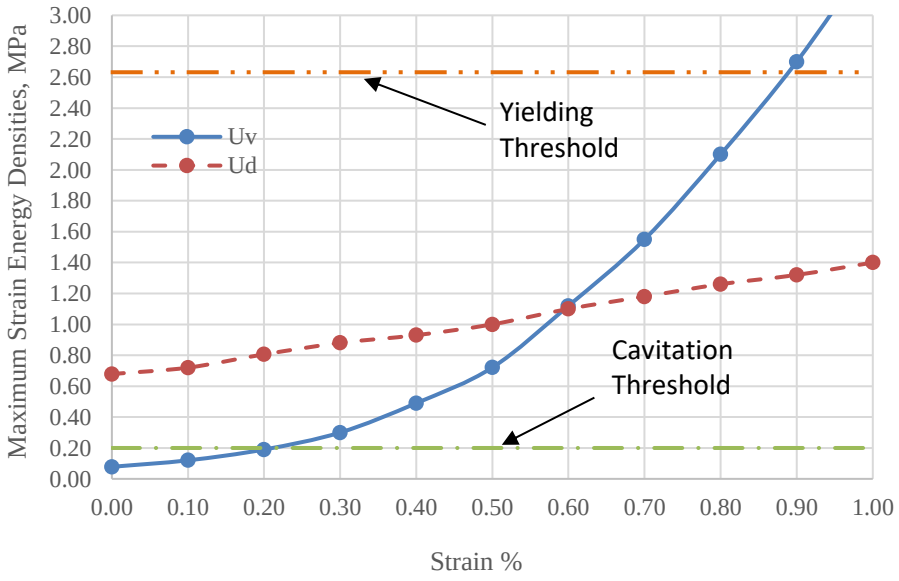


**Figure 55. The maximum values of dilatational energy density $U_v$ and distortional energy density $U_d$ attained within RVEs versus applied strain for RVE shown in Figure 53.**

**Table 2. Nodes with maximum dilatational and distortional energy densities for the RVE shown in Figure 53.**

| Strain % | Max dilatation node number | Max distortion node number |
|---|---|---|
| 0 | 45673 | 1059625 |
| 0.1 | 45670 | 41781 |
| 0.2 | 44757 | 41781 |
| 0.3 | 375 | 1057725 |
| 0.4 | 375 | 1057725 |
| 0.5 | 27908 | 1057725 |
| 0.6 | 27908 | 1057725 |
| 0.7 | 27908 | 1057725 |
| 0.8 | 27908 | 1057725 |
| 0.9 | 27908 | 1057725 |
| 1 | 27908 | 1057725 |

At least five realizations for each combination of fiber volume fraction (40%, 50%, and 60%) and percentage of nonuniformity (30%, 60% and 100%) are established. The RVEs as well as the position of maximum dilatational and distortional energy densities are shown in APPENDIX B. The same procedures in determining the first event of failure are conducted.

For all realizations, cavitation is highly suggested as the first event of failure under transverse tension. The strain required for cavitation is lower than that required for yielding providing that the principal stresses at the position of maximum $U_v$ are equal or nearly equal, Figures (56-58). It was found that the strain at which cavitation is suggested depends on the fiber volume fraction and the percentage of NU. This will be illustrated below.

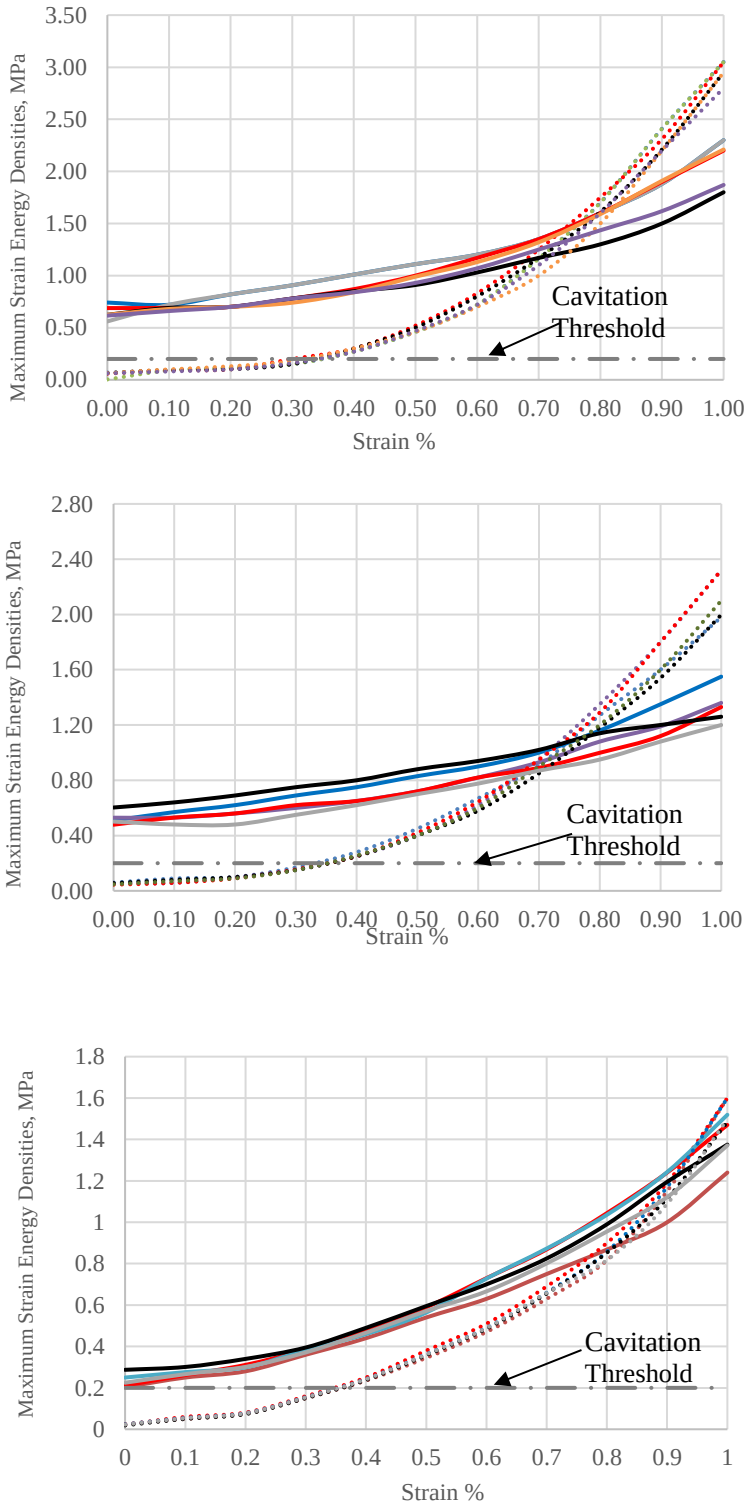


**Figure 56. The maximum values of dilatational $U_v$ and distortional $U_d$ energy densities attained within different RVEs versus applied strain for 40% fiber volume fraction and (a) 100%, (b) 60% and (c) 30% NU. Solid lines represent distortional energy density and dotted lines represent dilatational energy density.**

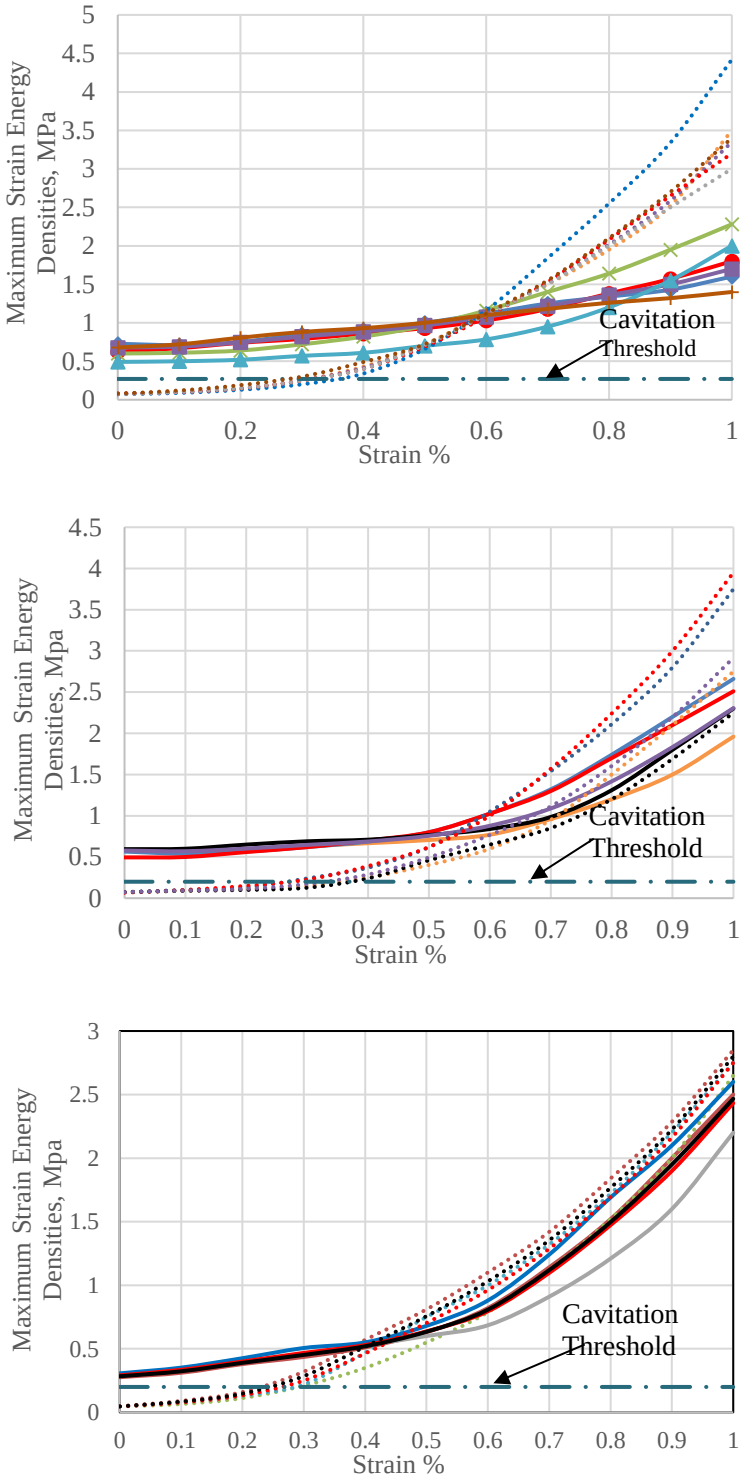


**Figure 57. The maximum values of dilatational $U_v$ and distortional $U_d$ energy densities attained within different RVEs versus applied strain for 50% fiber volume fraction and (a) 100%, (b) 60% and (c) 30% NU. Solid lines represent distortional energy density and dotted lines represent dilatational energy density.**

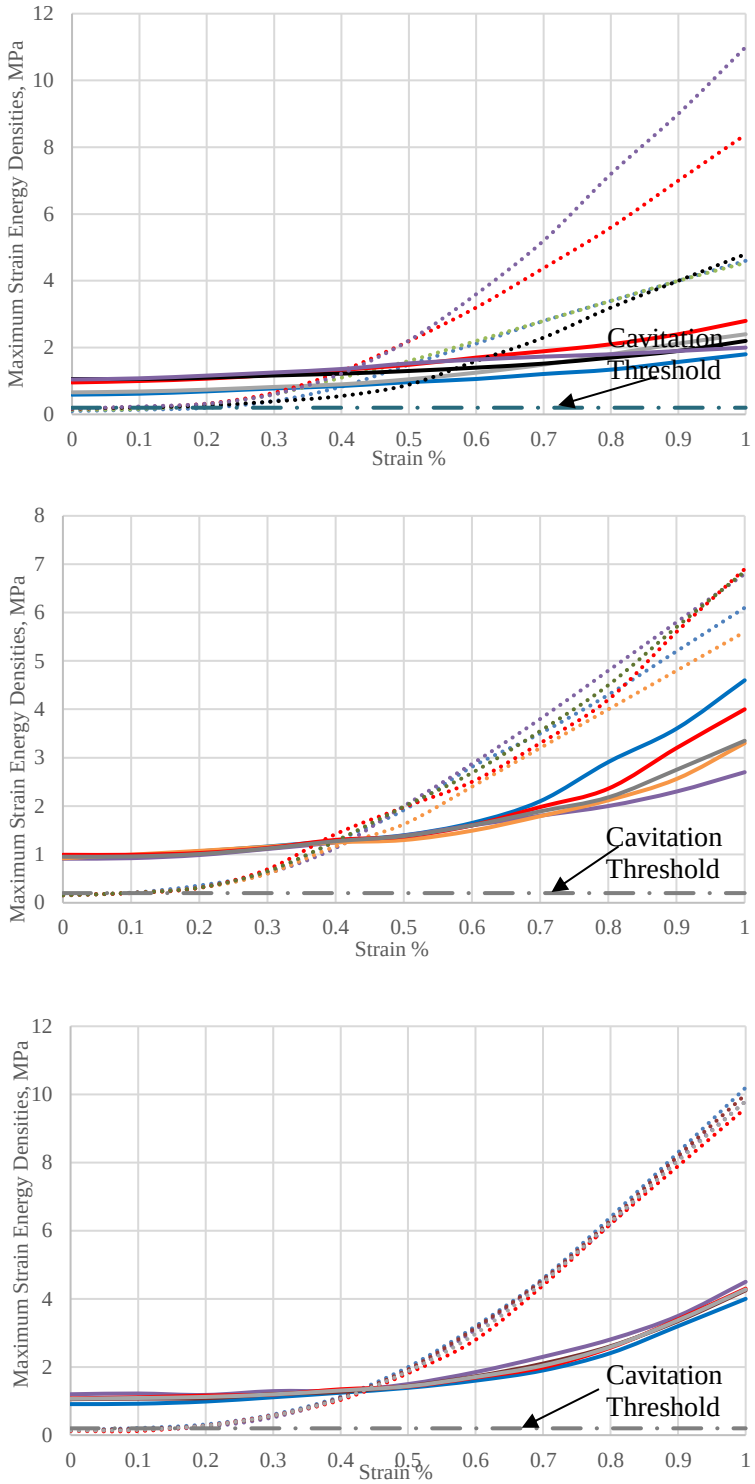


**Figure 58. The maximum values of dilatational $U_v$ and distortional $U_d$ energy densities attained within different RVEs versus applied strain for 60% fiber volume fraction and (a) 100%, (b) 60% and (c) 30% NU. Solid lines represent distortional energy density and dotted lines represent dilatational energy density.**

### 5.3.1. Effect of fiber volume fraction

At the same degree of nonuniformity, by increasing the fiber volume fraction, the strain for cavity formation is decreased. This is best illustrated when different fiber volume fractions are compared with RVEs of uniform distributions. In the figures below, Figure 59, a uniform distribution of 40% fiber volume fraction fulfils cavitation requirements at strain ~ 0.52%. But for higher fiber volume fraction, such as 60% the cavitation is fulfilled at strain ~ 0.33%. Another example is given in figure (60) for 40% and 50% fiber VF and 100% nonuniformity. For the 40% fiber volume fraction, cavitation is to take place at ~ 0.45% strain, but for the 50% VF, it is to occur at ~0.36% strain.

### 5.3.2. Effect of degree of nonuniformity

The applied strain at which cavitation occurs is reduced when the fiber distribution is nonuniform versus when it is uniform. This effect can be attributed to the higher probability of finding fibers close enough to induce sufficiently high principal stresses to reach the condition for cavitation. For example, the figures above for the 40% FVF and uniform distribution (Figure 59 (a)) and 100% nonuniformity (Figure 60 (a)) show that for the uniform distribution cavitation is to occur at strain ~0.52, but when a 100% NU is created, this strain is lowered to be ~0.45%. The cavitation threshold is reached at ~0.28% strain.

Also, when compared to the uniform distribution, it can be observed that the distortional strain energy gives lower values in the uniform distribution than that given under any degree of nonuniformity even the 30%. This could be due to the smaller inter-fiber distances when given a degree of nonuniformity other than the uniform pattern.

For the 60% VF, because of the high density, the strain for cavitation does not change much at any degree of nonuniformity. This could be due to the closeness of fibers that makes it more difficult to apply large values of nonuniformities.

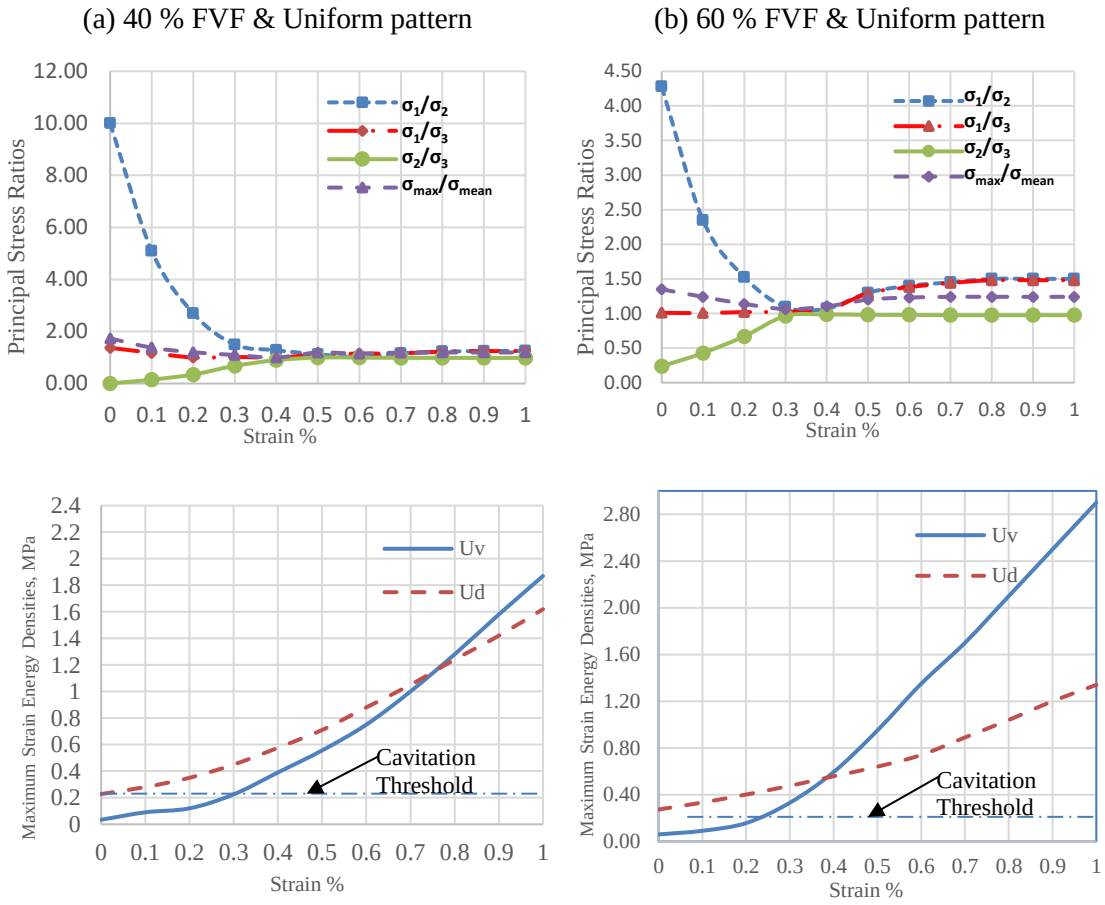


**Figure 59. Effect of FVF on the cavitation strain for (a) 40% FVF and (b) 60% FVF with uniform fiber distribution.**

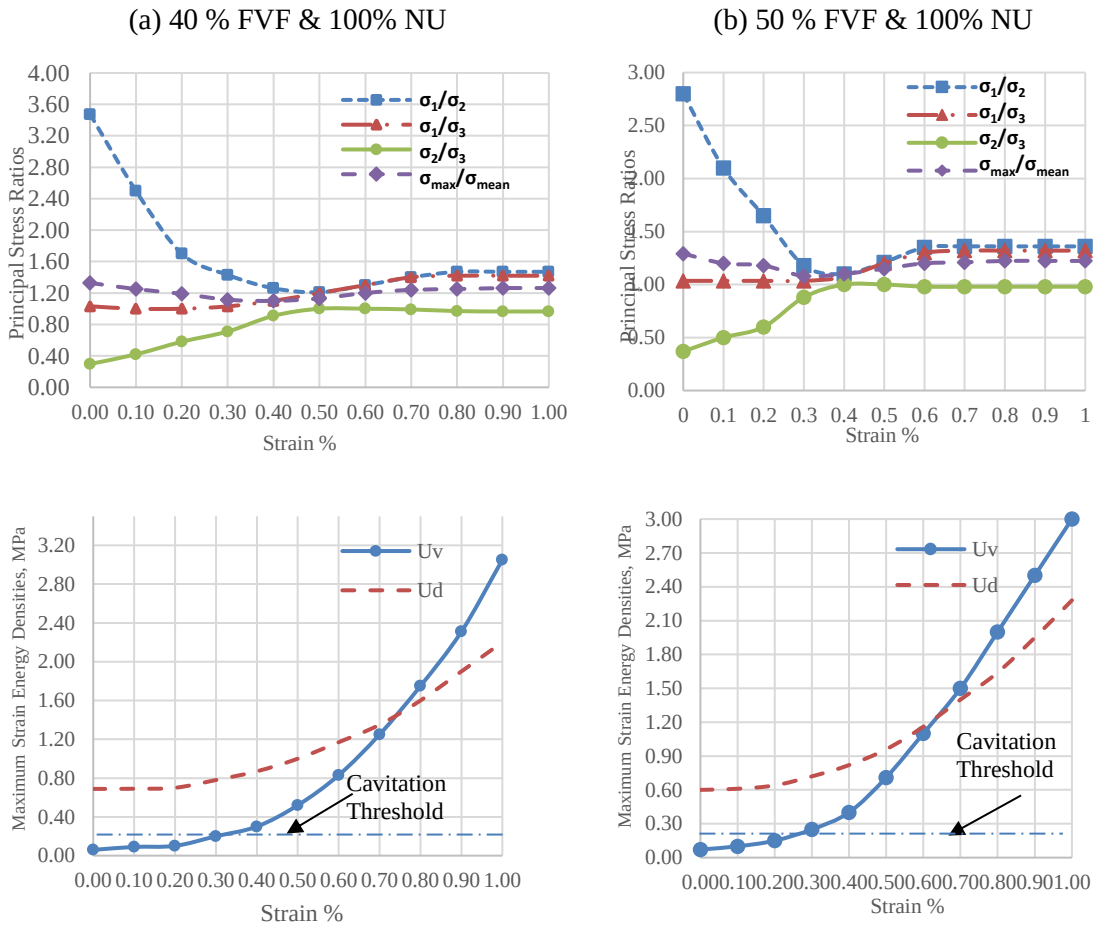


**Figure 60. Effect of FVF on the cavitation strain for (a) 40% FVF and (b) 50% FVF with 100% nonuniformity.**

Figure 61 summarizes the effect of fiber distribution nonuniformity in terms of the applied mechanical strain at which cavitation initiates for all three fiber volume fraction cases studied. As the plot shows, the effect of nonuniformity of fiber distribution is consistent at all three fiber volume fractions. Also, note that the strains for cavitation also reduce as the fiber volume fraction increases.

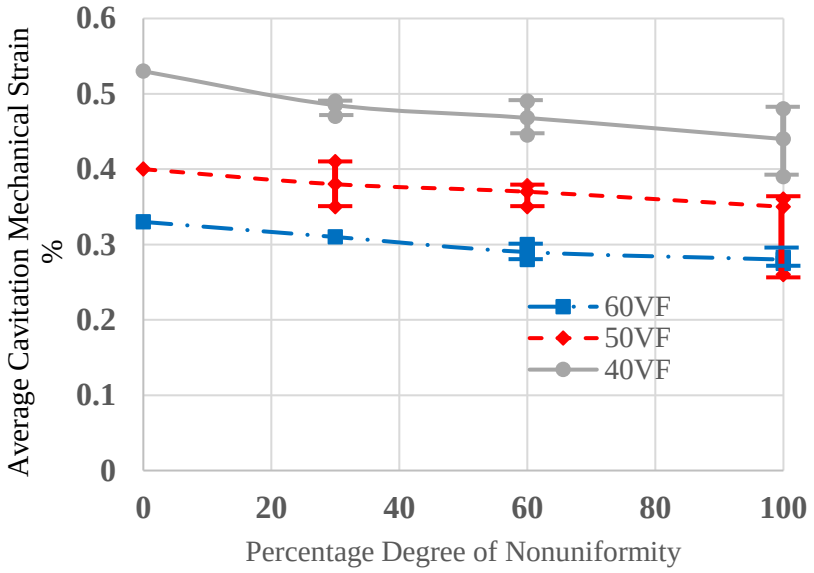


**Figure 61. The average mechanical strain at onset of cavitation versus the percent degree of nonuniformity for 40%, 50%, and 60 % fiber volume fraction in addition to maximum and minimum values.**

### 5.3.3. Effect of matrix/fiber stiffness ratio

Figure 62 shows the applied strain averaged over at least five RVE realizations at which the cavitation criterion is satisfied for different matrix/fiber stiffness ratios ($E_m/Ef$) plotted for the 50% fiber volume fraction and the 100% degree of nonuniformity. It can be observed that this strain increases with increasing $E_m/E_f$ ratio and approaches a plateau when this ratio is higher than 0.04. This trend is in agreement with a recent numerical study [156], which found that the microstructure of unidirectional composites strongly affects effective properties at high fiber volume fractions and high contrasts of constituent properties.

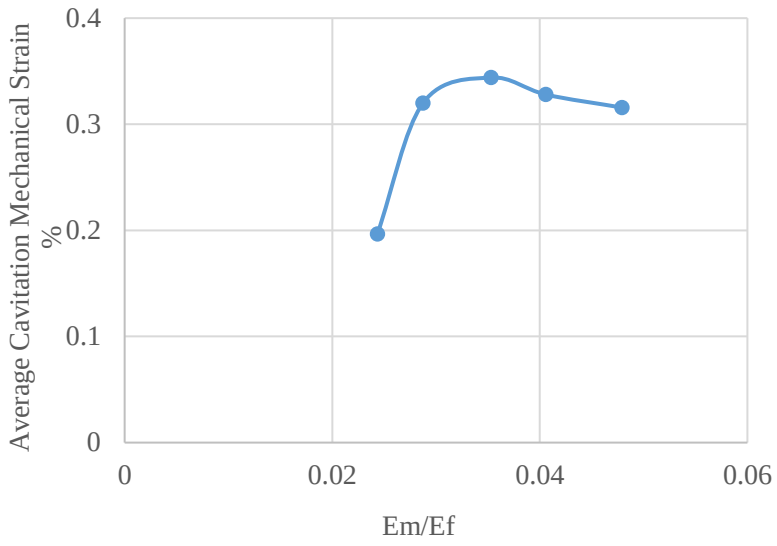


**Figure 62.The effect of matrix/fiber stiffness ratio on the average mechanical strain at cavitation for 50% fiber volume fraction and 100% nonuniformity.**

### 5.4. The effect of the presence of voids

Preliminary tests are conducted using 2D RVEs under transverse tension with the presence of a void. Its effect on damage initiation mechanism is studied. The void is taken as an area with very low material properties (e.g; very low stiffness value) compared to that of the matrix. Variables, such as the void shape, size, and position, are investigated. To illustrate the effect of the presence of a void in the RVE, consider the RVE in Figure 53. The position of the maximum dilatational energy density is pointed out. At this position, a cavity is suggested to be formed at ~0.3% transverse tensile strain. A void is then added near this position. The FEA is run again under different transverse tensile displacements as illustrated above.

Consider a void with a circular shape as shown in figure 63 (a). The node of maximum dilatational energy density is pointed out. The principal stress ratios along with the ratio between the maximum to the mean principal stresses are plotted for the node having

the maximum $U_v$, Figure 63 (b). The maximum energy densities are plotted in figure 63 (c). When the void is added, the position of maximum dilatational energy density is not changed. Besides, the principal stresses are nearly equal at strain ~0.3%. At this strain the dilatational energy density reaches the critical value for cavitation. This finding which is similar to the case without voids. The void is now added, in a position far away from the initial cavity position, Figure 64 (a). It is also found that cavitation requirements are fulfilled at nearly the same transverse strain as shown in figures 64(a) and (b).

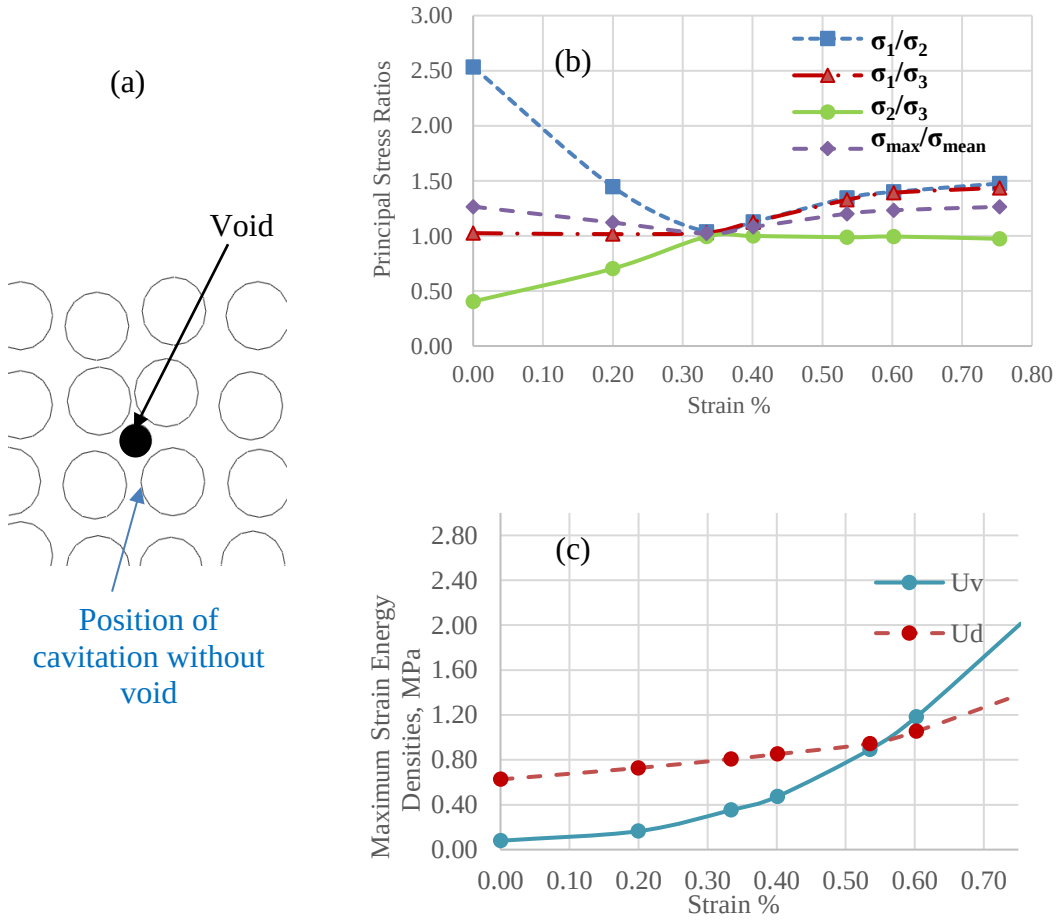


**Figure 63. The effect of the presence of circular void on cavitation near the initial cavity site, (a) part of the original RVE showing the void and the position of cavitation without voids, (b) The principal stress ratios and the ratio of maximum/mean principal stress versus applied strain and (c) The maximum values of dilatational energy density $U_v$ and distortional energy density $U_d$ attained within RVEs versus applied strain.**

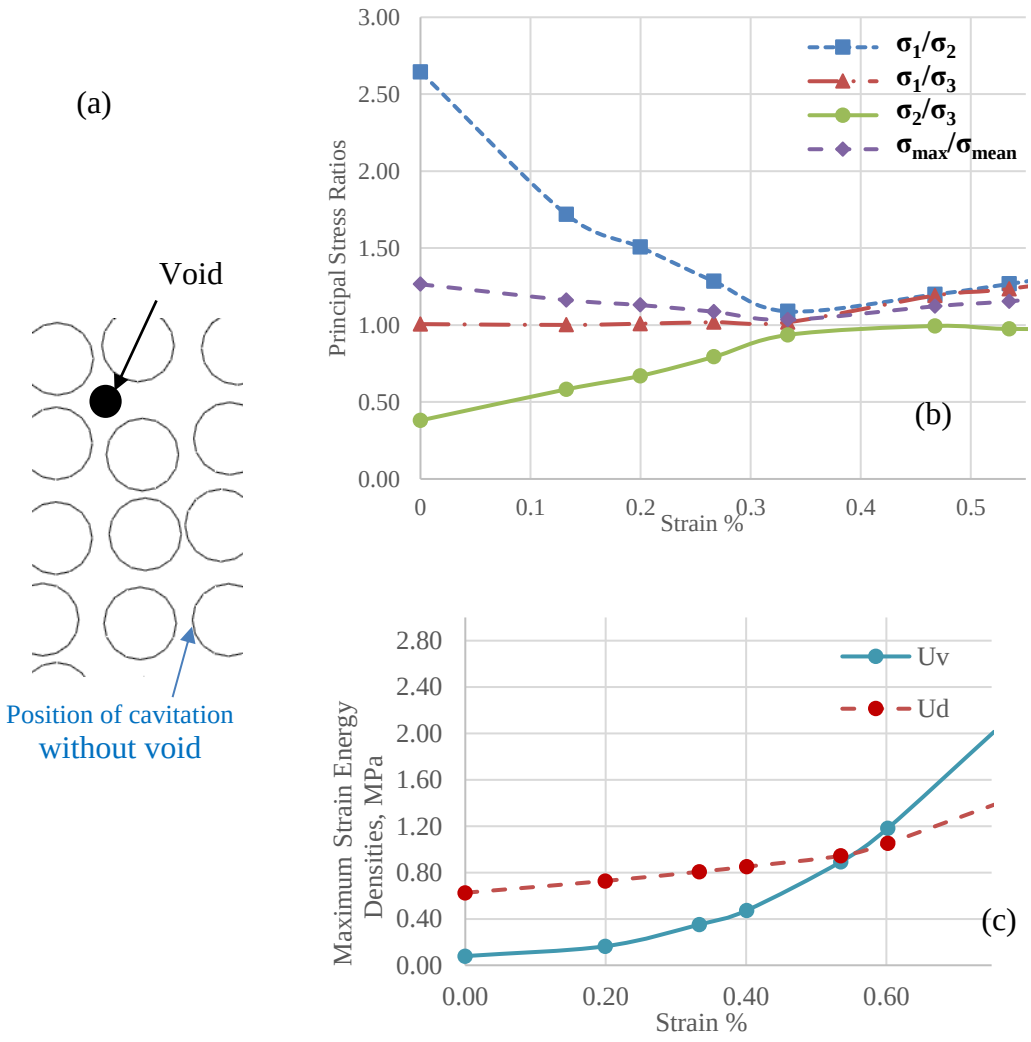


**Figure 64. The effect of the presence of circular void on cavitation away from the initial cavity site, (a) part of the original RVE showing the void and the position of cavitation without voids, (b) The principal stress ratios and the ratio of maximum/mean principal stress versus applied strain and (c) The maximum values of dilatational energy density $U_v$ and distortional energy density $U_d$ attained within RVEs versus applied strain.**

The presence of elliptical voids with different aspect ratios and in horizontal and vertical positions with respect to loading directions is investigated. For example, figure 65 (a) shows an elliptical void with a low aspect ratio ~2:1. The void is placed such that the major axis is parallel to the loading direction. The strain required for cavitation is slightly decreased to be ~0.27% instead of ~0.3. In addition, the principal stress ratios difference is increased.

When the elliptical void is placed vertically, as shown in Figure 66, the node at which cavitation occurs is changed.

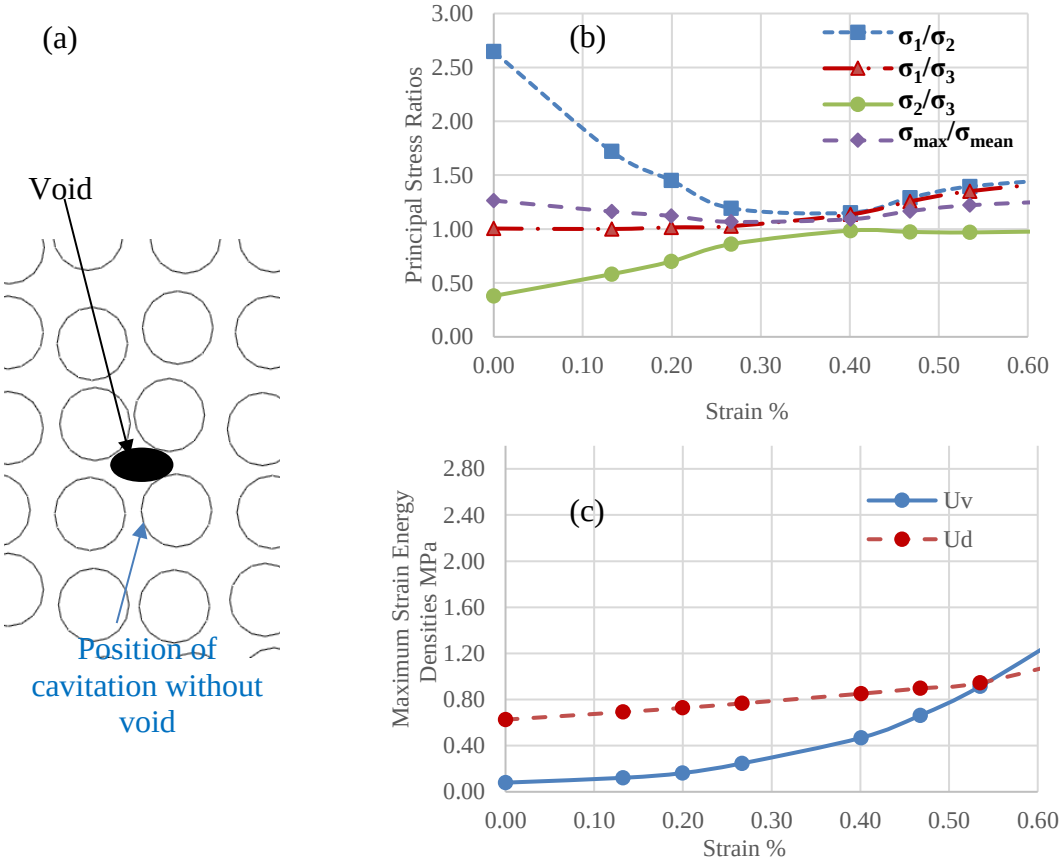


**Figure 65. The effect of the presence of elliptical void on cavitation placed horizontally with loading direction, (a) part of the original RVE showing the void and the position of cavitation without voids, (b) The principal stress ratios and the ratio of maximum/mean principal stress versus applied strain and (c) The maximum values of dilatational energy density $U_v$ and distortional energy density $U_d$ attained within RVEs versus applied strain.**

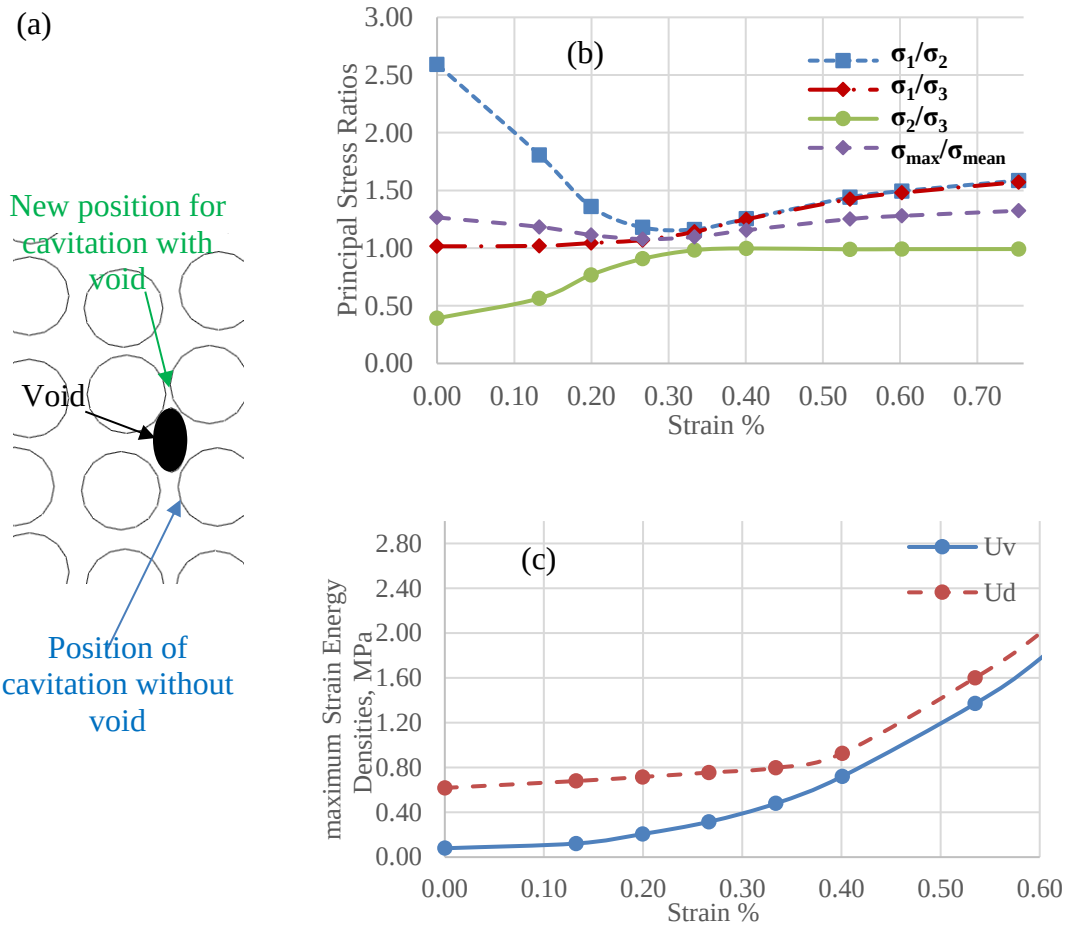


**Figure 66. The effect of the presence of elliptical void on cavitation placed vertically with loading direction, (a) part of the original RVE showing the void and the position of cavitation with and without void, (b) The principal stress ratios and the ratio of maximum/mean principal stress versus applied strain and (c) The maximum values of dilatational energy density $U_v$ and distortional energy density $U_d$ attained within RVEs versus applied strain.**

In Figure 67, it can be observed that when the aspect ratio of the void is relatively high, the cavitation requirements in establishing a hydrostatic stress state is not achieved at all applied transverse strains. The maximum distortional energy density is obtained at the tip of the void and thus yielding is suggested to initiate at this site.

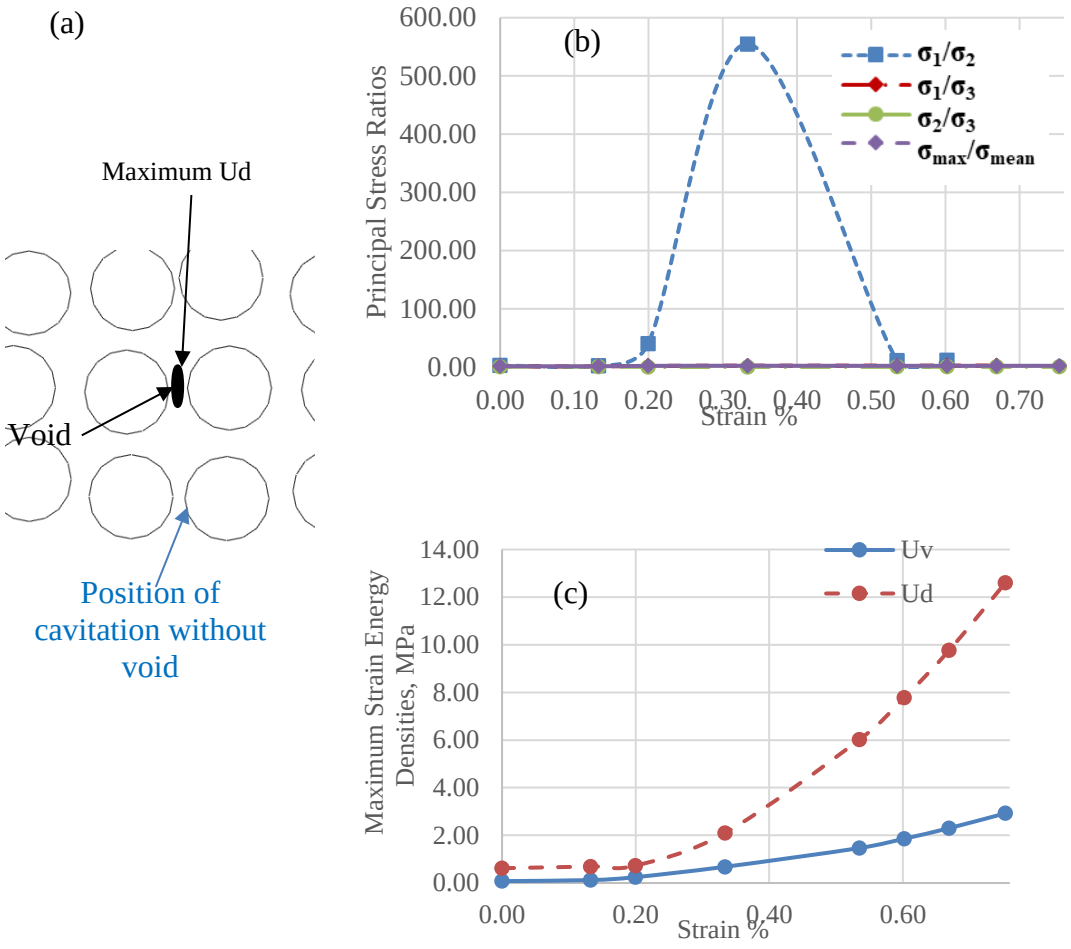


**Figure 67. The effect of the presence of elliptical void with high aspect ratio on cavitation placed vertically with loading direction, (a) part of the original RVE showing the void and the position of cavitation with and without void, (b) The principal stress ratios and the ratio of maximum/mean principal stress versus applied strain and (c) The maximum values of dilatational energy density $U_v$ and distortional energy density $U_d$ attained within RVEs versus applied strain.**

## 5.5. Summary and conclusion

This chapter examined the effects of manufacturing induced disorder in fiber distribution within composites on the initiation of first failure event under transversely applied tension. By constructing RVE realizations using the proposed algorithm, and analyzing those in a finite element model, the local stress fields have been calculated. Relevant point-failure criteria have been applied for brittle cavitation and yielding to predict initiation of the first failure event. Following specific conclusions can be drawn.

- Stress and failure analysis of RVE realizations for all cases conducted indicate that brittle cavitation is the earliest failure event under transverse tension of unidirectional composites. The earliest yielding occurs at locations where the fibers are very close and the matrix develops compressive stresses.
- The mechanical strain at the onset of cavitation decreases as the degree of nonuniformity increases. This occurred at all three fiber volume fractions considered in this study. The constituent properties used in the study were typical of a glass/epoxy composite. The mechanical strain to onset of cavitation is affected significantly at low matrix/fiber stiffness ratios. It increases as this ratio increases and approaches a constant value at high ratios.
- From preliminary results, it is found that the presence of voids seems to either alter the cavitation position or prevent a hydrostatic stress state from being created at all applied strains. Voids shape, position and size could be considered parameters in studying the effect of voids on damage initiation by cavitation. Further research should be conducted to make a better assessment on the subject.

# 6. DAMAGE INITIATION UNDER AXIAL SHEAR LOADING [1]

As mentioned before, matrix cracking can be observed when inclined loading or shear loading is applied. Studying damage initiation using RVEs under axial shear loading cannot be done in a 2-Dimensional model; instead, three dimensional RVEs should be constructed. When the axial shear loading is applied using the same inner window concept as illustrated in the previous chapter, it was found that local stress and strain fields are influenced by the edge effects. To avoid these edge effects, periodic boundary conditions (PBCs) are imposed.

In what follows, application of the PBC is illustrated. The local stress and strain fields resulting from conducted FEA under axial shear load are monitored. The finite element results are obtained for established RVEs with different FVFs and degrees of NU, using our algorithm described in chapter 4. Failure analysis is then conducted

## 6.1. Periodic boundary conditions

PBCs are expressed as coupling constraint equations applied on the relative displacement of opposite faces of the RVE. The degree of freedom as well as the far field strain are considered variables. The periodic boundary equations are applied to opposite nodes in the RVE. The RVE mesh is generated in a way ensuring equal number of nodes for any two opposite faces. Following the procedure in [195], consider an RVE with a square

[1] Reprinted with a permission from "Damage Initiation in Unidirectional Fiber Reinforced Polymeric Composites Under Transverse and Shear Loading", by Sarah A. Elnekhaily, Ramesh Talreja, 2017, Proceedings of the American Society for Composites: Thirty-second Technical Conference, 2017. Lancaster, PA: DEStech Publications, Inc.

cross section with side length L and thickness t that has its sides coincide with the *xyz* coordinate system. The constraint equations are:

$$U_z = u(x, y, t) - u(x, y, 0) \quad (14)$$

$$U_y = u(x, L/2, z) - u(x, -L/2, z) \quad (15)$$

$$U_x = u(L/2, y, z) - u(-L/2, y, z) \quad (16)$$

For axial (parallel shear) loading mode, Ux = (0, 0, δs) where δs is the applied displacement.

PBCs are imposed on two opposite faces. It is essential that the number of nodes at each face is equal to that of the opposite face. The nodes at the edges and at the corners are over-constrained because they are shared between two and three different faces respectively. The equations are implemented in the software ABAQUS using proper keywords in a python script, according to ABAQUS documentation [196] for the implementation of multi-point constraints.

Consider a 3D RVE as shown in Figure 68. To constrain each pair of faces together, the nodes in one face will be considered as master nodes, while the nodes in the opposite face will be considered as slave nodes. Reference nodes are specified through which loads will be applied. Reference node 0 ($RN_0$) is node 20, Reference node x ($RN_x$) is node 26, Reference node y ($RN_y$) is node1 and Reference node z ($RN_z$) is node 22.

Master faces are taken as those in the positive axes directions, and slave faces are in the opposite direction. For example, along the x axis, the master face will include nodes (7,8,9,17,18,19, 26, 27 and 28).

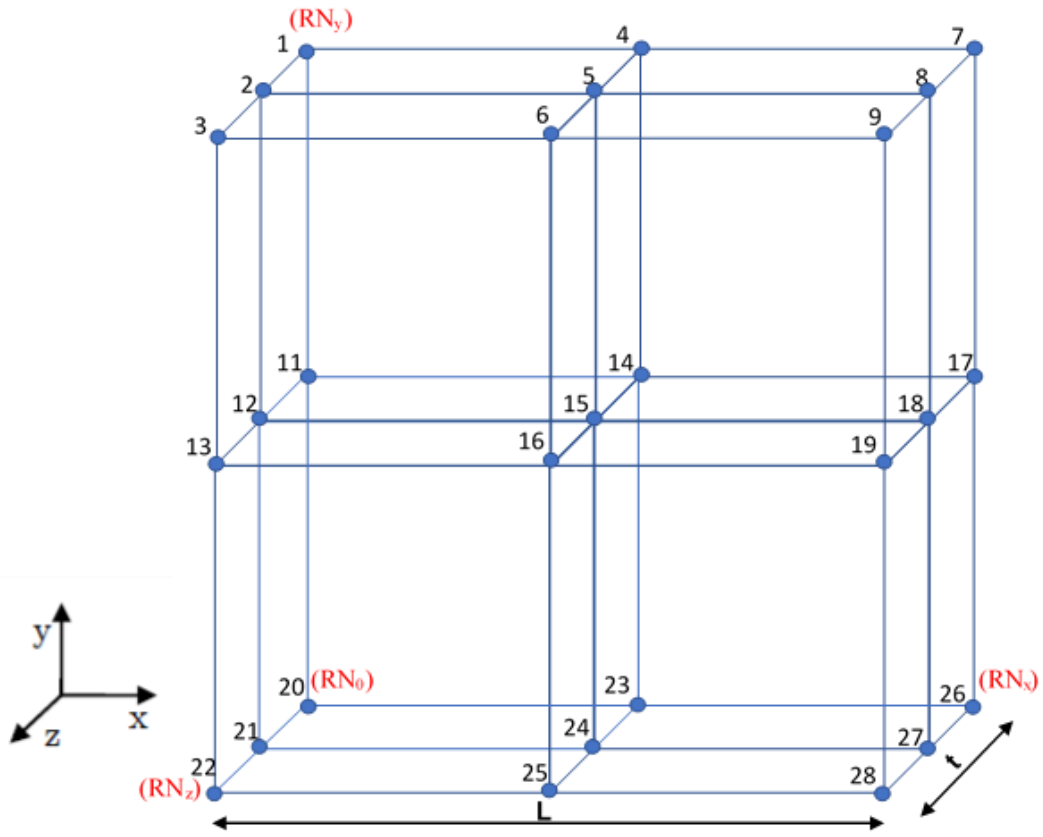


**Figure 68. Nodes numbering of RVE for application of PBCs.**

The slave face will include (1,2,3,11,12,13,20,21 and 22). The same will be applied to the faces along the y and z axes.

Along the x axis for the left and right faces, the PB equations are implemented as follows:

$$\begin{aligned}
\vec{u}^{26} - \vec{u}^{20} &= \vec{u}^{26} - \vec{u}^{20} \\
\vec{u}^{7} - \vec{u}^{1} &= \vec{u}^{26} - \vec{u}^{20} \\
\vec{u}^{8} - \vec{u}^{2} &= \vec{u}^{26} - \vec{u}^{20} \\
\vec{u}^{9} - \vec{u}^{3} &= \vec{u}^{26} - \vec{u}^{20} \\
\vec{u}^{17} - \vec{u}^{11} &= \vec{u}^{26} - \vec{u}^{20} \\
\vec{u}^{18} - \vec{u}^{12} &= \vec{u}^{26} - \vec{u}^{20} \\
\vec{u}^{19} - \vec{u}^{13} &= \vec{u}^{26} - \vec{u}^{20} \\
\vec{u}^{27} - \vec{u}^{21} &= \vec{u}^{26} - \vec{u}^{20} \\
\vec{u}^{28} - \vec{u}^{22} &= \vec{u}^{26} - \vec{u}^{20}
\end{aligned} \tag{17}$$

The first constraint relation in (17) will be ignored as it is an identity. The same procedure will be applied to the three-other face pairs. Along the y axis, the following equations are implemented.

$$\begin{gathered}
\vec{u}^{1} - \vec{u}^{20} = \vec{u}^{1} - \vec{u}^{20} \\
\vec{u}^{2} - \vec{u}^{21} = \vec{u}^{1} - \vec{u}^{20} \\
\vec{u}^{3} - \vec{u}^{22} = \vec{u}^{1} - \vec{u}^{20} \\
\vec{u}^{4} - \vec{u}^{23} = \vec{u}^{1} - \vec{u}^{20} \\
\vec{u}^{5} - \vec{u}^{24} = \vec{u}^{1} - \vec{u}^{20} \\
\vec{u}^{6} - \vec{u}^{25} = \vec{u}^{1} - \vec{u}^{20} \\
\vec{u}^{7} - \vec{u}^{26} = \vec{u}^{1} - \vec{u}^{20} \\
\vec{u}^{8} - \vec{u}^{27} = \vec{u}^{1} - \vec{u}^{20} \\
\vec{u}^{9} - \vec{u}^{28} = \vec{u}^{1} - \vec{u}^{20}
\end{gathered} \tag{18}$$

The first relation in (26) is also an identity; that is why it will be ignored. There is a condition in implementing the constraint equations in the finite element software ABAQUS. This condition requires that any node that was already implemented in any constraint equation should not be used again in another equation. That is why the last three equations in (18) are discarded. The master nodes in these equations were already implemented previously in equations (17).

Again, for the front and back faces (along the z axis), constraint equations below are implemented.

$$\begin{gathered}
\vec{u}^{22} - \vec{u}^{20} = \vec{u}^{22} - \vec{u}^{20} \\
\vec{u}^{13} - \vec{u}^{11} = \vec{u}^{22} - \vec{u}^{20} \\
\vec{u}^{16} - \vec{u}^{14} = \vec{u}^{22} - \vec{u}^{20} \\
\vec{u}^{25} - \vec{u}^{23} = \vec{u}^{22} - \vec{u}^{20} \\
\vec{u}^{3} - \vec{u}^{1} = \vec{u}^{22} - \vec{u}^{20} \\
\vec{u}^{6} - \vec{u}^{4} = \vec{u}^{22} - \vec{u}^{20} \\
\vec{u}^{9} - \vec{u}^{7} = \vec{u}^{22} - \vec{u}^{20} \\
\vec{u}^{28} - \vec{u}^{26} = \vec{u}^{22} - \vec{u}^{20} \\
\vec{u}^{19} - \vec{u}^{17} = \vec{u}^{22} - \vec{u}^{20}
\end{gathered} \tag{19}$$

Here too, the first constraint relation in (19) is an identity. The last five equations should be ignored because the master nodes were implemented in other constraint equations as shown above.

A summary of the constraint conditions implemented for the 3D RVEs is given in equations (20):

$$\begin{aligned}
\vec{u}^{7} - \vec{u}^{1} &= \vec{u}^{26} - \vec{u}^{20} \\
\vec{u}^{8} - \vec{u}^{2} &= \vec{u}^{26} - \vec{u}^{20} \\
\vec{u}^{9} - \vec{u}^{3} &= \vec{u}^{26} - \vec{u}^{20} \\
\vec{u}^{17} - \vec{u}^{11} &= \vec{u}^{26} - \vec{u}^{20} \\
\vec{u}^{18} - \vec{u}^{12} &= \vec{u}^{26} - \vec{u}^{20} \\
\vec{u}^{19} - \vec{u}^{13} &= \vec{u}^{26} - \vec{u}^{20} \\
\vec{u}^{27} - \vec{u}^{21} &= \vec{u}^{26} - \vec{u}^{20} \\
\vec{u}^{28} - \vec{u}^{22} &= \vec{u}^{26} - \vec{u}^{20} \\
\vec{u}^{2} - \vec{u}^{21} &= \vec{u}^{1} - \vec{u}^{20} \\
\vec{u}^{3} - \vec{u}^{22} &= \vec{u}^{1} - \vec{u}^{20} \\
\vec{u}^{4} - \vec{u}^{23} &= \vec{u}^{1} - \vec{u}^{20} \\
\vec{u}^{5} - \vec{u}^{24} &= \vec{u}^{1} - \vec{u}^{20} \\
\vec{u}^{6} - \vec{u}^{25} &= \vec{u}^{1} - \vec{u}^{20} \\
\vec{u}^{13} - \vec{u}^{11} &= \vec{u}^{22} - \vec{u}^{20} \\
\vec{u}^{16} - \vec{u}^{14} &= \vec{u}^{22} - \vec{u}^{20} \\
\vec{u}^{22} - \vec{u}^{20} &= \vec{u}^{22} - \vec{u}^{20} \\
\vec{u}^{25} - \vec{u}^{23} &= \vec{u}^{22} - \vec{u}^{20}
\end{aligned} \qquad (20)$$

Transverse load and axial shear load can be applied to the reference node $RN_x$ through displacements and the constraint conditions are as follows:

**Table 3. Applications of different load types using PBCs**

| Load type | $RN_0$ ($u_x$,$u_y$,$u_z$) | $RN_x$ ($u_x$,$u_y$,$u_z$) | $RN_y$ ($u_x$,$u_y$,$u_z$) | $RN_z$ ($u_x$,$u_y$,$u_z$) |
|---|---|---|---|---|
| Axial Shear | (0,0,0) | ($\varepsilon$, 0, $\delta_z$) | (0, $\varepsilon$, 0) | (0, 0, $\varepsilon$) |
| Combined transverse tension and axial shear | (0,0,0) | ($\delta_x$, 0, $\delta_z$) | (0, $\varepsilon$, 0) | (0, 0, $\varepsilon$) |
| Uniaxial tension | (0,0,0) | ($\delta_x$, 0, 0) | (0, $\varepsilon$, 0) | (0, 0, $\varepsilon$) |

$\delta_x$ and $\delta_z$ are the displacements applied at RNx in the x and z directions, respectively, and $\varepsilon$ indicates an unconstrained condition.

Five realizations of 3D RVE, with 14 x 14 fibers and square cross section with ~200,000 linear hexahedral elements of type C3D8R, are generated. The RVE thickness is at least an element size as shown in figure 69. The maximum dilatational and distortional energy densities are determined at each applied shear strain applied after a thermal cooldown.

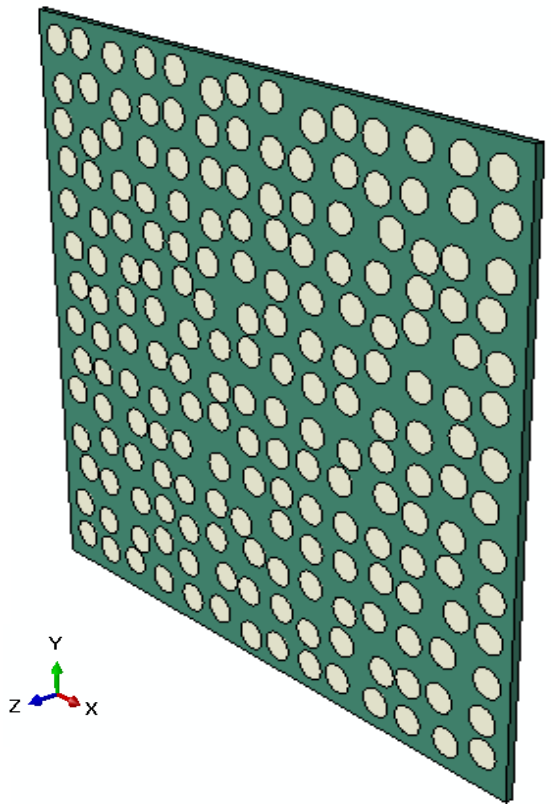


**Figure 69. 3D RVE construction with total 14x14 fibers.**

Results of dilatational and distortional energy densities as well as principal stress ratios, were compared when PBCs are applied versus ordinary boundary conditions, as in chapter 5 for transverse tensile displacements. Similar results were found in both cases for different values of fiber volume fraction and degree of nonuniformity. For example, figure

70 (a & b) shows the maximum dilatational and distortional energy densities when determined at each applied transverse tensile strain after thermal cooldown for an RVE having 40% FVF and 100% NU, with ordinary BCs and PBCs, respectively. Also, the principal stress ratio curves in figure 71 (a & b) for the same conditions, shows that cavitation has higher probability at around 0.4% strain for the two boundary conditions. This indicates that the size of the RVE with 14x14 fibers is adequate for local failure analysis of a unidirectional composite. Also, this gives us confidence about the periodic boundary equations that are implemented.

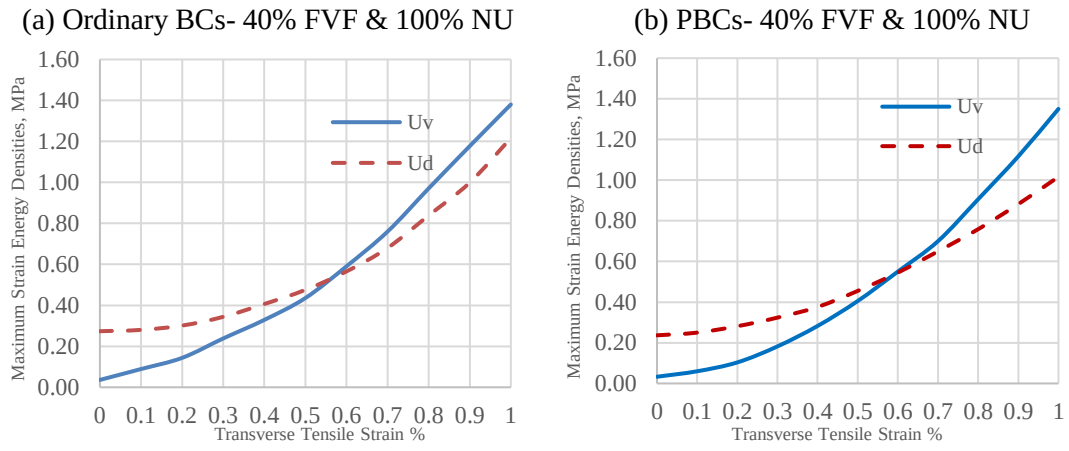


**Figure 70. The maximum values of dilatational energy density $U_v$ and distortional energy density $U_d$ attained within RVEs versus applied transverse tensile strain with (a) Ordinary boundary conditions and (b) Periodic boundary conditions (PBCs) for 40% fiber volume fraction and 100% degree of nonuniformity.**

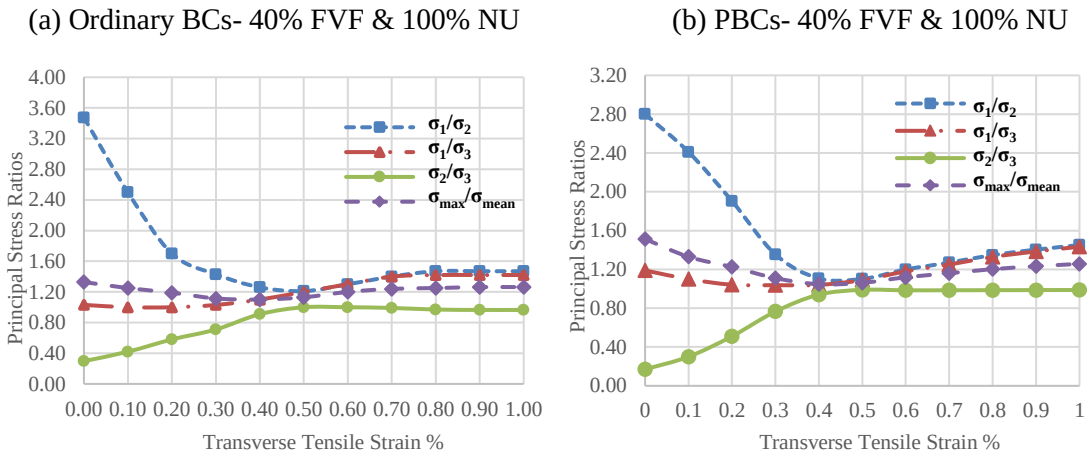


**Figure 71. The principal stress ratios and the ratio of maximum/mean principal stress versus applied transverse tensile strain with (a) Ordinary boundary conditions and (b) Periodic boundary conditions (PBCs) for 40% fiber volume fraction and 100% degree of nonuniformity.**

## 6.2. Failure analysis

For three fiber volume fractions (40 %, 54 % and 60 %), the maximum dilatational energy density is nearly constant with shear loading, and its value is relatively small compared to the distortional energy density. For example, in figure 72, both the maximum dilatational and distortional energy densities are plotted for 54% fiber volume fraction and 100% nonuniformity. The dilatational energy density has a nearly constant value at all applied shear strains. This value is ~ 0.043 MPa, which is significantly lower than the critical value or brittle cavitation. In the meanwhile, the distortional energy density is increasing with applied shear strain. Also, for the same RVE, the condition of the equality of principal stress ratios for cavitation to occur is not fulfilled throughout the virtual test as shown in figure 73. Similar Observations were found for the other fiber volume fractions and other degrees of nonuniformity, e.g., Figures 74 and 75.

For all considered fiber volume fractions and different degrees of fiber nonuniformity, the strain at which the maximum distortional energy density reaches its critical value is found to decrease with increasing the degree of NU, and the maximum distortional energy density occurs in the matrix between closest fibers throughout the thickness. This could be due to the decrease in the inter-fiber distance when the fiber nonuniformity is increased.

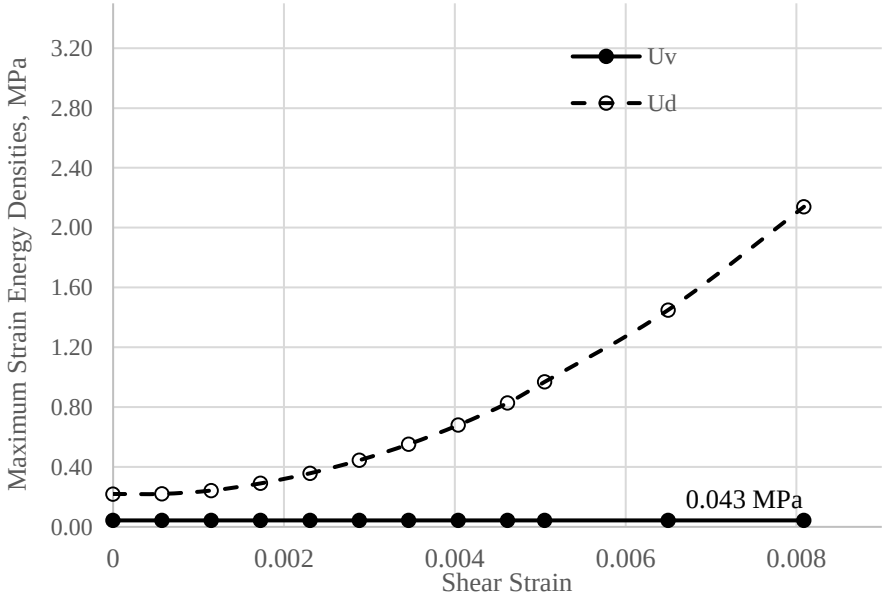


**Figure 72. The maximum values of dilatational energy density $U_v$ and distortional energy density $U_d$ attained within RVEs versus applied axial shear strain for 54% fiber volume fraction and 100% degree of nonuniformity. A nearly constant value of Uv =0.043 MPa is maintained at all applied shear strain values.**

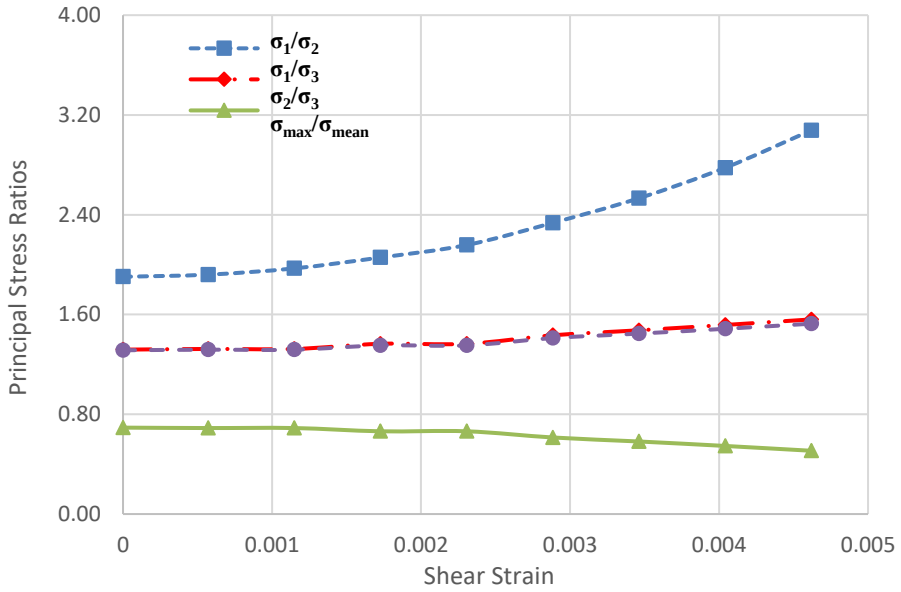


**Figure 73. The principal stress ratios and the ratio of maximum/mean principal stress versus applied axial shear strain for 54% fiber volume fraction and 100% degree of nonuniformity.**

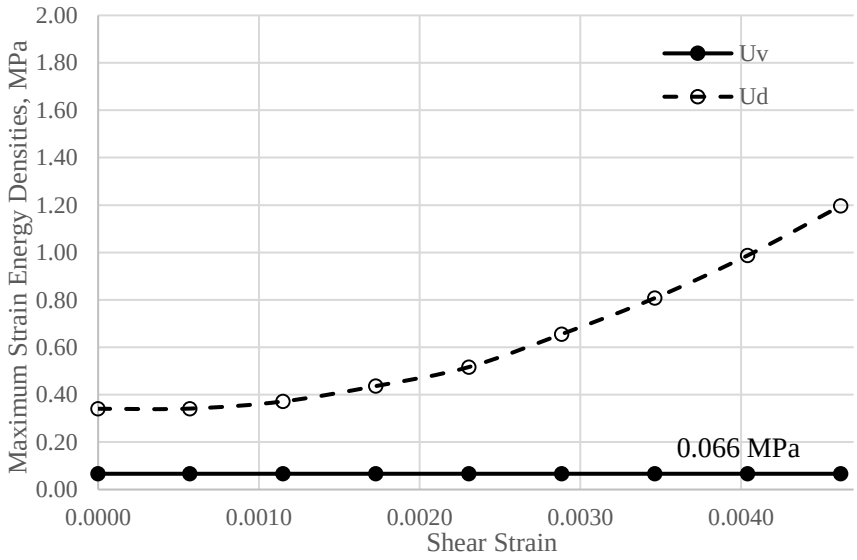


**Figure 74. The maximum values of dilatational energy density $U_v$ and distortional energy density $U_d$ attained within RVEs versus applied axial shear strain for 54% fiber volume fraction and 60% degree of nonuniformity. A nearly constant value of Uv =0.066 MPa is maintained at all applied shear strain values.**

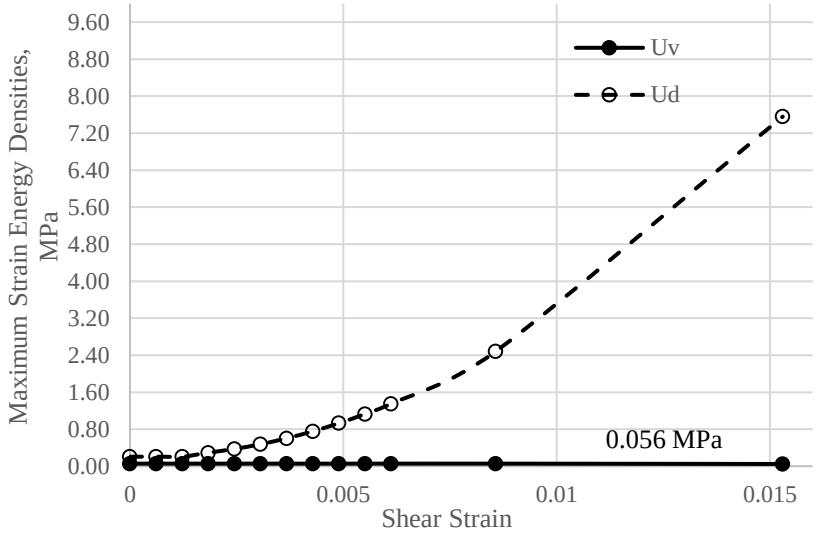


**Figure 75. The maximum values of dilatational energy density $U_v$ and distortional energy density $U_d$ attained within RVEs versus applied axial shear strain for 60% fiber volume fraction and 100% degree of nonuniformity. A nearly constant value of Uv =0.056 MPa is maintained at all applied shear strain values.**

## 6.3. Results and discussion

### 6.3.1. Effect of degree of nonuniformity

For a given fiber volume fraction, the strain at which the maximum distortional energy density meets the yielding criterion is found to decrease as the degree of nonuniformity increases. This is likely due to the decrease of interfiber distances with increasing degree of nonuniformity. Figures (76 – 78) show the effect of the degree of nonuniformity on the average value of the maximum distortional energy density for the 40%, 54% and 60% fiber volume fractions. The matrix stiffness value for this case is 2.07 GPa, and the critical distortional energy density equals 1.564 MPa. As seen in the figures (76-78), the applied shear strain at which yielding occurs reduces significantly when fibers are distributed nonuniformly. However, the sensitivity of this strain to the degree of nonuniformity is small in the range of 30-100% for the 40% and 54% fiber volume fractions.

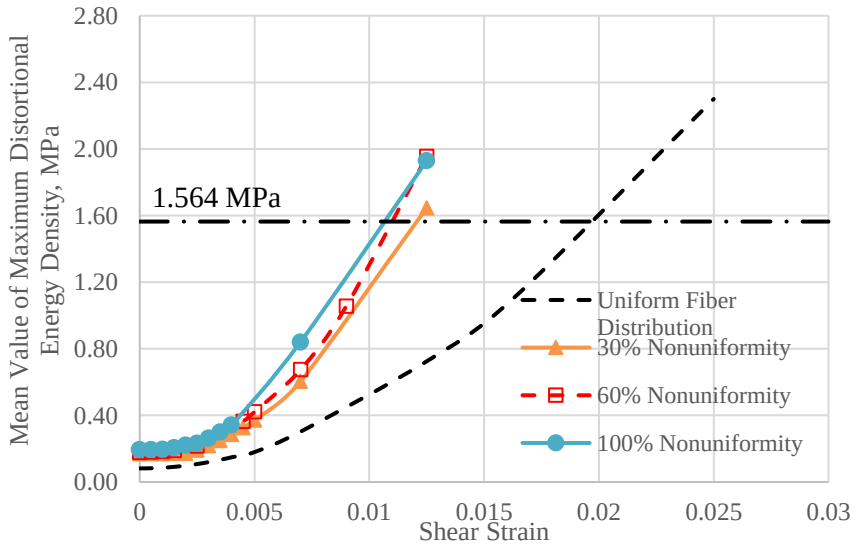


**Figure 76. The mean of the maximum values of distortional energy density $U_d$ attained within RVEs versus applied axial shear strain for 40% fiber volume fraction and different degree of nonuniformity. The values plotted are averages of multiple RVE realizations.**

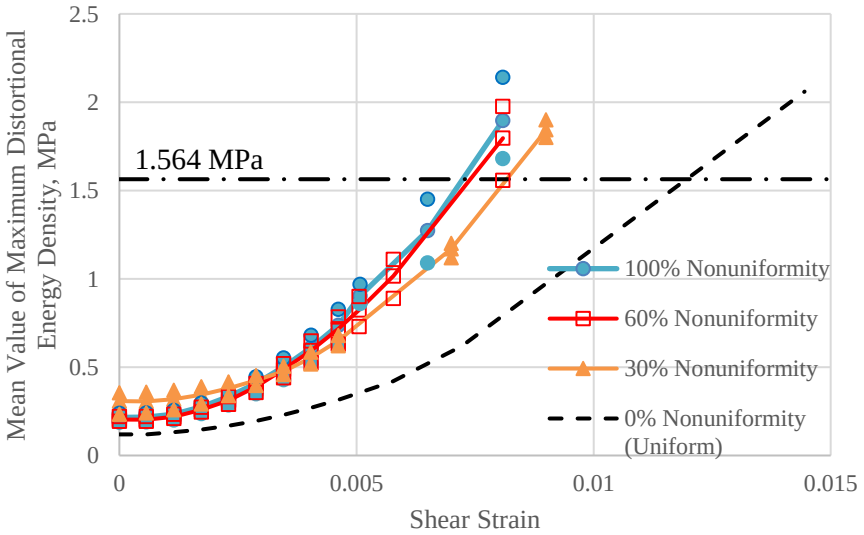


**Figure 77. The mean of the maximum values of distortional energy density $U_d$ attained within RVEs versus applied axial shear strain for 54% fiber volume fraction and different degree of nonuniformity. The values plotted are averages of multiple RVE realizations with maximum and minimum values.**

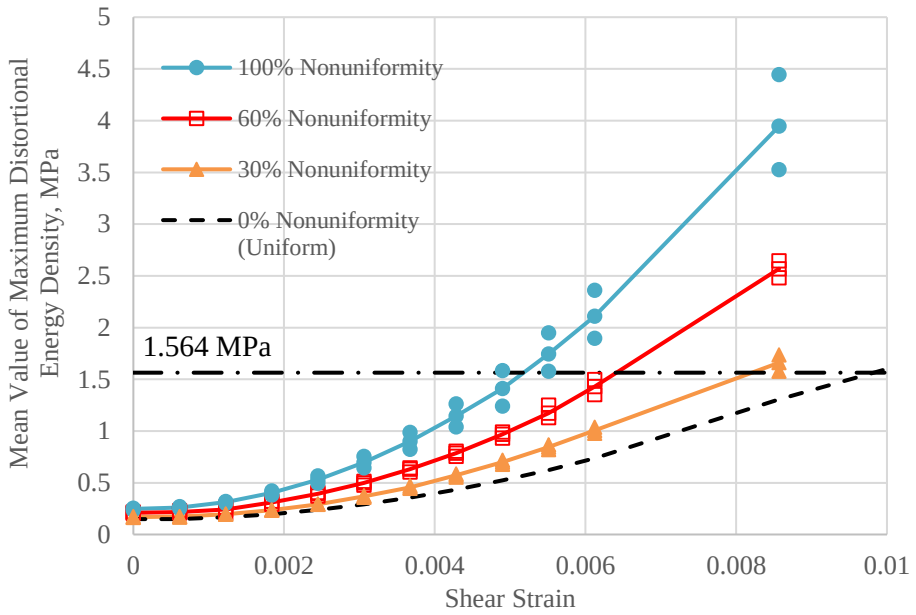


**Figure 78. The mean of the maximum values of distortional energy density $U_d$ attained within RVEs versus applied axial shear strain for 60% fiber volume fraction and different degree of nonuniformity. The values plotted are averages of multiple RVE realizations with maximum and minimum values.**

### 6.3.2. Effect of fiber volume fraction

For higher fiber volume fractions, with the same degree of nonuniformity, the strain at which the maximum distortional energy density reaches the threshold is found to decrease. In Figure 79, the maximum values of distortional energy density $U_d$ attained within the RVEs are plotted versus the applied axial shear strain for 40%, 54% and 60% fiber volume fractions and 100% nonuniformity. It can be observed that by increasing the fiber volume fraction from 40% to 60%, the strain at which yielding occurs is decreased. Also, the distortional energy band is narrower for higher fiber volume fractions. Similar results are observed in the other degrees of nonuniformities, e.g., Figure 80 for zero degree of nonuniformity.

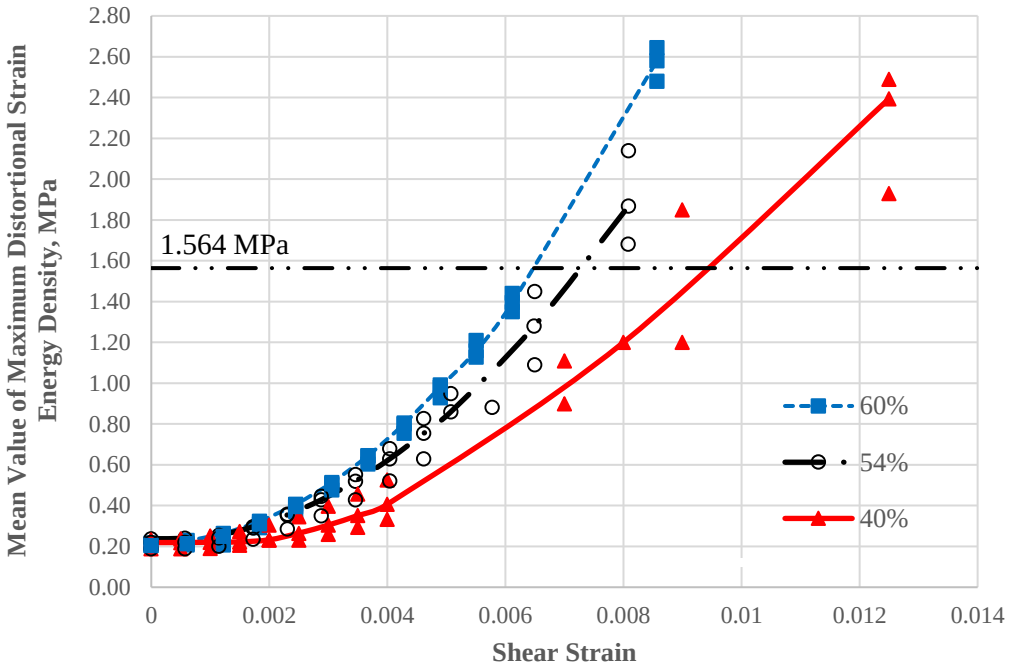


**Figure 79. The maximum values of distortional energy density $U_d$ attained within RVEs versus applied axial shear strain for 40%, 54% and 60% fiber volume fraction and 100 % of nonuniformity.**

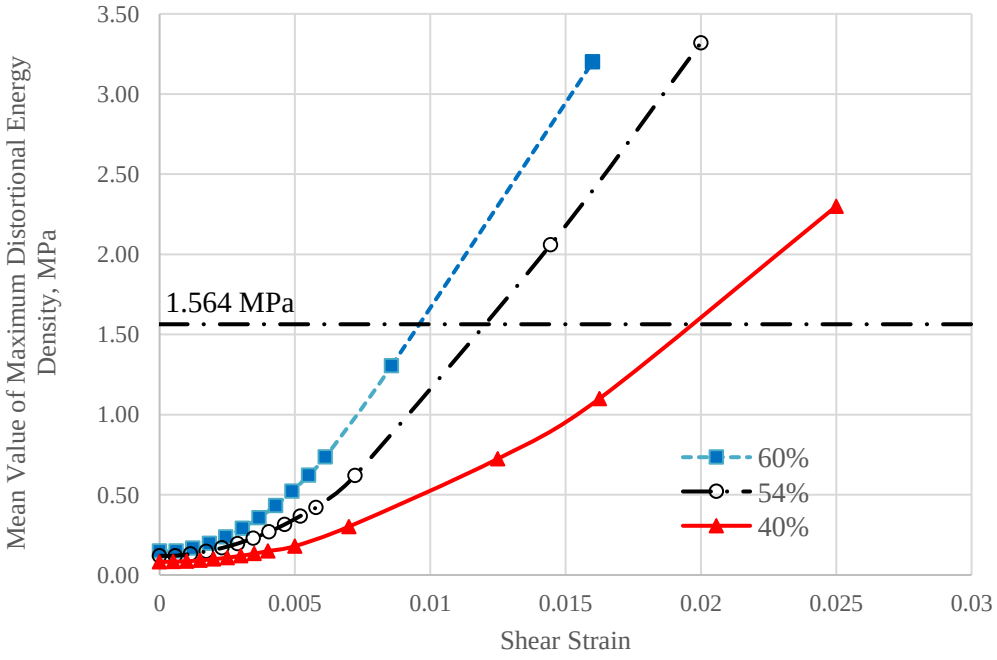


**Figure 80. The maximum values of distortional energy density $U_d$ attained within RVEs versus applied axial shear strain for 40%, 54% and 60% fiber volume fraction and 0% of NU (uniform distribution).**

### 6.3.3. Effect of matrix stiffness

Two matrix stiffness values (2.07 GPa and 3.35 GPa) are compared with respect to the stain at which yielding will occur. For the three fiber volume fractions (40%, 54% and 60%) with different degrees of nonuniformity, it is found that the applied shear strain at which yielding initiates is increased as the matrix stiffness is increased. In Figure 81 the results for 54% fiber volume fraction and 60% nonuniformity are shown. The yield strength of 85 MPa is taken for a matrix of Young's modulus 2.07 GPa, which is typical for DGEBA/DETA epoxy [76], and the value 140 MPa is used for the other case of MTM57 epoxy system [191]. In Figure 81, the values of the distortional energy density are plotted corresponding to these yield strength values. The mechanical strain for yielding to initiate is found to be ~ 0.008 for the 3.35 GPa matrix stiffness and ~ 0.007 for the 2.07 GPa matrix stiffness. Similar results are observed for the other volume fractions and degrees of nonuniformity. e.g., Figure 82 for 40% fiber volume fraction and uniform distribution are shown.

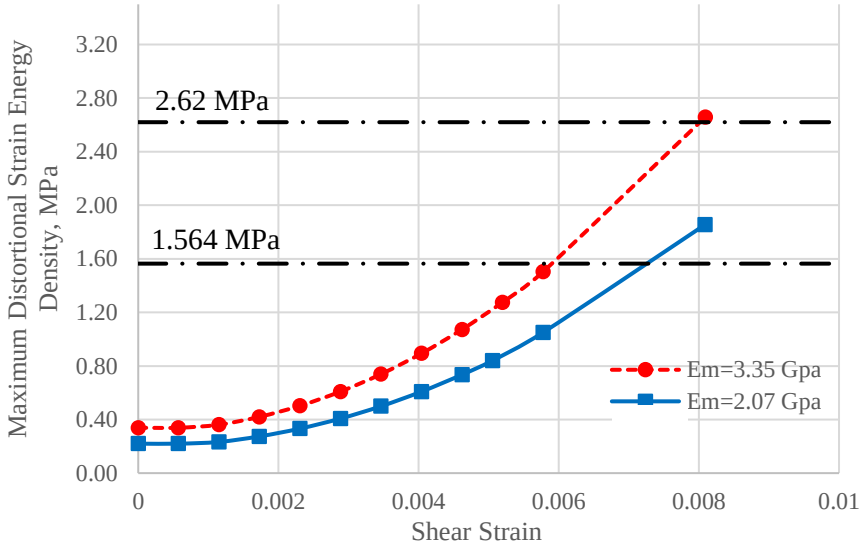


**Figure 81. The maximum values of distortional energy density $U_d$ attained within RVEs versus applied axial shear strain for 54% fiber volume fraction and 60% nonuniformity for two matrix stiffness values; 2.07 and 3.35 GPa.**

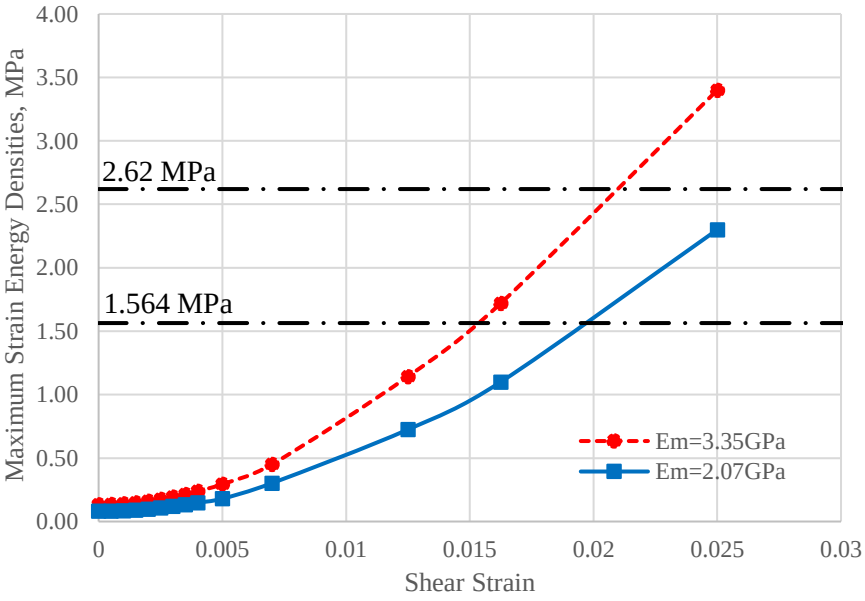


**Figure 82. The maximum values of distortional energy density $U_d$ attained within RVEs versus applied axial shear strain for 40% fiber volume fraction and 0% nonuniformity for two matrix stiffness values; 2.07 and 3.35 GPa.**

## 6.4. Summary and conclusion

In this chapter, the first event of failure has been examined under axial shear loading of unidirectional glass/epoxy composites. The random fiber distributions resulting from manufacturing have been quantified in terms of degrees of nonuniformity. For a selected degree of nonuniformity, the fiber distributions have been generated in representative volume elements by an algorithm established for the purpose. With finite element analysis, parametric studies have been conducted to investigate the effects of the degree of nonuniformity, fiber volume fraction and matrix stiffness on damage initiation. Periodic boundary condition is applied to be able to impose the axial shear load. The PBC gives similar results to ordinary boundary condition when transverse tension is applied to the RVEs. Below are some conclusions that can be addressed:

- Under axial shear loading, the earliest yielding occurs at locations where the fibers take very close spacing and throughout the RVE thickness.
- The mechanical strain at the onset of yielding decreases as the degree of nonuniformity increases for the investigated fiber volume fractions (40%, 54% and 60%).
- The mechanical strain at which yielding initiates is decreased by increasing the fiber volume fraction for the same degree of nonuniformity.
- By increasing the matrix stiffness, the mechanical strain at which yielding initiates is increased for the same fiber volume fraction and same degree of nonuniformity.

# 7. DAMAGE INITIATION UNDER BIAXIAL LOADING

While in service, various composites suffer from complex loading conditions either static or dynamic, e.g. the wing of an airplane as it is subjected to both bending and torsional type of loadings. This multiaxial loading affects composites in a way that leads to a progressive degradation of the material stiffness due to the evolution of off-axis matrix cracks [197-211]. A biaxial loading is known to be the simplest case of a multiaxial loading. Many researches have studied the effect of biaxial loading on composites by combining two different loading types. Certain specimen shapes are found to be suitable for such tests. These are tubular, cruciform and off-axis flat specimens as shown in Figure 83.

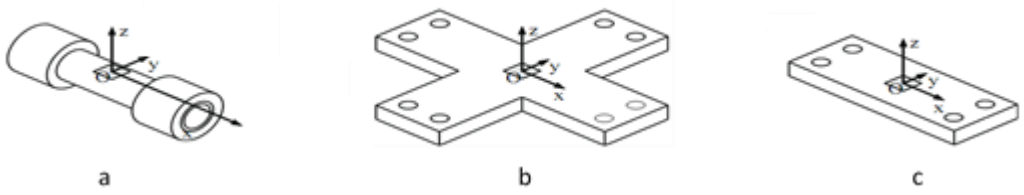


**Figure 83. A schematic illustration of commonly used biaxial fatigue specimens: a) Tubular, b) Cruciform and c) Off-axis flat. Reprinted from [212]**

The most encountered types of biaxial loadings are as follows [211-223]:

1) longitudinal loading and internal pressure on tubular specimens [213-216];

2) longitudinal loading along with torsion on tubular specimens [217,218]

3) biaxial tension and/or compression applied to flat cruciform specimens [219,220] and

4) flat specimens under biaxial bending.

Other methods also include off-axis loading applied to a unidirectional composite coupon [221,222,223].

In [224], it was found that the failure and damage behavior will mainly depend on the local stress state achieved inside the materials regardless of the shape and the type of external applied loads. This conclusion was affirmed through a comparison between flat specimens and tubular ones made from the same material -E-glass/epoxy pre-preg. Uniaxial fatigue tests were conducted on flat coupons with a pre-selected off-axis angle θ and ply thickness. The local stress state is meant to be created such that it is similar to that in the tubular specimens during tension-torsion test.

Complex stress states are difficult to be studied experimentally, but they can be simulated. Studying the effect of biaxial loading using virtual tests has been of interest to many researches in the past two decades [160,180,225-233].

In this chapter, two cases of biaxial loadings will be applied to relevant RVEs with different FVF and different degree of NU: 1) Equi-biaxial transverse tension and 2) combined axial shear and transverse tension. Appropriate boundary conditions are applied for each loading case.

## 7.1. Equi-biaxial tensile load

### 7.1.1. Applied boundary condition

An equi-biaxial tensile load is applied to the 2D RVEs. As with the uniaxial loading case, the RVEs were first subjected to a thermal cooldown from a stress-free state. Displacements were then applied to the RVE boundaries as shown in Figure 84.

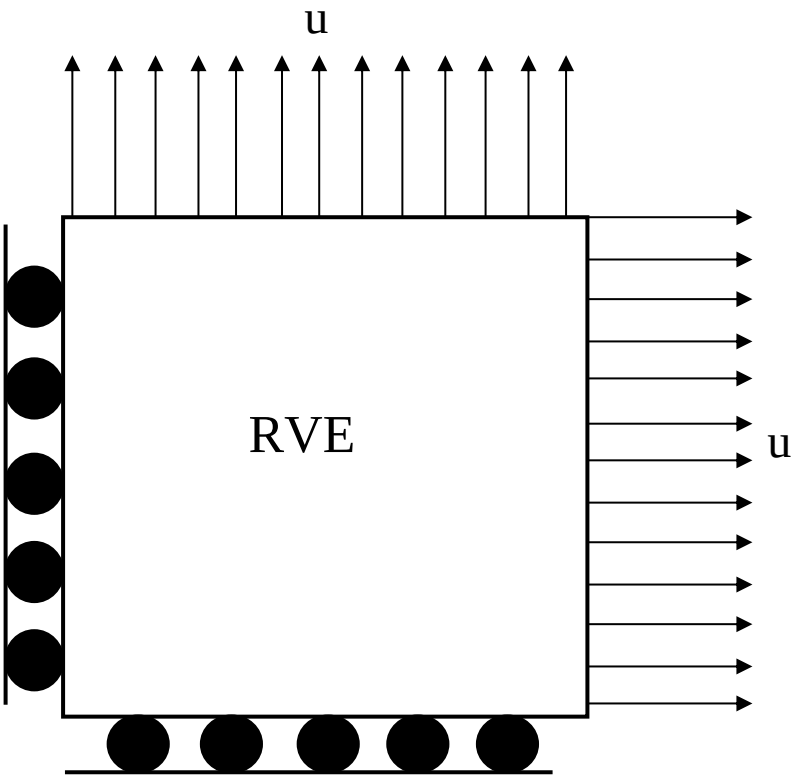


**Figure 84. Boundary conditions for an equi-biaxial displacement load.**

### 7.1.2. Failure analysis

Consider an RVE with 50% FVF and 100% NU. Both the maximum strain energy densities (distortional and dilatational) are monitored at all applied strains. The principal stress ratios are plotted for the site of maximum dilatational energy density at each applied strain, given in Figure 85. The principal stresses are nearly equal at ~0.35% strain for the two loading cases. Also, at this strain, the maximum dilatational energy density reaches its threshold value (a maximum of ~0.13-0.2 MPa as suggested in [76]). Thus, cavitation is suggested to be the first event of damage. Under biaxial load, the distortional energy density has higher values, compared to the dilatational energy density, at low applied strains. When

the applied biaxial strain is increased, the distortional energy is decreased. This finding is similar to what obtained in [194] when an equi-biaxial tensile load was applied to a RVE constructed using a methodology provided by the researcher.

When an equi-biaxial load is applied, it is found that the hydrostatic stress state is generated in the matrix between two fibers that are aligned with respect to either of the applied loads. On the other hand, yielding locations are present between the closest fiber pairs.

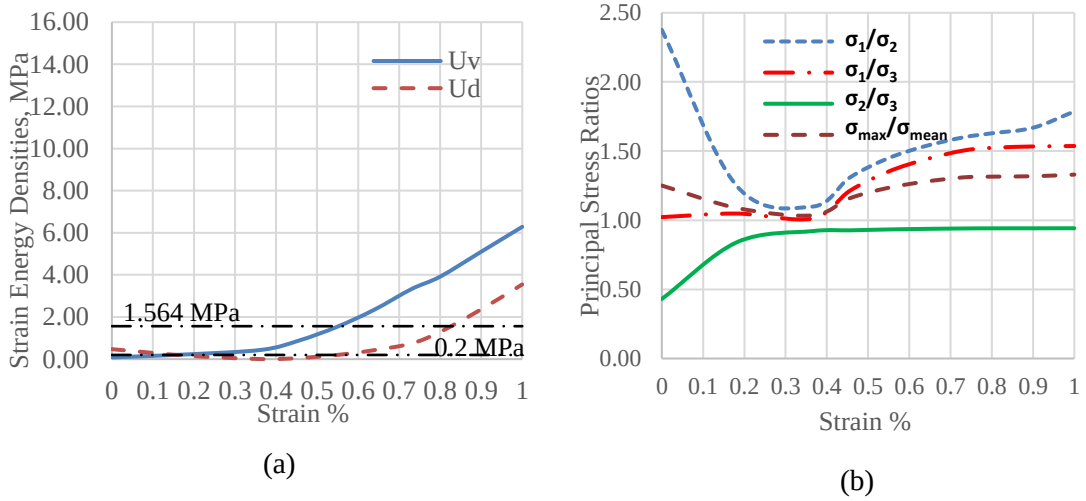


**Figure 85. (a)The maximum values of dilatational energy density Uv and distortional energy density Ud and (b) Principal stress ratios and the ratio of maximum/mean principal stress, attained within RVEs versus applied strain under equi-biaxial tensile loads.**

### 7.2. Axial shear and transverse tensile load

A commonly used parameter in many investigations in the field of biaxial loading on composite materials is the biaxiality ratio λ (shear / axial or transverse normal loads). Many studies have concluded the importance of such parameter on the damage and failure behavior and fatigue life of FRP composites [213,214,217,225,226].

Capela et al. [225], studied the fatigue behavior of tubular specimens made from carbon fiber composite. The fatigue test was conducted under different torsion-bending biaxial load ratios. They concluded that the fatigue strength is decreased when increasing the shear component.

Wang et al. [213] concluded that increasing the shear component in the biaxial tension/torsion fatigue test reduced the fatigue life appreciably. Similar results were obtained in [227] when conducting a tension/torsion fatigue test on graphite FRP-tube composite.

Quaresimin et al. [218, 226] conducted tension-torsion fatigue tests on several configurations of glass/epoxy prepregs. They found that by increasing the load ratio, the crack initiation life is reduced.

Based on available data in the literature, Quaresimin et al. [212] concluded that the local biaxial stress ratio established in the material affects to a great extent its fatigue and failure behavior.

It can thus be concluded that a multiaxial loading or even the simplified biaxial loading affect the failure behavior of the composite. From all different biaxial loading conditions, the presence of axial shear is of great interest when dealing with the matrix-dominated damage behavior [218].

Two different mechanisms are expected to occur under transverse tension and axial shear. In chapter 5, it was found that cavitation is likely under transverse tension for all fiber volume fractions and studied degrees of nonuniformity at relevant applied strain values. When only axial shear is applied, cavitation requirements are not fulfilled and thus, yielding is likely as the first event of damage.

In this section, the effect of the simultaneous axial shear and transverse tensile loads through a biaxiality stress ratio (λ) (axial shear /transverse tensile stress) on cavitation will be investigated. The effect of fiber volume fractions and degrees of nonuniformity will also be studied. Applying different loads is established through applying different biaxiality ratios on 14x14 three dimensional RVEs. The RVEs are constructed with the algorithm discussed in chapter 4 and the loads are applied under periodic boundary conditions following the same procedure as in the previous chapter.

### 7.2.1. Boundary condition

To avoid edge effects when applying axial shear stresses, periodic boundary conditions are imposed to 3D RVEs as illustrated in chapter 6. The Young's modulus, Poisson's ratio and thermal expansion coefficient of the fibers are $E_f$ = 72 GPa, $\upsilon_f$ = 0.2 and $\alpha_f$ =5x10$^{-6}$, respectively, and the corresponding values for the matrix are $E_m$ = 2.07 GPa, $\upsilon_m$ = 0.345 and $\alpha_m$ = 66x10$^{-6}$, Table 4. Finite element analyses are conducted using the software ABAQUS to RVEs with different FVFs (40%, 54% and 60%) and different degree of NU (0%, 60% and 100 %). The simultaneous axial shear and transverse tensile loads are imposed on the RVE boundaries as indicated in table 3.

**Table 4. Materials properties for combined axial shear and transverse tension**

| | Young's modulus (GPa) | Poisson's ratio | Thermal expansion Coefficient ($10^{-6}$ / $^{o}$C) |
|---|---|---|---|
| **Fiber** | 72 | 0.2 | 5 |
| **Epoxy** | 2.07 | 0.345 | 66 |

### 7.2.2. Failure analysis

Different axial shear to transverse tensile stress ratios are imposed on the RVEs; ratios such as 1/1, 1/2, 1/4,1/8, …. and 1/100 as well as $\lambda = 0$ (for transverse tension only) with transverse tensile stresses up to 90 MPa.

At each biaxiality stress ratio, local stress and strain fields from conducted FEA are monitored. The maximum distortional and dilatational strain energy densities are determined as well as their positions. Both the principal stress ratios and the maximum distortional and dilatational strain energy densities are plotted from which requirements for cavity formation are checked. These requirements include; 1) The dilatational energy density equals or exceeds the critical value for cavitation and 2) the principal stress ratios are within 20% difference to maintain a hydrostatic stress state. The transverse tensile strain (stress) required for cavitation could then be determined. For each value of $\lambda$, the transverse tensile stress is incrementally increased and the axial shear stress is changed accordingly. Finally, in a single diagram, all applied ratios are presented and those at which cavitation is likely as a first failure event are distinguished from when yielding occurs.

To discuss it in more detail, consider a realization of 54% fiber volume fraction and 100% nonuniformity as shown in figure 86. Under transverse tensile load, the principal stress ratios and the ratio of maximum/mean principal stress versus applied transverse stress are plotted, Figure 87. The principal stress ratios are nearly equal at a tensile stress of ~23 MPa. Also, the maximum values of dilatational energy density $U_v$ and distortional energy density $U_d$ versus the applied transverse stress are given for the same realization, Figure 88. At this stress, the dilatational energy density exceeds the threshold value (~0.2 MPa [76]). On the other hand, the distortional energy density at this stress has a value of ~0.2 MPa which is

lower than the threshold value required for yielding (~1.56 MPa). A cavity can thus be suggested to form at this stress value which is expected to take place as discussed in chapter 5.

By examining the positions of both maximum dilatational and distortional energy densities, it is found that the maximum dilatational is within the matrix between two adjacent fibers positioned horizontally to the transverse tension, while the maximum distortional energy density is established in the matrix in the midpoint between the closest pair of fibers throughout the RVE thickness.

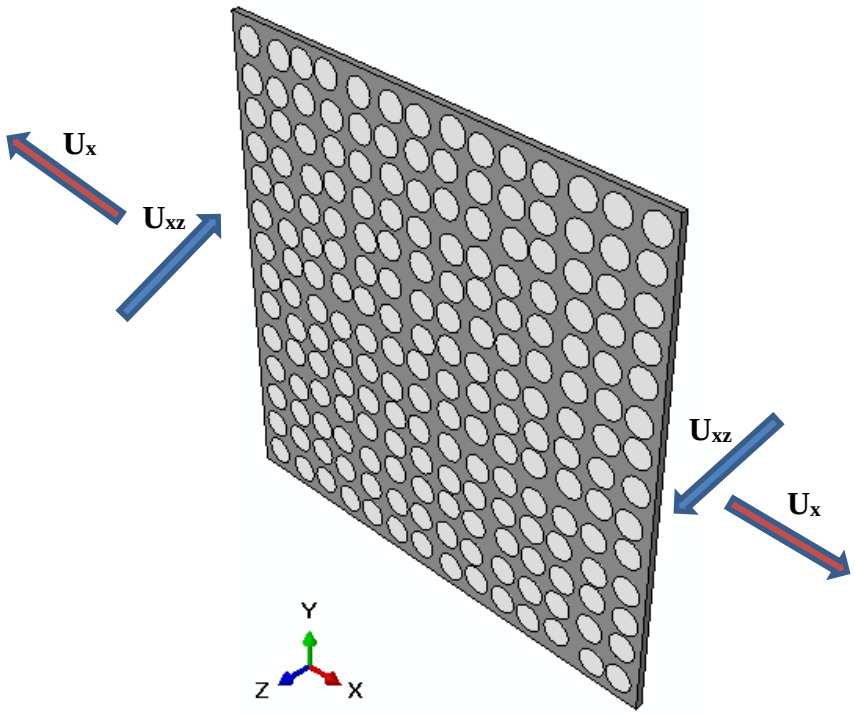


**Figure 86. A realization of 54% fiber volume fraction and 100 % nonuniformity.**

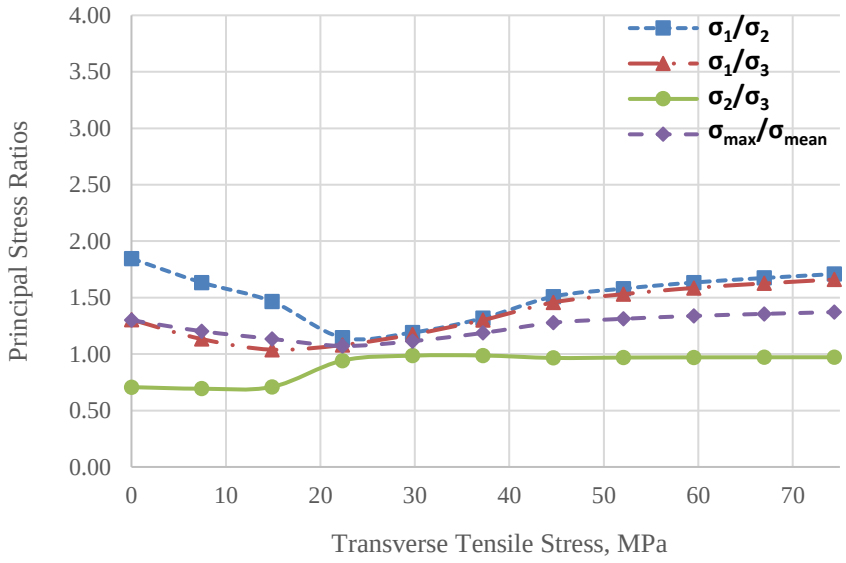


**Figure 87. The principal stress ratios and the ratio of maximum/mean principal stress versus applied transverse tensile stress for the realization shown in figure 86.**

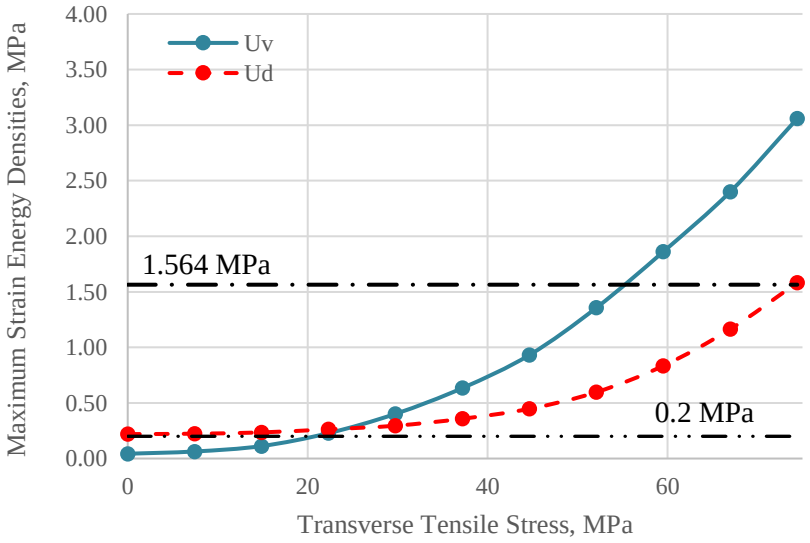


**Figure 88. The maximum values of dilatational energy density $U_v$ and distortional energy density $U_d$ attained within RVEs versus applied transverse stress for the realization shown in figure 86.**

The effect of axial shear stress $\sigma_{xz}$ on cavity formation is then investigated through conducting several finite element analyses with different biaxial stress ratios. When only axial shear stress is applied, $U_v$ has very low value that remains nearly constant with increasing the applied stress, as shown in the previous chapter. But when the axial shear stress is imposed along with transverse tension, the dilatational energy density has an appreciable value that is increased by increasing the applied stress as shown in the following figures. For example, at a biaxial ratio of 1/1 the principal stress ratios and maximum values of dilatational energy density $U_v$ and distortional energy density $U_d$ versus applied stress are constructed, Figures 89 and 90. It can be observed that cavitation requirement at achieving a hydrostatic tension is not fulfilled for all applied transverse stresses although the dilatational energy density reaches the critical value at transverse tensile stress ~ 19 MPa. It is worth mentioning that increasing the shear component (increasing $\lambda$) gives similar results and cavitation requirements are not fulfilled. In that case damage initiation through yielding is highly suggested. From this preliminary result, and to continue investigating the effect of the biaxial ratio $\lambda$ on cavity formation, stress ratios less than 1 are selected.

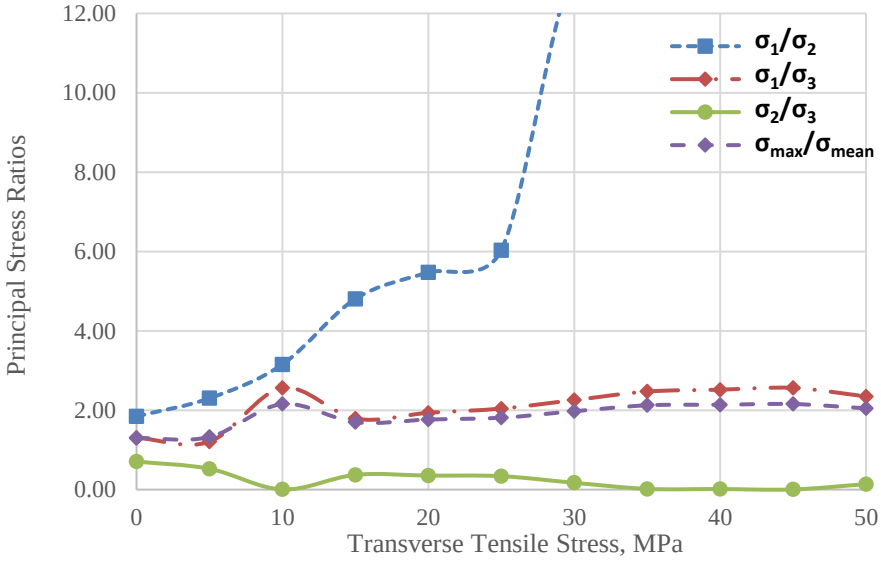


**Figure 89. The principal stress ratios and the ratio of maximum/mean principal stress versus applied transverse stress attained within RVEs at axial shear stress/ transverse tensile stress ratio of 1/1 for the realization shown in figure 86.**

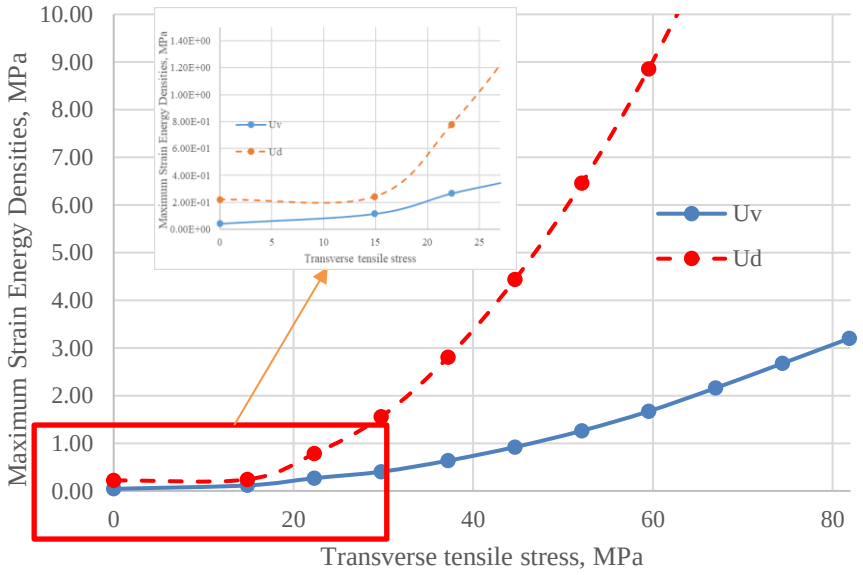


**Figure 90. The maximum values of dilatational energy density $U_v$ and distortional energy density $U_d$ attained within RVEs at axial shear stress/ transverse tensile stress ratio of 1/1 for the realization shown in figure 86.**

The same procedure is performed but with lower values of λ (1/8, 1/12, 1/20 and 1/100) as shown in the following figures (91-98). It is found that at stress ratios > 1/8, the cavitation requirements are not fulfilled. For example, at a biaxial ratio of 1/8 a hydrostatic stress state is not established at all applied transverse stress as observed from corresponding figures (91 and 92). When λ ~ 1/12, cavitation requirements comprising reaching the threshold value and having a hydrostatic stress state are maintained at a transverse tensile stress of ~ 23 MPa. This is observed at λ=1/12 and lower, as shown in figures (93-98) with λ=1/12, 1/20 and 1/100. This indicates that within certain stress ratios and under certain applied axial shear stress, cavitation is still a possible damage initiation mechanism. But, when the axial shear stress is relatively a large value, these requirements are hard to be maintained, instead, yielding as a damage initiation mechanism is to occur providing that $U_d$ reaches its threshold value for yielding.

The tensile stress required for yielding depends on λ. By increasing the biaxial ratio λ to be λ = 1/1, the tensile stress required for yielding is ~27 MPa as shown in Figure 90. Decreasing λ increases the transverse tensile stress necessary for yielding. For example, when λ=1/20 the tensile stress equals ~57 MPa as shown in (Figure 96) but when λ=1/100 it reaches ~78 MPa (Figure 98).

It is worth mentioning that similar observation was found for RVEs with FVF of 40% and 60% with different percentage of NU. In some cases, cavitation was found to occur at biaxial stress ratios λ <=1/7.

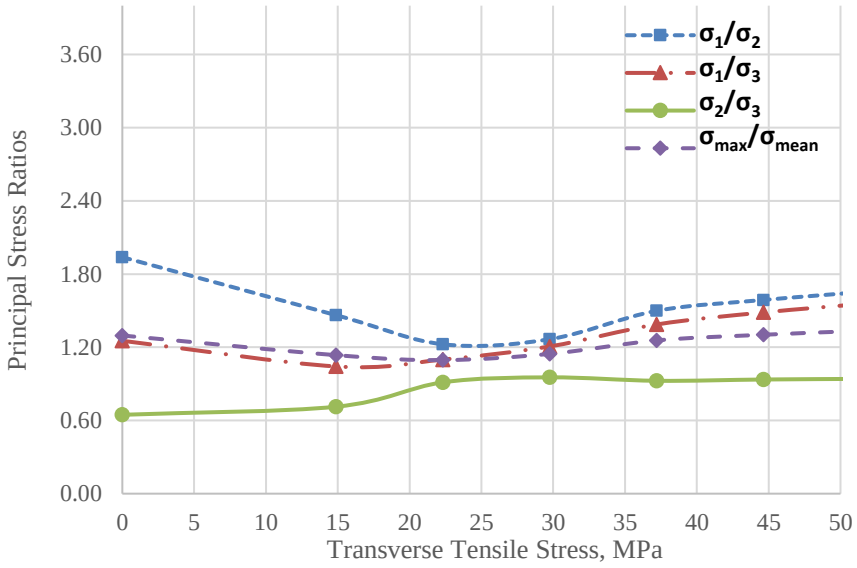


**Figure 91. The principal stress ratios and the ratio of maximum/mean principal stress versus applied transverse stress attained within RVEs at axial shear stress/ transverse tensile stress ratio of 1/8 for the realization shown in figure 86.**

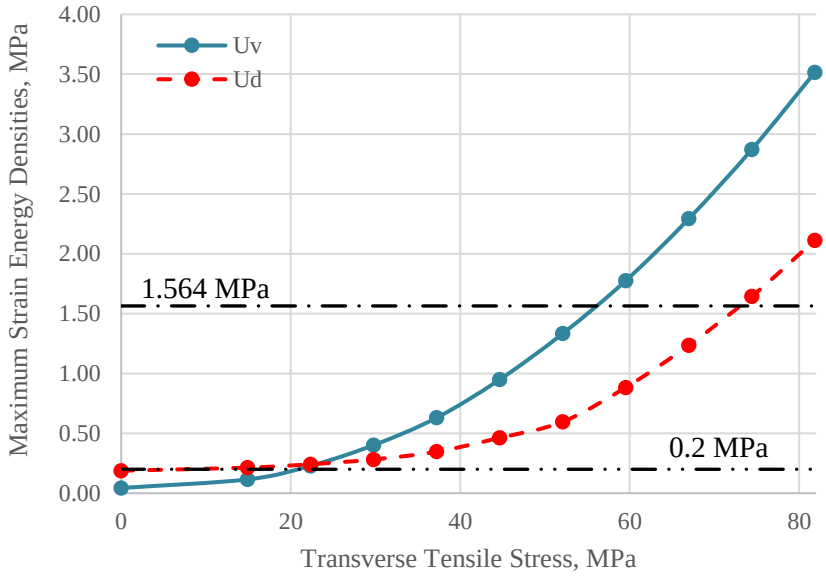


**Figure 92. The maximum values of dilatational energy density $U_v$ and distortional energy density $U_d$ attained within RVEs at axial shear stress/ transverse tensile stress ratio of 1/8 for the realization shown in figure 86.**

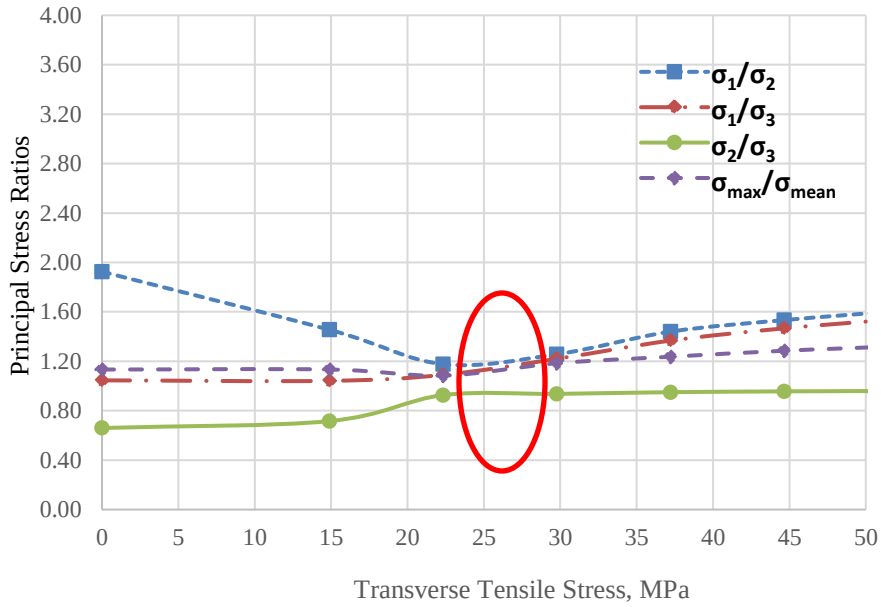


**Figure 93. The principal stress ratios and the ratio of maximum/mean principal stress versus applied transverse stress attained within RVEs at axial shear stress/ transverse tensile stress ratio of 1/12 for the realization shown in figure 86.**

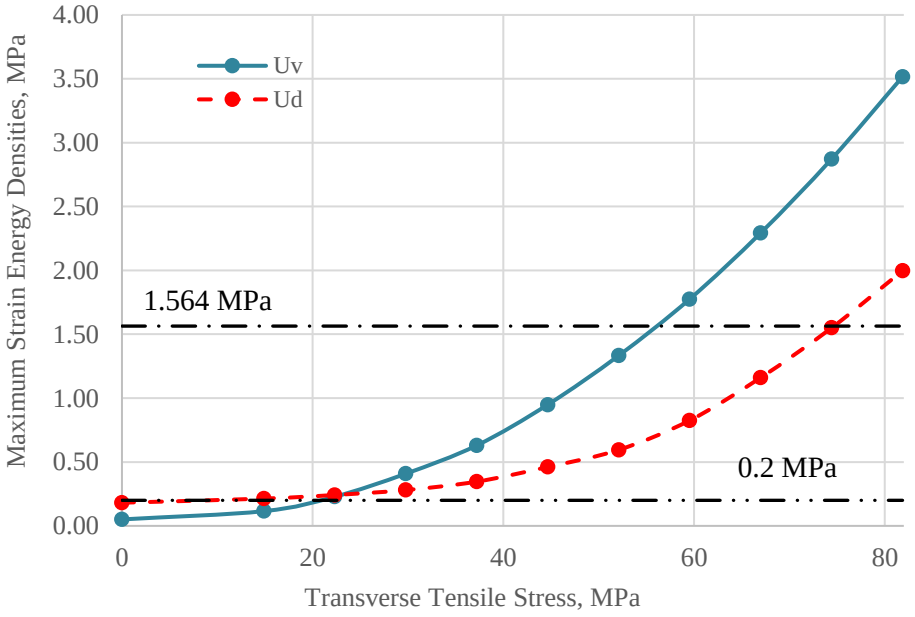


**Figure 94. The maximum values of dilatational energy density $U_v$ and distortional energy density $U_d$ attained within RVEs at axial shear stress/ transverse tensile stress ratio of 1/12 for the realization shown in figure 86.**

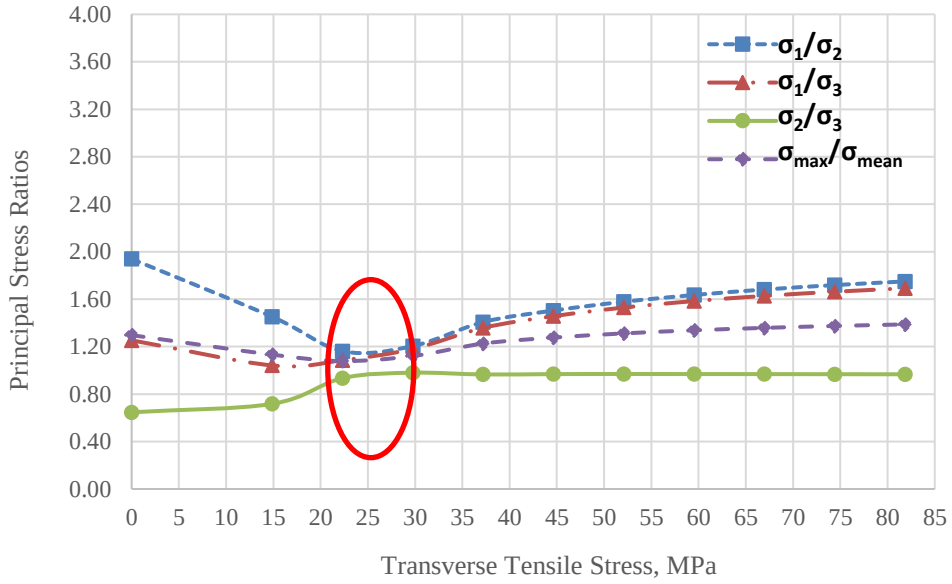


**Figure 95. The principal stress ratios and the ratio of maximum/mean principal stress versus applied transverse stress attained within RVEs at axial shear stress/ transverse tensile stress ratio of 1/20 for the realization shown in figure 86.**

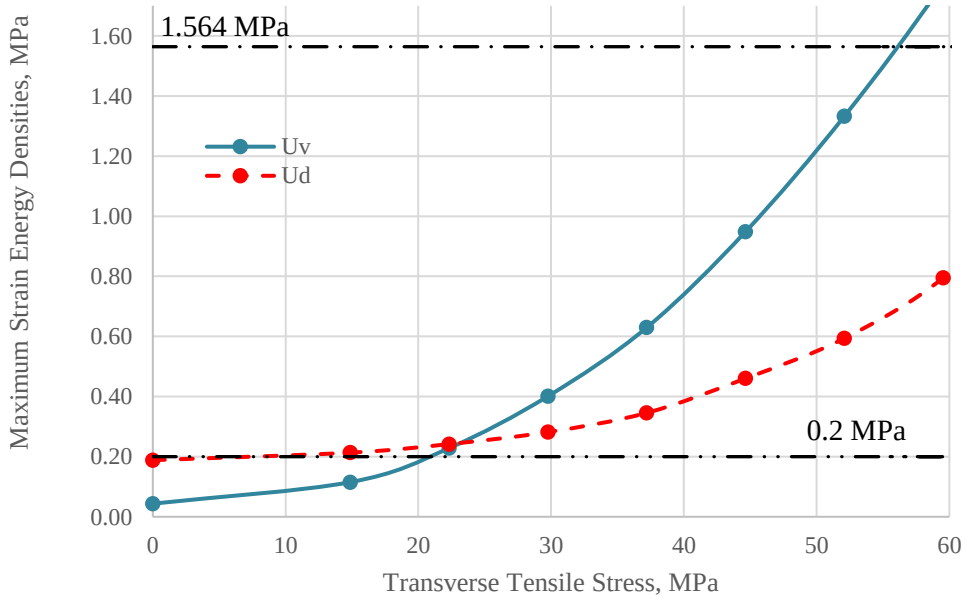


**Figure 96. The maximum values of dilatational energy density $U_v$ and distortional energy density $U_d$ attained within RVEs at axial shear stress/ transverse tensile stress ratio of 1/20 for the realization shown in figure 86.**

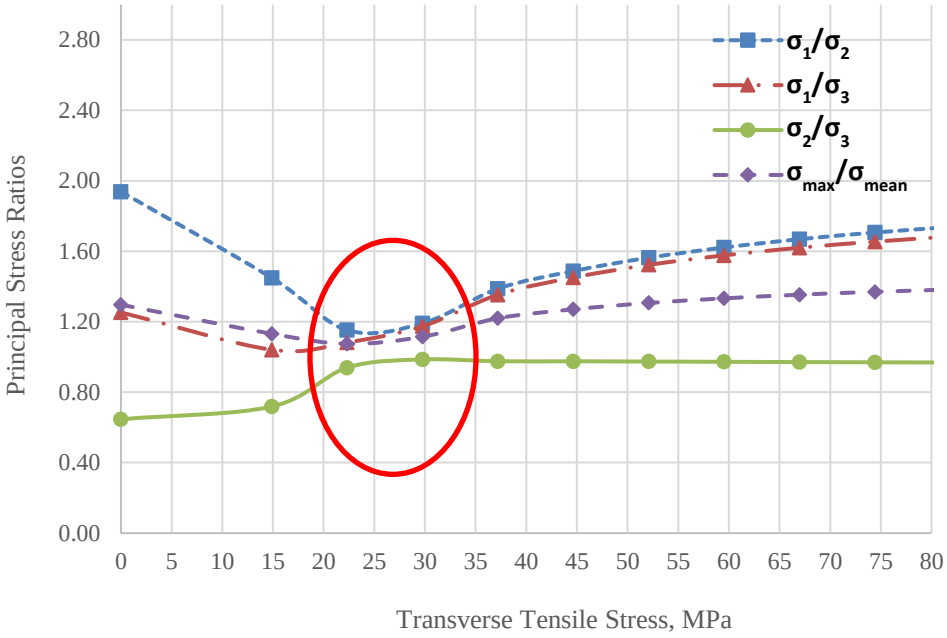


**Figure 97. The principal stress ratios and the ratio of maximum/mean principal stress versus applied transverse stress attained within RVEs at axial shear stress/ transverse tensile stress ratio of 1/100 for the realization shown in figure 86.**

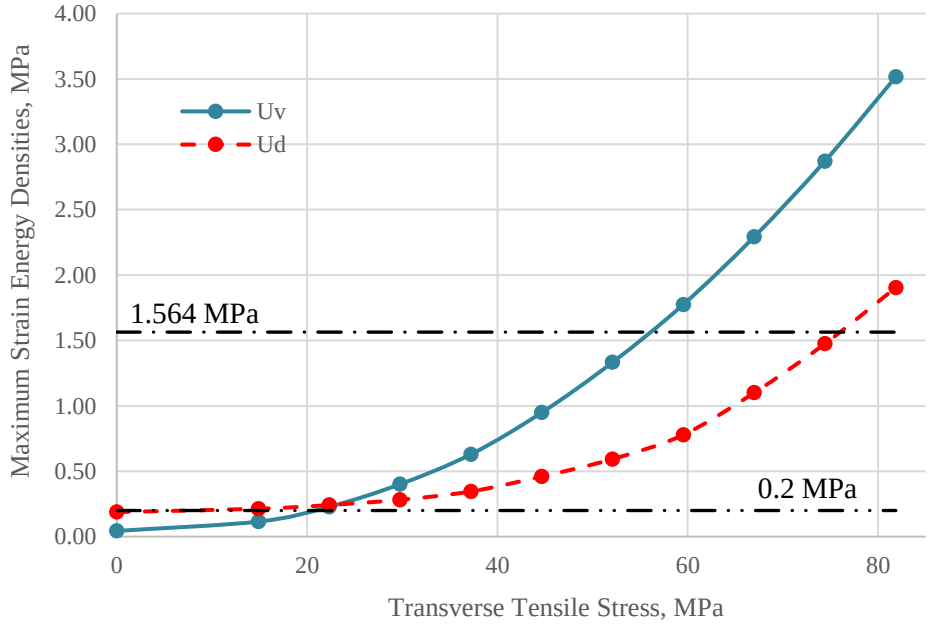


**Figure 98. The maximum values of dilatational energy density $U_v$ and distortional energy density $U_d$ attained within RVEs at axial shear stress/ transverse tensile stress ratio of 1/100 for the realization shown in figure 86.**

To summarize the whole results, biaxial stress ratios at which cavitation is likely are plotted in one diagram, figure 99. A band of these ratios is drawn, in which the solid line represents the ratios at which the difference of the three principal stresses is minimum and the maximum and minimum dashed lines represent ratios of cavitation where the three principal stresses' values are within the ±20% difference. Outside this band, cavitation requirements are not fulfilled, and thus, cavitation will not occur.

It seems obvious that cavity formation can take place only under certain λ values at certain shear and tensile stresses. For the realization shown in figure 86, a transverse tensile stress in the range (~20 ~ 30MPa) along with relatively small values of axial shear component up to ~3 MPa are required to form a cavity. This transverse tensile stress range is decreased by increasing the applied shear stress. Away from this range, cavitation requirements are not fulfilled.

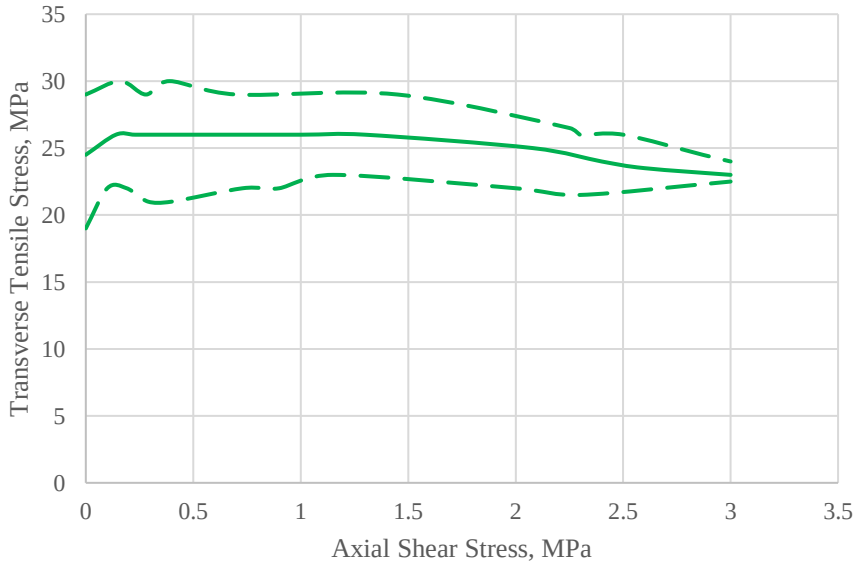


**Figure 99. Axial shear stress versus transverse tensile stress in MPa, for the realization shown in figure 86. Solid line represents the axial shear stress/ transverse tensile stress ratios with minimum principal stresses difference where cavitation requirements are fulfilled. The short-dashed lines describe the range in which the cavitation mechanism can occur because of the tolerance of 20% given to the attainment of hydrostatic tension.**

Below are examples of the results obtained for different RVEs under different combinations of fiber volume fraction (40% ,54%, and 60%) and degree of nonuniformity (0%, 60% and 100%), Figures (100-108).

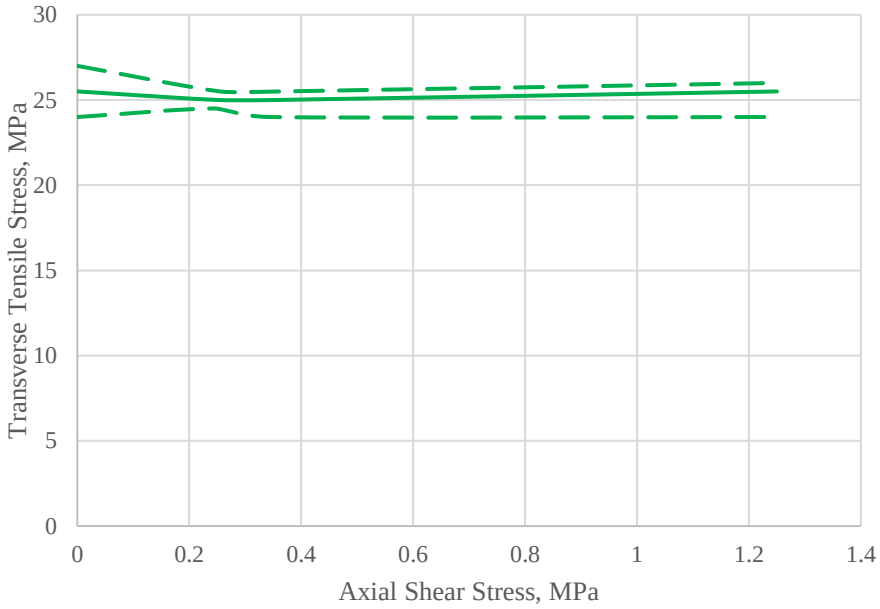


**Figure 100. Axial shear stress versus transverse tensile stress in MPa for 40% fiber volume fraction and 0% nonuniformity. Solid line represents the axial shear stress/ transverse tensile stress ratios with minimum principal stresses difference where cavitation requirements are fulfilled. The short-dashed lines describe the range in which the cavitation mechanism can occur because of the tolerance of 20% given to the attainment of hydrostatic tension.**

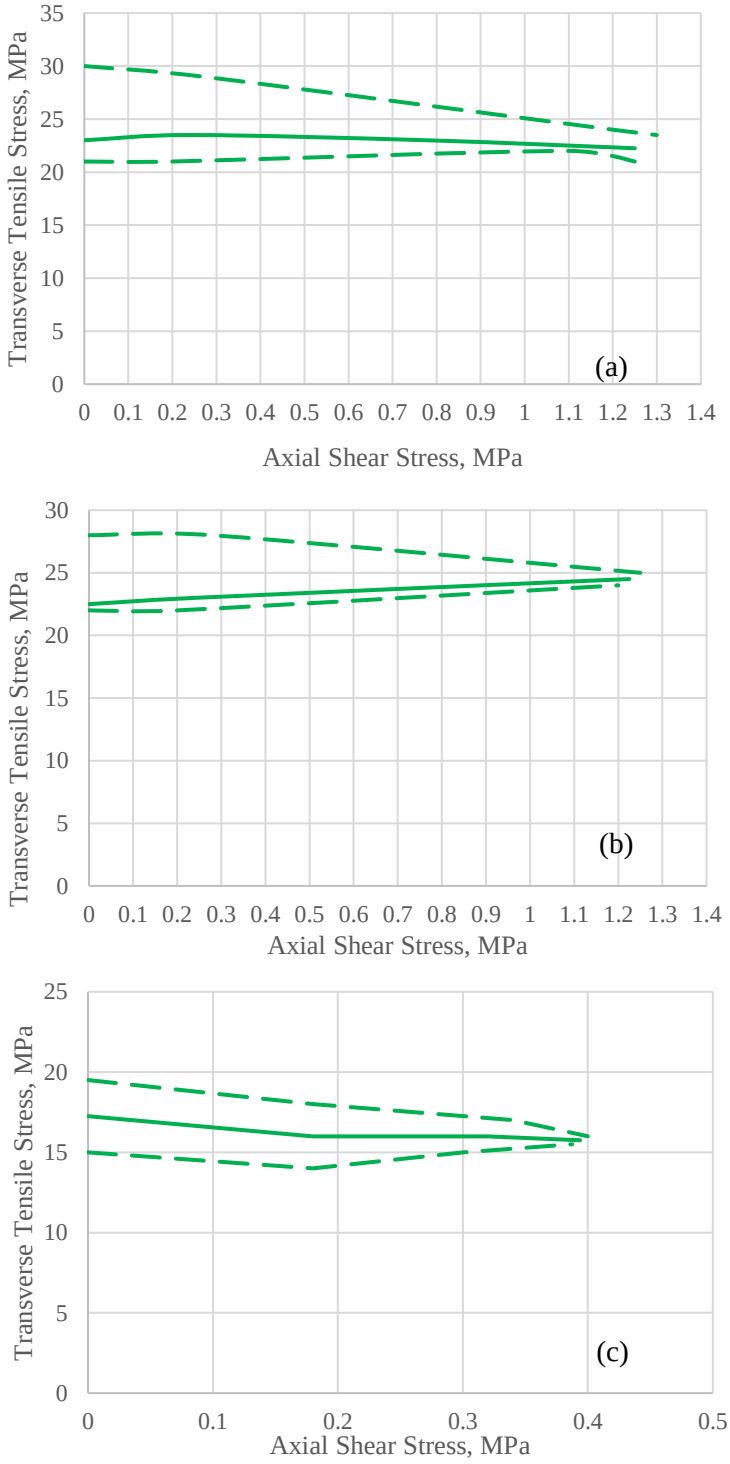


**Figure 101. Axial shear stress versus transverse tensile stress in MPa for 40% fiber volume fraction and 60% nonuniformity for three different realizations, a) realization 1, b) realization 2 and c) realization 3. Solid line represents the axial shear stress/ transverse tensile stress ratios with minimum principal stresses difference where cavitation requirements are fulfilled. The short-dashed lines describe the range in which the cavitation mechanism can occur because of the tolerance of 20% given to the attainment of hydrostatic tension.**

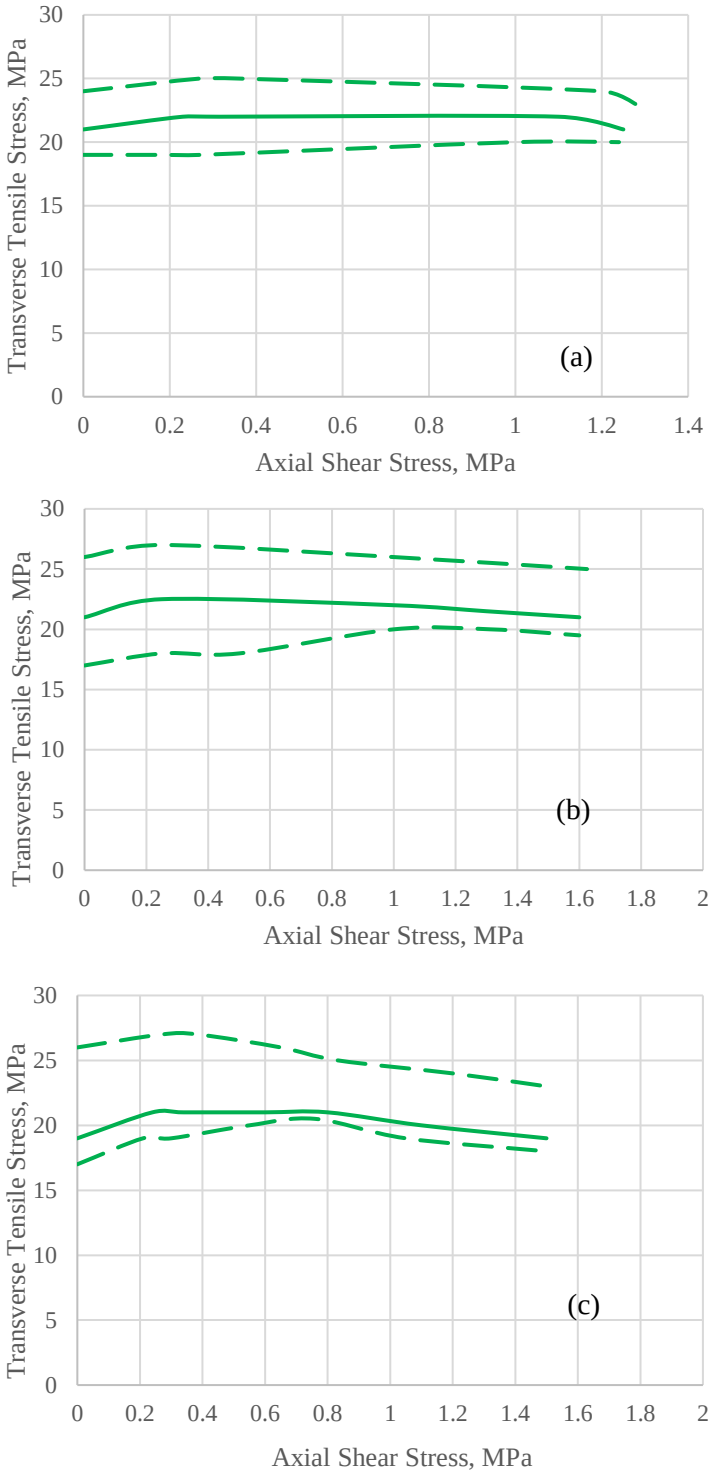


**Figure 102. Axial shear stress versus transverse tensile stress in MPa for 40% fiber volume fraction and 100% nonuniformity for three different realizations, a) realization 1, b) realization 2 and c) realization 3. Solid line represents the axial shear stress/ transverse tensile stress ratios with minimum principal stresses difference where cavitation requirements are fulfilled. The short-dashed lines describe the range in which the cavitation mechanism can occur because of the tolerance of 20% given to the attainment of hydrostatic tension.**

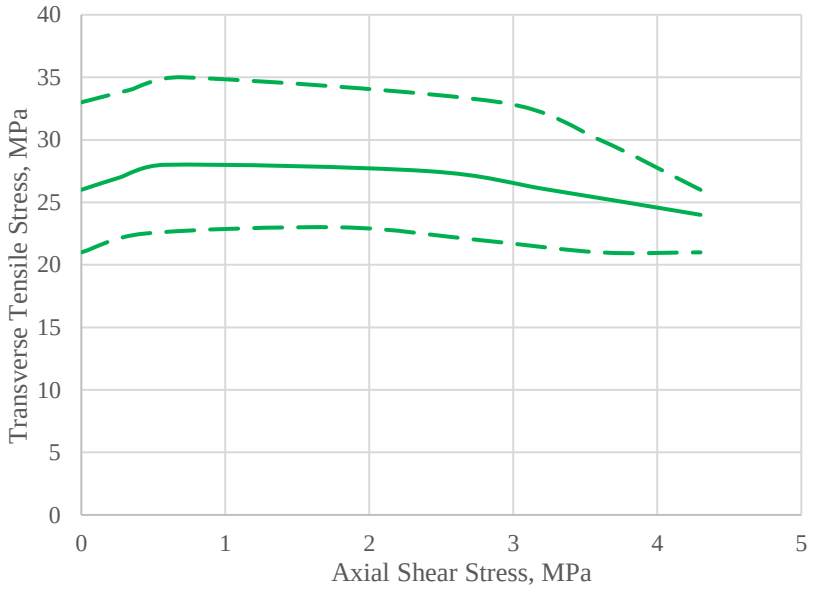


**Figure 103. Axial shear stress versus transverse tensile stress in MPa for 54% fiber volume fraction and 0% nonuniformity. Solid line represents the axial shear stress/ transverse tensile stress ratios with minimum principal stresses difference where cavitation requirements are fulfilled. The short-dashed lines describe the range in which the cavitation mechanism can occur because of the tolerance of 20% given to the attainment of hydrostatic tension.**

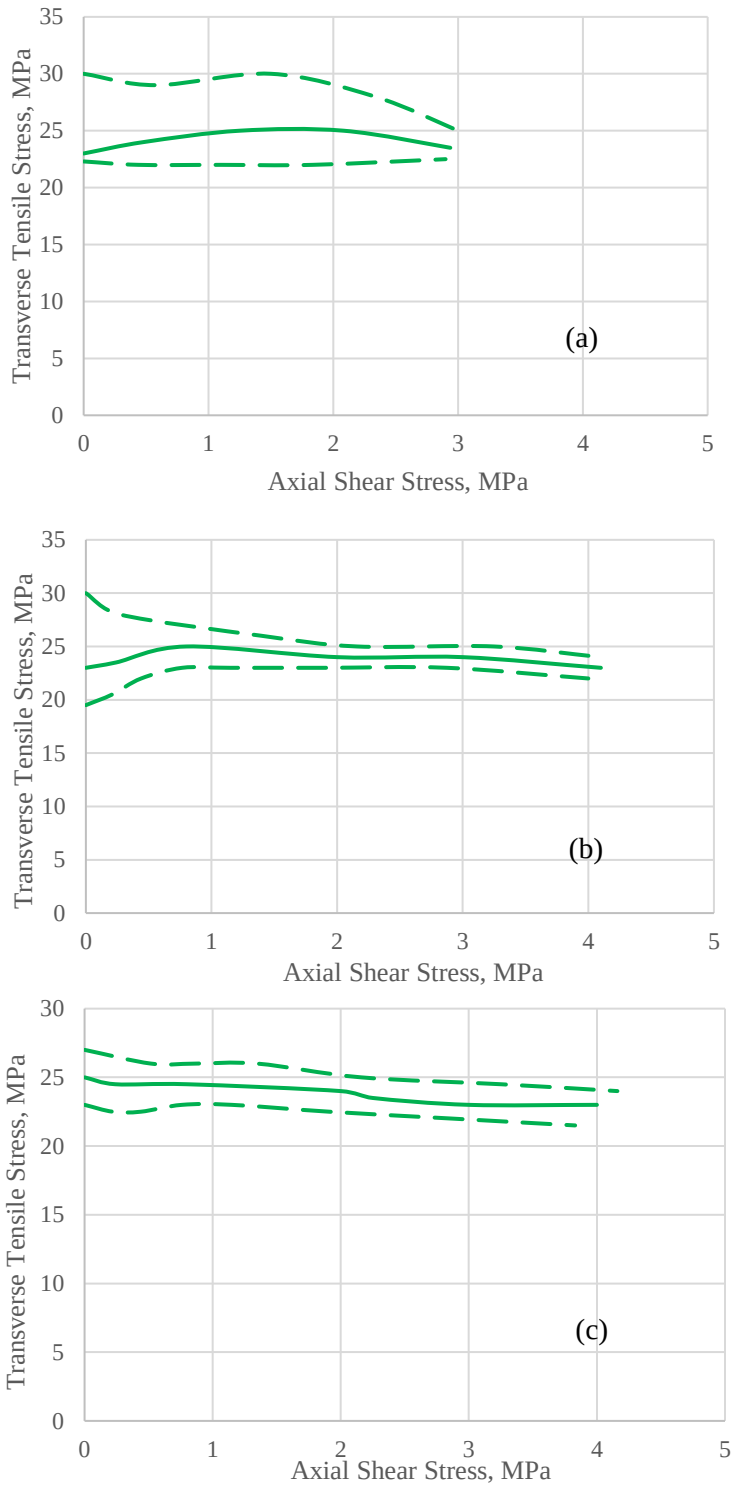


**Figure 104. Axial shear stress versus transverse tensile stress in MPa for 54% fiber volume fraction and 60% nonuniformity for three different realizations, a) realization 1, b) realization 2 and c) realization 3. Solid line represents the axial shear stress/ transverse tensile stress ratios with minimum principal stresses difference where cavitation requirements are fulfilled. The short-dashed lines describe the range in which the cavitation mechanism can occur because of the tolerance of 20% given to the attainment of hydrostatic tension.**

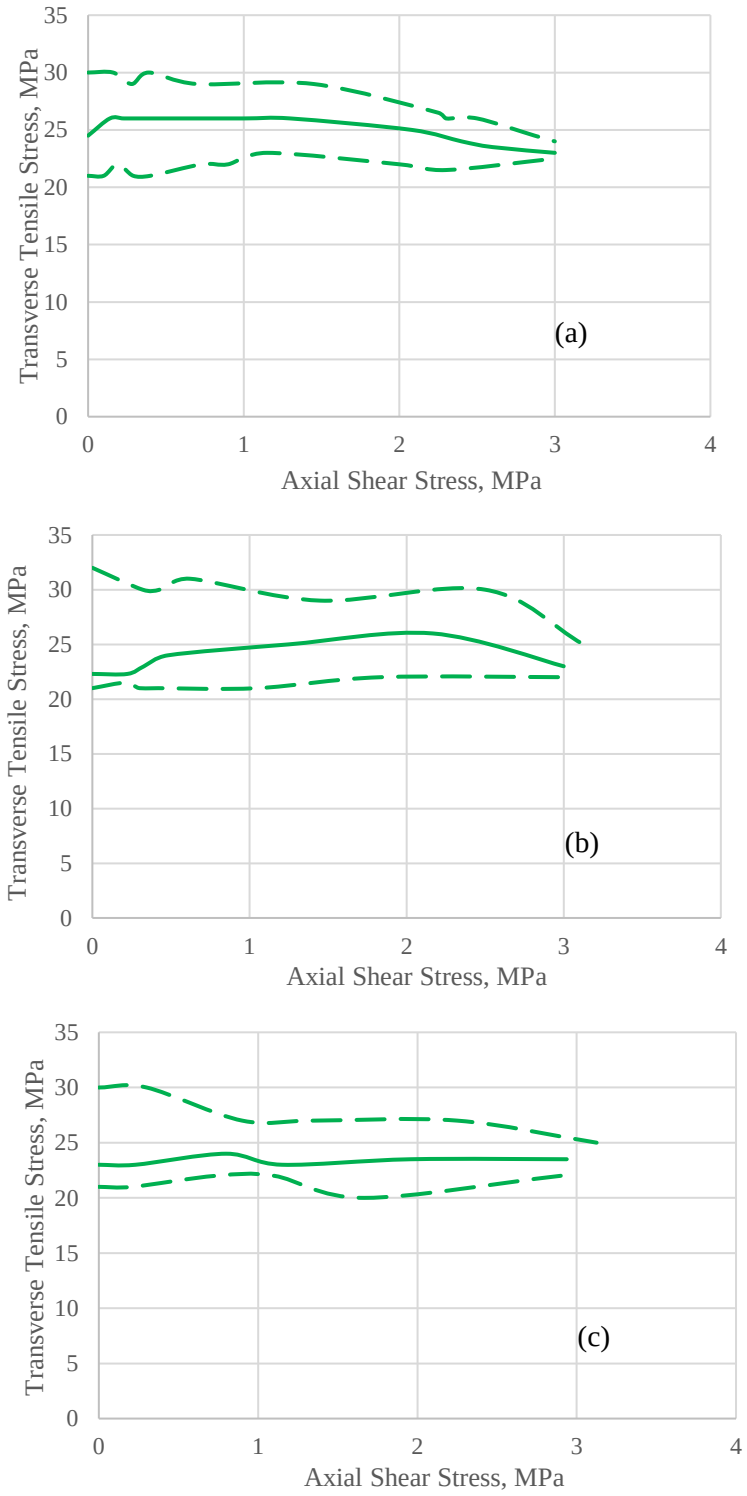


**Figure 105. Axial shear stress versus transverse tensile stress in MPa for 54% fiber volume fraction and 100% nonuniformity for three different realizations, a) realization 1, b) realization 2 and c) realization 3. Solid line represents the axial shear stress/ transverse tensile stress ratios with minimum principal stresses difference where cavitation requirements are fulfilled. The short-dashed lines describe the range in which the cavitation mechanism can occur because of the tolerance of 20% given to the attainment of hydrostatic tension.**

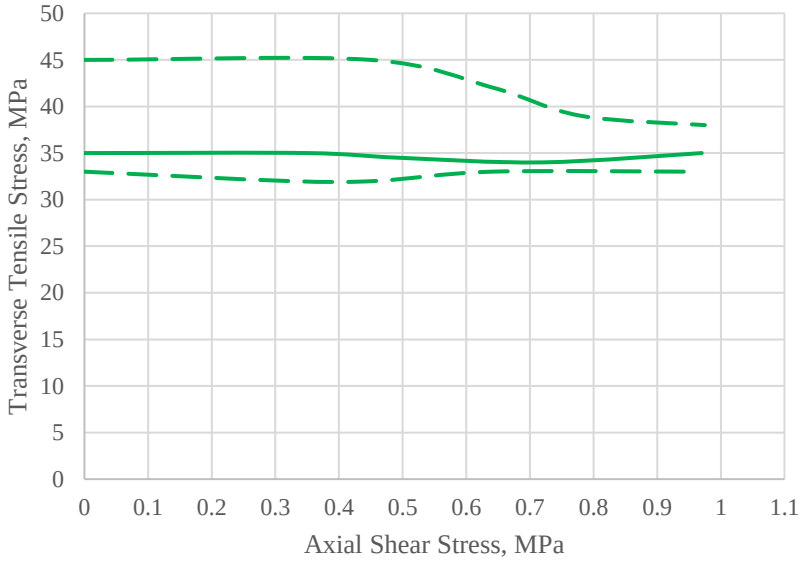


**Figure 106. Axial shear stress versus transverse tensile stress in MPa for 60% fiber volume fraction and 0% nonuniformity. Solid line represents the axial shear stress/ transverse tensile stress ratios with minimum principal stresses difference where cavitation requirements are fulfilled. The short-dashed lines describe the range in which the cavitation mechanism can occur because of the tolerance of 20% given to the attainment of hydrostatic tension.**

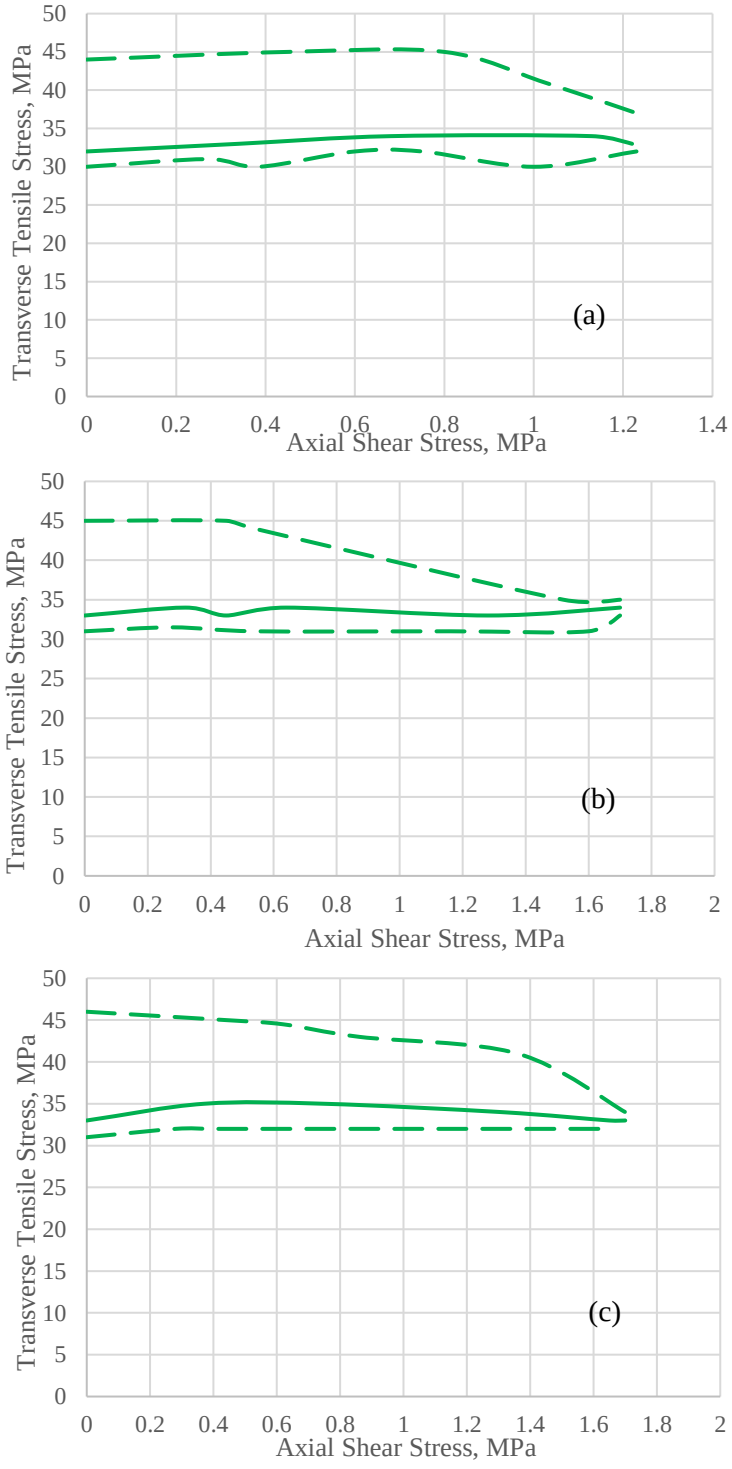


**Figure 107. Axial shear stress versus transverse tensile stress in MPa for 60% fiber volume fraction and 60% nonuniformity for three different realizations, a) realization 1, b) realization 2 and c) realization 3. Solid line represents the axial shear stress/ transverse tensile stress ratios with minimum principal stresses difference where cavitation requirements are fulfilled. The short-dashed lines describe the range in which the cavitation mechanism can occur because of the tolerance of 20% given to the attainment of hydrostatic tension.**

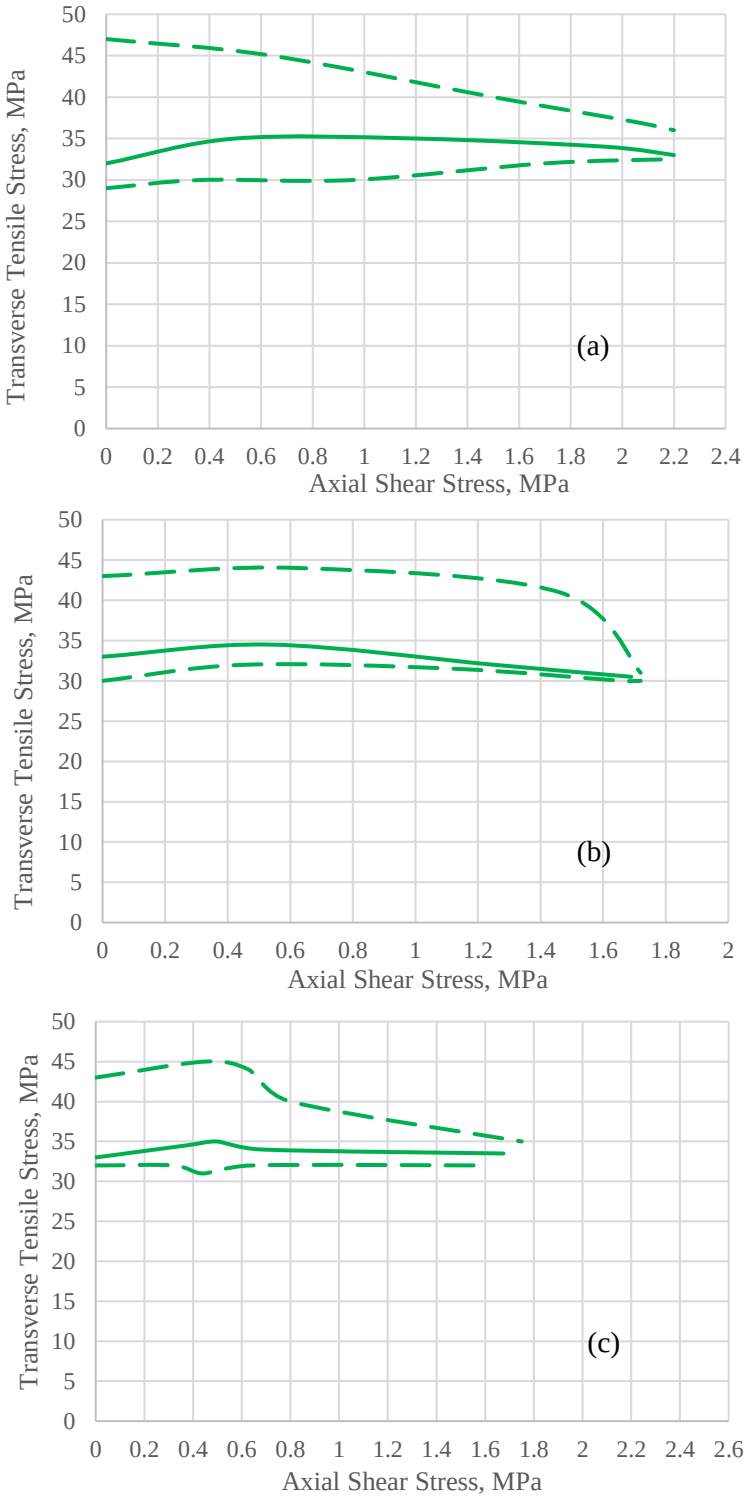


**Figure 108. Axial shear stress versus transverse tensile stress in MPa for 60% fiber volume fraction and 100% nonuniformity for three different realizations, a) realization 1, b) realization 2 and c) realization 3. Solid line represents the axial shear stress/ transverse tensile stress ratios with minimum principal stresses difference where cavitation requirements are fulfilled. The short-dashed lines describe the range in which the cavitation mechanism can occur because of the tolerance of 20% given to the attainment of hydrostatic tension.**

For each FVF and degree of NU, cavitation is suggested to be created at certain biaxiality stress ratios (λ) providing that the transverse stress is within certain values. The transverse stress is slightly changed with the applied shear stress. For example, for an RVE of 40% FVF and 100% NU in figure 102 (a), under tensile stress only the transverse stress values at which cavitation might occur in the range of ~ (19-24 MPa). This range becomes smaller by increasing the applied shear stress component to be ~ (21-23 MPa) at shear stress ~ 1.5 MPa. At all biaxiality ratios, within the drawn band, a cavity is possible to be formed. At very low and very large values of λ, cavitation requirements are not fulfilled.

### 7.2.3. Summary and conclusion

Two conditions of biaxial loading are applied to the constructed RVEs with different volume fractions and degree of nonuniformity. The first type is equi-biaxial transverse tensile load. This is performed to 2D RVEs with (40, 50 and 60 %) FVF and with (0,30, 60 and 100%) NU. The second type of biaxial load is combined axial shear and transverse tension. This is imposed to 3D RVEs with 40, 54 and 60 % FVF and with different % of NU (0, 60 and 100) under PBCs. Several conclusions could be addressed for both biaxial loading conditions.

#### 7.2.3.1. Under equi-biaxial transverse tension

- Cavitation is suggested to be the first event of failure. The strain at which cavitation forms is similar to that obtained under uniaxial transverse tension.
- The maximum distortional energy density shows lower values at all applied strains compared to the values obtained under uniaxial tensile load. Thus, the critical distortional energy density required for yielding will be maintained at larger strain values.

#### 7.2.3.2. Under combined axial shear and transverse tension

- A hydrostatic stress state is found to be established under certain values of λ, with specific values of transverse tensile stress and with relatively low values of the axial shear stress component. Under either very low or very large values of transverse tensile stress this hydrostatic stress state is eliminated. This effect is also found when large shear stresses are applied. These findings are observed for all FVFs and studied degrees of NU.
- The maximum biaxial stress ratio below which cavitation requirements are fulfilled equals to ~1/7.
- When cavitation becomes difficult to take place, the second possible damage mechanism (yielding), becomes feasible providing that the distortional energy density reaches its threshold value.
- By increasing the shear stress component, the transverse stress at which yielding might occur is increased.

# 8. CONCLUSION

This study has mainly examined the effects of manufacturing induced disorder in fiber distribution within fiber glass/epoxy composites on the initiation of first failure event under different loading conditions such as uniaxial transverse tension, equi-biaxial transverse tension, axial shear and a simultaneous axial shear and transverse tension.

Two energy based point failure criteria for the polymer matrix – critical dilatational energy density ($U_v$) and critical distortional energy density ($U_d$) – are considered. The critical ($U_v$) is taken from the literature [76] which is in the range ~0.13-0.2 MPa for the materials studied. This critical $U_v$ is assumed to be responsible for a brittle failure (cavitation) to take place at the onset of damage. The critical $U_d$, on the other hand, is believed to be responsible for yielding to occur when reached.

The degree of fibers' nonuniformity has been quantified by a linear measure of the displacements of fibers from their expected positions in a uniform square pattern. An algorithm is developed to construct a RVE that can establish different degrees of nonuniformity (e.g.; 0%, 30%, 60%, and 100%) and different FVFs (e.g.; 40%, 50%, 55% and 60%). RVEs are constructed using the "shaking model" in which the fibers are deviated from their uniform positions depending on the applied degree of nonuniformity. At least five different RVE realizations are created for each combination of FVF and the degree of NU, except for the 0 degree of NU (uniform distribution), where only one realization is possible. For each case, a statistical analysis of the fiber distribution is performed and represented by appropriate functions describing the interfiber distance characteristics such as Ripley's K

function and the pair distribution function as well as the nearest neighbor (First, second and third) and the nearest neighbor orientation functions.

The study of the damage initiation is carried out using micromechanical simulation of composites. The micromechanical study is conducted through finite element analysis on the constructed RVEs. The RVEs are subjected to a thermal cool down = - 82$^{o}$, then the mechanical load is applied using appropriate boundary conditions.

**8.1. Conclusion**

Based on the statistical and failure analyses one can conclude that:

- The algorithm proposed in this study is capable of creating different degrees of nonuniform distribution of fibers. Increasing the NU from 0% to 100% changes the fibers distribution from a uniform pattern to a more like Poisson's distribution. This is observed from statistical functions such as K(r) and g(r) functions for all examined FVFs and degrees of NU. However, the impact of nonuniformity is lowered when high FVFs are considered e.g.; 60%.
- An RVE should be large enough to contain all possible irregularities that might initiate damage. Based on that, and considering that interfiber distances are essential in the distribution of the local stress and strain fields, the nearest neighbor functions are utilized in determining the minimum RVE size. In fact, the first nearest neighbor function is found to be adequate for the purpose.
- Based on the nearest neighbor functions and the local stress fields in the form of Mises stress and dilatational energy density under transverse tension and axial shear loads, it was found that a minimum RVE size, containing ~200 fibers, is adequate

for all fiber volume fractions considered (40%, 50%, 54% and 60%) and all degrees of NU.

- Damage initiation through cavitation as a brittle damage behavior in polymers is likely as the first failure event when a transverse tension exists. Cavitation occurs when a hydrostatic stress state is established in the matrix between two close pair of fibers that lie in parallel to the transverse load direction. For the FVFs considered (40, 50 and 60%) and degrees of NU (0%, 30%, 60%, and 100%), the strain required for cavitation to occur has a lower value compared to that required for yielding. The maximum distortional strain energy occurs between the two fibers that have the minimum interfiber distance within the RVE.
- The mechanical strain at the onset of cavitation decreases as the degree of nonuniformity increases. This occurred at all FVFs considered in this study. The constituent properties used in the study were typical of a glass/epoxy composite.
- On conducting FEA under combined axial shear with transverse tension for different FVFs (40%, 54% and 60%) and different % of NU (0%, 60% and 100%) reveals that cavitation is observed to initiate damage only at certain biaxial stress ratios $\lambda$ within a specific transverse tensile stresses. The maximum biaxial stress ratio below which cavitation requirements are fulfilled equals to ~1/7. Away from these ratios, yielding is suggested as the first failure event providing that the maximum distortional energy density reaches the threshold value.
- Under axial shear loading only, the earliest matrix yielding occurs at locations of the minimum interfiber distance throughout the 3D RVE thickness. The mechanical strain at the onset of yielding decreases as the degree of nonuniformity increases for

the investigated FVFs (40%, 54% and 60%). Under the same NU, this strain is decreased by increasing the RVE fiber volume fraction.

- The matrix stiffness or the matrix/ fiber stiffness ratio found to be an important parameter that cannot be ignored. Under transverse tension, the mechanical strain to onset of cavitation is affected significantly at low matrix/fiber stiffness ratios. It increases as this ratio increases and approaches a constant value at high ratios. Also, when an axial shear is applied, the mechanical strain at which yielding initiates is found to increase by increasing the matrix stiffness for the same FVF and same degree of NU.
- Preliminary results from virtual tests, conducted under transverse tension with the presence of voids, revealed that voids shape, position and size could be considered parameters that affect the damage initiation mechanism. Further research should be conducted to make a better assessment on the subject.

**8.2. Recommended future work**

1- Voids, in the UD composite matrix, are known to be one of the most common manufacturing defects. In present work, it has been shown that the presence of a void, alters the local stress field. In addition, parameters, such as the shape, size, and position of such voids, could affect the damage initiation mechanism that takes place. Studying the effect of voids on damage initiation should be performed experimentally as well as theoretically and/or numerically.

2- More effort should be made to determine the interface properties, especially those that are related to fracture and damage, such as fracture toughness.

3- Damage propagation should be studied with the presence of different manufacturing defects, including different degrees of fibers' distribution nonuniformity.

4- The validity of proposed algorithm to create the composites RVEs, should be examined under different uniaxial/ multiaxial loading conditions, such as compression loading and transverse shear loading.

# REFERENCES


1- C. T. Herakovich, “Mechanics of Composites: A Historical Review”, J. Mechanics Research Communications **41** (2012) 1– 20.

2- R.E. Shaeffer, *Reinforced Concrete: Preliminary Design for Architects and Builders*, McGraw-Hill (1992).

3- C. W. Condit, "The First Reinforced-Concrete Skyscraper the Ingalls Building in Cincinnati and its Place in Structural History", J. Technology and Culture **9 (**1) (1968) 1-33.

4- https://www.asbestos.com/companies/owens-corning-fiberglas.php

5- B. D. Agarwal, L. J. Broutman, K. Chandrashekhara, *Analysis and Performance of Fiber Composites*, 3rd Edition (2006) 1-61.

6- L. Mishnaevsky Jr., K. Branner, H. N. Petersen, J. Beauson, M. McGugan, B. F. Sørensen, "Materials for Wind Turbine Blades: An Overview", J. Materials **10** (11) (2017) 1285.

7-http://www.windpowerengineering.com/business-news-projects/manufacturing-evolution-wind-turbine-blades/

8- https://www.export.gov/article?id=Egypt-Renewable-Energy

9- https://energy.gov/eere/wind/wind-vision

10- J. LLorca, C. González, J.M. Molina-Aldareguía, J. Segurado, R. Seltzer, F. Sket, Rodríguez M, Sádaba S, Muñoz R, Canal LP. "Multiscale Modeling of Composite Materials: A Roadmap Towards Virtual Testing", J. Advanced Matererials, **23** (2011) 5130-5147.

11- J. LLorca, C. González, J.M. Molina-Aldareguía, C.S. Lopes, “Multiscale Modeling of Composites” J. The Minerals, Metals & Materials Society (JOM) **65** (2013) 215-225.

12- D. Brigante, *New Composite Materials: Selection, Design, and Application*, Edition 1, Springer International Publishing, (2014).

13- ASTM D4762-16 Standard Guide for Testing Polymer Matrix Composite Materials, ASTM International, West Conshohocken, PA, (2016)

14- W. J. Cantwell, J. Morton, "The Significance of Damage and Defects and Their Detection in Composite Materials: A Review", J. Strain Analysis **27** (1) (1992).

15- J. A. Nairn, in *Polymer Matrix Composites*, eds., R. Talreja and J. Å. E. Manson (2000) 403-432.

16- D. G. Harlow, S. L. Phoenix, "The Chain-Of-Bundles Probability Model for The Strength of Fibrous Materials I: Analysis and Conjectures", J. Composite Materials **12** (1978) 195–214.

17- Y. Swolfs, R. M. McMeeking, I. Verpoest, L. Gorbatikh’ “Matrix Cracks Around Fibre Breaks and Their Effect on Stress Redistribution and Failure Development in Unidirectional Composites”, J. Composites Science and Technology **108** (2015) 16–22.

18- S. L. Phoenix, R. L. Smith. "A Comparison of Probabilistic Techniques for The Strength of Fibrous Materials Under Local Load-Sharing Among Fibers". Int J. Solids Struct **19** (6) (1983) 479–96.

19- R. L. Smith, S. L. Phoenix, M. R. Greenfield, R. B. Henstenburg, R. E. Pitt. "Lower-Tail Approximations for The Probability of Failure of Three-Dimensional Fibrous Composites with Hexagonal Geometry", Proc Royal Soc London Ser A: Math Phys Eng Sci **388** (1795) (1983) 353–91.

20- A. E. Scott, I. Sinclair, S. M. Spearing, A. Thionnet, A. R.Bunsell." Damage Accumulation in A Carbon/Epoxy Composite: Comparison Between a Multiscale Model and Computed Tomography Experimental Results". J. Composites Part A **43** (9) (2012) 1514–22.

21- D. Raz-Ben Aroush, E. Maire, C. Gauthier, S. Youssef, P. Cloetens, H.D. Wagner, “A Study of Fracture of Unidirectional Composites Using in Situ High-Resolution Synchrotron X-Ray Microtomography”, J. Composites Science and Technology **66** (2006) 1348–1353.

22- H. Fukuda, " Stress Concentration Factors in Unidirectional Composites with Random Fiber Spacing", J. Composites Science and Technology **22** (2) (1985) 153–63.

23- Z Xia, W. A. Curtin, T. Okabe, "Green’s Function Vs. Shear-Lag Models of Damage and Failure in Fiber Composites", J. Composites Science and Technology **62** (10–11) (2002) 1279–88.

24- Z Xia, T. Okabe, W. A. Curtin, "Shear-Lag Versus Finite Element Models for Stress Transfer in Fiber-Reinforced Composites", J. Composites Science and Technology **62** (9) (2002) 1141–9.

25- Y. Swolfs, L. Gorbatikh, V. Romanov, S. Orlova, S. V. Lomov, I. Verpoest, "Stress Concentrations in An Impregnated Fibre Bundle with Random Fibre Packing", J. Composites Science and Technology **74** (2013) 113–20.

26- Y. Swolfs, L. Gorbatikh, I. Verpoest, "Stress Concentrations in Hybrid Unidirectional Fibre-Reinforced Composites with Random Fibre Packings", J. Composites Science and Technology **85** (2013) 10–6.

27- M. R. Nedele, M. R. Wisnom, "Three-Dimensional Finite Element Analysis of The Stress Concentration at a Single Fibre Break", J. Composites Science and Technology **51** (4) (1994) 517–24.

28- S. Behzadi, F.R. Jones, “The Effect of Temperature on Stress Transfer Between a Broken Fibre and the Adjacent Fibres in Unidirectional Fibre Composites”, J. Composites Science and Technology **68** (13) (2008) 2690–6.

29- Z. Xia, W. A. Curtin, P. W. M. Peters, “Multiscale Modeling of Failure in Metal Matrix Composites”, J. Acta Mater **49** (2) (2001) 273–87.

30- A. Thionnet, H.Y. Chou, A. Bunsell, “Fibre Break Processes in Unidirectional Composites”, J. Composites: Part A **65** (2014) 148–160.

31- L. Zhuang, R. Talreja, J. Varna, “Tensile Failure of Unidirectional Composites from a Local Fracture Plane”, J. Composites Science and Technology **133** (2016) 119-127.

32- B. W. Rosen, "Mechanics of Composite Strengthening”, Fiber Composite Materials, American Society of Metals (1964) 37-45.

33- C. R. Chaplin, "Compressive Fracture in Unidirectional Glass-Reinforced Plastics", J. Materials Science **12** (1977) 347-352.

34- H. T. Hahn, M.M. Sohi, S. Moon, “Compression Failure Mechanisms of Composite Structures”, NASA Contractor Report 3988 (1986).

35- A. S. Argon, "Fracture of Composites", Treatise of Material Science and Technology, Vol. **I**. New York, NY: Academic Press (1972) 79–114.

36- N. A. Fleck, B. Budiansky, "Compressive Failure of Fibre Composites Due to Microbuckling", in Inelastic Deformation of Composite Materials, G. J. Dvorak, ed., Springer-Verlag (1990) 235-274.

37- S. H. Lee, A. M. Waas, “Compressive Response and Failure of Fiber Reinforced Unidirectional Composites”, Int J. Fracture **100** (1999) 275–306.

38- A. M. Waas, C. R. Schultheisz, "Compressive Failure of Composites, Parts I and II", Progress in Aerospace Sciences **32** (1995) 1–78.

39- T. J. Vogler, S. Kyriakides,” On the Initiation and Growth of Kink Bands in Fiber Composites: Part 1. Experiments”, Int J. Solids and Structures **38** (2001) 2639-2651.

40- T. J. Vogler, S. Y. Hsu, S. Kyriakides," Composite Failure Under Combined Compression and Shear", Int J. Solids and Structures **37** (2000) 1765-1791.

41- S. Pimenta, R. Gutkin, S. T. Pinho, P. Robinson," A Micromechanical Model for Kink-Band Formation: Part II- Numerical Modeling", J. Composites Science and Technology, **69** (2009) 956-964.

42- T.J. Vogler, S. Kyriakides," On the Axial Propagation of Kink Bands in Fiber Composites: Part I Experiments", Int J. Solids and Structures **36** (1999) 557-574.

43- A. Jumahat, C. Soutis, “Fracture Mechanisms and Failure Analysis of Carbon Fibre/Toughened Epoxy Composites Subjected to Compressive Loading”, J. Composite Structures **92**(2) (2010) 295-305.

44- C. González, J. LLorca, "Mechanical Behavior of Unidirectional Fiber-Reinforced Polymers Under Transverse Compression: Microscopic Mechanisms and Modeling", J. Composites Science and Technology **67** (2007) 2795–2806.

45- K. Niu, R. Talreja, "Modeling of Compressive Failure in Fiber Reinforced Composites", Int J Solids and Structures **37** (17) (2000) 2405-2428.

46- B. W. Rosen, "Tensile Failure of Fibrous Composites", J. AIAA (Am Inst Aeron Astronaut) **2** (1964) 1985–91.

47- H. Schuerch. “Prediction of Compressive Strength in Uniaxial Boron Fiber-Metal Matrix Composite Materials”. J. AIAA (Am Inst Aeron Astronaut) **4** (1) (1966) 102–6.

48- B. Budiansky, “Micromechanics”, J. Computers and Structures **16** (1) (1983) 3–12.

49- R. R. Effendi, J. -J. Barrau, D. Guedra-Degeorges, “Failure Mechanism Analysis Under Compression Loading of Unidirectional Carbon/Epoxy Composites Using Micromechanical Modelling”, J. Composite Structures **31**(2) (1995) 87–98.

50- P.M. Jelf, N.A.Fleck," Compression Failure Mechanisms In Unidirectional Composites", J. Composite Materials, Vol.**26** (18) (1992) 2706-2726.

51- S. Kyriakides, A. E. Ruff, “Aspects of The Failure and Postfailure Of Fiber Composites in Compression”, J. Composite Materials **31** (20) (1997) 2000–2037.

52- S. Y. Hsu, T. J. Vogler, S. Kyriakides, “Compressive Strength Predictions for Fiber Composites”, J. Applied Mechanics **65** (1998) 7–16.

53- S. Pimenta, R. Gutkin, S. T. Pinho, P. Robinson, "A Micromechanical Model for Kink-Band Formation: Part I- Experimental Study and Numerical Modeling", J. Composites Science and Technology **69** (7-8) (2009) 948–955.

54- N.K. Kar, Y. Hu, E. Barjasteh, and S.R. Nutt, “Tension–Tension Fatigue of Hybrid Composite Rods”, J. Composites: Part B **43** (5) (2012) 2115-2124.

55- T.A. Collings, “Transverse Compressive Behaviour of Unidirectional Carbon Fibre Reinforced Plastics", J. Composites **5** (3) (1974) 108-116.

56- I. M. Daniel, J.-J. Luo, P.M. Schubel, B.T. Werner, “Interfiber/Interlaminar Failure of Composites Under Multi-Axial States of Stress”, J. Composites Science and Technology, **69** (2009) 764-771.

57- S. Y. Hsu, T. J. Vogler, and S. Kyriakides, “Inelastic Behavior of An AS4/PEEK Composite Under Combined Transverse Compression and Shear. Pt. II. Modeling”, Int. J. Plasticity **15** (1999) 807–836.

58- Y.K. Huang, P.H. Frings, and E. Hennes, “Mechanical Properties of Zylon/Epoxy Composite", J. Composites: Part B **33** (2002) 109-115.

59- B. Fiedler, M. Hojo, S. Ochiai, K. Schulte, and M. Ando, “Failure Behavior of An Epoxy Matrix Under Different Kinds of Static Loading", J. Composites Science and Technology **61** (2001) 1615-1624.

60- R. Quinson, J. Perez, M. Rink, and A. Pavan, “Yield Criteria for Amorphous Glassy Polymers”, J. Materials Science **32** (1997) 1371–1379.

61- A. F. Yee, J. Du and M. D. Thouless, "Toughening of Epoxies", Ch. 26, 225-267 in Polymer Blends - Volume **2**: Performance, John Wiley & Sons (2000).

62- H.W. Zhou, H.Y. Yi, L.L. Gui, G.M. Dai, R.D. Peng, H.W. Wang, Leon Mishnaevsky Jr., “Compressive Damage Mechanism of GFRP Composites Under Off-Axis Loading: Experimental and Numerical Investigations”, J. Composites: Part B **55** (2013) 119–127.

63- V. Romanov, S. V. Lomov, Y. Swolfs, S. Orlova, L. Gorbatikh, I. Verpoest, "Statistical Analysis of Real and Simulated Fibre Arrangements in Unidirectional Composites", J. Composites Science and Technology **87** (2013) 126–134.

64- E.K. Gamstedt, B.A. Sjögren, “Micromechanisms In Tension-Compression Fatigue of Composite Laminates Containing Transverse Plies”, J. Composites Science and Technology, **59** (1999) 167-178.

65- I. M. Daniel, G. Anastassopoulos, J.-W. Lee, “Experimental Micro- Mechanics of Brittle-Matrix Composites”. ASME Winter Annual Meeting, AMD **102** (1989) 133-46.

66- R. Pyrz. “Quantitative Description of The Microstructure of Composites. Part I: Morphology of Unidirectional Composite Systems”, J. Composites Science and Technology **50** (1994) 197-208.

67- R. Pyrz, "Interpretation of Disorder and Fractal Dimensions in Transversely Loaded Unidirectional Composites", J. Polymers and Polymer Composites **1**(4) (1993) 283-95.

68- I. M. Daniel, G. Anastassopoulos, "Failure Mechanisms and Damage Evolution in Crossply Ceramic-Matrix Composites", Int J. Solids and Structures **32** (1995) 341-55.

69- J. Koyanagi, S. Yoneyama, A. Nemoto, J. D. D. Melo, “Time and Temperature Dependence of Carbon/Epoxy Interface Strength”, J. Composites Science and Technology **70** (2010) 1395–1400.

70- T. Hobbiebrunken, M. Hojo, T. Adachi, C. De Jong, B. Fiedler, “Evaluation of Interfacial Strength In CF/Epoxies Using FEM and In-Situ Experiments”, J. Composites: Part A **37** (2006) 2248–2256.

71- A. Plumtree, L. Shi. “Fatigue Damage Evolution in Off-Axis Unidirectional CFR”, Int J. Fatigue **24** (2002) 155–159.

72- E. K. Gamstedt, O. Redon, P. Brøndsted, “Fatigue Dissipation and Failure in Unidirectional and Angle-Ply Glass Fibre/Carbon Fibre Hybrid Laminates”, Key Engineering Materials **221** (2002) 213-220.

73- R. Talreja, “Assessment of The Fundamentals of Failure Theories for Composite Materials,” J. Composites Science and Technology **105** (2014) 190–201.

74- L. E. Asp, L. A. Berglund, R. Talreja, “Prediction of Matrix-Initiated Transverse Failure in Polymer Composites”, J. Composites Science and Technology **56** (1996) 1089-1097.

75- L. E. Asp, L. A. Berglund, “Effects of a Composite-Like Stress State on the Fracture of Epoxies”, J. Composites Science and Technology **53** (1995) 27-37.

76- L. E. Asp, L. A. Berglund, R. Talreja, “A Criterion for Crack Initiation in Glassy Polymers Subjected to a Composite-Like Stress State”, J. Composites Science and Technology **56** (1996) 1291-1301.

77- M. I. Naji, S. V. Hoa “Curing of Thick Angle-Bend Thermoset Composite Part: Curing Process Modification for Uniform Thickness and Uniform Fiber Volume Fraction Distribution”, J. Reinforced Plastics and Composites **18** (8) (1999) 702-723.

78- S. V. Hoa, *Principles of The Manufacturing of Composite Materials*. Lancaster, PA 17601: DEStech Publications, Inc (2009).

79- C. González, J.J. Vilatela, J.M. Molina-Aldareguía, C.S. Lopes, J. LLorca, “Structural Composites for Multifunctional Applications: Current Challenges and Future Trends”, Progress in Materials Science **89** (2017) 194–251

80- C. D. Mangin, A.C. Rudd, K. N. Long, K. CGE. *Liquid moulding technologies*. Woodhead Publishing (1997).

81- S. Advani, K. -T. Hsiao, "Manufacturing Techniques for Polymer Matrix Composites (PMCs)". Woodhead Publishing Series in Composites Science and Engineering; (2012)

82- J. Frketic, T. Dickens, S. Ramakrishnan, “Automated Manufacturing and Processing of Fiber-Reinforced Polymer (FRP) Composites: An Additive Review of Contemporary and Modern Techniques for Advanced Materials Manufacturing”, J. Additive Manufacturing **14** (2017) 69-86.

83- M. Perner, S.Algermissen, R. Keimer, H. P. Monner, “Avoiding Defects In Manufacturing Processes: A Review For Automated CFRP Production”, J. Robotics and Computer-Integrated Manufacturing **38** (2016) 82-92.

84- B.N. Fedulov, F.K. Antonov, A.A. Safonov, A.E. Ushakov, S.V. Lomow, “Influence of Fibre Misalignment and Voids on Composite Laminate Strength”, J. Composite Materials **49** (23) (2015) 2887-2896.

85- Y. K. Hamidi, M. C. Altan, “Spatial Variation of Void Morphology in Resin Transfer Molded E-Glass Epoxy Composites”, J. Materials Science Letters **22** (2003) 1813-1816.

86- Y. K. Hamidi, L. Aktas, M. C. Altan, “Formation of Microscopic Voids in Resin Transfer Molded Composites”, J. Engineering Materials and Technology **126** (2004) 420-426.

87- R.D.Adams, P.Cawley, “A Review Of Defect Types And Nondestructive Testing Techniques For Composites And Bonded Joints”, J. NDT International **21**(4) (August 1988) 208-222.

88- M. P. F. Sutcliffe, S. L. Lemanski, A. E. Scott, “Measurement of Fibre Waviness in Industrial Composite Components”, J. Composites Science and Technology **72** (16) (2012) 2016-2023.

89- K. Mizukami, Y. Mizutani, Ke. Kimura, A. Sato, A. Todoroki, Y. Suzuki, “Detection of In-Plane Fiber Waviness in Cross-Ply CFRP Laminates Using Layer Selectable Eddy Current Method”, J. Composites Part A: Applied Science and Manufacturing **82** (2016) 108-118.

90- A. A. Gusev, P. J. Hine, I. M. Ward, “Fiber Packing and Elastic Properties of a Transversely Random Unidirectional Glass/Epoxy Composite”, J. Composites Science and Technology **60** (2000) 535-541.

91- N. Patel, L. L. James., “Effects of Fiber Mat Architecture on Void Formation and Removal in Liquid Composite Molding”, J. Polymer Composites **16** (1995) 386–99.

92- P. A. Carraro, L. Maragoni, M. Quaresimin, “Influence of Manufacturing Induced Defects on Damage Initiation and Propagation in Carbon/Epoxy NCF Laminates”, J. Advanced Manufactring: Polymers and Composites Science **1** (2015) 44-53.

93- M. Hojo, M. Mizuno, T. Hobbiebrunken, T. Adachi, M. Tanaka, S. K. Ha, “Effect of Fiber Array Irregularities on Microscopic Interfacial Normal Stress States of Transversely Loaded UD-CFRP from Viewpoint of Failure Initiation”, J. Composites Science and Technology **69** (2009) 1726–1734.

94- N. Vejen, R. Pyrz, “Transverse Crack Growth in Glass/Epoxy Composites with Extractly Positioned Long Fibres, part I: Experimental”, J. Composites Part B: Engineering **32** (7) (2001) 557-564.

95- B.F. Sørensen, R. Talreja, “Effects of Nonuniformity Of Fiber Distribution on Thermally-Induced Residual Stresses and Cracking in Ceramic Matrix Composites”, J. Mechanics of Materials **16** (1993) 351-363.

96- M. P. I. M Eijpe, P. C Powell, “Determination of Residual Shear Stresses in Composites by A Modified Layer-Removal Method”, J. Materials Science **33** (8) (1998) 2019–2026.

97- J. P. Favre, “Residual Thermal Stresses in Fibre Reinforced Composite Materials—A Review”, J. The Mechanical Behavior of Materials **1**(1–4) (1988) 37–53.

98- L.G. Zhao, N.A. Warrior, A.C. Long, “A Micromechanical Study of Residual Stress and Its Effect on Transverse Failure in Polymer–Matrix Composites”, Int. J. Solids and Structures **43** (2006) 5449–5467.

99- L. Yang, Y. Yan, J. Ma, B. Liu, “Effects of Inter-Fiber Spacing and Thermal Residual Stress on Transverse Failure of Fiber-Reinforced Polymer–Matrix Composites”, J. Computational Materials Science **68** (2013) 255–262.

100- P.P. Parlevliet, H.E.N. Bersee, A. Beukers, “Residual Stresses in Thermoplastic Composites – A Study of The Literature. Part III: Effects of Thermal Residual Stresses”, J. Composites Part A: Appl. Sci. Manuf. **38** (2007) 1581–1596.

101- Z. H. Zhu, S. Gong’ “Thermal Stresses in Fiber Reinforced Composites”, the 19th international conference on composite materials (1993).

102- J. Li1, X.Y. Liu, X. Yao, Y. Yuan, “A Micromechanical Debonding Analysis of Fiber-Reinforced Composites Due to Curing Residual Stress”, J. Reinforced Plastics and Composites **34** (12) (2015) 962–971.

103- H. E. Gascoigne, “Residual Surface Stress in Laminated Cross-Ply Fibre-Epoxy Composite Materials”, J. Experimental Mechanics **34** (1994) 27–36.

104- N. J. Rendler, I. Vigness, “Hole-Drilling Strain Gauge Method of Measuring Residual Stress”, J. Experimental Mechanics **6** (1966) 577–586.

105- P. J. Withers, H. Bhadeshia, “Residual stress. Part1 – Measurement techniques”, J. Materials Science and Technology **17** (4) (2001) 355-365.

106- G.S. Schajer, “Measurement of Non-Uniform Residual Stresses Using the Hole-Drilling Method. Part I—Stress Calculation Procedures”, J. Engineering Materials and Technology **110** (1988) 338–343.

107- R. Y. Kim, H. T. Hahn, “Effect of Curing Stress on The First Ply-Failure in Composite Laminates”, J. Composite Materials **13** (1979) 2–16.

108- H. Dannenberg, “Determination of Stresses in Cured Epoxy Resins”, SPE J. **21** (77) (1965) 669–675.

109- O. Kesler, J. Matejicek, S. Sampath, S. Suresh, T. Gnaeupel-Herold, P. C. Brand, H. J. Prask, “Measurement of Residual Stress in Plasma-Sprayed Metallic, Ceramic and Composite Coatings”, J. Materials Science and Engineering A **257** (1998) 215–224.

110- B. Benedikt, M. Kumosa, P. K Predecki, L. Kumosa, M. G. Castelli, J. K. Sutter, “An Analysis of Residual Thermal Stress in A Unidirectional Graphite/PMR-15 Composite Based on X-Ray Diffraction Measurements”, J. Composites Science and Technology **61** (2001) 1977–1994.

110- J. Watts, G. Hilmas, W. G. Fahrenholtz, D. Brown, B. Clausen, “Stress Measurements in Zrb2–Sic Composites Using Raman Spectroscopy and Neutron Diffraction”, J. The European Ceramic Society **30** (2010) 2165–2171.

112- K. Grodecki, A. Wysmolek, R. Stepniewski, J. M. Baranowski, W. Hofman, E. Tymicki, K. Grasza, “Raman Piezospectroscopy Of Phonons in Bulk 6H–Sic”, J. Acta Physica Polonic A **116** (2009) 947–949.

113- D. Ghosh, G. Subhash, N. Orlovskaya, “Measurement of Scratch-Induced Residual Stress Within Sic Grains in Zrb2–Sic Composite Using Micro- Raman Spectroscopy”, J. Acta Mater. **56** (2008) 5345–5354.

114- N. Fist, J. Dinan, R. Stadelmann, N. Orlovskaya, “In Situ Three Point Bending Device for Measurements of Vibrational Response of Ceramics Under Stress by Micro Raman Spectroscopy”, Advances in Applied Ceramics, **111** (2012) 433–439.

115- O. G. Kravchenko, C. Li, A. Strachan, S. G. Kravchenko, R. B. Pipes, “Prediction of The Chemical and Thermal Shrinkage in A Thermoset Polymer”, J. Composites Part A: Applied Science and Manufacturing **66 (**2014) 35-43.

116- C. Li, A. Strachan, “Molecular Simulations of Crosslinking Process of Thermosetting Polymers”, J. Polymer **51** (25) (2010) 6058-6070.

117- O. G. Kravchenko, S. G. Kravchenko, R. B. Pipes, “Cure History Dependence of Residual Deformation an A Thermosetting Laminate”, J. Composites Part A: Applied Science and Manufacturing **99** (2017) 186-197.

118- A. J. Fletcher, J. L. Oakeshott, “Thermal Residual Microstress Generation during the Processing of Unidirectional Carbon Fibre/Epoxy Resin Composites: Random Fibre Arrays”, J. Composites **25** (8) (1994) 806–813.

119- T. Nakamura, S. Suresh, “Effects of Thermal Residual Stresses and Fiber Packing on Deformation of Metal-Matrix Composites”, J. Acta Metall. Mater. **41** (6) (1993) 1665–1681.

120- V. N. Bulsara, R. Talreja, J. Qu, “Damage Initiation under Transverse Loading of Unidirectional Composites with Arbitrarily Distributed Fibers”, J. Composites Science and Technology **59** (1999) 673-682.

121- K. K. Jin, J. H. Oh, S. K. Ha, “Effect of Fiber Arrangement on Residual Thermal Stress Distributions in a Unidirectional Composite”, J. Composite Materials **41** (5) (2007) 591-611.

122- M. Hojo, M. Mizuno, T. Hobbiebrunken, T. Adachi, M. Tanaka & S. K. Ha, “Geometrical Range of Microscopic Stress Distribution Change Due to Fibre Array

Irregularities for Thermally and Transversely Loaded CF/Epoxy Composites", J. Plastics, Rubber and Composites Macromolecular Engineering **39** (2) (2013) 99-106.

123- S. L. Agius, M. Joosten, B. Trippit, C. H. Wang, T.Hilditch, "Rapidly Cured Epoxy/Anhydride Composites: Effect of Residual Stress on Laminate Shear Strength", J. Composites Part A: Applied Science and Manufacturing **90** (2016) 125-136.

124- A. S. Nielsen, R. Pyrz, "The Effect of Cooling Rate on Thermal Residual Strains in Carbon/Polypropylene Microcomposites", J. Science and Engineering of Composite Materials **7** (1–2) (1998) 1–22.

125- W. J. Unger, J. S. Hansen, "The Effect of Cooling Rate and Annealing on Residual Stress Development in Graphite Fibre Reinforced PEEK Laminates", J. Composite Materials **29** (1993) 108–37.

126- M. J. Hinton, A. S. Kaddour, P. D. Soden, *Failure Criteria in Fibre Reinforced Polymer Composites: The World-Wide Failure Exercise*, Elsevier, Oxford (2004).

127- M. J. Hinton, A. S. Kaddour, P. D. Soden, "A Comparison of The Predictive Capabilities of Current Failure Theories for Composite Laminates, Judged Against Experimental Evidence", J. Composites Science and Technology **62**(12–13) (2002) 1725–1797.

128- I. M. Daniel, "Failure of Composite Materials", J. Strain **43** (1) (2007) 4–12.

129- U. Icardi, S. Locatto, G. Student, A. Longo, "Assessment of Recent Theories for Predicting Failure of Composite Laminates", J. Applied Mechanics Reviews **60** (2) (2007) 76–86.

130- T. E. Tay, G. Liu, V. B. C. Tan, X. S. Sun, D. C. Pham, "Progressive Failure Analysis of Composites", J. Composite Materials **42** (18) (2008) 1921 - 1966.

131- C. T. Herakovich, *Mechanics of Fibrous Composite*, John Wiley & Sons, Inc., New York (1998).

132- S.W. Tsai. Strength theories of filamentary structures. In R.T. Schwartz and H.S. Schwartz, editors, *Fundamental Aspects of Fiber Reinforced Plastic Composites*, 3–11. Wiley International (1968).

133- S. W. Tsai, E. M. Wu, " A General Theory of Strength for Anisotropic Materials", J. Composite Materials **5** (1) (1971) 58–80.

134- O. Hoffman, "The Brittle Strength of Orthotropic Materials", J. Composite Materials **1** (1967) 200–6.

135- Z. Hashin, "Failure Criteria for Unidirectional Fiber Composites", J. Applied Mechanics **47** (1980) 329–334.

136- C. G. Davila, P. P. Camanho, C. A. Rose, "Failure Criteria for FRP Laminates", J. Composite Materials **39** (4) (2005) 323-345.

137- A. Puck, H. Schürmann, "Failure Analysis of FRP Laminates by Means of Physically Based Phenomenological Models", J. Composites Science and Technology **58** (1998) 1045–67.

138- R. M. Christensen, "Stress Based Yield/Failure Criteria for Fiber Composites", Int J. Solids and Structures **34** (5) (1997) 529-543.

139- K. Rohwer, "Models for Intralaminar Damage and Failure of Fiber Composites - A Review", Facta Universitatis, Mechanical Engineering **14** (1) (2016) 1 - 19.

140- Z. H. Stachurski, "Deformation Mechanisms and Yield Strength in Amorphous Polymers", J. Progress in Polymer Science **22** (1997) 407-474.

141- I. Yarovsky, E. Evans, “Computer Simulation of Structure and Properties of Crosslinked Polymers: Application to Epoxy Resins”, J. Polymer **43** (3) (2002) 963–9.

142- C. Wu, W. Xu, “Atomistic Molecular Modelling of Crosslinked Epoxy Resin”, J. Polymer **47** (16) (2006) 6004–9.

143- H. B. Fan, M. M. Yuen, “Material Properties of The Cross-Linked Epoxy Resin Compound Predicted by Molecular Dynamics Simulation”, J. Polymer **48** (7) (2007) 2174–8.

144- V. Varshney, S. S. Patnaik, A. K. Roy, B. L. Farmer, “A Molecular Dynamics Study of Epoxy-Based Networks: Cross-Linking Procedure and Prediction of Molecular and Material Properties”, J. Macromolecules **41** (18) (2008) 6837–42.

145- A. Bandyopadhyay, P.K. Valavala, T. C. Clancy, K. E. Wise, G. M. Odegard, “Molecular Modeling of Crosslinked Epoxy Polymers: The Effect of Crosslink Density on Thermomechanical Properties”, J. Polymer **52** (11) (2011) 2445–52.

146- C. Li, A. Strachan., “Molecular Dynamics Predictions of Thermal and Mechanical Properties of Thermoset Polymer epon862/detda”, J. Polymer **52** (13) (2011) 2920–8.

147- S. Yang, J. Qu, “Computing Thermomechanical Properties of Crosslinked Epoxy by Molecular Dynamic Simulations”, J. Polymer **53** (21) (2012) 4806–17.

148- C. Li, G. A. Medvedev, E.-W. Lee, J. Kim, J. M. Caruthers, A. Strachan, “Molecular Dynamics Simulations and Experimental Studies of The Thermomechanical Response of An Epoxy Thermoset Polymer”, J. Polymer **53** (19) (2012) 4222–30.

149- G. M. Odegard, B. D. Jensen, S. Gowtham, J. Wu, J. He, Z. Zhang., "Predicting Mechanical Response of Crosslinked Epoxy Using Reaxff", J. Chemical Physics Letters **591** (2014) 175–8.

150- S. Masoumi, B. Arab, H. Valipour., "A Study of Thermo-Mechanical Properties of The Cross-Linked Epoxy: An Atomistic Simulation", J. Polymer **70** (2015) 351–60.

151- Y. Fu, J. G. Michopoulos, J-H. Song, "On Investigating the Thermomechanical Properties of Cross-Linked Epoxy Via Molecular Dynamics Analysis", J. Nanoscale and Microscale Thermophysical Engineering **21**(1) (2017) 8–25.

152- A. Neogi, N. Mitra, R. Talreja, "Cavitation in Epoxies Under Composite-Like Stress States", J. Composites: Part A **106** (2018) 52–58.

153- C. T. Sun, R. S. Vaidya, "Prediction of Composite Properties from A Representative Volume Element", J. Composites Science and Technology **56** (1996) 171-17.

154- T. Zhang, Y. Yan, "A Comparison Between Random Model and Periodic Model for Fiber-Reinforced Composites Based on a New Method for Generating Fiber Distributions", J. Polymer Composites **38** (2017) 77-86

155- D. Trias, J. Costa, J.A. Mayugo, J.E. Hurtado, "Random Models Versus Periodic Models for Fibre Reinforced Composites", J. Computational Materials Science **38** (2006) 316–324.

156- D. Beicha, T. Kanit, Y. Brunet, A. Imad, A. El Moumen, Y. Khelfaoui, "Effective Transverse Elastic Properties of Unidirectional Fiber Reinforced Composites", J. Mechanics of Materials **102** (2016) 47–53.

157- L. Bouaoune, Y. Brunet, A. El Moumen, T. Kanit, H. Mazouz, "Random Versus Periodic Microstructures for Elasticity of Fibers Reinforced Composites", J. Composites Part B **103** (2016) 68-73.

158- R. Hill, “Elastic Properties of Reinforced Solids: Some Theoretical Principles”, J. The Mechanics and Physics of Solids **11** (1963) 357-372.

159- W.J. Drugan and J.R. Willis, “A Micromechanics-Based Nonlocal Constitutive Equation and Estimates of Representative Volume Element Sizefor Elastic Composites”, J. The Mechanics and Physics of Solids **44** (4) (1996) 497–524.

160- E. Totry, C. González, J. LLorca, “Failure Locus of Fiber-Reinforced Composites under Transverse Compression and Out-Of-Plane Shear”, J. Composites Science and Technology **68** (2008) 829–839.

161- D. Trias, J. Costa, A. Turon, J.E. Hurtado, “Determination of the Critical Size of a Statistical Representative Volume Element (SRVE) for Carbon Reinforced Polymers”, J. Acta Materialia **54** (2006) 3471–3484.

162- T.J. Vaughan, C.T. McCarthy, “A Combined Experimental–Numerical Approach for Generating Statistically Equivalent Fibre Distributions for High Strength Laminated Composite Materials”, J. Composites Science and Technology **70** (2010) 291–297.

163- A.R. Melro, P.P. Camanho, S.T. Pinho, “Generation of Random Distribution of Fibres in Long-Fibre Reinforced Composites”, J. Composites Science and Technology **68** (2008) 2092–2102.

164- L. Riaño, L. Belec, Y. Joliff, “Validation of a Representative Volume Element for Unidirectional Fiber Reinforced Composites: Case of a Monotonic Traction in its Cross Section”, J. Composite Structures **154** (2016) 11–16.

165- D. Sawas, G. Stefanou, M. Papadrakakis, “Determination of RVE Size for Random Composites with Local Volume Fraction Variation”, J. Computer Methods in Applied Mechanics and Engineering **305** (2016) 340–358.

166- Y. Ismail, D. Yang, J. Ye, “Discrete Element Method for Generating Random Fibre Distributions in Micromechanical Models of Fibre Reinforced Composite Laminates”, J. Composites Part B **90** (2016) 485-492.

167- Y. Ismail, Y. Sheng, D. Yang, J. Ye, “Discrete Element Modelling of Unidirectional Fibre-Reinforced Polymers under Transverse Tension”, J. Composites: Part B **73** (2015) 118–125.

168- L. Yang, Y. Yan, Z. Ran, Y. Liu, “A New Method for Generating Random Fibre Distributions for Fibre Reinforced Composites”, J. Composites Science and Technology **76** (2013) 14–20.

169- R. Pyrz, “Correlation of Microstructure Variability and Local Stress Field in Two-Phase Materials”, J. Materials Science and Engineering, A **177** (1994) 253-259.

170- B. Widom, “Random sequential addition of hard sphere to a volume”. J Chemical Physics **44** (10) (1965) 3888–94.

171- A. Wongsto, S. Li, “Micromechanical FE Analysis of UD Fibre-Reinforced Composites with Fibres Distributed at Random Over the Transverse Cross-Section”, J. Composites: Part A **36** (2005) 1246–1266.

172- M.V. Pathan, V.L. Tagarielli, S. Patsias, P.M. Baiz-Villafranca, “A New Algorithm to Generate Representative Volume Elements of Composites with Cylindrical or Spherical Fillers”, J. Composites Part B **110** (2017) 267-278.

173- B. D. Ripley, “Modelling Spatial Patterns”, J. Royal Statistical Society. Series B **39** (2) (1977) 172-212.

174- T. Matsuda, N. Ohno, H. Tanaka, and T. Shimizu, “Effects of Fibre Distribution on Elastic-Viscoplastic Behaviour of Long Fibre-Reinforced Laminates”. Int J. Mechanical Sciences, **45** (10) (2003)1583–1598.

175- T. Matsuda, N. Ohno, H. Tanaka, T. Shimizu. “Homogenized In-Plane Elastic-Viscoplastic Behavior of Long Fibre-Reinforced Laminates”. JSME Int J., Series A, **45** (4) (2002) 538–544.

176- Z. Shan, A. M. Gokhale, “Representative Volume Element for Non-Uniform Micro-Structure”, J. Computational Materials Science **24** (2002) 361–379.

177- E. Totry, C. González, J. LLorca, “Influence of The Loading Path on the Strength of Fiber-Reinforced Composites Subjected to Transverse Compression and Shear”, Int J. Solids and Structures **45** (2008) 1663–1675.

178- W. R. McLendon, J. D. Whitcomb, “Influence of Thermally Induced Microstress and Microstructural Randomness on Transverse Strength of Unidirectional Composites”, J. Composite Materials **50** (11) (2016) 1467–1481.

179- Z. Xia, Y. Zhang, F. Ellyin, “A Unified Periodical Boundary Conditions for Representative Volume Elements of Composites and Applications”, Int J. Solids and Structures **40** (2003) 1907–1921.

180- F. Naya, C. González, C.S. Lopes, S. Van der Veen, F. Pons, “Computational Micromechanics of the Transverse and Shear Behavior of Unidirectional Fiber Reinforced Polymers Including Environmental Effects”, J. Composites: Part A **92** (2017) 146–157.

181- T.J. Vaughan, C.T. McCarthy, “Micromechanical Modelling of the Transverse Damage Behaviour in Fibre Reinforced Composites”, J. Composites Science and Technology **71** (2011) 388–396.

182- K. Tanaka, K. Minoshima, W. Grela, K. Komai, “Characterization of The Aramid/Epoxy Interfacial Properties by Means of Pull-Out Test and Influence of Water Absorption”, J. Composites Science and Technology **62** (2002) 2169–77.

183- T. Ramanathan, A. Bismarck, E, Schulz, K. Subramanian. “Investigation of The Influence of Acidic and Basic Surface Groups on Carbon Fibres On the Interfacial Shear Strength In An Epoxy Matrix By Means Of Single-Fibre Pull Out Test", J. Composites Science and Technology **61** (2001) 599–605.

184- X-F. Zhou, H. D. Wagner, S. R. Nutt, “Interfacial Properties of Polymer Composites Measured by Push-Out and Fragmentation Test”, J. Composite A **32** (2001) 1543–51.

185- F. Hoecker, J. Karger-Kocsis, “Effects of The Interface on The Mechanical Response Of CF/EP Microcomposites And Macrocomposites”, J. Composites **25** (7) (1994) 729–38.

186- H. Ho, L. T. Drzal, “Evaluation of Interfacial Mechanical Properties of Fiber Reinforced Composites Using the Microindentation Method", J. Composite A **27** (1996) 961–71.

187- S. F. Zhandarov, E. V. Pisanova. “The Local Bond Strength and Its Determination by Fragmentation and Pull-Out Tests”, J. Composites Science and Technology **57** (1997) 957–64.

188- M. J. Pitkethly, J. P. Favre, U.Gaur, J. Jakubowski, S. F. Mudrich, D .L. Caldwell, L. T. Drzal, M. Nardin, H. D. Wagner, L. Di Landro, A. Hampe, J. P. Armistead, M.

Desaeger, I. Verpoest “A Round-Robin Programme On Interfacial Test Methods”, J. Composites Science and Technology **48** (1993) 205–14.

189- M. Hojo, K. Terashima, Y.Igarashi, M. Shida, O. Shojiro, T. Inoue, Y. Sawada, Y. Suzuki, “Interfacial Fracture In Model Composites Under Static And Fatigue Loadings—Mechanism Consideration Based On Experimental And Analytical Approaches”, Materials science research international **2.** Special Technical Publication (2001) 189–96.

190- S. Zhandarov, Edith Mäder, “Characterization of Fiber/Matrix Interface Strength: Applicability of Different Tests, Approaches and Parameters”, J. Composites Science and Technology **65** (1) (2005) 149-160.

191- J. M. Molina-Aldareguía, M. Rodríguez, C. González, J. LLorca. “An Experimental and Numerical Study of The Influence of Local Effects on The Application of The Fibre Push-In Tests,” J. Philosophical Magazine **91** (7-9) (2011) 1293-1307.

192- J. N. Sultan, F. J. McGarry, “Effect of Rubber Particle Size on Deformation Mechanisms in Glassy Epoxy,” J. Polymer Engineering and Science **13** (1) (1973) 29-34.

193- R. S. Kody, A. J. Lesser, “Deformation and Yield of Epoxy Networks in Constrained States of Stress,” J. Materials Science **32** (1997) 5637-5643.

194- V. N. Bulsara, PhD thesis, Effects of Fiber Spatial Distribution and Interphase on Transverse Damage in Fiber-Reinforced Ceramic Matrix Composites, (1998), Georgia Institute of Technology, Atlanta, Georgia.

195- J. Segurado, J. Llorca, “A Numerical Approximation to The Elastic Properties of Sphere-Reinforced Composites” J. the Mechanics and Physics of Solid **50** (2002) 2107 – 2121.

196- ABAQUS (2014) `ABAQUS Documentation', Dassault Systèmes, Providence, RI, USA.

197- M.C. Lafarie-Frenot, C. H_enaff-Gardin, “Formation and Growth Of 90_ Ply Fatigue Cracks in Carbon/Epoxy Laminates”, J. Composites Science and Technology **40** (1991) 307-324.

198- J. Tong, F.J. Guild, S.L. Ogin, P.A. Smith, “Off-Axis Fatigue Crack Growth and The Associated Energy Release Rate in Composite Laminates”, J. Applied Composite Materials **4** (1997) 349-359

199- J. Tong, “Three Stages of Fatigue Crack Growth in GFRP Composite Laminates”, J. Engineering Materials and Technology (ASME) **123** (2001) 139-143.

200- J. Tong, “Characteristics of Fatigue Crack Growth in GFRP Laminates”, Int. J. Fatigue **24** (2002) 291-297.

201- A.W. Wharmby, F. Ellyin, “Damage Growth in Constrained Angle-Ply Laminates Under Cyclic Loading”, J. Composites Science and Technology **62** (2002) 1239-1247.

202- T. Yokozeki, T. Aoki, T. Ishikawa, “Fatigue Growth of Matrix Cracks in The Transverse Direction of CFRP Laminates”, J. Composites Science and Technology **62** (2002) 1223-1229.

203- M. Quaresimin, P.A. Carraro, L. Pilgaard Mikkelsen, N. Lucato, L. Vivian, P. Brøndsted, B.F. Sørensen, J. Varna, R. Talreja, “Reprint Of: Damage Evolution Under

Internal and External Multiaxial Cyclic Stress State: A Comparative Analysis", J. Composites Part B Engineering **61** (2014) 282-290

204- S. Adden, P. Horst, "Damage Propagation in Non-Crimp Fabrics Under Bi-Axial Static and Fatigue Loading", J. Composites Science and Technology **66** (2006) 626-633.

205- S. Adden, P. Horst, "Stiffness Degradation Under Fatigue in Multiaxially Loaded Non-Crimped-Fabrics", Int. J. Fatigue **32** (2010) 108-122.

206- J. Zhang, K. P. Herrmann, "Stiffness Degradation Induced by Multilayer Intralaminar Cracking in Composite Laminates", J. Composites Part A **30** (1999) 683–706.

207- M. Kashtalyan, C. Soutis, "Stiffness Degradation in Cross-Ply Laminates Damaged by Transverse Cracking and Splitting", J. Composites Part A **31** (2000) 335–51.

208- P. Lundmark, J. Varna, "Constitutive Relationships for Laminates with Ply Cracks in In-Plane Loading". Int J. Damage Mechanics **14** (3) (2005) 235–59.

209- C. V. Singh, R. Talreja, "Analysis of Multiple Off-Axis Ply Cracks in Composite Laminates". Int J Solids Struct **45** (16) (2008) 4574–89.

210- P. A. Carraro, M. Quaresimin, "A Stiffness Degradation Model for Cracked Multidirectional Laminates with Cracks in Multiple Layers". Int J Solids Struct **58** (2015) 34–51.

211- A.S. Chen and F.L. Matthews, "A Review of Multiaxial/Biaxial Loading Tests for Composite Materials", Composites **24** (1993) 395-406.

212- M. Quaresimin, L. Susmel, R. Talreja, "Fatigue Behaviour and Life Assessment of Composite Laminates Under Multiaxial Loadings", Int J. Fatigue **32** (2010) 2–16.

213- S. S.Wang, E.S.-M. Chim, D. F. Socie, "Biaxial Fatigue of Fiber-Reinforced Composites at Cryogenic Temperatures. Part I: Fatigue Fracture Life and Mechanisms", Transactions of the ASME **104** (1982) 128-136.

214- P. H. Francis, D. E. Walrath, D. N. Weed, "First Ply Failure of G/E Laminates Under Biaxial Loadings", J. Fibre Science and Technology **12** (2) (1979) 97-110.

215- D. Perreux, E. Joseph, "The Effect of Frequency on the Fatigue Performance of Filament-Wound Pipes Under Biaxial Loading: Experimental Results and Damage Model", J. Composites Science and Technology **57** (1997) 353-364.

216- L. Gemi, A. Akdemir, "Progressive Fatigue Failure Behavior of Glass/Epoxy (±75)2 filament-Wound Pipes Under Pure Internal Pressure", J. Materials and Design **30** (2009) 4293–4298.

217- H. Kawakami, T. J. Fujii, Y. Morita, "Fatigue Degradation and Life Prediction of Glass Fabric Polymer Composite under Tension/Torsion Biaxial Loadings", J. Reinforced Plastics and Composites **15** (2) (1996) 183-195.

218- M. Quaresimin, P. A. Carraro, "On the Investigation of the Biaxial Fatigue Behaviour of Unidirectional Composites", J. Composites: Part B **54** (2013) 200–208.

219- E. W. Smith, K. J. Pascoe, "Biaxial Fatigue of Glass–Fibre Reinforced Composite. Part1: Fatigue and Fracture Behaviour. In: Brown M, Miller KJ, editors. Biaxial and multiaxial fatigue, EGF3. London: Mechanical Engineering Publications; (1989) 367–396.

220- A. Smits, D. V. Hemelrijck, T. P. Philippidis, A. Cardon, "Design of a Cruciform Specimen for Biaxial Testing of fibre Reinforced Composite Laminates", J. Composites Science and Technology **66** (2006) 964–975.

221- I. M. Daniel, “Deformation and Failure of Composite Laminates with Cracks in Biaxial Stress Fields”, Proc Sixth lnt Conf on Experimental Stress Analysis. Munich. West Germany (1978) (VDI-Berichte) No 313.

222- R. Olsson, "A Survey of Test Methods for Multiaxial and Out-of-Plane Strength of Composite Laminates", J. Composites Science and Technology **71** (2011) 773–783.

223- M. M. Shokrieh, L. B. Lessard, "Multiaxial Fatigue Behavior of Unidirectional Plies Based on Uniaxial Fatigue Experiments II. Experimental Evaluation", Int J. Fatigue **19** (3) (1997) 209-217.

224- M. Quaresimin, P. A. Carraro, L. P. Mikkelsen, N. Lucato, L. Vivian, P. Brøndsted, B. F. Sørensen, J. Varna, R. Talreja, " Damage Evolution under Cyclic Multiaxial Stress State: A Comparative Analysis between Glass/Epoxy Laminates and Tubes", J. Composites: Part B **61** (2014) 282–290

225- C. Capela, J. A. M. Ferreira, T. Febra, J. D. Costa, "Fatigue Strength of Tubular Carbon fibre Composites Under Bending/Torsion Loading", Int J. Fatigue **70** (2015) 216–222.

226- M. Quaresimin, P. A. Carraro, "Damage Initiation and Evolution in Glass/Epoxy Tubes Subjected to Combined Tension–Torsion Fatigue Loading", Int J. Fatigue **63** (2014) 25–35.

227- S. Adden, "Characterization of Stiffness Degradation Caused by Fatigue Damage in Textile Composites Using Circumferential Plate Acoustic Waves", J. Composites Science and Technology **68** (2008) 1616–1623.

228- R. Ansari, M. K. Hassanzadeh Aghdam, “Micromechanics-Based Viscoelastic Analysis of Carbon Nanotube-Reinforced Composites Subjected to Uniaxial and Biaxial Loading”, J. Composites Part B: Engineering **90** (1) (2016) 512-522.

229- Y. Ismail, D. Yang, J. Ye, “A DEM Model for Visualising Damage Evolution and Predicting Failure Envelope of Composite Laminae Under Biaxial Loads”, J. Composites Part B: Engineering **102** (1) (2016) 9-28.

230- L.P. Canal, J. Segurado, J. LLorca, “Failure Surface of Epoxy-Modified Fiber-Reinforced Composites Under Transverse Tension and Out-Of-Plane Shear", Int J. Solids and Structures **46** (11) (2009) 2265-2274.

231- D. O’Dwyer, N. O’Dowd, C. McCarthy, “Investigation of Strain Hardening Effects Under In-Plane Shear of Unidirectional Composite Materials”, J. Computational Materials Science **64** (2012) 179-182.

232- E. Totry, J.M. Molina-Aldareguía, C. González, J. LLorca, “Effect of Fiber, Matrix and Interface Properties on The In-Plane Shear Deformation of Carbon-Fiber Reinforced Composites”, J. Composites Science and Technology **70** (6) (2010) 970-980.

233- P. Potluri, V. S. Thammandra., “Influence of Uniaxial and Biaxial Tension on Meso-Scale Geometry and Strain Fields in A Woven Composite”, J. Composite Structures **77** (3) (2007) 405-418.

# APPENDIX A

## NEAREST NEIGHBOR FUNCTIONS FOR DIFFERENT RVE REALIZATIONS

In this appendix, the first, second and third nearest neighbor functions are plotted for different RVE sizes having (16, 100,400 and 484 fibers) with 40% and 60% FVFs and with different degrees of NU (100%, 60% and 30%). The smallest RVEs, containing 16 fibers, show fewer frequency peaks compared to the larger RVE sizes, containing 400 and 484 fibers, for the three nearest functions considered. The large RVE sizes > 400 fibers, show a frequency distribution that is more uniform than smaller ones.

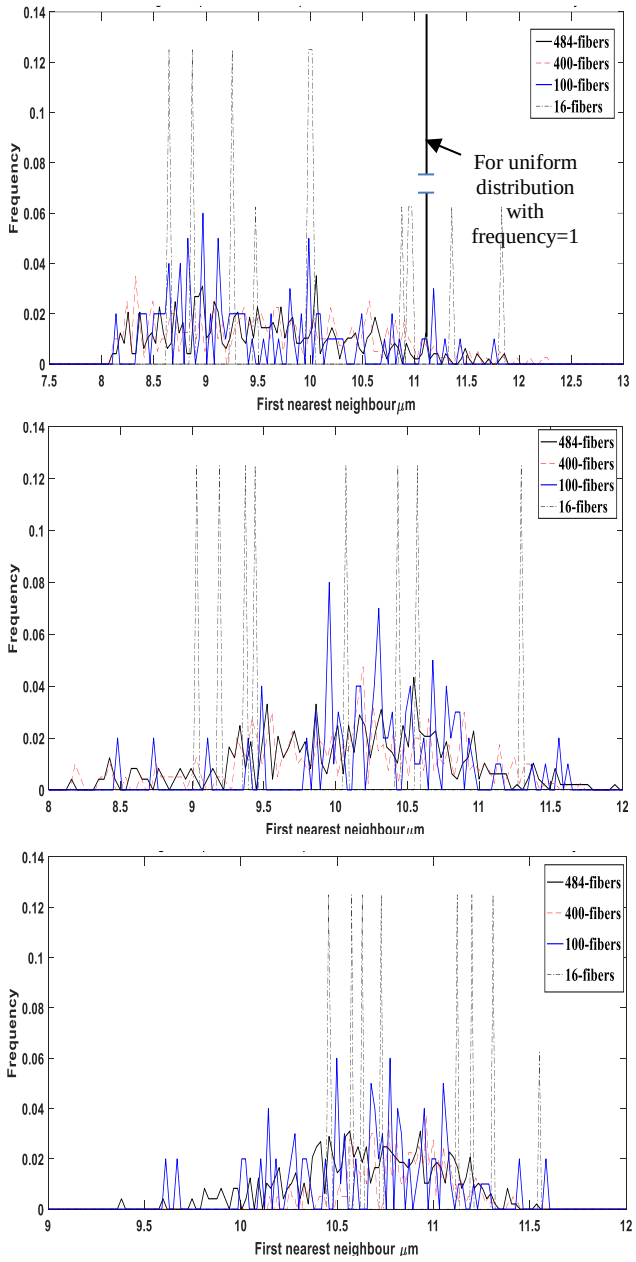


**Figure 109. Frequency of occurrence of the first nearest neighbor distance (from center to center) in µm within the RVE realizations for 40% fiber volume fraction and degrees of NU of (a)100%, (b) 60% and (c) 30% for 484, 400, 100 and 16 fibers in an RVE.**

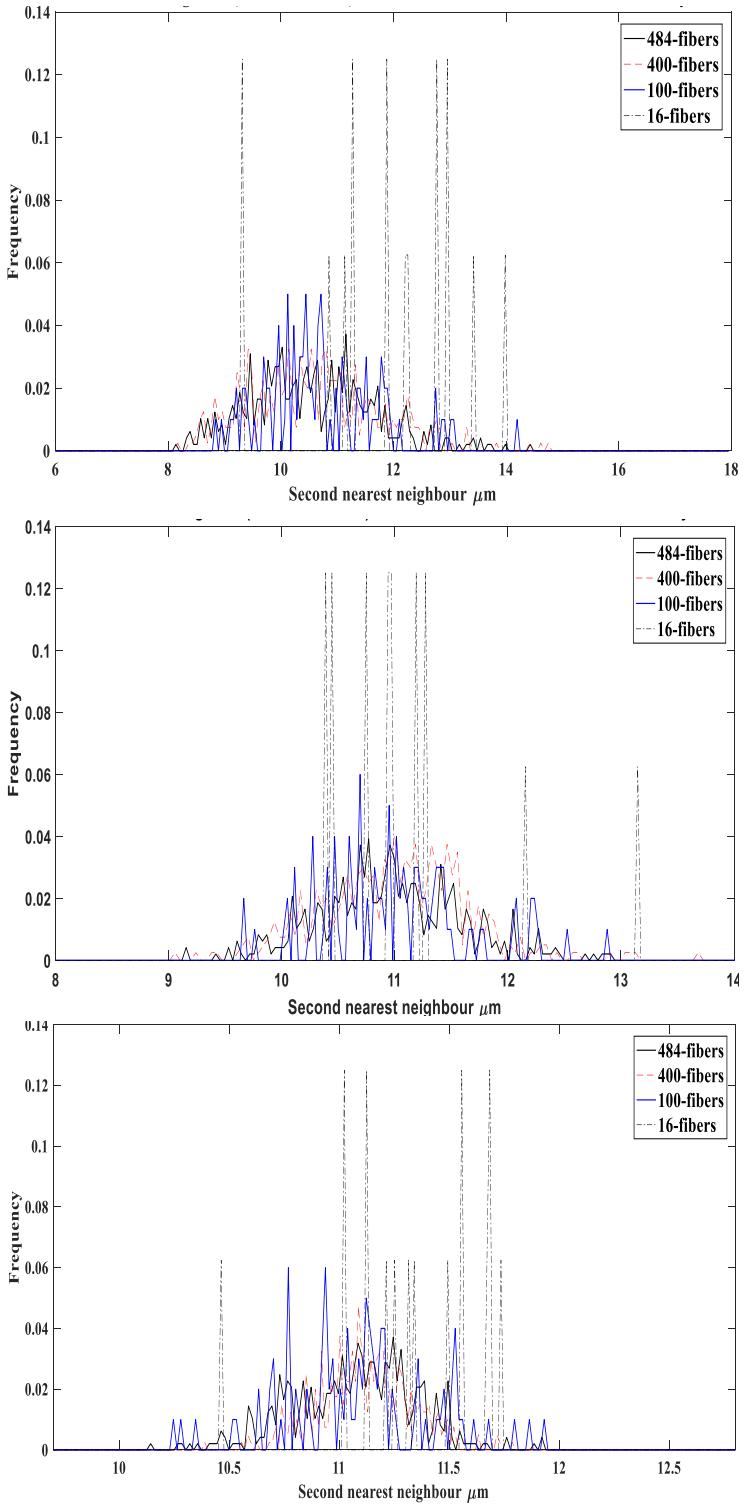


**Figure 110. Frequency of occurrence of the second nearest neighbor distance (from center to center) in µm within the RVE realizations for 40% fiber volume fraction and degrees of NU of (a)100%, (b) 60% and (c) 30% for 484, 400, 100 and 16 fibers in an RVE.**

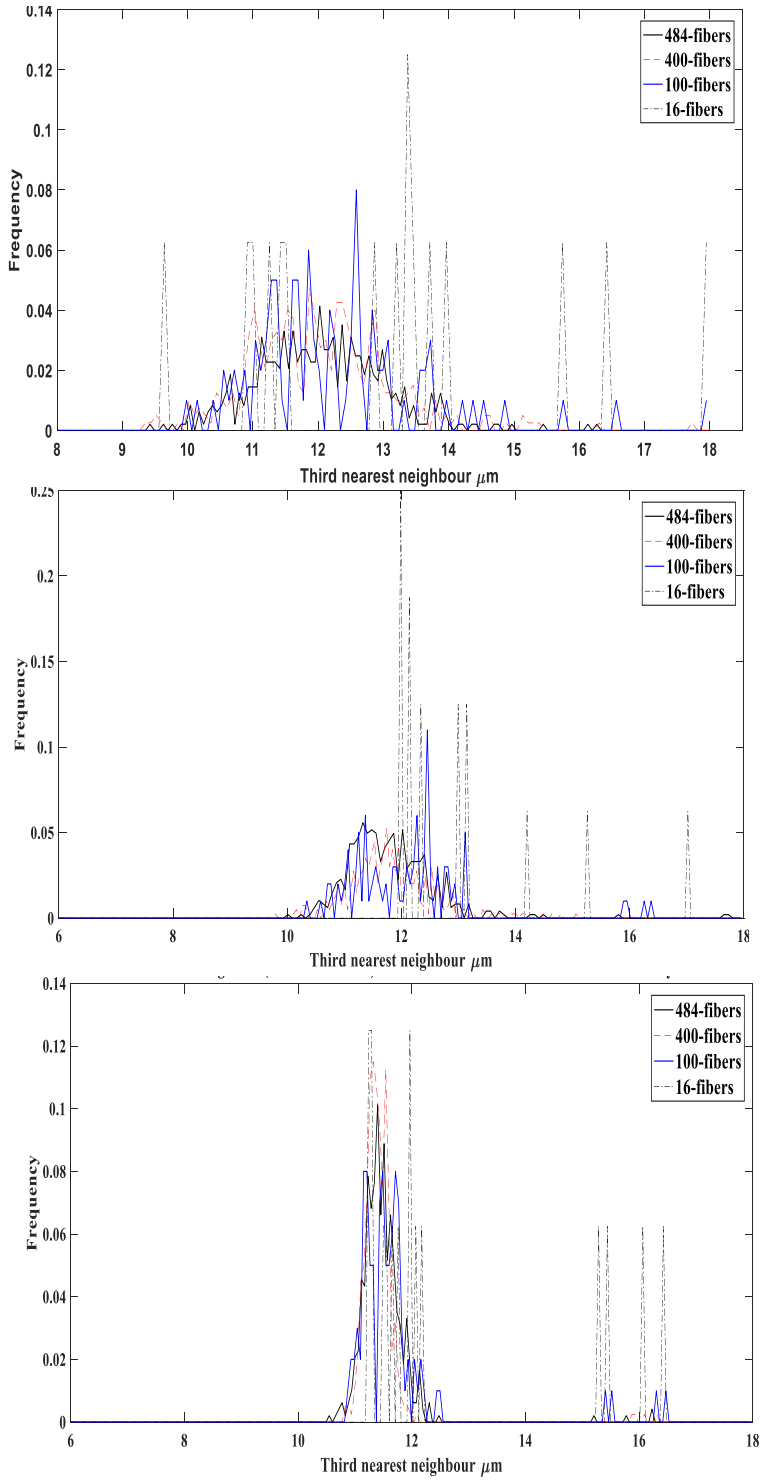


**Figure 111. Frequency of occurrence of the third nearest neighbor distance (from center to center) in μm within the RVE realizations for 40% fiber volume fraction and degrees of NU of (a)100%, (b) 60% and (c) 30% for 484, 400, 100 and 16 fibers in an RVE.**

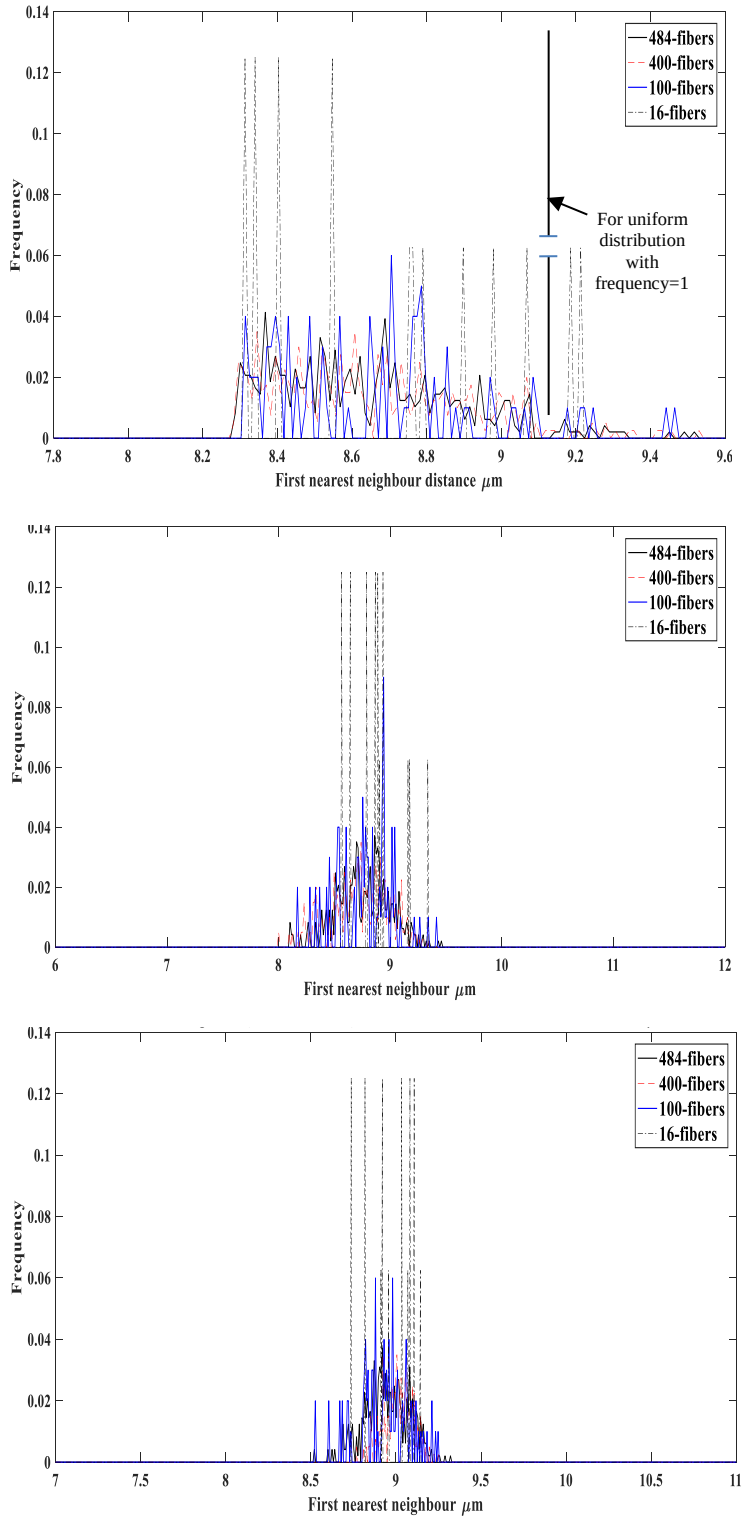


**Figure 112. Frequency of occurrence of the first nearest neighbor distance (from center to center) in µm within the RVE realizations for 60% fiber volume fraction and degrees of NU of (a)100%, (b) 60% and (c) 30% for 484, 400, 100 and 16 fibers in an RVE.**

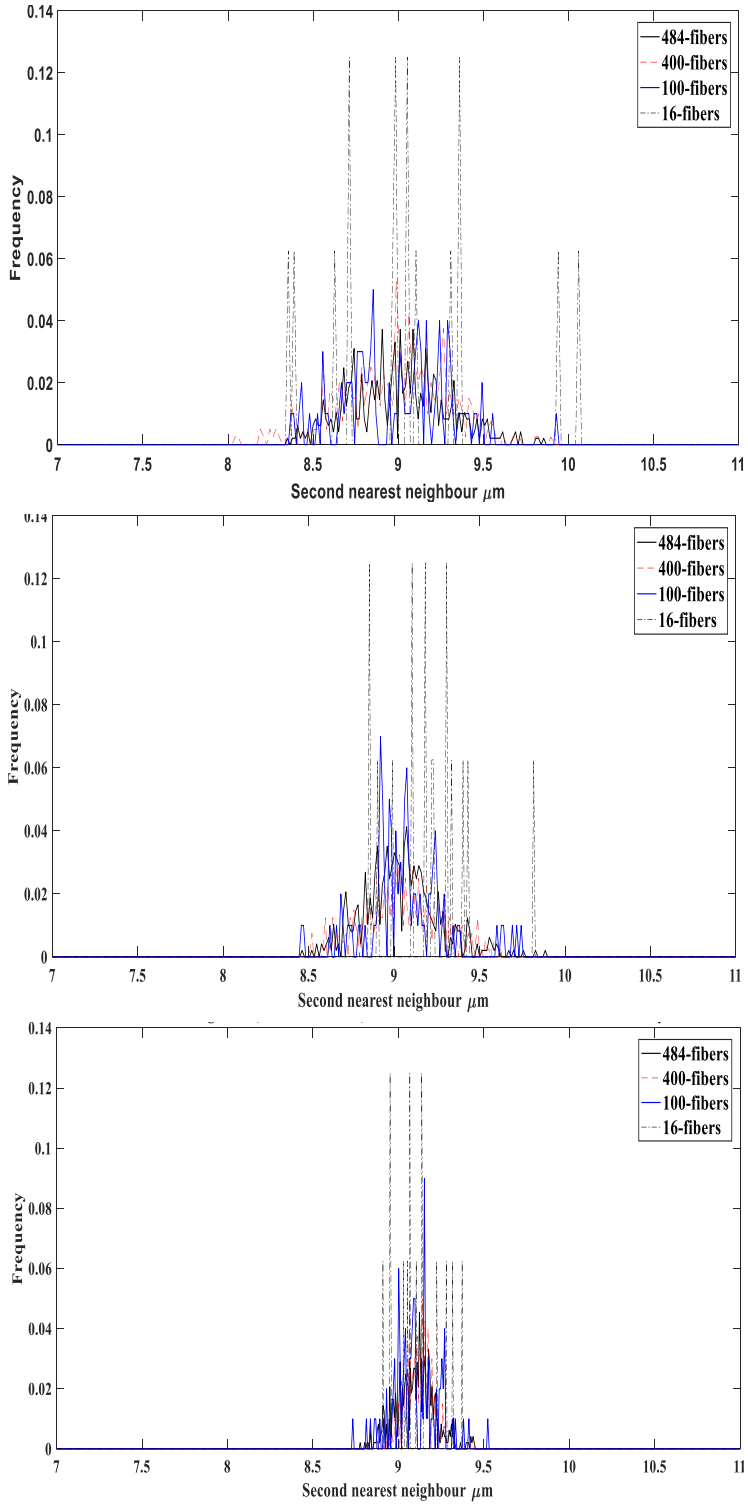


**Figure 113. Frequency of occurrence of the second nearest neighbor distance (from center to center) in µm within the RVE realizations for 60% fiber volume fraction and degrees of NU of (a)100%, (b) 60% and (c) 30% for 484, 400, 100 and 16 fibers in an RVE.**

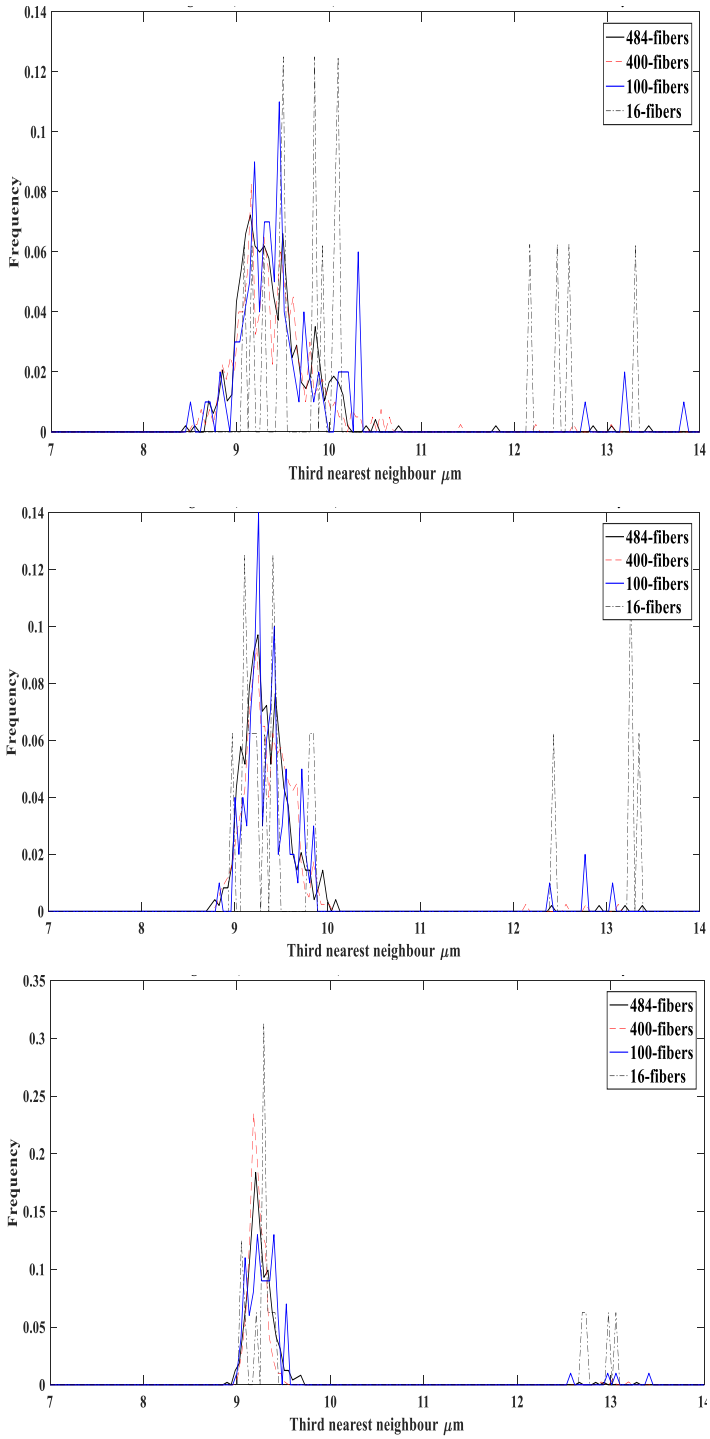


**Figure 114. Frequency of occurrence of the third nearest neighbor distance (from center to center) in µm within the RVE realizations for 60% fiber volume fraction and degrees of NU of (a)100%, (b) 60% and (c) 30% for 484, 400, 100 and 16 fibers in an RVE.**

# APPENDIX B

## DAMAGE INITIATION SITES

In this Appendix, different realizations are shown with different FVFs and different degrees of NU. The realizations also show the positions of maximum dilatational and maximum distortional energy densities, where cavitation is likely in the former, while yielding is likely in the latter. It can be observed that the maximum dilatational energy density occurs between two fibers aligned with the direction of the applied transverse tension, the x direction.

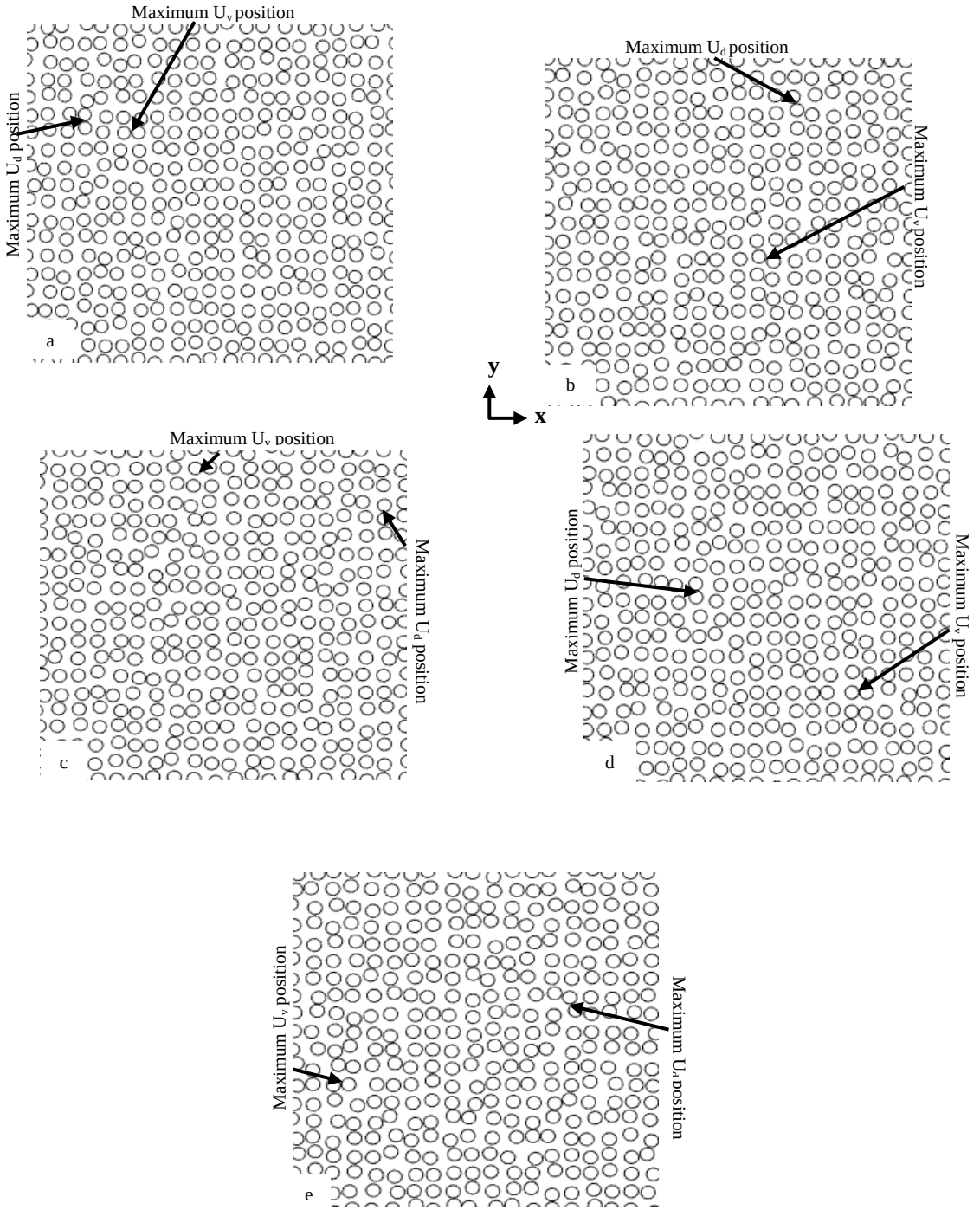


**Figure 115. Different RVEs (a-e) with 40% fiber volume fraction and 100% nonuniformity, showing the position of maximum dilatational $U_v$ and maximum distortional $U_d$ energy densities under transverse loading.**

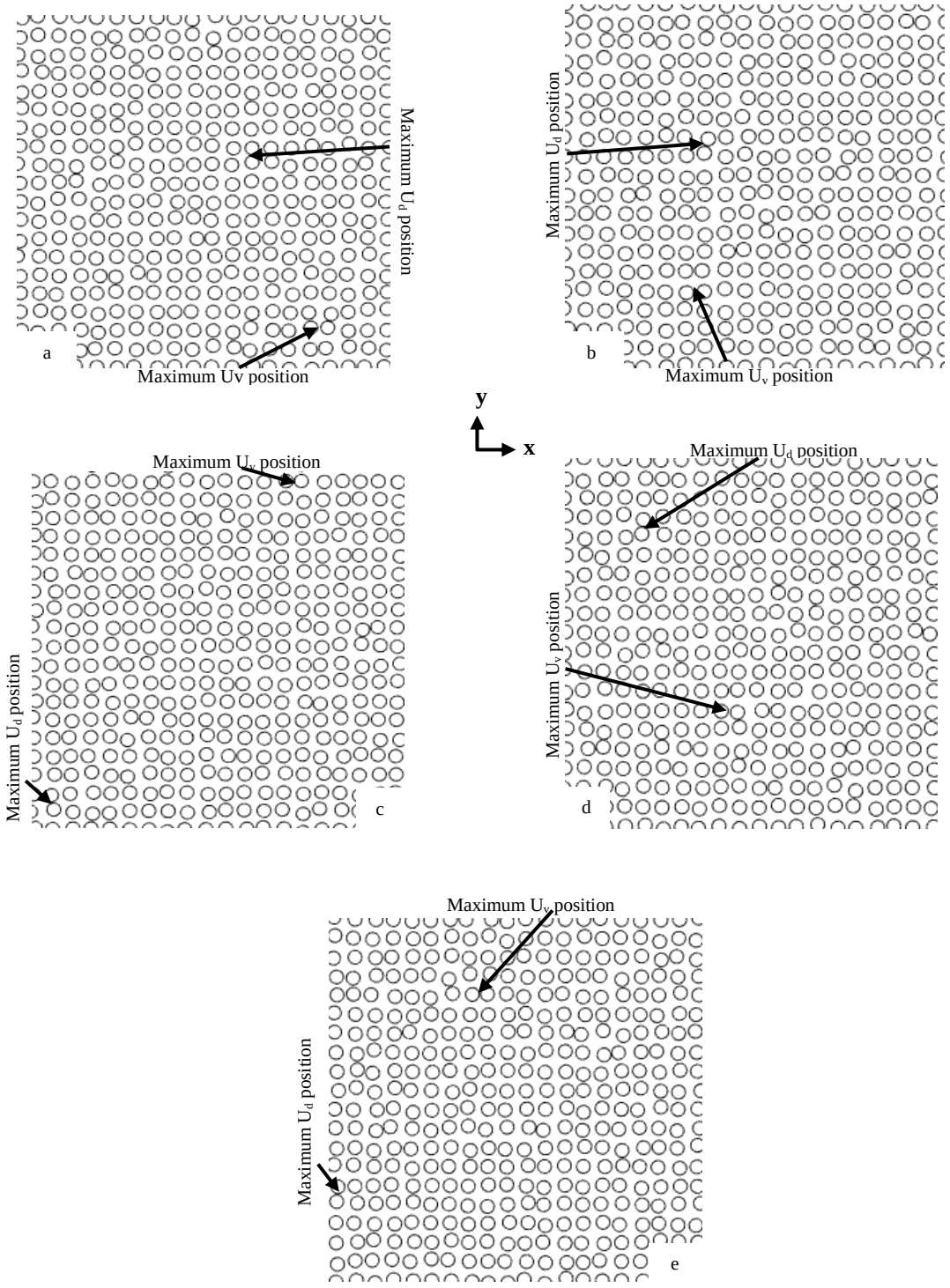


**Figure 116. Different RVEs (a-e) with 40% fiber volume fraction and 60% nonuniformity, showing the position of maximum dilatational Uv and maximum distortional Ud energy densities under transverse loading.**

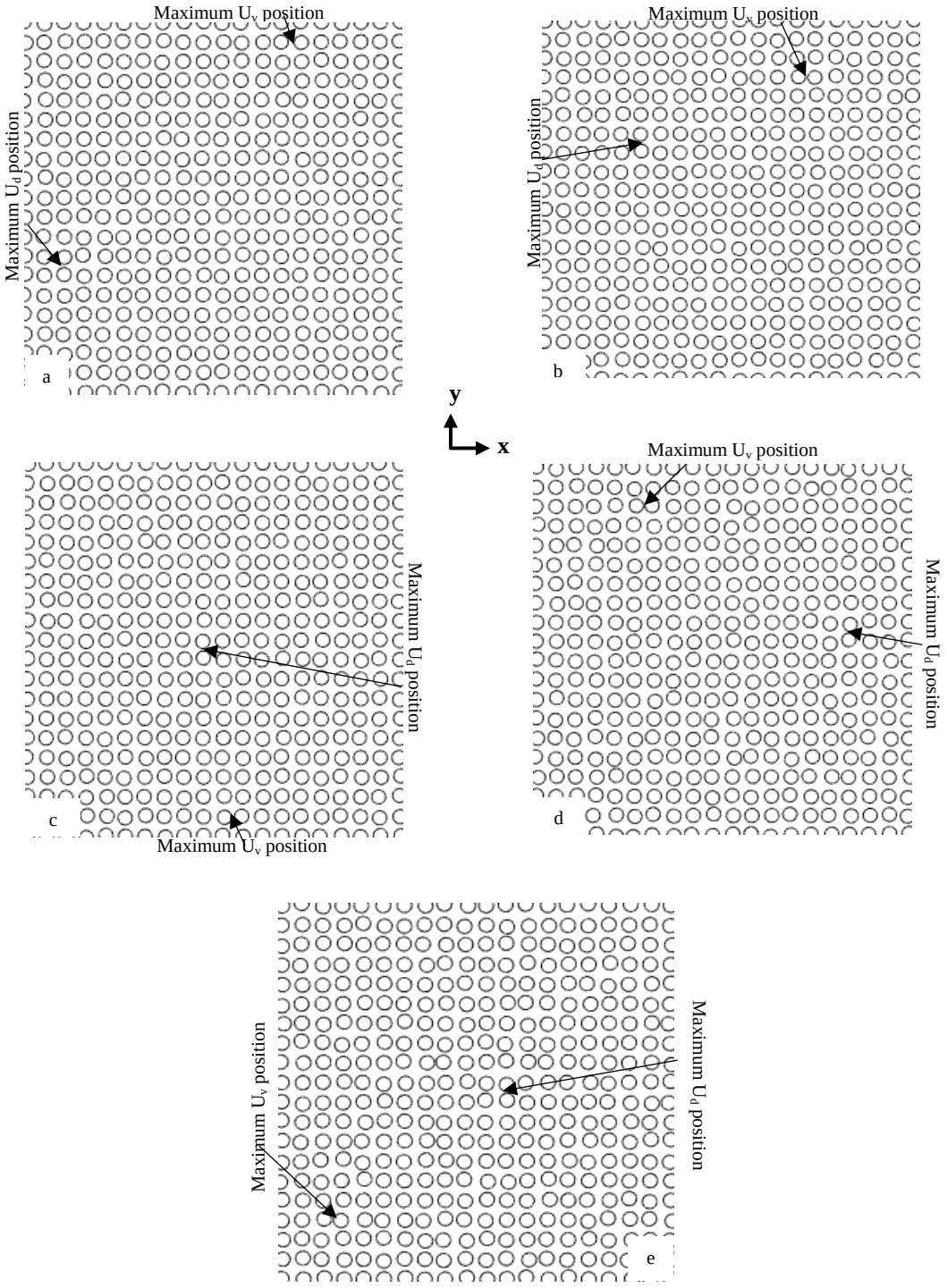


**Figure 117. Different RVEs (a-e) with 40% fiber volume fraction and 30% nonuniformity, showing the position of maximum dilatational Uv and maximum distortional Ud energy densities under transverse loading.**

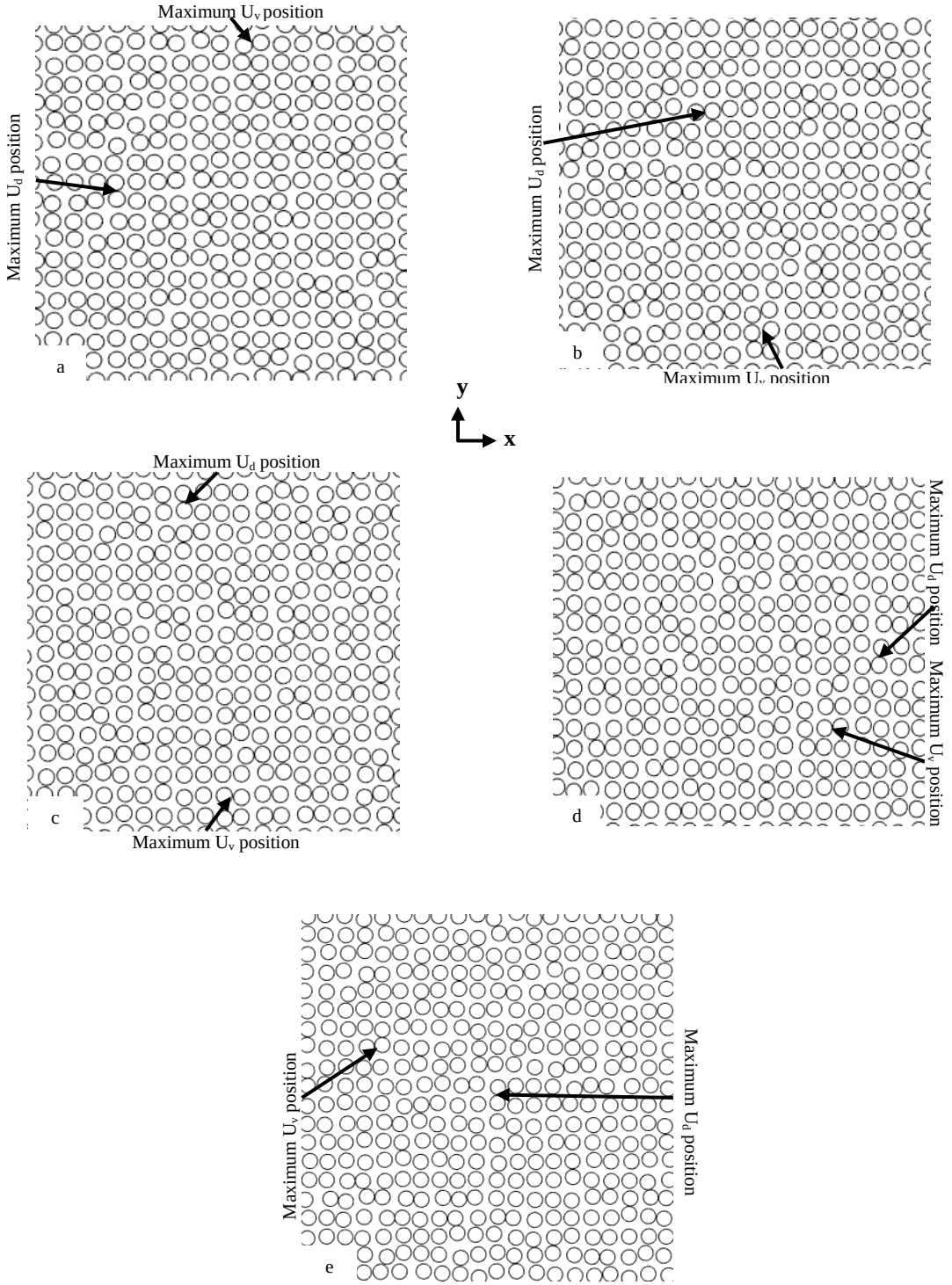


**Figure 118. Different RVEs (a-e) with 50% fiber volume fraction and 100% nonuniformity, showing the position of maximum dilatational Uv and maximum distortional Ud energy densities under transverse loading.**

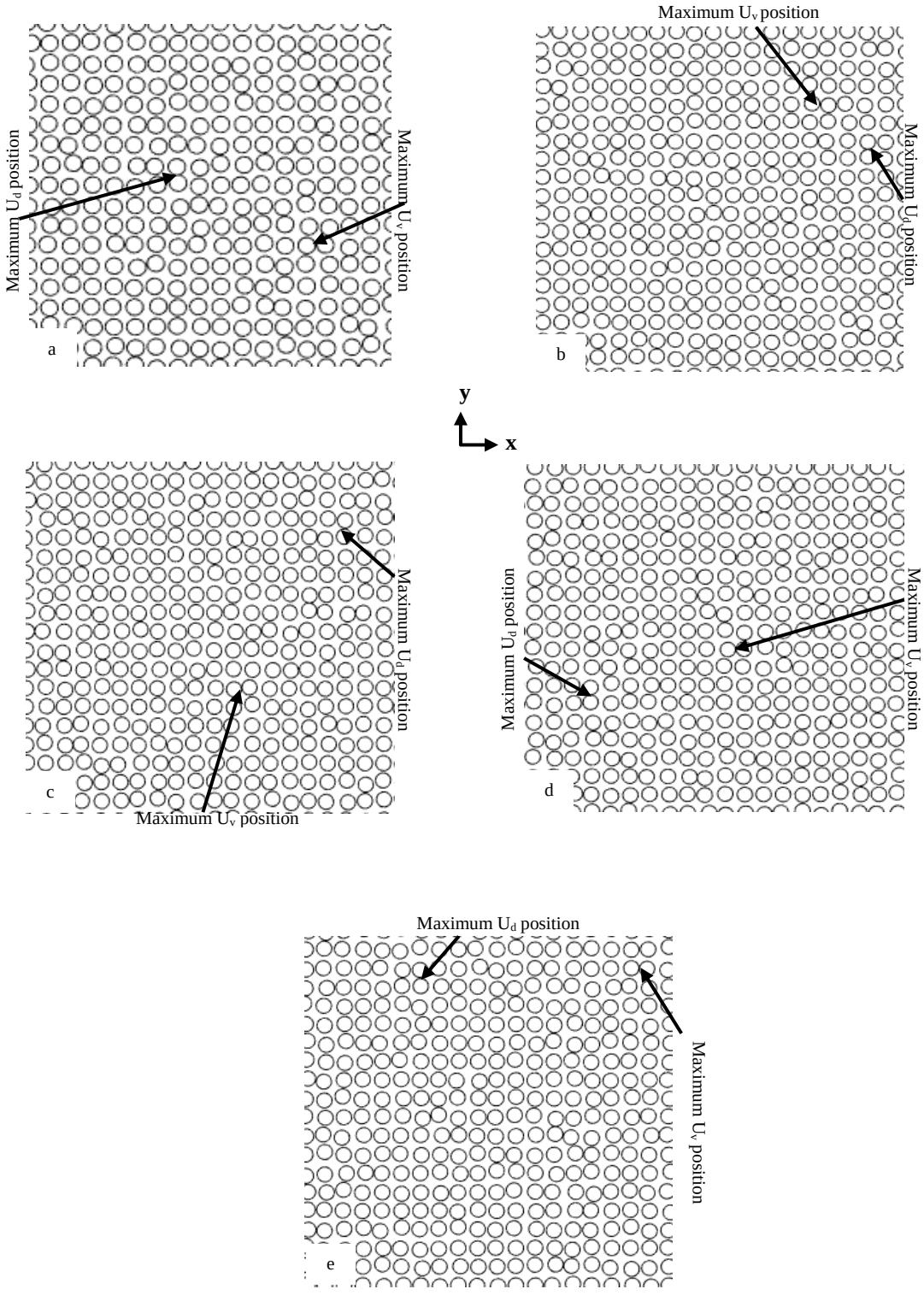


**Figure 119. Different RVEs (a-e) with 50% fiber volume fraction and 60% nonuniformity, showing the position of maximum dilatational Uv and maximum distortional Ud energy densities under transverse loading.**

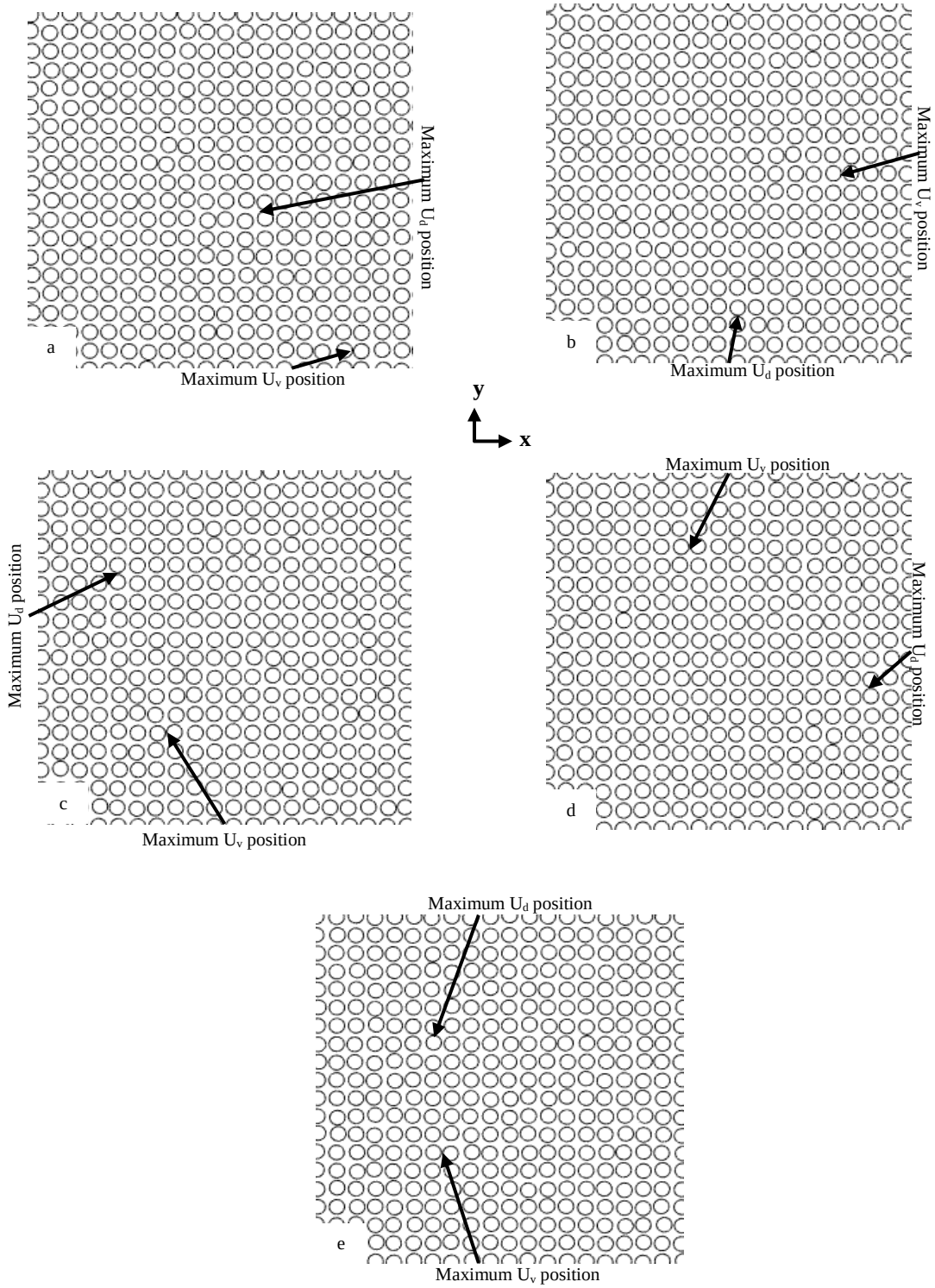


**Figure 120. Different RVEs (a-e) with 50% fiber volume fraction and 30% nonuniformity, showing the position of maximum dilatational Uv and maximum distortional Ud energy densities under transverse loading.**

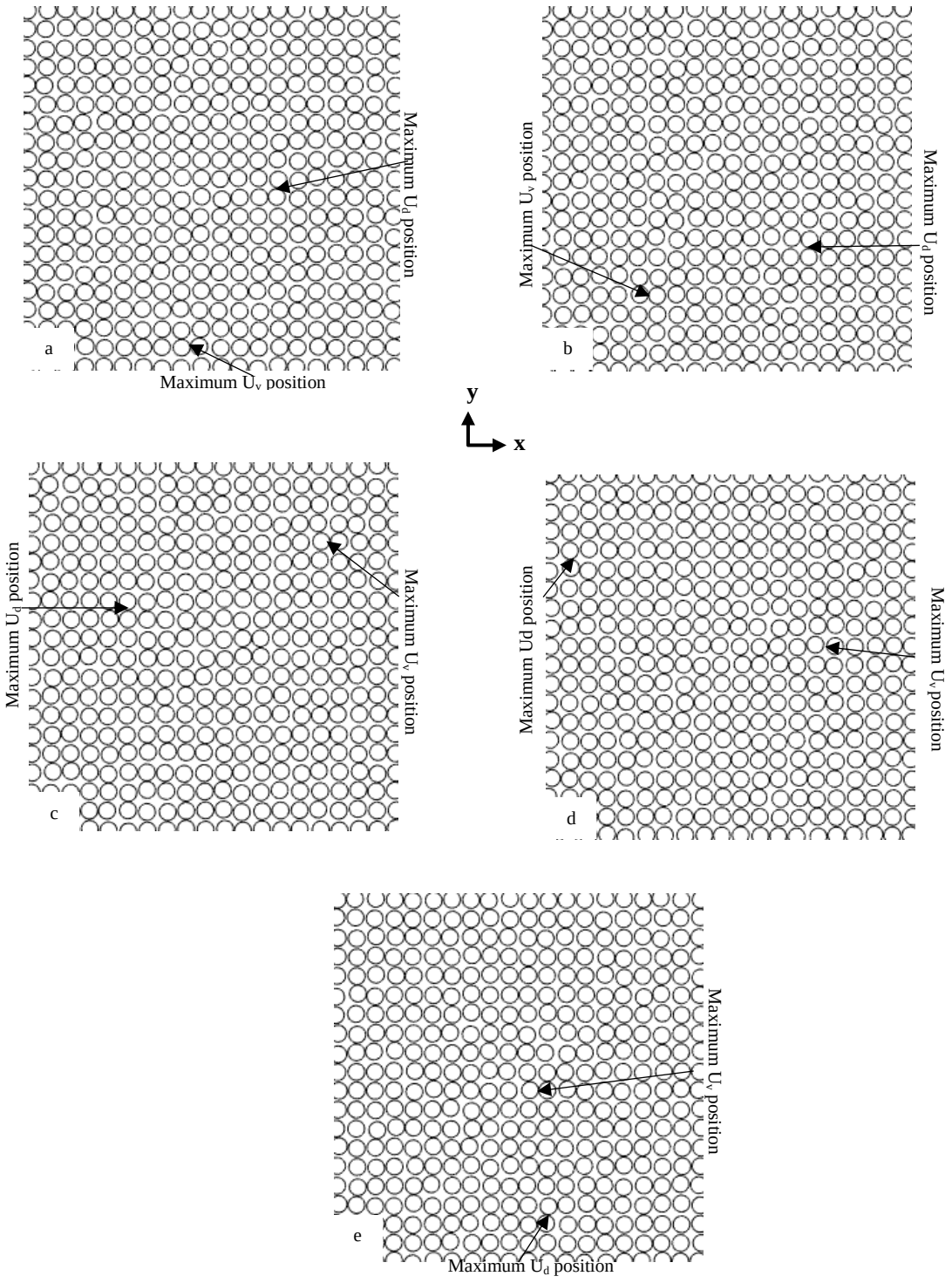


**Figure 121. Different RVEs (a-e) with 60% fiber volume fraction and 100% nonuniformity, showing the position of maximum dilatational Uv and maximum distortional Ud energy densities under transverse loading.**

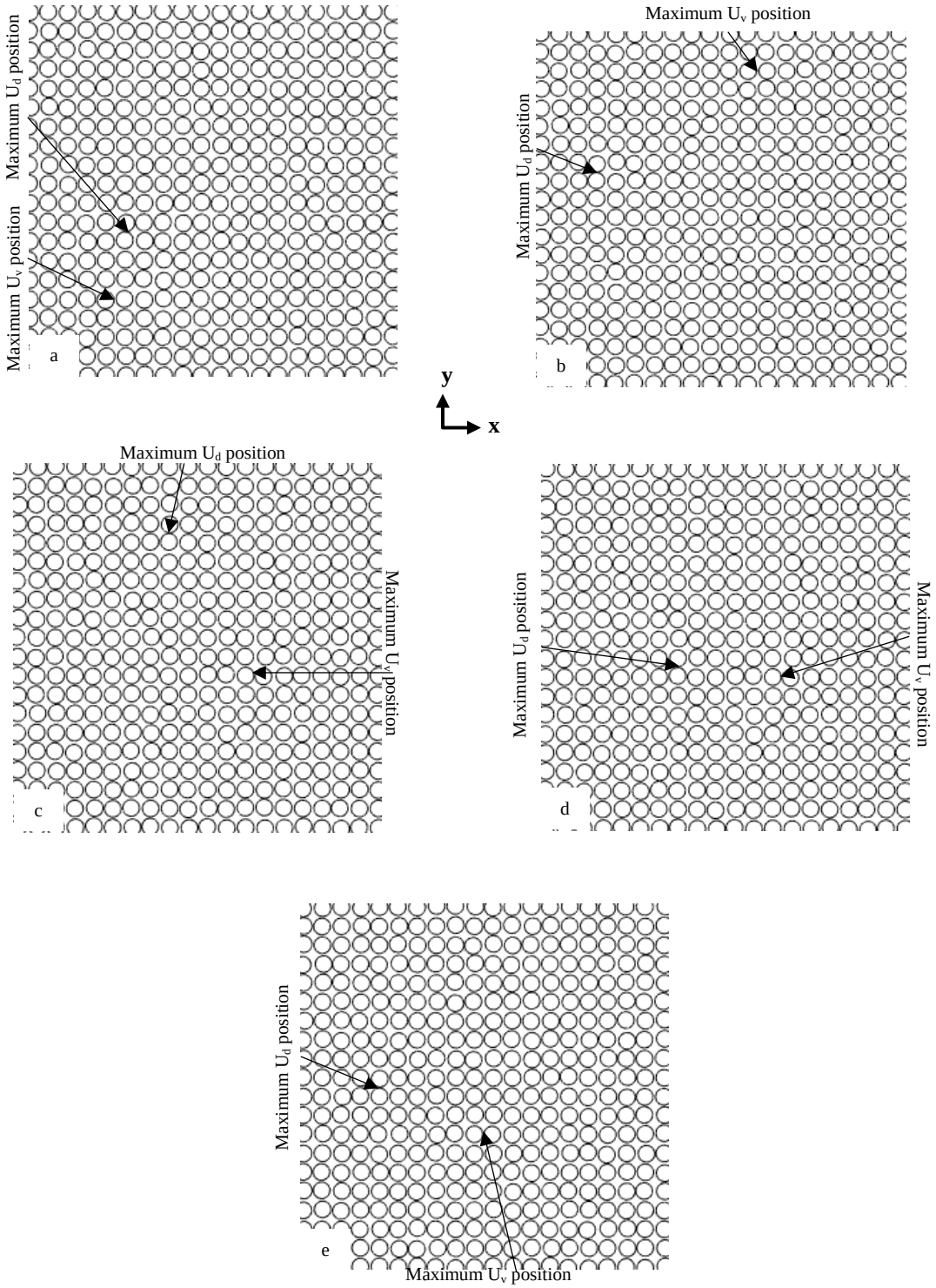


**Figure 122. Different RVEs (a-e) with 60% fiber volume fraction and 60% nonuniformity, showing the position of maximum dilatational Uv and maximum distortional Ud energy densities under transverse loading.**

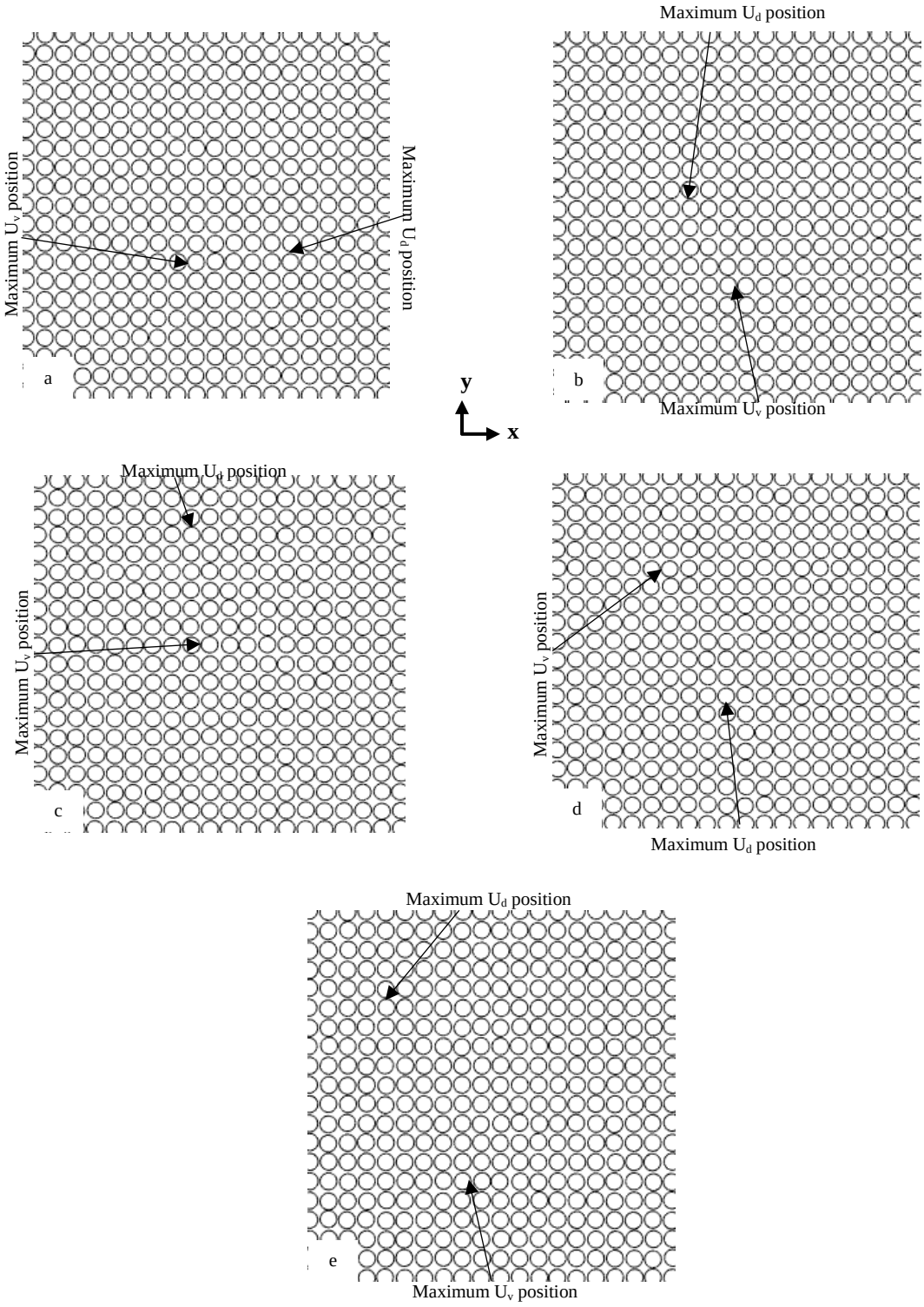


**Figure 123. Different RVEs (a-e) with 60% fiber volume fraction and 30% nonuniformity, showing the position of maximum dilatational Uv and maximum distortional Ud energy densities under transverse loading.**